Dissertation zur Erlangung des Doktorgrades
der Fakultät für Chemie und Pharmazie
der Ludwig-Maximilians-Universität München

Defect Passivation Strategies for Enhanced Longevity and Performance in Lead and Lead-Free Based Photovoltaics

Ali Buyruk

aus

Kadıköy, Turkey

2023

Erklärung

Diese Dissertation wurde im Sinne von § 7 der Promotionsordnung vom 28.November 2011 von Frau Prof. Dr. Tayebeh Ameri betreut von der Fakultät für Chemie und Pharmazie vertreten.

Eidesstattliche Versicherung

Diese Dissertation wurde eigenständig und ohne unerlaubte Hilfe bearbeitet.

München, 28.05.2024

_____

Ali Buyruk

Dissertation eingereicht am:	06.12.2023
Erstgutachter:	Prof. Dr. Tayebeh Ameri
Zweitgutachter:	Prof. Dr. Achim Hartschuh
Mündliche Prüfung am:	19.12.2023

Acknowledgement

I am still trying to figure out where to start with this writing, but all I know is that this work is ending. And it's an extraordinary feeling to complete this end with a writing. So, why does it feel strange? Let's take a look together. It all started in the early years of life, trying to understand the system around me. My first curiosity began when I visited my mother's village during summer vacation. I watched and questioned nature, the animals, the people, and everything that belonged to that village. When I got a little older, I watched space movies with my father in the evenings before going to bed, and of course, astronauts and their curious adventures. Then suddenly, my desire to become an astronaut and this relentless curiosity brought me here. But I became a chemist, not an astronaut.

I have now come to the end of a 5-year PhD process I have been researching. How can I explain how these five years have passed and what they have left in me? But I enjoyed it very much. Would you ask me? Which job or whatever it is can give you so much curiosity, questioning, and finally learning something new? My answer is to research and pursue your curiosity. For example, you will do a study that week, and you have some plans floating around in your head; I could be more organised, but you immediately produce a couple of sets of solar cells. But, you didn't find what you hoped for, and crazy questions are running around in your head, and they're running around in your head without you realising it, while you're eating, while you're taking the train home, even while you have daily conversations with people. At the end of this process, with a few concrete ideas in your head, you immediately go to the lab, and in the closed world, the glove box, you start experimenting with your ideas one by one... Do you know what the most attractive thing is? As a result of those studies, the data you obtain coincide with the abstract thoughts you have designed and solved in your head. Then you turn around and say to yourself, I know this job. This process of questioning-idea formation and the circle that continues with experimentation draws you further into this world; this time, your desire increases exponentially.

Ahhh, and then there are the realities of life: what will I do after my PhD? Post-doctoral research, short-term job contracts, an uncertain future, and the chain of these stressful questions... No, I should leave academia and find a job. I should earn money; who knows, I will have an unlimited job contract with a higher salary. But, on the other hand, it's a monotonous work life, and you are away from the pleasure of questioning and thinking and your relentless thoughts and the accompanying experiments and their confirmation. I wish everyone could have a job where they could do what they want, but that is not possible in our system. So, this is where the story of a person who goes back and forth but cannot break away from the urge to research comes to an end. I am thrilled because I experienced the happiness of writing and expressing myself uncensored for the first time.

Then, I would like to thank my supervisor, Prof. Dr Tayebeh Ameri, who contributed to this story and provided me with all kinds of material, moral, and scientific support, and Prof. Dr Thomas Bein, who opened his laboratory to us and allowed us to test our dreams with experiments. Also, instead of writing names here, I will write them directly so that no one gets offended and I don't forget them in my old age. Thank you to the entire AK BEIN group. Of course, the most important thank you goes to my sister, Neşe Buyruk, who has helped me a lot on my way to becoming a researcher.

Dili, dini, rengi ne olursa olsun, iyiler iyidir.

Hacı Bektaş Veli

Abstract

Halide perovskites have gained considerable attention in different research areas because of their unique properties and diverse applications in optoelectronics. These materials possess outstanding features, including adjustable and direct bandgaps, high electron and hole mobility, strong light absorption capabilities, and an impressive defect tolerance, resulting in extended carrier lifetimes and diffusion lengths. Halide perovskites stand out because of their ease of production, which extends to methods that can be carried out at room temperature. This combination of exceptional qualities paves the way for developing high-performance thin-film optoelectronic devices that can be manufactured using cost-effective techniques, notably solution-based methods. Consequently, "organic-inorganic electronics" has experienced substantial growth and exploration.

Nonetheless, this material's inherent chemical and structural characteristics, coupled with its low-temperature processing methods, unavoidably result in deleterious defects at both the surface and grain boundaries (GBs) of the perovskite's polycrystalline structure. These defects can considerably undermine the solar cell performance and overall material stability.

Furthermore, concerns over the environmental impact of lead (Pb) have driven the search for lead-free alternatives. This quest has led to investigating divalent metals like tin (Sn^{2+}) or germanium (Ge^{2+}), although these alternatives have encountered stability issues. Another promising approach involves heterovalent substitution, in which a trivalent cation such as Bi^{3+} is combined with a monovalent cation like Ag^{+} to create double perovskites, resulting in compounds with the chemical formula $A_2M'M''X_6$ (examples include $Cs_2AgBiBr_6$, $Cs_2AgInCl_6$, $Cs_2AgSbCl_6$, etc.). In contrast to traditional perovskite materials, emerging substances like silver-bismuth halides, characterised by their chemical formula $Ag_aBi_bX_{a+3b}$ and rudorffite structures, are gaining attention as potential light absorbers in solar cells. Their appeal is based on several key attributes, including their appropriate band gap energy (Eg) and remarkable light-absorbing properties.

In this thesis, our primary focus was to investigate the defects at the surfaces and grain boundaries of polycrystalline lead-based perovskite materials and lead-free silver-bismuth halides. These defects significantly negatively impact the performance and stability of photovoltaic devices using these materials. To address these naturally occurring defects, we explored various materials and concepts to develop potential solutions.

The opening section of this thesis, designated as *Chapter 1*, begins by elucidating the theoretical foundations of the relevant research area. Commencing with an exploration of semiconductors, the chapter subsequently delves into the practical applications of these materials, focusing mainly on solar

cells. It then discusses an alternative and promising material used in solar cells: lead-containing perovskite-based materials. Continuing within this class, attention is given to more stable subcategories, notably those characterised by low dimensionality, such as 2D and 1D variations. The chapter concludes by examining the Rudorffite material class, which offers a silver-bismuth halide-based alternative to mitigate concerns related to the toxicity of lead-based perovskite materials.

The subsequent *second chapter* provides introductory information regarding characterisation techniques commonly employed in these studies.

Chapter 3 of the thesis delves into applying 1,10-phenanthroline, a bidentate chelating ligand, at the methylammonium lead iodide ($MAPbI_3$) film interface and the hole-transport layer. This compound serves a dual purpose, acting as a passivating agent for surface defects involving under-coordinated lead ions and as a means to convert excess or unreacted lead iodide (PbI_2) at interfaces into neutralised and beneficial species (PbI_2(1,10-phen)x, with x being 1 or 2). This transformation is crucial for enabling efficient hole transfer at the modified interface and enhancing long-term stability. The efficacy of 1,10-phenanthroline in healing defects is confirmed through a comprehensive set of techniques, including photoluminescence measurements (both steady-state and time-resolved), space-charge limited current (SCLC) measurements, light intensity-dependent JV measurements, and Fourier-transform photocurrent spectroscopy (FTPS). Additionally, advanced X-ray scattering methods, nano-Fourier transform infrared (nano-FTIR) spectroscopy, and high-angle annular dark-field scanning transmission electron microscopy (HAADF-STEM) are employed to provide a detailed analysis of the structure and chemical composition at the nanoscale of the perovskite surface following treatment.

Chapter 4 of the thesis introduces the application of a novel organic cation, 2-(thiophene-2yl-)pyridine-1-ium iodide (ThPyI), at the surface of 3D methylammonium lead iodide (MAPI) perovskite films, as well as its incorporation into the bulk structure. ThPyI is used either as a passivator on top of 3D MAPI to create surface-passivated films with an additional stable 1D perovskite phase, formed as a product of the unreacted surface PbI2 and organic cation or independently introduced into the 3D MAPI precursor to achieve bulk passivation. In both approaches, ThPyI leads to improved power conversion efficiency (PCE) and enhanced stability in solar cells. Moreover, advanced characterisation techniques, such as Grazing Incidence Wide-Angle X-ray Scattering (GIWAXS), confirm that ThPyI promotes the preferred orientation of bulk MAPI slabs, enhancing charge transport. Notably, the bulk-passivated 3D configuration demonstrates excellent stability, with 84% PCE retained after 2000 hours of exposure without encapsulation. This study introduces innovative strategies for using organic spacers with diverse binding motifs and passivation techniques to address defects in hybrid 3D/1D perovskite solar cells.

The last chapter of the thesis focuses on applying a well-established material, poly(2,5-dimercapto-1,3,4-thiadiazole), to enhance the efficiency and stability of solar cells based on Ag_3BiI_6.

The central strategy in this chapter involves using in-situ polymerisation for bulk treatment to passivate the detrimental defects within the internal structure of Ag_3BiI_6. The study shows that polymer-treated Ag_3BiI_6 films can enhance efficiency and maintain stability when utilised in solar applications, underlining their potential as a safer and more sustainable option for solar energy conversion.

Table of Contents

Contents

List of Abbreviations

A	Absorbance
ABI	Silver-bismuth halides
BE	Back electrode
BPVE	Bulk photovoltaic effect
BSE	Back-scattered electrons
CB	Conduction band
CBM	Conduction band minimum
CIGS	Copper indium gallium selenide
CRT	Cathode ray tube
EF	Fermi level energy
Eg	Band gap energy
EL	Electroluminescence
EQE	External quantum efficiency
ETL	Electron transport layer
ETM	Electron transporting material
EV	Vacuum level energy
FA	Formadinium
FF	Fill factor
FS	Forward scan
FTO	Fluorine-doped tin oxide
FWHM	Full width at half maximum
HI	Hysteresis index
HOIP	Hybrid organic-inorganic perovskite
HTL	Hole transport layer
HTM	Hole transporting material

IC	Integrated circuit
ITO	Indium tin-oxide
Jsc	Short-circuit current
J-V	Current-voltage
LEC	Light-emitting electrochemical cell
LED	Light-emitting diode
MA	Methylammonium
$MAPbI_3$	Methylammonium lead iodide
MAPI	Methylammonium lead iodide
MPP	Maximum power point
OIHPs	Organic-inorganic lead halide perovskites
OLED	Organic light-emitting diodes
Pb	Lead
PCE	Power conversion efficiency
PL	Photoluminescence
PSC	Perovskite solar cell
PV	Photovoltaic
PXRD	Powder X-ray diffraction
RMS	Root-mean-square
RS	Reverse scan
SE	Secondary electrons
SEM	Scanning Electron Microscopy
Si	Silicon
S-Q	Schockley-Queisser
T	Transmission
TCO	Transparent conductive oxide
TCSPC	Time-Correlated Single Photon Counting

TEM	Transmission Electron Microscopy
UPS	Ultraviolet Photoelectron Spectroscopy
UV-Vis	Ultraviolet-Visible
VBM	Valence band maximum
V_{oc}	Open-circuit voltage

1 Introduction

1.1 Semiconductors

Solid-state materials fall into three basic categories based on electrical conductivity: conductors, semiconductors, and insulators. The critical materials for these three classes are displayed in Figure 1.1, along with their matching resistivities ($\rho = 1/\sigma$) and electrical conductivities (σ). Conductors, which include metals like silver and aluminium, have high conductivities, usually falling in the range of 10^4 to 10^6 S.cm^{-1}. In contrast, insulators with extremely low conductivities include fused quartz and glass, usually in the range of 10^{-18} to 10^{-8} S.cm^{-1}.[1]

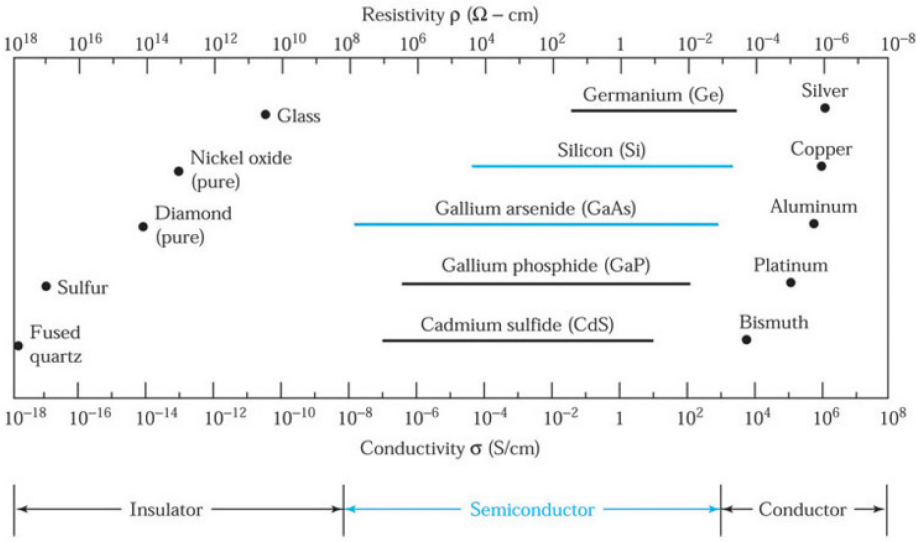

Figure 1.1 The typical range of conductivities for insulators, semiconductors, and conductors.[1]

Since the early nineteenth century, several semiconductors have been the focus of research into the study of semiconductor materials. Column IV is occupied by element semiconductors, which comprise individual atom species like silicon (Si) and germanium (Ge). Germanium was a popular semiconductor material in the early 1950s. Nevertheless, silicon has become a viable substitute, effectively replacing germanium as the leading semiconductor material since the early 1960s.[2]

Among these types of potential semiconductors, silicon has potential in semiconductor services. Several factors contribute to the preference for silicon. Silicon-based devices exhibit superior properties at room temperature, and high-quality silicon dioxide can be thermally grown, enhancing their utility. Additionally, economic considerations play a role, as device-grade silicon is more cost-effective than other semiconductor materials. Silicon, available in silica and silicates, constitutes 25% of the Earth's crust, with silicon ranking second only to oxygen in terms of abundance. Presently, silicon stands as

one of the most extensively studied elements in the periodic table, and silicon technology surpasses all other semiconductor technologies in terms of advancement and applicability.

There are 18 primary devices, each with more than 140 variations associated with them. Interestingly, these diverse devices can be assembled using a relatively small set of fundamental device building blocks.[3] Some of the significant semiconductor devices arranged in chronological order are shown in Table 1.1.[4]

Year	Semiconductor Device[a]	Author(s)/Inventor(s)
1874	Metal-semiconductor contact[b]	Braun
1907	Light emitting diode[b]	Round
1947	Bipolar transistor	Bardeen, Brattain, and Shockley
1949	*p–n* junction[b]	Shockley
1952	Thyristor	Ebers
1954	Solar cell[b]	Chapin, Fuller, and Pearson
1957	Heterojunction bipolar transistor	Kroemer
1958	Tunnel diode[b]	Esaki
1960	MOSFET	Kahng and Atalla
1962	Laser[b]	Hall et al.
1963	Heterostructure laser[b]	Kroemer, Alferov and Kazarinov
1963	Transferred-electron diode[b]	Gunn
1965	IMPATT diode[b]	Johnston, DeLoach, and Cohen
1966	MESFET	Mead
1967	Nonvolatile semiconductor memory	Kahng and Sze
1970	Charge-coupled device	Boyle and Smith
1974	Resonant tunneling diode[b]	Chang, Esaki, and Tsu
1980	MODFET	Mimura et al.
2004	5 nm MOSFET	Yang et al.

Table 1.1 Some of the significant semiconductor devices in chronological order.

MODFET stands for modulation-doped field-effect transistor; a MOSFET stands for metal-oxide-semiconductor field-effect transistor; and MESFET stands for the metal-semiconductor field-effect transistor. B denotes a device with two terminals; other devices have three or four terminals.

1.2 Solar Cells

Solar cells, which use three main processes to turn light into current, are devices made to convert sunlight directly into electricity (Figure 1.2).[5] The bulk photovoltaic effect (also known as the shift current effect), photoconductivity, and the photovoltaic effect. A p-n junction usually is necessary for the photovoltaic effect. Here, photo-induced charges (holes and electrons) in p-type and n-type materials are separated, transferred, and then gathered at an electrode to produce photocurrent. Becquerel made the first demonstration of the photoelectric effect in 1839.[6]

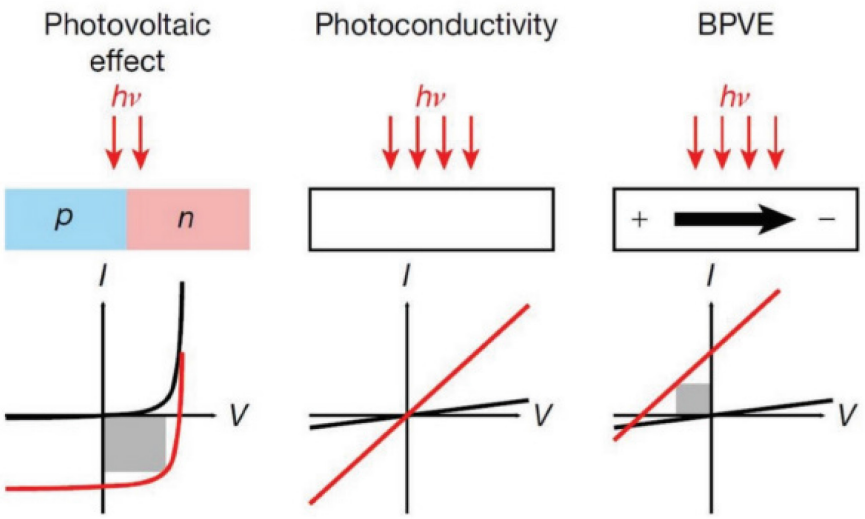

Figure 1.2 There are different mechanisms to convert light into electrical current, as depicted in the current (I) versus voltage (V) plots. The black lines represent the I-V characteristics in the dark, while the red lines represent the I-V characteristics under illumination. The grey rectangles indicate the output power. In this context, "BPVE" stands for the bulk photovoltaic effect.

The p-n junction solar cell, represented in Figure 1.3, comprises several components, including a shallow p-n connection on the surface, a back ohmic contact encircling the whole rear surface, a front ohmic contact stripe and fingers, and a front antireflection coating surface. It is noted that when incident light, coming from the air (refractive index, n = 1), strikes the semiconductor silicon (with a refractive index of n = 3.5), approximately 31% of the incoming light is reflected and not available for conversion to electrical energy within the silicon solar cell. Reducing this surface reflection is essential to enhance the cell's efficiency.

It is crucial to remember that photons with energies lower than the bandgap (Eg) do not affect the output of the solar cell when examining the sun spectrum. On the other hand, photons with energy above the bandgap (Eg) provide Eg energy to the cell's output, and any energy above Eg is lost as heat. The intrinsic electric field keeps electron-hole pairs (EHPs) apart as they form inside the depletion layer. As a result, the inherent voltage, determined by the energy gap (Eg), limits the potential difference. It is important to remember that in a semiconductor, photons are only absorbed at energies greater than the bandgap. Because of the narrow solar spectrum, the light-generated current diminishes as the energy gap increases. This suggests that maximizing a solar cell's efficiency depends on the selected semiconductor material and bandgap.

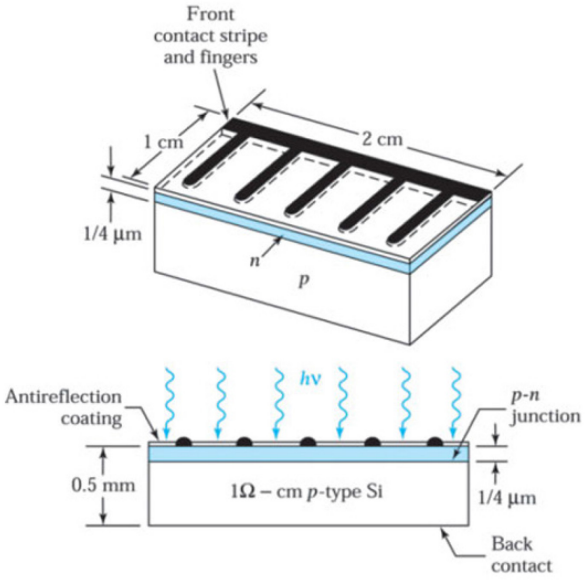

Figure 1.3 Schematic representation of a silicon p-n junction solar cell.[7]

To derive the conversion efficiency of a solar cell, the energy band diagram of a p-n junction is considered under solar radiation, as depicted in Figure 1.4a. The solar cell's open-circuit voltage (V_{OC}) depends on the intensity of incident light. Notably, the efficiency of a solar cell is not critically dependent on the bandgap of the semiconductor material. Semiconductors with bandgaps ranging from 1 to 2 electron volts (eV) can all be considered suitable for use in solar cells.

Figure 1.4 b showcases the equivalent circuit for a solar cell, a key tool in analysing its electrical behaviour. This circuit, featuring a constant-current source parallel to the junction, is instrumental in determining the solar cell's performance characteristics, including conversion efficiency. The current source, denoted as IL, results from the excitation of excess charge carriers by solar radiation. It represents the diode saturation current, and RL is the load resistance.

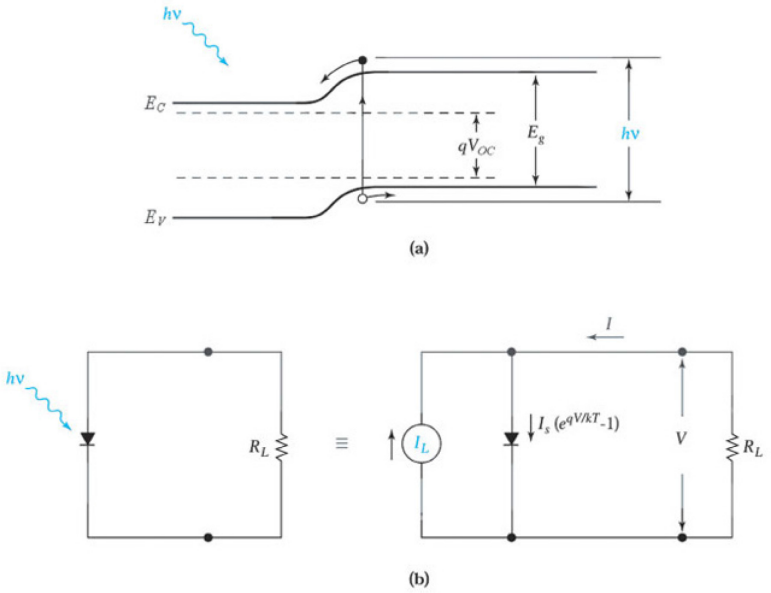

Figure 1.4 (a) A p-n junction solar cell's energy band diagram under solar radiation. (b) An idealized circuit representation of a solar cell.[1]

A solar cell's power conversion efficiency is determined by

$$\eta = \frac{I_m V_m}{P_{in}} = \frac{I_L\left[V_{OC} - \frac{kT}{q}\ln\left(1+\frac{qV_m}{kT}\right) - \frac{kT}{q}\right]}{P_{in}} \tag{1.1}$$

or

$$\eta \quad \frac{FF \cdot I_{SC} V_{OC}}{P_{in}}, \tag{1.2}$$

where Pin is the incident power, and FF is the fill factor defined as

$$FF \equiv \frac{I_m V_m}{I_{SC} V_{OC}} \cong 1 \quad \frac{kT}{qV_{OC}}\ln\left(1+\frac{qV_m}{kT}\right) \quad \frac{kT}{qV_{OC}}, \tag{1.3}$$

1.3 Perovskite Solar Cells

The unique properties and wide variety of optoelectronic applications of halide perovskites have led to their fast investigation. Longer carrier lifetimes and diffusion lengths demonstrate these materials' remarkable qualities, including adjustable and direct bandgaps, [8-13] high electron and hole mobilities, [14-16] strong light absorption capabilities,[17] and remarkable defect resistance. Low rates of nonradiative recombination are also evident in these materials.[18-20] What sets halide perovskites apart is their ease of fabrication, which extends to room-temperature deposition methods.[21-22] This remarkable combination of qualities opens the door to developing high-performance thin-film optoelectronic devices that can be produced using cost-effective processes, such as solution-based methods. As a result, the "organic-inorganic electronics" field has witnessed significant growth and exploration.[23]

Though early research concentrated on thin-film transistors [24-26] and light-emitting diodes,[27–29] halide perovskites have most recently made significant progress in photovoltaics. Over the past ten years, PSCs—perovskite solar cells—have rapidly advanced power conversion efficiency (PCE) compared to other thin-film technologies.[30-35] This development highlights halide perovskites' enormous potential for solar energy applications. At this point, PSCs (perovskite solar cells) have surpassed 26% in power conversion efficiencies (PCEs).[36]

The perovskite family includes a variety of structural variations, but they are all related by a common motif that comes from the crystal lattice of the original perovskite mineral, $CaTiO_3$. The chemical formula ABX_3 can be used to express this structure. In this structure, the shared corners of BX6 octahedra create an extended three-dimensional network. Within this framework, A cations occupy the cuboctahedral spaces. The structure's stability results from electrostatic interactions between the A-site cations and the anionic B-X framework (Figure 1.5a). In some cases, hydrogen bonding may occur between organic A cations and halogen anions, although this interaction is complicated by dynamic disorder at processing-relevant temperatures and is irrelevant for all inorganic compositions.[37]

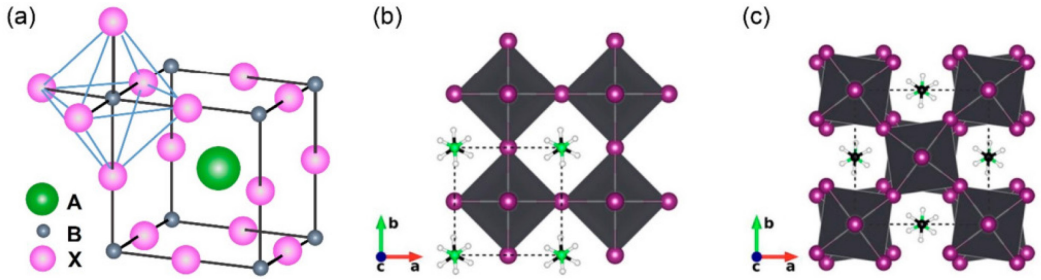

Figure 1.5 (a) The crystal structure of the three-dimensional perovskites: the A cations (green spheres) live in the spaces between the BX6 octahedra. In contrast, the X anions (pink spheres) are situated at the vertices and B cations (grey spheres) at their centres. $MAPbI_3$'s schematic structural depiction showing that in the (b) pseudocubic and (c) tetragonal phases, MA stands for methylammonium.[38–39]

Some conditions must be fulfilled in order for this structure to form. X is an anion, and A and B are cations in most cases. In order to preserve charge balance (for example, in halide perovskites), the total of A and B's valences needs to be three times that of X. Moreover, due to restrictions on the relative sizes of the ions, the structure can only hold a specific combination of ions. The limitations are commonly expressed in terms of the Goldschmidt tolerance factor, represented by the letter "t," which is determined by considering the ionic radii of rA, rB, and rX.[40]

$$t = \frac{\boldsymbol{rA}+\boldsymbol{rB}}{\sqrt{\boldsymbol{2}}(\boldsymbol{rB}+\boldsymbol{rX})} \tag{1.4}$$

Empirically, the 3D perovskite structure is typically favoured when the Goldschmidt tolerance factor, denoted as "t," falls within the range of 0.8 to 1.63.[41] Additionally, another factor known as the octahedral factor, denoted as "μ" and calculated as the ratio of the ionic radii of the B and X atoms ($\mu = r_B/r_X$), plays a significant role in determining the preferred coordination of B atoms with X atoms. In the context of the perovskite structure, μ assesses whether the B atoms tend to adopt octahedral coordination with X atoms or whether they prefer coordination numbers that are either larger or smaller. Generally, B atoms exhibit a preference for octahedral coordination with X atoms when μ falls within the range of 0.4 to 0.9.[42] Within the category of perovskite materials, only Cs (Cesium), MA (Methylammonium) and FA (Formamidinium) cations are considered "established." Other cations, such as Na (Sodium), K (Potassium), Rb (Rubidium), imidazolium, ethylamine, and guanidinium, are not suitable for consideration as they are either too small or too large for the perovskite structure (Figure 1.6).[43]

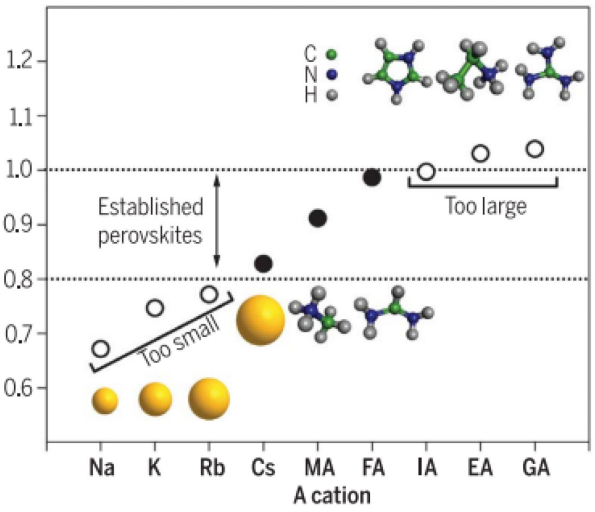

Figure 1.6 The tolerance factor (t) for $APbI_3$ perovskite varies with different A cations.

The typical configuration of perovskite solar cells (PSCs) is p-i-n or n-i-p. Figure 1.7a shows that this arrangement places the nominally intrinsic perovskite absorber between an n-type electron transport layer (ETL) and a p-type hole transport layer (HTL). As shown in Figure 1.7b, this structure may incorporate a mesoporous scaffold that is either insulating or semiconducting.

While the perovskite absorber is generally considered intrinsic (i), its exact characteristics can depend on fabrication conditions and the substrate. However, the perovskite layer typically has lower doping than the adjacent materials, which means it has a relatively minor effect on the built-in electric field within the device. The anode and cathode connect to the ETL and HTL, respectively, and these contact points can be made of metals or transparent conducting oxides (TCOs). For consistency, it is conventionally assumed that the anode and cathode are the terminals responsible for extracting electrons and holes, respectively (Figure 1.7c). This terminology aligns with the direction of current flow during average power generation in the device.[44]

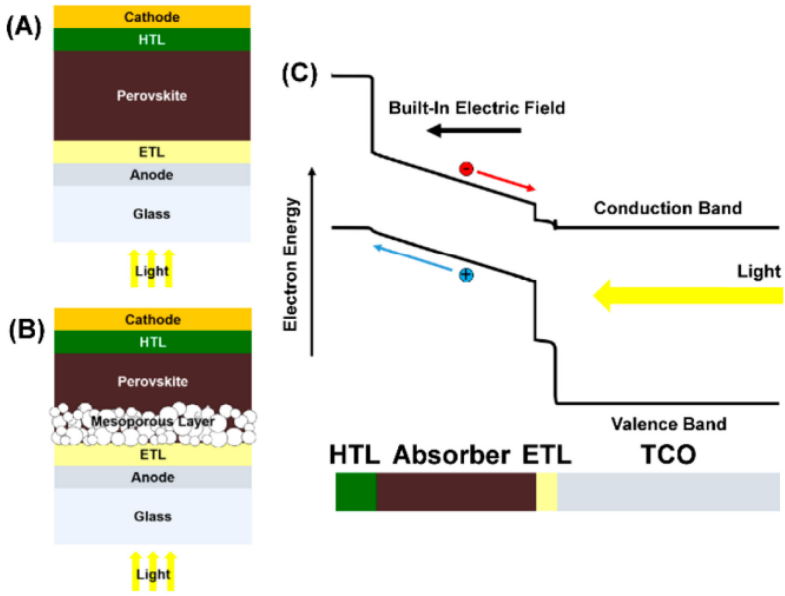

Figure 1.7 Common perovskite solar cell (PSC) architectures: (a) planar PSC, (b) mesoporous PSC, and (c) band diagram of a PSC.

1.4 Low-Dimensional Perovskite Solar Cells

Larger organic cations are challenging to integrate into the three-dimensional (3D) perovskite lattice when they are added to the structure of halide perovskites. Lower-dimensional structures instead emerge as a result. Two-dimensional (2D) halide perovskites are a typical example of a lower-dimensional structure (Figure 1.8).

2D halide perovskites can be envisioned as if you "cleave" the 3D perovskite structure along a specific crystallographic plane, creating thin sheets. In order to meet the surface metal coordination sites, halide ions are added to the inorganic metal-halide framework found in these sheets. As spacers, the bigger organic cations are positioned between these inorganic layers. Different crystallographic directions, such as ⟨100⟩, ⟨110⟩, or ⟨111⟩, might cause the specific cleavage plane. This can lead to distinct orientations of 2D perovskites, such as ⟨100⟩-oriented, ⟨110⟩-oriented, and ⟨111⟩-oriented 2D perovskites. The bulk crystalline materials are made of stacks of these sheets.[45]

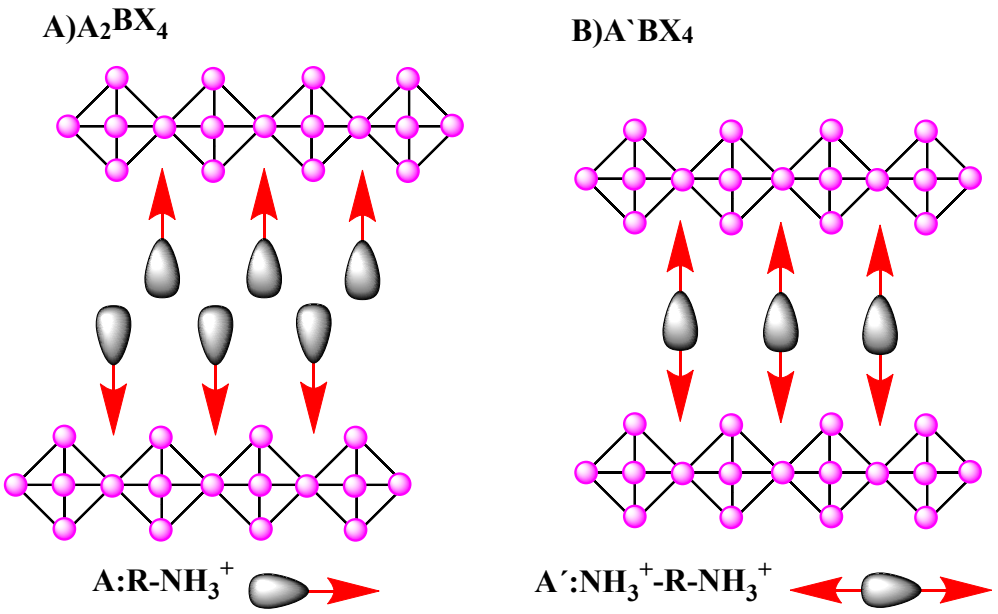

Figure 1.8 In the context of 2D perovskites, there are two possible crystal structures:

A_2BX_4 Structure: In the A_2BX_4 structure, for every BX_4 repeat unit, two monovalent organic cations are attached to the inorganic sheet. This arrangement forms a bilayer of organic cations between the inorganic sheets. The interaction between these layers, a crucial aspect of the structure, is precisely controlled by van der Waals forces, demonstrating a deep understanding of the system.

**A`$BX_4$ Structure**: Each organic cation in the A`BX_4 structure has two positively charged tethering groups at either end. As a result, every cation in the structure can attach to and tether two nearby inorganic sheets.

These 2D structures, often called Ruddlesden−Popper phases for monovalent A cations or Dion−Jacobson phases for divalent A` cations, represent a distinct category of materials.[46] The Ruddlesden−Popper phases are more extensively studied and can be described by the generalised chemical formula $A_2A_{n-1}B_nX3_{n+1}$. In these structures, each layer of the 3D perovskite is composed of n octahedral layers of metal halides, making them distinct from the typical 3D perovskite structure. These quasi-2D structures have unique properties and can be tailored for various applications.

The typical structure of 2D perovskites involves corner-sharing between the perovskite layers. However, some exceptions exist where 2D perovskites exhibit edge-sharing and face-sharing configurations, as depicted in Figure 1.9. This variation in connection modes can be controlled by adjusting the length of the organic amines used in the material, allowing for a degree of structural flexibility and tunability.[47]

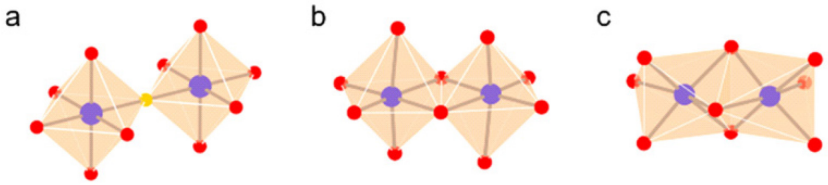

Figure 1.9 Connectivity modes in 2D perovskite: (a) corner-sharing, (b) edge-sharing, and (c) face-sharing.

2D perovskites, including pure 2D, quasi-2D perovskites, and 2D/3D (in a stacked form, Figure 1.10), have recently emerged as a promising family of photovoltaic materials. They have shown the potential to address the stability issues associated with traditional 3D perovskites in perovskite solar cells (PSCs). Introducing an insulating spacer layer in 2D perovskites imparts inherent long-term stability to these materials. This stability is attributed to several factors, including hydrophobicity, the suppression of ion migration, and a higher formation energy, which collectively contribute to improved durability and reliability in PSC applications.[48-50]

Solution processing of 3D polycrystalline perovskite films frequently leads to surface defects, including undercoordinated lead halide clusters and MA/FA/I element chemical vacancies. Furthermore, noticeable fractures and pinholes frequently occur during crystallization. These flaws cause a large amount of energy loss due to charge recombination, explicitly affecting the device's open-circuit voltage (Voc). Furthermore, when perovskite is exposed to air that contains oxygen and humidity, physical barriers and chemical element vacancies hasten the material's breakdown.

To overcome these obstacles, 3D perovskite films are coated with 2D perovskite. This integration corrects the defects by interacting with undercoordinated lead clusters, filling cation/anion vacancies with organic iodonium salt, and embedding them into surface borders, pinholes, and cracks. This leads to the forming of an integrated crystal structure, which significantly raises the calibre of perovskite films.

3D perovskite materials are susceptible to decomposition when exposed to humidity, which worsens their instability. To address this instability problem, 2D perovskite is used as a protective block layer on the 3D perovskite film. This protective layer prevents the penetration of humidity and oxygen, and it also suppresses ion migration. Consequently, it enhances hydrophobicity and contributes to more considerable formation energy, making the perovskite solar cell more stable under varying environmental conditions.

Stacking 2D/3D perovskite in a heterostructure creates distinct energy levels for carrier transport. Specifically, higher energy levels are found in the 2D perovskite, while lower energy levels are present

in the 3D counterpart. This difference in energy levels facilitates enhanced charge transfer and extraction processes, ultimately leading to improved photovoltaic performance in these devices.[51]

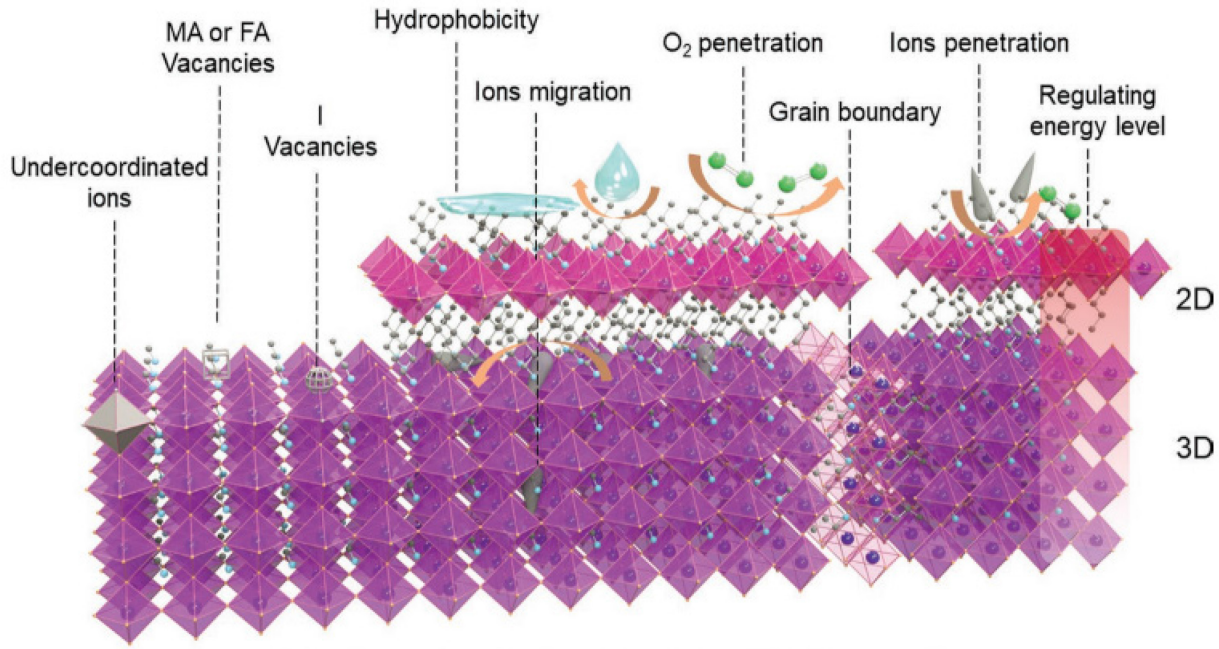

Figure 1.10 Surface passivation of 3D perovskite using 2D perovskite. This process effectively repairs defects such as vacancies or excess elements. Additionally, a robust 2D capping layer is formed, which acts as a barrier to prevent the penetration of oxygen and moisture. Furthermore, the modified energy levels in the structure enhance the efficiency of charge transfer and collection.[51]

While 2D perovskites exhibit remarkable stability, they can introduce specific unfavourable characteristics during the device assembly. These issues arise from the presence of large organic cations, which can have several adverse effects, such as reducing carrier mobility, leading to charge accumulation, and hindering the processes of charge separation and extraction.[52]

Apart from their 2D and 3D equivalents, an additional category of inorganic-organic metal halides was discovered. The strictly corner-sharing MX6 octahedral connectivity that distinguishes true perovskites is absent from these compounds. Instead, as illustrated in Figure 1.9b,c, the MX6 octahedra in these compounds have combinations of corner, edge, and face-sharing connectivity and edge- and face-sharing motifs. These distinctions have led to their aggregate designation as "perovskitoids"[53]; Figure 1.11[54] provides a representative example. Since the edge- and face-sharing motifs help to stabilize the $5s^2$ (Sn^{2+}) or $6s^2$ (Pb^{2+}) orbital energies, which are typically dominant near the top of the valence bands in proper p rovskites, perovskitoids often display more robust environmental stability than proper perovskites. For example, compared to their 3D perovskite counterparts, 1D perovskitoid structures such as $CsPbI_3$ and $CsSnI_3$ are substantially more stable.[55]

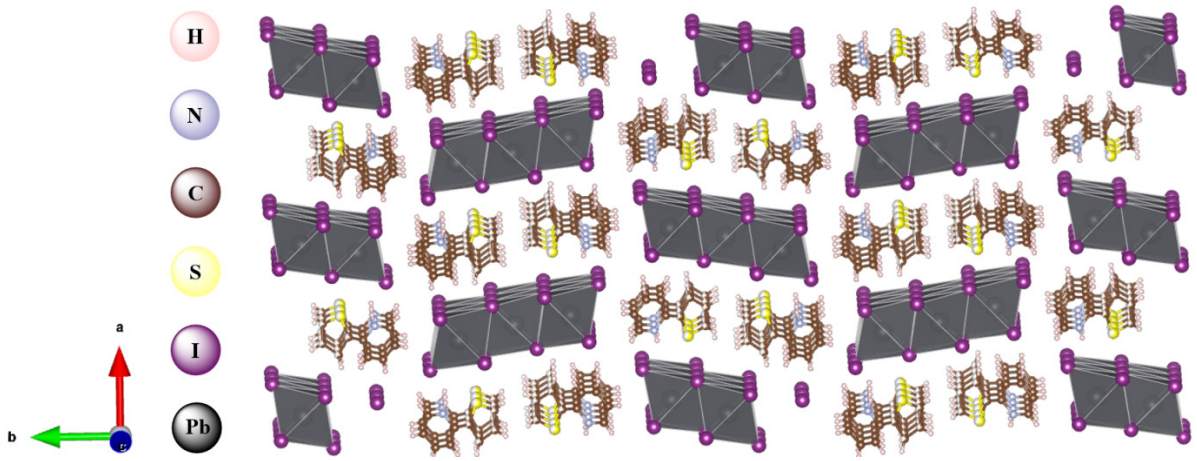

Figure 1.11 An example to 1D perovskitoid crystal structure.

1.5 Rudorffites; Silver−Bismuth Halides, $Ag_aBi_bX_{a+3b}$

Lead halide perovskites that combine organic and inorganic elements (OIHPs) show great promise as photovoltaic (PV) materials. In recent years, researchers have successfully harnessed their unique properties, such as significant absorption coefficients, small exciton binding energies, and high carrier mobilities, to enhance the power conversion efficiency (PCE) of OIHP solar cells. The PCE has increased to over 26.0%, making them competitive with silicon-based solar cells, which have traditionally dominated the PV market.[36,56]

Despite their exceptional performance, one significant hurdle for the widespread commercialisation of perovskite solar cells remains the environmental toxicity associated with using lead (Pb) in these materials. The toxicity of lead poses a challenge and concern for developing and adopting perovskite solar cell technology. Addressing these environmental concerns is a crucial aspect of advancing perovskite solar cell technology for broader use in the solar energy industry.[57]

Unlike perovskite materials, materials inspired by perovskite, such as rudorffite structures and silver-bismuth halides with the chemical formula $Ag_aBi_bX_{a+3b}$, are becoming good alternatives for use as light absorbers in solar cells. Their excellent light absorption qualities and appropriate band gap energy (Eg) are two important aspects that draw people in.[58]

Silver-bismuth halides have much reduced Eg in the range of 1.6 to 1.93 eV (direct band gaps) in comparison to double perovskites and A_3BiX_9 compounds (where A can be Cs^+, Rb^+, or $CH_3NH_3^+$ and X^- is I^-, Br^-, or Cl^-). Double perovskites and A_3BiX_9 compounds often have high indirect band gaps (Eg > 2.0 eV). Because of this feature, they are more advantageous to utilize in photovoltaic (PV) applications.[59-60]

Silver iodobismuthates ($Ag_aBi_bI_{a+3b}$) exhibit different structural arrangements based on the composition, shown in Figure 1.12, particularly the relative amounts of silver and bismuth ions:[61]

Rhombohedral $CdCl_2$-Type Structure (R m3 Symmetry), typically found in silver-rich compositions where a> 1; Cubic Defect Spinel Structure (Fd3m Symmetry), found in bismuth-rich compositions where b > 1.

The term "defect spinel structure" refers to the structural arrangement in silver iodobismuthates. It highlights the presence of vacant sites, which vary depending on the composition. The relative proportions of silver and bismuth ions influence the choice of structural type.

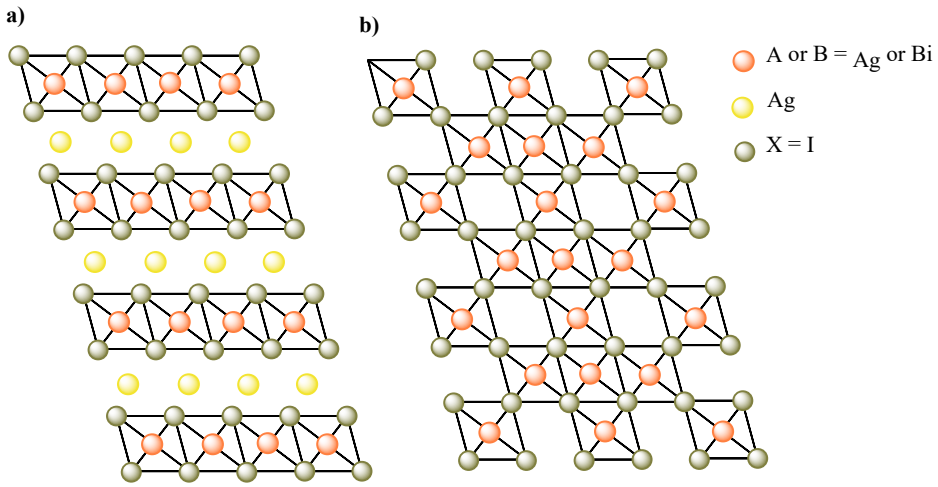

Figure 1.12 Crystal structures of $Ag_aBi_bI_{a+3b}$: a) $CdCl_2$-type rhombohedral phase and b) cubic defect-spinel phase (yellow – Ag^+, orange – Bi^{3+} or Ag^+, green – I^-).

Specifically, silver-bismuth iodide (ABI) ternary systems have been reported to possess high absorption coefficients in the range of 105 to 106 cm^{-1}, regardless of their composition. This high absorption coefficient is advantageous for thin-film photovoltaic applications. Various ABI compounds, including Ag_3BiI_6, Ag_2BiI_5, $AgBiI_4$, $AgBi_2I_7$, $AgBi_3I_{10}$, and others with different AgI-to-BiI_3 ratios, have been employed in the development of solar cells.[62-69]. These materials promise to enhance the efficiency of thin-film photovoltaic devices.

1.6 Solar Cells Passivation

Perovskite solar cell (PSC) technology is considered one of the most promising candidates to compete with commercially available photovoltaic technologies such as crystalline silicon and copper indium gallium selenide (CIGS).[70] This is due to several remarkable properties, including high device efficiency, ease of solution processing, low-temperature fabrication, tunability in chemical composition, and the potential for low-cost production.[71-77] However, perovskite materials' chemical and structural characteristics, combined with their low-temperature processing methods, can lead to detrimental defects (Figure 1.13) at the material's surface and grain boundaries within the polycrystalline structure.[78-80] These defects can significantly negatively impact the photovoltaic performance and stability of perovskite solar cells.[81-83]

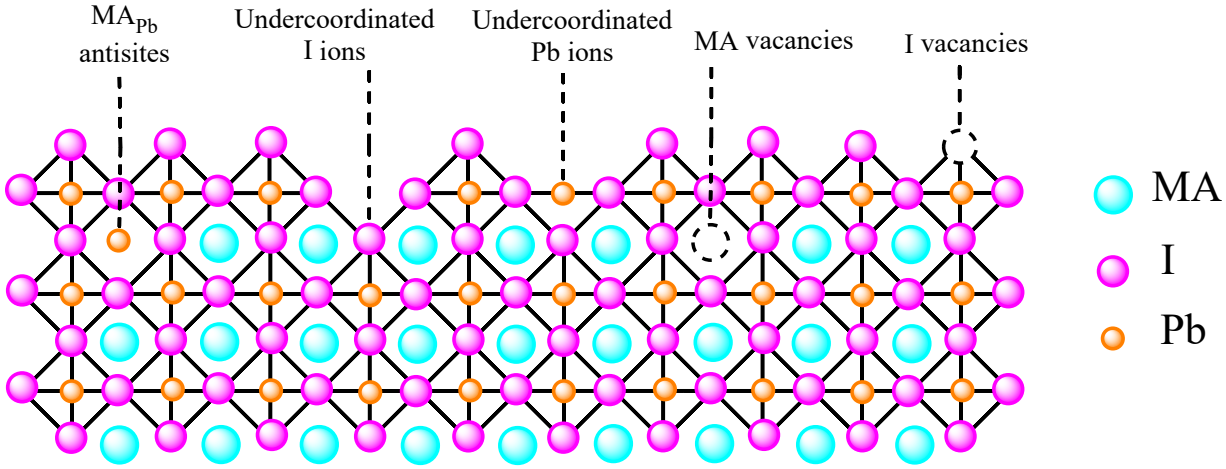

Figure 1.13) Schematic diagram of defect types in $MAPbI_3$ perovskite

Defects positioned deep within the band gaps possess characteristics akin to Shockley-Read-Hall non-radiative recombination centres. These defects play a significant role in causing a short minority carrier lifetime, thereby contributing to the low open-circuit voltage (Voc). A review of all possible intrinsic point defects in the case of $CH_3NH_3PbI_3$ reveals that defects with low formation energies, like Pb atoms on CH_3NH_3 sites (Pb_{MA}), I vacancies (V_I), CH_3NH_3 molecules on I sites (MA_I), CH_3NH_3 interstitials (Ii), CH_3NH_3 molecules on Pb sites (MA_{Pb}), CH_3NH_3 vacancies (V_{MA}), Pb vacancies (V_{Pb}), and CH_3NH_3 interstitials (MAi), exhibit very shallow transition energy levels (as shown in Figure 1.14).[84]

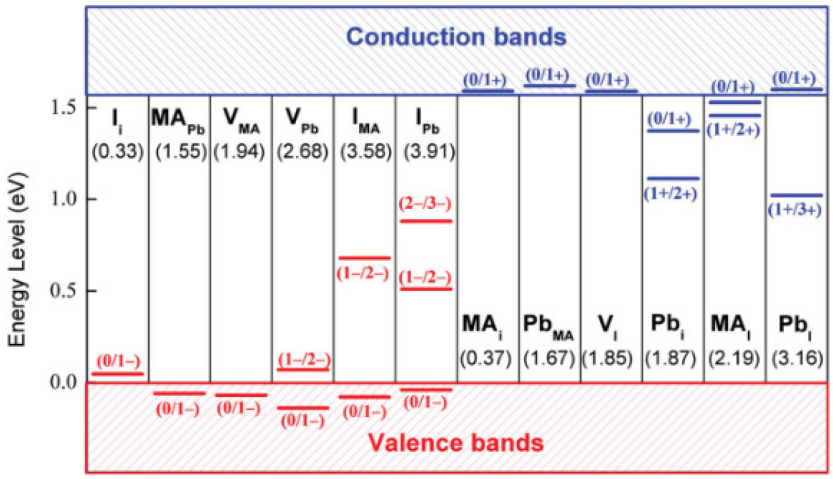

Figure 1.14) Calculated transition energy levels of different defects in $MAPbI_3$ perovskite. The formation energies of each defect are shown in parentheses.

Passivation is indeed an effective strategy used in materials science and engineering to make materials less susceptible to external factors or environmental conditions. In the context of perovskite solar cells and other semiconductor devices, passivation aims to reduce defects and suppress ion movement, contributing to improved stability and performance. Passivating the surface or interfaces of the material can become more resistant to factors such as humidity, oxygen, or ion migration, which can otherwise lead to degradation and reduced device efficiency.

The primary purpose of passivation involves the application of specific chemical substances to interact with defect sites, either at the surface or within the bulk of perovskite materials, as illustrated in Figure 1.15. This interaction results in the formation of chemical bonds, which can be either covalent (involving the sharing of electrons, Figure 1.15a) or ionic (involving the electrostatic attraction between ions).[85-86] Additionally, non-covalent interactions among molecules, such as halogen bonding and hydrogen bonding, based on electrostatic forces of attraction (Figure 1.15b,c), can reduce defects in perovskite materials. Halogen bonding is particularly effective at addressing electron-rich defects with negative charges,[87-88] while hydrogen bonding can address positively and negatively charged defects.[89] It's important to note that these advantageous intermolecular interactions often involve establishing chemical bonds between the passivating agents and the defect sites, further reinforcing the effectiveness of chemical passivation.

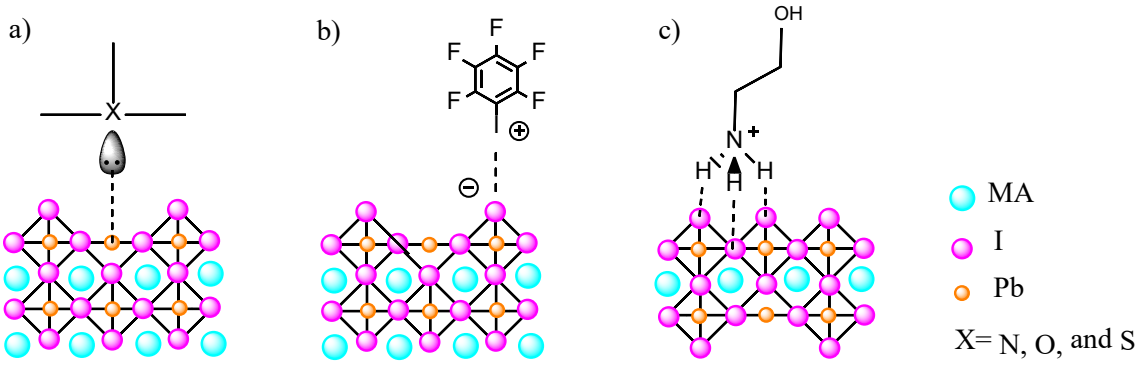

Figure 1.15) A schematic representation illustrating various interactions between perovskite defects and passivation agent

1.7 Outline of the Thesis

In this thesis, our main focus was to comprehensively investigate the defects that emerge at the surface and grain boundaries of polycrystalline lead-based perovskite materials and lead-free silver-bismuth halides. These defects substantially negatively impact the performance and stability of photovoltaic devices using these materials. To address these naturally occurring defects, we explored various materials and concepts to develop potential solutions.

Chapter 3 of the thesis delves into applying 1,10-phenanthroline, a bidentate chelating ligand, at the methylammonium lead iodide (MAPbI3) film interface and the hole-transport layer. This compound serves a dual purpose, acting as a passivating agent for surface defects involving under-coordinated lead ions and as a means to convert excess or unreacted lead iodide (PbI_2) at interfaces into neutralised and beneficial species (PbI_2(1,10-phen)x, with x being 1 or 2). This transformation is crucial for enabling efficient hole transfer at the modified interface and enhancing long-term stability.

Chapter 4 of the thesis presents the application of a novel organic cation, 2-(thiophene-2yl-)pyridine-1-ium iodide (ThPyI), at the surface of 3D methylammonium lead iodide (MAPI) perovskite films, and also in its bulk structure. ThPyI is used either as a passivator on top of 3D MAPI to create surface-passivated films with an additional stable 1D perovskite phase, as a product of the unreacted surface PbI2 and organic cation or introduced independently into the 3D MAPI precursor to achieve bulk passivation.

Chapter 5 of the thesis demonstrates how a well-established material, poly(2,5-dimercapto-1,3,4-thiadiazole), is utilised to improve the efficiency and stability of solar cells based on Ag_3BiI_6. This approach shows that a passivation strategy can be applied to this material, which offers an alternative to toxic lead (Pb)-based perovskite solar cells, providing a Pb-free solution for photovoltaic applications.

The critical strategy involves a bulk polymer treatment to address detrimental defects within the internal structure of Ag_3BiI_6. These defects can significantly impact the performance and stability of photovoltaic devices. The study reveals that polymer-treated Ag_3BiI_6 films can maintain stability when used in solar applications, highlighting their potential as a safer, more sustainable option for solar energy conversion.

1.8 References

1. Sze, Simon Min. *Semiconductor devices: physics and technology*. John wiley & sons, **2008**.
2. HILSUM, C. Semiconductors (2nd edn). *Physics Bulletin*, **1979**, 30.12: 528.
3. NG, Kwok Kwok. *Complete guide to semiconductor devices*. IEEE Press, **2002**.
4. Semiconductor Devices: Pioneering Papers, World Sci., Singapore, **1991**.
5. ZHANG, Y. J., et al. Enhanced intrinsic photovoltaic effect in tungsten disulfide nanotubes. *Nature*, **2019**, 570.7761: 349-353.
6. E. R. Bequerel, C. R. Acad. Sci. **1839**, 9, 145.
7. CHAPIN, Daryl M.; FULLER, Calvin S.; PEARSON, Gerald L. A new silicon p-n junction photocell for converting solar radiation into electrical power. *Journal of applied physics*, **1954**, 25.5: 676-677.
8. Knutson, J.; Martin, J. D.; Mitzi, D. B. Tuning the Band Gap in Hybrid Tin Iodide Perovskite Semiconductors Using Structural Templating. Inorg. Chem. **2005**, 44, 4699−4705.
9. Fang, Y.; Dong, Q.; Shao, Y.; Yuan, Y.; Huang, J. Highly Narrowband Perovskite Single-Crystal Photodetectors Enabled by Surface-Charge Recombination. Nat. Photonics **2015**, 9, 679−686.
10. Eperon, G. E.; Stranks, S. D.; Menelaou, C.; Johnston, M. B.; Herz, L. M.; Snaith, H. J. Formamidinium Lead Trihalide: a Broadly Tunable Perovskite for Efficient Planar Heterojunction Solar Cells. Energy Environ. Sci. 2014, 7, 982−988.
11. Song, J.; Li, J.; Li, X.; Xu, L.; Dong, Y.; Zeng, H. Quantum Dot Light-Emitting Diodes Based on Inorganic Perovskite Cesium Lead Halides (CsPbX3). Adv. Mater. **2015**, 27, 7162−7167.
12. Hu, H.; Salim, T.; Chen, B.; Lam, Y. M. Molecularly Engineered Organic-Inorganic Hybrid Perovskite with Multiple Quantum Well Structure for Multicolored Light-Emitting Diodes. Sci. Rep. **2016**, 6, 33546.
13. Wang, N.; Cheng, L.; Ge, R.; Zhang, S.; Miao, Y.; Zou, W.; Yi, C.; Sun, Y.; Cao, Y.; Yang, R.; et al. Perovskite Light-Emitting Diodes Based on Solution-Processed Self-Organized Multiple Quantum Wells. Nat. Photonics **2016**, 10, 699−704.
14. Mante, P. A.; Stoumpos, C. C.; Kanatzidis, M. G.; Yartsev, A. Electron-Acoustic Phonon Coupling in Single Crystal CH3NH3PbI3 Perovskites Revealed by Coherent Acoustic Phonons. Nat. Commun. **2017**, 8, 14398.
15. Wehrenfennig, C.; Eperon, G. E.; Johnston, M. B.; Snaith, H. J.; Herz, L. M. High Charge Carrier Mobilities and Lifetimes in Organolead Trihalide Perovskites. Adv. Mater. **2014**, 26, 1584−1589.

16. Reid, O. G.; Yang, M.; Kopidakis, N.; Zhu, K.; Rumbles, G. Grain-Size-Limited Mobility in Methylammonium Lead Iodide Perovskite Thin Films. ACS Energy Lett. **2016**, 1, 561−565.
17. Green, M. A.; Ho-Baillie, A.; Snaith, H. J. The Emergence of Perovskite Solar Cells. Nat. Photonics **2014**, 8, 506−514.
18. Xing, G.; Mathews, N.; Sun, S.; Lim, S. S.; Lam, Y. M.; Gratzel,¨M.; Mhaisalkar, S.; Sum, T. C. Long-Range Balanced Electron- and Hole-Transport Lengths in Organic-Inorganic CH3NH3PbI3. Science **2013**, 342, 344−347.
19. Stranks, S. D.; Eperon, G. E.; Grancini, G.; Menelaou, C.; Alcocer, M. J.; Leijtens, T.; Herz, L. M.; Petrozza, A.; Snaith, H. J. Electron-Hole Diffusion Lengths Exceeding 1 Micrometer in an Organometal Trihalide Perovskite Absorber. Science **2013**, 342, 341−344.
20. Yin, W. J.; Shi, T.; Yan, Y. Unique Properties of Halide Perovskites as Possible Origins of the Superior Solar Cell Performance. Adv. Mater. **2014**, 26, 4653−4658.
21. Han, Q.; Bai, Y.; Liu, J.; Du, K.-Z.; Li, T.; Ji, D.; Zhou, Y.; Cao, C.; Shin, D.; Ding, J.; et al. Additive Engineering for HighPerformance Room-Temperature-Processed Perovskite Absorbers with Micron-Size Grains and Microsecond-Range Carrier Lifetimes. Energy Environ. Sci. **2017**, 10, 2365−2371.
22. Matsui, T.; Seo, J. Y.; Saliba, M.; Zakeeruddin, S. M.; Gratzel,¨M. Room-Temperature Formation of Highly Crystalline Multication Perovskites for Efficient, Low-Cost Solar Cells. Adv. Mater. **2017**, 29, 1606258.
23. Mitzi, D. B.; Chondroudis, K.; Kagan, C. R. Organic-Inorganic Electronics. IBM J. Res. Dev. **2001**, 45, 29−45.
24. Kagan, C. R.; Mitzi, D. B.; Dimitrakopoulos, C. D. OrganicInorganic Hybrid Materials as Semiconducting Channels in Thin-Film Field-Effect Transistors. Science **1999**, 286, 945−947.
25. Mitzi, D. B.; Dimitrakopoulos, C. D.; Kosbar, L. L. Structurally Tailored Organic-Inorganic Perovskites: Optical Properties and Solution-Processed Channel Materials for Thin-Film Transistors. Chem. Mater. **2001**, 13, 3728−3740.
26. Mitzi, D. B.; Dimitrakopoulos, C. D.; Rosner, J.; Medeiros, D. R.; Xu, Z.; Noyan, C. Hybrid Field-Effect Transistor Based on a LowTemperature Melt-Processed Channel Layer. Adv. Mater. **2002**, 14, 1772−1776.
27. Era, M.; Morimoto, S.; Tsutsui, T.; Saito, S. Organic - Inorganic Heterostructure Electroluminescent Device Using a Layered Perovskite Semiconductor (C6H5C2H4NH3)2PbI4. Appl. Phys. Lett. **1994**, 65, 676−678
28. Hattori, T.; Taira, T.; Era, M.; Tsutsui, T.; Saito, S. Highly Efficient Electroluminescence

from a Heterostructure Device Combined with Emissive Layered-Perovskite and an ElectronTransporting Organic Compound. Chem. Phys. Lett. **1996**, 254, 103−108.

29. Chondroudis, K.; Mitzi, D. B. Electroluminescence from an Organic-Inorganic Perovskite Incorporating a Quaterthiophene Dye within Lead Halide Perovskite Layers. Chem. Mater. **1999**, 11, 3028− 3030.
30. Best Research Cell Efficiencies. National Renewable Energy Laboratory. https://www.nrel.gov/pv/assets/images/efficiency-chart20180716.jpg (accessed Aug 12, **2018**).
31. Saliba, M.; Matsui, T.; Seo, J. Y.; Domanski, K.; Correa-Baena, J. P.; Nazeeruddin, M. K.; Zakeeruddin, S. M.; Tress, W.; Abate, A.; Hagfeldt, A.; et al. Cesium-Containing Triple Cation Perovskite Solar Cells: Improved Stability, Reproducibility and High Efficiency. Energy Environ. Sci. **2016**, 9, 1989−1997.
32. Saliba, M.; Matsui, T.; Domanski, K.; Seo, J.-Y.; Ummadisingu, A.; Zakeeruddin, S. M.; Correa-Baena, J.-P.; Tress, W.; Abate, A.; Hagfeldt, A.; et al. Incorporation of Rubidium Cations into Perovskite Solar Cells Improves Photovoltaic Performance. Science **2016**, 354, 206−209.
33. Yang, W. S.; Noh, J. H.; Jeon, N. J.; Kim, Y. C.; Ryu, S.; Seo, J.; Seok, S. I. High-Performance Photovoltaic Perovskite Layers Fabricated through Intramolecular Exchange. Science **2015**, 348, 1234−1237.
34. Yang, W. S.; Park, B.-W.; Jung, E. H.; Jeon, N. J.; Kim, Y. C.; Lee, D. U.; Shin, S. S.; Seo, J.; Kim, E. K.; Noh, J. H.; et al. Iodide Management in Formamidinium-Lead-Halide-Based Perovskite Layers for Efficient Solar Cells. Science **2017**, 356, 1376−1379.
35. Shin, S. S.; Yeom, E. J.; Yang, W. S.; Hur, S.; Kim, M. G.; Im, J.; Seo, J.; Noh, J. H.; Seok, S. I. Colloidally Prepared La-Doped BaSnO3 Electrodes for Efficient, Photostable Perovskite Solar Cells. Science **2017**, 356, 167−171.
36. https://www.nrel.gov/pv/cell-efficiency.html (Rev. 09.27.2023)
37. Svane, K. L.; Forse, A. C.; Grey, C. P.; Kieslich, G.; Cheetham, A. K.; Walsh, A.; Butler, K. T. How Strong Is the Hydrogen Bond in Hybrid Perovskites? J. Phys. Chem. Lett. **2017**, 8, 6154−6159.
38. Park, N.-G. Perovskite Solar Cells: An Emerging Photovoltaic Technology. Mater. Mater. Today **2015**, 18, 65−72.
39. Egger, D. A.; Kronik, L. Role of Dispersive Interactions in Determining Structural Properties of Organic−Inorganic Halide Perovskites: Insights from First-Principles Calculations. J. Phys. Chem. Lett. **2014**, 5, 2728−2733.
40. Goldschmidt, V. M. Die Gesetze der Krystallochemie. Naturwissenschaften **1926**, 14, 477−485.

41. Saparov, B.; Mitzi, D. B. Organic-Inorganic Perovskites: Structural Versatility for Functional Materials Design. Chem. Rev. **2016**, 116, 4558−4596.
42. Li, C.; Lu, X.; Ding, W.; Feng, L.; Gao, Y.; Guo, Z. Formability of ABX3 (X = F, Cl, Br, I) Halide Perovskites. Acta Crystallogr., Sect. B: Struct. Sci. **2008**, 64, 702−707.
43. Correa-Baena, Juan-Pablo, et al. Promises and challenges of perovskite solar cells. *Science*, **2017**, 358.6364: 739-744.
44. Knutson, Jeremy L.; Martin, James D.; Mitzi, David B. Tuning the band gap in hybrid tin iodide perovskite semiconductors using structural templating. *Inorganic chemistry*, **2005**, 44.13: 4699-4705.
45. Katan, C.; Mercier, N.; Even, J. Quantum and Dielectric Confinement Effects in Lower-Dimensional Hybrid Perovskite Semiconductors. Chem. Rev. **2019**, 119, 3140−3192.
46. Mao, L.; Ke, W.; Pedesseau, L.; Wu, Y.; Katan, C.; Even, J.; Wasielewski, M. R.; Stoumpos, C. C.; Kanatzidis, M. G. Hybrid DionJacobson 2D Lead Iodide Perovskites. J. Am. Chem. Soc. **2018**, 140, 3775−3783.
47. L. Mao, C. C. Stoumpos, M. G. Kanatzidis, J. Am. Chem. Soc. **2019**, 141, 1171.
48. G. Wu, X. Li, J. Zhou, J. Zhang, X. Zhang, X. Leng, P. Wang, M. Chen, D. Zhang, K. Zhao, Adv. Mater. **2019**, 31, 1903889.
49. X. Zhang, G. Wu, S. Yang, W. Fu, Z. Zhang, C. Chen, W. Liu, J. Yan, W. Yang, H. Chen, Small **2017**, 13, 1700611.
50. G. Wu, N. Ahmad, Y. Zhang, J. Mater. Chem. C **2021**, 9, 9851.
51. WU, Guangbao, et al. Surface passivation using 2D perovskites toward efficient and stable perovskite solar cells. *Advanced Materials*, **2022**, 34.8: 2105635.
52. Gao, Lili, et al. Improved environmental stability and solar cell efficiency of (MA, FA) PbI3 perovskite using a wide-band-gap 1D thiazolium lead iodide capping layer strategy. *ACS Energy Letters*, **2019**, 4.7: 1763-1769.
53. Stoumpos, C. C.; Mao, L.; Malliakas, C. D.; Kanatzidis, M. G. Structure–band gap relationships in hexagonal polytypes and low-dimensional structures of hybrid tin iodide perovskites. *Inorg. Chem.* **2017**, *56* (1), 56– 73.
54. Buyruk, Ali, et al. A Novel Multi-Functional Thiophene-Based Organic Cation as Passivation, Crystalline Orientation, and Organic Spacer Agent for Low-Dimensional 3D/1D Perovskite Solar Cells. *Advanced Optical Materials*, **2023**, 2300267.
55. Chung, I.; Song, J.-H.; Im, J.; Androulakis, J.; Malliakas, C. D.; Li, H.; Freeman, A. J.; Kenney, J. T.; Kanatzidis, M. G. CsSnI3: semiconductor or metal? High electrical conductivity and strong near-infrared photoluminescence from a single material. High hole mobility and phase-transitions. *J. Am. Chem. Soc.* **2012**, *134* (20), 8579– 8587,
56. Jena, A. K.; Kulkarni, A.; Miyasaka, T. Halide Perovskite Photovoltaics: Background,

Status, and Future Prospects. Chem. Rev. 2019, 119 (5), 3036−3103.

57. Ding, G.; Zheng, Y.; Xiao, X.; Cheng, H.; Zhang, G.; Shi, Y.; Shao, Y. Sustainable Development of Perovskite Solar Cells: Keeping a Balance between Toxicity and Efficiency. Journal of Materials Chemistry A **2022**, 10, 8159−8171.
58. Turkevych, I.; Kazaoui, S.; Ito, E.; Urano, T.; Yamada, K.; Tomiyasu, H.; Yamagishi, H.; Kondo, M.; Aramaki, S. Photovoltaic Rudorffites: Lead-Free Silver Bismuth Halides Alternative to Hybrid Lead Halide Perovskites. ChemSusChem **2017**, 10 (19), 3754−3759.
59. Mei, J.; Liu, M.; Vivo, P.; Pecunia, V. Two-Dimensional Antimony-Based Perovskite-Inspired Materials for High-Performance Self-Powered Photodetectors. Adv. Funct Mater. **2021**, 31 (50), 2106295.
60. Pecunia, V.; Occhipinti, L. G.; Chakraborty, A.; Pan, Y.; Peng, Y. Lead-Free Halide Perovskite Photovoltaics: Challenges, Open Questions, and Opportunities. APL Materials **2020**, 8, 100901.
61. A. Koedtruad, M. Goto, M. Amano Patino, Z. Tan, H. Guo, T. Nakamura, T. Handa, W.-T. Chen, Y.-C. Chuang, H.-S. Sheu, T. Saito, D. Kan, Y. Kanemitsu, A. Wakamiya, Y. Shimakawa, J. Mater. Chem. A **2019**, 7, 5583.
62. Yi, Z.; Zhang, T.; Ban, H.; Shao, H.; Gong, X.; Wu, M.; Liang, G.; Zhang, X. L.; Shen, Y.; Wang, M. AgBi3I10 Rudorffite for Photovoltaic Application. Sol. Energy **2020**, 206, 436−442.
63. Zhu, H.; Erbing, A.; Wu, H.; Man, G. J.; Mukherjee, S.; Kamal, C.; Johansson, M. B.; Rensmo, H.; Odelius, M.; Johansson, E. M. J. Tuning the Bandgap in Silver Bismuth Iodide Materials by Partly Substituting Bismuth with Antimony for Improved Solar Cell Performance. ACS Appl. Energy Mater. **2020**, 3 (8), 7372−7382.
64. Wu, H.; Zhu, H.; Erbing, A.; Johansson, M. B.; Mukherjee, S.; Man, G. J.; Rensmo, H.; Odelius, M.; Johansson, E. M. J. Bandgap Tuning of Silver Bismuth Iodide via Controllable Bromide Substitution for Improved Photovoltaic Performance. ACS Appl. Energy Mater. **2019**, 2 (8), 5356−5362.
65. Zhai, W.; Huang, L.; Cui, X.; Li, G.; Zhang, Z.; Chen, P.; Li, Y.; Tang, Y.; Lin, L.; Yan, Z.; Liu, J. M. Tuning the Morphology and Optoelectronic Properties of AgBiI4 Film through Isopropanol Treatment. J. Mater. Chem. C Mater. **2022**, 10 (13), 5321−5327.
66. Wang, Y.; Liu, Y.; Shi, X.; Huang, L.; Tong, J.; Wang, G.; Pan, D. Alkali-Metal-Ion-Doping Strategy to Improve the Photovoltaic Properties of Ag2BiI5solar Cells. New J. Chem. **2021**, 45 (31), 14158−14166.
67. Tu, J.; Kou, C.; Liu, M.; Lu, H.; Liu, Y.; Tan, H.; Li, W.; Bo, Z. The Preparation of Ag_3BiBr_6 Films and Their Preliminary Use for Solution Processed Photovoltaics. SN Appl. Sci. **2019**.

68. Kulkarni, A.; Ü nlü, F.; Pant, N.; Kaur, J.; Bohr, C.; Jena, A. K.; Ö z, S.; Yanagida, M.; Shirai, Y.; Ikegami, M.; Miyano, K.; Tachibana, Y.; Chakraborty, S.; Mathur, S.; Miyasaka, T. Concerted Ion Migration and Diffusion-Induced Degradation in Lead-Free Ag3BiI6 Rudorffite Solar Cells under Ambient Conditions. Solar RRL **2021**, 5 (8), 2100077.

69. Correa Guerrero, N. B., Guo, Z., Shibayama, N., Jena, A. K., & Miyasaka, T. (2023). A Semitransparent Silver–Bismuth Iodide Solar Cell with V oc above 0.8 V for Indoor Photovoltaics. ACS Applied Energy Materials, 6(20), 10274-10284.

70. Torabi, N.; Behjat, A.; Zhou, Y.; Docampo, P.; Stoddard, R. J.; Hillhouse, H. W.; Ameri, T. Progress and Challenges in Perovskite Photovoltaics from Single- to Multi-Junction Cells. *Materials Today Energy* **2019,** *12*, 70-94

71. https://www.nrel.gov/pv/assets/pdfs/best-research-cell-efficiencies.

72. Abdi-Jalebi, M.; Dar, M. I.; Senanayak, S. P.; Sadhanala, A.; Andaji-Garmaroudi, Z.; Pazos-Outón, L. M.; Richter, J. M.; Pearson, A. J.; Sirringhaus, H.; Grätzel, M. Charge Extraction Via Graded Doping of Hole Transport Layers Gives Highly Luminescent and Stable Metal Halide Perovskite Devices. *Science advances* **2019,** *5* (2), eaav2012.

73. Jung, E. H.; Jeon, N. J.; Park, E. Y.; Moon, C. S.; Shin, T. J.; Yang, T.-Y.; Noh, J. H.; Seo, J. Efficient, Stable and Scalable Perovskite Solar Cells Using Poly (3-Hexylthiophene). *Nature* **2019,** *567* (7749), 511-515.

74. Liu, Y.; Akin, S.; Pan, L.; Uchida, R.; Arora, N.; Milić, J. V.; Hinderhofer, A.; Schreiber, F.; Uhl, A. R.; Zakeeruddin, S. M. Ultrahydrophobic 3d/2d Fluoroarene Bilayer-Based Water-Resistant Perovskite Solar Cells with Efficiencies Exceeding 22%. *Science advances* **2019,** *5* (6), 2543.

75. C. Long-Range Balanced Electron-and Hole-Transport Lengths in Organic-Inorganic Ch3nh3pbi3. *Science* **2013,** *342* (6156), 344-347.

76. Lee, M. M.; Teuscher, J.; Miyasaka, T.; Murakami, T. N.; Snaith, H. J. Efficient Hybrid Solar Cells Based on Meso-Superstructured Organometal Halide Perovskites. *Science* **2012,** *338* (6107), 643-647.

77. De Wolf, S.; Holovsky, J.; Moon, S.-J.; Löper, P.; Niesen, B.; Ledinsky, M.; Haug, F.-J.; Yum, J.-H.; Ballif, C. Organometallic Halide Perovskites: Sharp Optical Absorption Edge and Its Relation to Photovoltaic Performance. *The journal of physical chemistry letters* **2014,** *5* (6), 1035-1039.

78. Guo, Y.; Sato, W.; Shoyama, K.; Halim, H.; Itabashi, Y.; Shang, R.; Nakamura, E. Citric Acid Modulated Growth of Oriented Lead Perovskite Crystals for Efficient Solar Cells. *Journal of the American Chemical Society* **2017,** *139* (28), 9598-9604.

79. Yi, C.; Luo, J.; Meloni, S.; Boziki, A.; Ashari-Astani, N.; Grätzel, C.; Zakeeruddin, S. M.; Röthlisberger, U.; Grätzel, M. Entropic Stabilization of Mixed a-Cation Abx 3 Metal Halide

Perovskites for High Performance Perovskite Solar Cells. *Energy & Environmental Science* **2016,** *9* (2), 656-662.

80. Liu, L.; Mei, A.; Liu, T.; Jiang, P.; Sheng, Y.; Zhang, L.; Han, H. Fully Printable Mesoscopic Perovskite Solar Cells with Organic Silane Self-Assembled Monolayer. *Journal of the American Chemical Society* **2015,** *137* (5), 1790-1793.
81. Cao, J.; Lv, X.; Zhang, P.; Chuong, T. T.; Wu, B.; Feng, X.; Shan, C.; Liu, J.; Tang, Y. Plant Sunscreen and Co (Ii)/(Iii) Porphyrins for Uv-Resistant and Thermally Stable Perovskite Solar Cells: From Natural to Artificial. *Advanced Materials* **2018,** *30* (27), 1800568.
82. Zheng, X.; Chen, B.; Dai, J.; Fang, Y.; Bai, Y.; Lin, Y.; Wei, H.; Zeng, X. C.; Huang, J. Defect Passivation in Hybrid Perovskite Solar Cells Using Quaternary Ammonium Halide Anions and Cations. *Nature Energy* **2017,** *2* (7), 1-9.
83. Zhao, T.; Chueh, C.-C.; Chen, Q.; Rajagopal, A.; Jen, A. K.-Y. Defect Passivation of Organic–Inorganic Hybrid Perovskites by Diammonium Iodide toward High-Performance Photovoltaic Devices. *ACS Energy Letters* **2016,** *1* (4), 757-763.
84. Yin, Wan-Jian; Shi, Tingting; Yan, Yanfa. Unique properties of halide perovskites as possible origins of the superior solar cell performance. *Advanced materials*, **2014**, 26.27: 4653-4658.
85. J. Kim, A. Ho-Baillie and S. Huang, Sol. RRL, **2019**, 3, 1800302.
86. S. Akin, N. Arora, S. M. Zakeeruddin, M. Gra¨tzel, R. H. Friend and M. I. Dar, Adv. Energy Mater., **2020**, 10, 1903090.
87. A. Abate, M. Saliba, D. J. Hollman, S. D. Stranks, K. Wojciechowski, R. Avolio, G. Grancini, A. Petrozza and H. J. Snaith, Nano Lett., **2014**, 14, 3247–3254.
88. P. Metrangolo, L. Canil, A. Abate, G. Terraneo and G. Cavallo, Angew. Chem., Int. Ed., **2022**, 61, e202114793.
89. M. A. Ruiz-Preciado, D. J. Kubicki, A. Hofstetter, L. McGovern, M. H. Futscher, A. Ummadisingu, R. GershoniPoranne, S. M. Zakeeruddin, B. Ehrler, L. Emsley, J. V. Milic´ and M. Gra¨tzel, J. Am. Chem. Soc., 2020, 142, 1645–1654.

2 Characterization Techniques

2.1 X-Ray Diffraction (XRD)

X-ray diffraction is a common technique for analysing crystalline formations and figuring out interatomic distances. This method relies on the constructive interference between monochromatic X-rays and a crystalline sample. As shown in Figure 2.1, the X-rays are produced by a cathode ray tube (in an X-ray source), filtered to produce monochromaticity, collimated to achieve concentration, and then directed at the specimen.

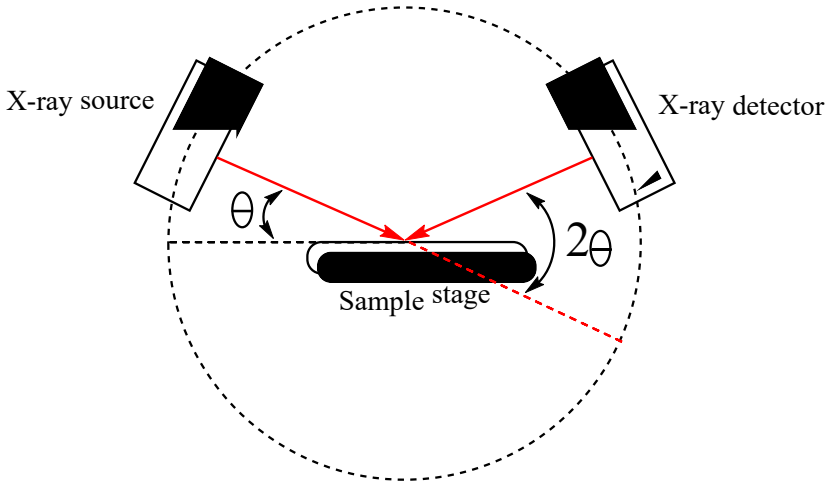

Figure 2.1 Schematic arrangement of XRD Diffractometer components

According to Bragg's Law, incident X-rays that interact with the specimen cause constructive interference, which results in a diffracted X-ray.

$$\lambda = 2d\sin\theta \tag{2.1}$$

This law defines constructive interference, where X-ray wavelength (W) = λ, incident angle (θ), and spacing (d) between atomic planes in the crystalline phase, as shown in Figure 2.2. The powdered material's random orientation ensures that all conceivable diffraction pathways inside the lattice are covered when the sample is systematically scanned across a range of 2θ angles. Converting diffraction peaks into d-spacings aids in the identification of the substance under study by comparing the resultant d-spacings with reference patterns.

The intensity of the reflected X-rays is carefully recorded while the sample and detector rotate. Constructive interference arises when the incident X-rays striking the sample follow Bragg's law in geometric alignment, leading to an intensity peak. A specialised detector captures and processes this X-ray signal, converting it into a count rate.[1]

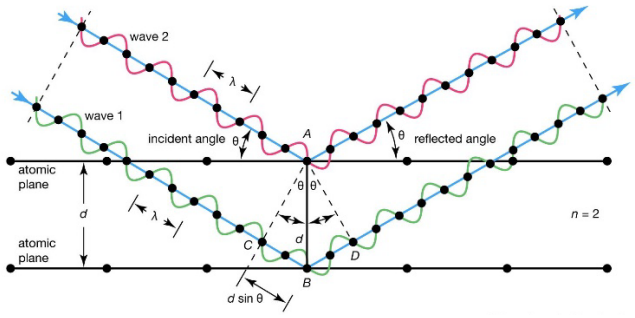

Figure 2.2 X-ray diffraction in a crystal lattice is shown schematically. The scattering centres (atoms) are shown by two black circles in the atomic planes. θ is the angle of incidence of X-rays. The spacing between reflecting planes is denoted by d.

An X-ray tube, a sample holder, and an X-ray detector are the three main components of an X-ray diffractometer, as seen in Figure 2.1. In a cathode ray tube, heating a filament releases electrons, which in turn produces X-rays. These electrons are then driven toward a target by an applied voltage and collide with the target material. These electrons produce distinctive X-ray spectra when they have enough energy to displace the target material's inner shell electrons. These spectra consist of several elements, the most prevalent ones being Kα and Kβ.

Specifically, Kα is made up of the subcomponents $K\alpha_1$ and $K\alpha_2$. $K\alpha_1$ has twice the intensity and a slightly shorter wavelength than Kα2. For the selected target material, which may comprise elements like copper (Cu), iron (Fe), molybdenum (Mo), or chromium (Cr), the particular wavelengths of these components are unique. Filtering methods, like foils or crystal monochrometers, are crucial for obtaining the monochromatic X-rays required for diffraction. Given the close alignment of Kα1 and $K\alpha_2$ wavelengths, it is common practice to utilise a weighted average. CuKα radiation with a wavelength of 1.5418 Å is produced by single-crystal diffraction on copper, the most common target material. The X-rays are directed towards the sample with great care in collimation.

2.2 Ultraviolet-Visible (UV-Vis) Absorption Spectroscopy

The field of absorption spectroscopy that falls within the ultraviolet-visible spectral range is known as ultraviolet-visible spectroscopy or UV-Vis. Complementary features are shown by absorption and fluorescence (or photoluminescence) spectroscopy, where photoluminescence is produced by transitions from the excited state back to the ground state. On the other hand, photons are absorbed during the opposite process, which involves going from the ground state to the excited state. The Beer-Lambert law measures the extent of absorption.

$$A = -log\frac{I}{I_0} \tag{2.2}$$

The absorbance 'A' is determined using the formula where 'A' represents the absorbance, 'I_0' is the intensity of the incident light, and 'I' is the transmitted intensity (in equation 2.2). These parameters are specific to a given wavelength of light.

According to the Beer-Lambert Law, the concentration of a material in a solution is directly correlated with A of the solution:

$$A = \epsilon cL \tag{2.3}$$

L is the optical path length, c is the solution's concentration, and ϵ is the molar extinction coefficient.[3]
Interactions between light and the sample can manifest in three primary ways: (i) absorption, (ii) transmission, and (iii) reflection, along with potential scattering. To ensure accurate measurements, a systematic procedure is followed:

Systematic measurements are carried out in controlled environments to characterize the interactions between light and a sample. In order to achieve 100% transmittance (%T), light transmission must be measured in the transmission port without any sample to create the instrument's baseline measurement. 100% reflectance (%R) is obtained by inserting a Spectralon white standard into the reflectance port. At the transmission port, transmittance (%T) values are noted for both the sample and a reference. In order to accurately analyze the reflected light, the sample is placed outside the integrating sphere for reflectance (%R) measurements.

The percentage of absorbed light, denoted as %A, can be computed using the equation:

$$\%A = 1 - \%T - \%R \tag{2.4}$$

The absorbance, represented by A, is then determined by:

$$A = -\log(1 - \%A) \tag{2.5}$$

$$A_{film} = A_{sample} - A_{reference} \tag{2.6}$$

Furthermore, a flexible method for figuring out semiconductor band gaps is the Tauc plot. This plot effectively illustrates the relationship between the energy of the incoming light and the material's absorption coefficient. The x-axis represents the energy of the incident light (hυ). Meanwhile, the y-axis shows (αhυ)^(1/r), where α is the material's absorption coefficient, and r is the exponent that describes the transition's nature. For direct allowed transitions, r=1/2, while r=2 for indirect permitted transitions. Plotting the square of the absorption coefficient with photon energy and fitting a straight line to the graph allows us to calculate the band gap. The band gap for semiconductors with a direct band gap is represented by the junction point of the linear fit and the energy axis. In semiconductors with an indirect band gap, on the other hand, the band gap is found using the junction point of the linear fit between the energy axis and the square root of the absorption coefficient and photon energy.

2.3 Photoluminescence (PL) Spectroscopy

Photoluminescence spectroscopy is a widely utilised characterisation method, especially for semiconductor materials, and it holds particular significance in the analysis of halide perovskite solar cell materials. This technique provides valuable insights into the recombination dynamics and mechanisms, along with information about the internal electrochemical potential of free charge carriers. Photoluminescence spectroscopy can be applied to single semiconductor layers, layer configurations that include transport layers, and entire solar cells, offering a comprehensive understanding of the materials' photophysical properties.[4]

This is fundamentally based on the measurement of photons emitted from a semiconductor, a process arising from radiative recombination. Radiative recombination necessitates the participation of both an electron and a hole in a recombination event (as depicted in Figure 2.3b). Once the photon is internally generated through radiative recombination, it can follow one of two paths: it can either be emitted from the sample, contributing to the emission spectrum, or the sample itself might reabsorb it before it can exit the material. Conversely, electron-hole recombination can also occur without the emission of photons through non-radiative processes. This type of recombination is influenced by surface states, bulk defects, and traps within the material (Figure 2.3a). These non-radiative processes lead to the loss of energy without the generation of light, and they play a significant role in the photophysics of semiconductor materials.[5]

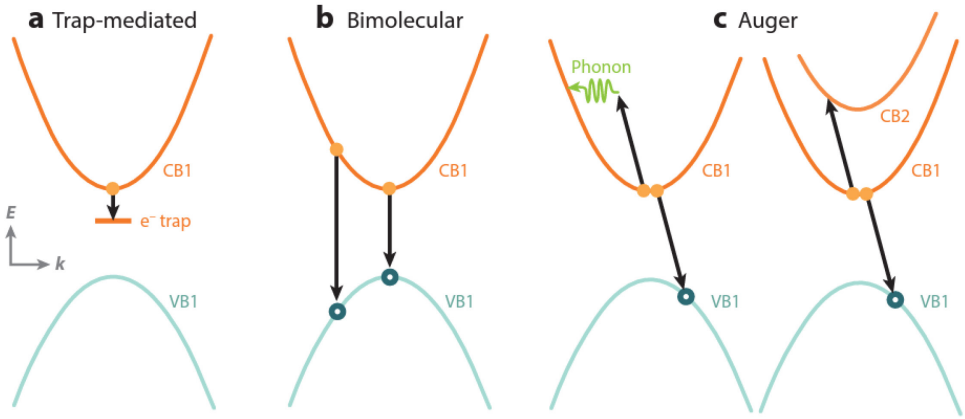

Figure 2.3 Schematic illustration of recombination mechanisms active inorganic-inorganic metal halide perovskites.

2.4 Time-Correlated Single Photon Counting (TCSPC)

Time-Correlated Single Photon Counting (TCSPC) characterises materials according to their fluorescence. It differs from steady-state techniques since it uses time-resolved spectroscopy to evaluate photoluminescence (PL). In TCSPC, a sample is excited by a short light pulse, and then the signal strength is measured as a function of time while the sample decays in low light. The time needed for a fluorescent sample's light intensity to drop to 1/e of its starting intensity is known as the sample's lifetime. The lifespan is the average amount of time a molecule stays excited.

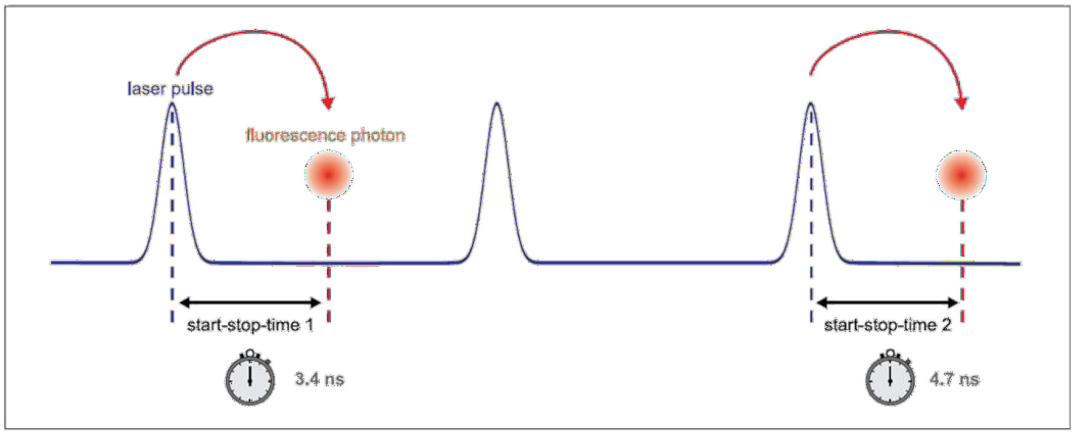

Figure 2.4 Measurement of start-stop times in TCSPC.

As seen in Figure 2.4, the TCSPC instrument measures the time that passes between the excitation source producing a pulse and the photon's emission. The intensity of the photons released is measured and plotted against time using this data. A single photon must be measured simultaneously, and a histogram must represent each photon (Figure 2.5).[6] Following the accumulation of many photons, a decay curve is produced. The straight proportionality between the emission intensity and the probability of detecting a photon at a given time justifies using photon count data.

By monitoring the decay of photoluminescence over time, we can investigate the radiative recombination of charge carriers versus non-radiative recombination processes within the system, which can provide valuable information on the recombination mechanism of free charge carriers and extract relevant information about them.

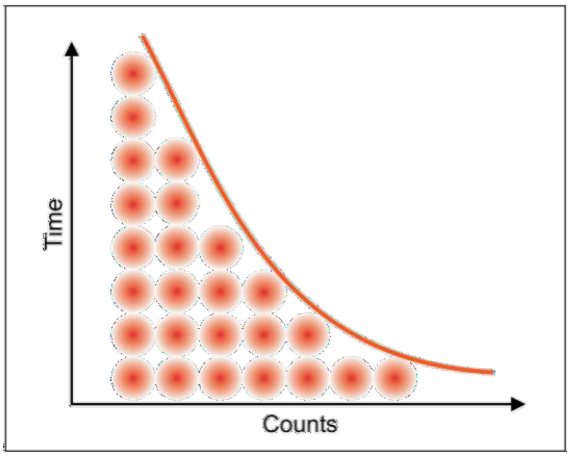

Figure 2.5 Histogram of start-stop times with TCSPC measurements.

2.5 Electron Microscopies

Electron microscopy, in its various forms, such as scanning electron microscopy (SEM) for examining bulk samples or transmission electron microscopy (TEM) for thin specimens, offers the capability not only to visualise specific locations with sub-angstrom precision but also to analyse the microstructural characteristics, chemical compositions, as well as electrical and optoelectronic attributes of individual layers and their interfaces within thin-film solar cells.

2.5.1 Transmission Electron Microscopy (TEM)

Transmission electron microscopy (TEM) and related methods are valuable tools for imaging and analysis at atomic scales. Additionally, without requiring the laborious specimen preparations needed for TEM, scanning electron microscopy (SEM) techniques are frequently used to explore different material properties within individual layers. However, TEM has certain clear benefits, especially when investigating the properties of grain boundaries, interfaces between layers, or other sub-nanometer-scale features.

An electron beam, usually accelerated to energies between 80 and 1200 keV, is emitted by an electron cannon attached to a transmission electron microscope. As shown in Figure 2.6, the way these electrons interact with the sample varies depending on whether they are in the scanning TEM (STEM) or conventional TEM (CTEM) modes. In CTEM mode, an electron beam almost parallel to the specimen is irradiated, allowing for electron diffraction and imaging within a designated area of interest. The beam can be concentrated on a specific location and scanned throughout the region of interest using contemporary microscopes with electron probe sizes less than 0.1 nm. This allows for compositional analysis, electron diffraction, and high-resolution imaging.[7]

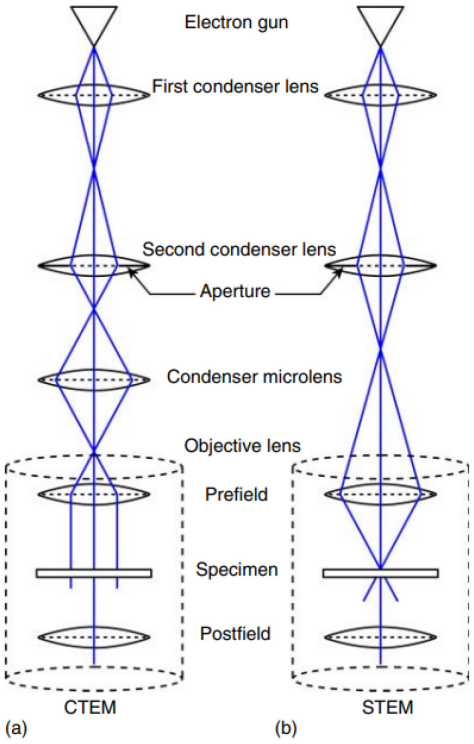

Figure 2.6 Diagrams illustrating the lens arrangements in the upper section of a transmission electron microscope (TEM) and their effects on the trajectories of electron beams in conventional TEM (CTEM) (a) and scanning TEM (STEM) (b). [7]

Once electrons are produced from a source, the electron beam is concentrated and amplified using magnetic lenses. Figure 2.6 shows how a transmission electron microscope (TEM) is configured. The condenser lenses control the electron beam, which passes through the condenser aperture and strikes the sample's surface. Beams that are transmitted through the objective lens are the result of electrons being scattered elastically. The picture is formed within the objective lens, and the objective and a selected area aperture are used to choose the elastically dispersed electrons that form the microscope's image. The beam then moves on to a system of magnification, and the final image is shown on a monitor.

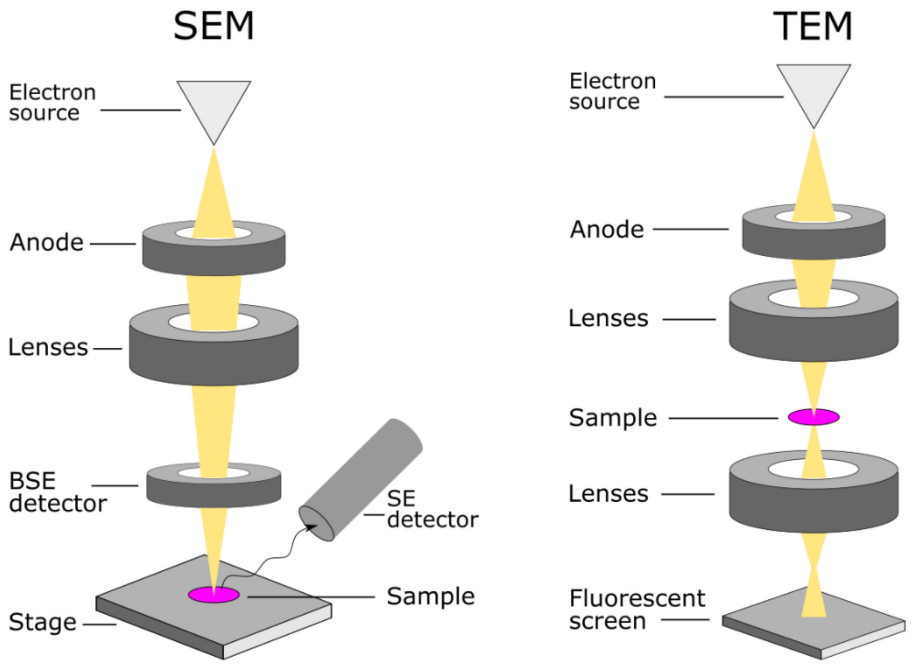

Figure 2.7 Schematic illustrations comparing SEM and TEM.[8]

To choose between diffracted or direct electron beams for imaging, an objective aperture can be placed in the objective lens's back-focal plane. This process enhances the contrast in a transmission electron microscopy (TEM) image. Suppose the objective aperture is placed over the diffraction pattern's central (000) reflection. In that case, an image that mostly shows the direct electron beam can be obtained while blocking some diffracted beams. This results in a bright area in the picture, known as the bright-field (BF) imaging method. Alternatively, selecting diffracted beams via the objective aperture makes the central region turn black. This method is known as the dark-field (DF) imaging technique.

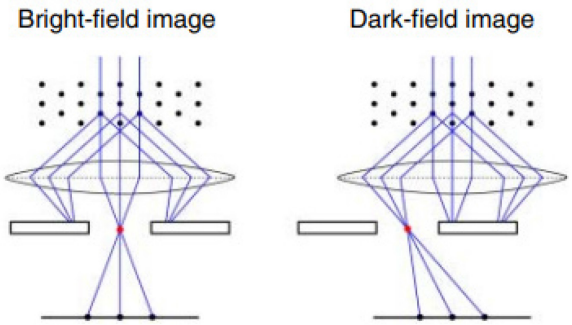

Figure 2.8 Schematics of BF and DF imaging in the CTEM mode of the microscope.[7]

2.5.2 Scanning Electron Microscopy (SEM)

A specialist tool called a scanning electron microscope (SEM) uses a focussed electron beam to scan a specimen's surface and take pictures of it. The sample's atoms and electrons interact to produce signals that provide details about the sample's chemical makeup and surface structure.

In an SEM, the electrons used for imaging are either secondary electrons (SEs) or backscattered electrons (BSEs). Both types are emitted from the specimen when exposed to the electron beam. Secondary electrons have energies ranging from 0 to 50 electronvolts (eV), while backscattered electrons have energies from 50 eV up to the power of the primary electron beam. Detectors capture emitted electrons, and the signal adjusts the brightness of a cathode ray tube, creating the SEM image. Each point on the sample's surface that the electron beam interacts with is directly mapped to a corresponding point on the CRT screen.[9]

Backscattered electrons help image thin films and provide insights into a material's crystal symmetry and orientation when diffraction occurs at specific atomic planes.[10]

When a sample is excited by an energy source, such as an electron beam in an electron microscope, it releases some of the absorbed energy by ejecting a core-shell electron. A higher-energy outer-shell electron fills the vacant position, emitting the energy difference as an X-ray with a characteristic spectrum that identifies the originating atom. Energy-dispersive X-ray spectroscopy (EDS), or EDX or XEDS, is used for materials' chemical characterisation and elemental analysis.

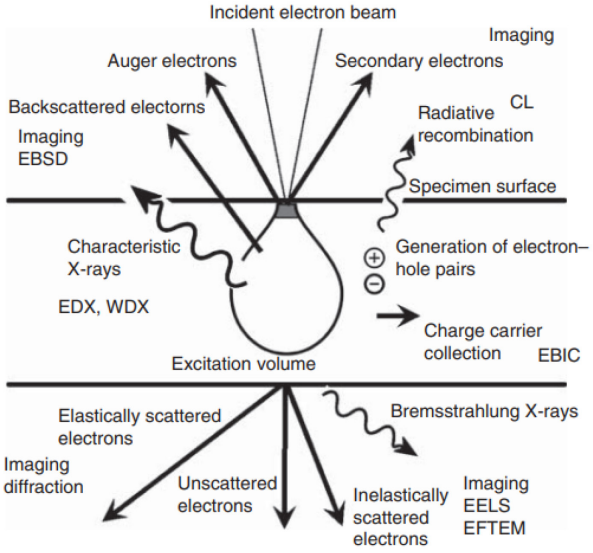

Figure 2.9 Various emissions of electrons and photons when an electron beam irradiates a semiconducting sample.[7]

2.6 Raman Spectroscopy

Raman spectroscopy is a commonly used spectroscopic method for determining molecules' vibrational modes. This technique is frequently used in chemistry to create a unique structural signature that helps to identify molecules.

The technique is based on a phenomenon known as Raman scattering, which is an inelastic photon scattering. A monochromatic light source is employed, most commonly a near-ultraviolet, near-infrared, or visible laser (X-rays can also be used). The energy of the laser photons is shifted, either up or down, as seen in Figure 2.10, by the interaction of the laser light with molecules, phonons, or other excitations in the system. This energy transfer reveals essential details regarding the system's vibrational modes. Another method that offers comparable but complementing data is infrared spectroscopy.[11]

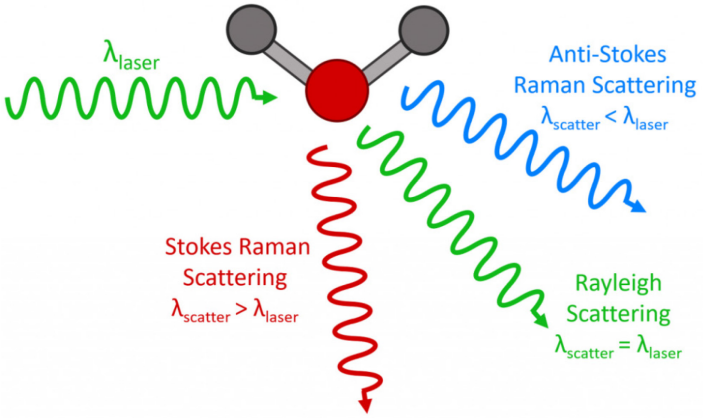

Figure 2.10 Three scattering processes occur when light interacts with a molecule.[12]

2.7 Infrared Spectroscopy

The goal of infrared spectroscopy, also known as vibrational spectroscopy or IR spectroscopy, is to measure how infrared light interacts with matter through processes like absorption, emission, and reflection. This analytical instrument plays a crucial role in analysing and identifying chemical compounds or functional groups in various states, such as liquids, solids, and gases. In actual use, infrared spectroscopy is a valuable technique for identifying and authenticating known and unknown samples and characterising novel materials.

The electromagnetic spectrum's infrared portion is typically divided into three primary regions:

- Near Infrared (NIR), which includes wavelengths between 0.7 and 2.5 micrometres (μm), or 14,000 and 4,000 wave numbers (cm^{-1})
- Mid Infrared (MIR), which includes wavelengths between 2.5 and 25 μm (4,000 and 400 cm^{-1})
- Far Infrared (FIR), which includes wavelengths between 25 and 1,000 μm (400 to 10 cm^{-1})

The longest wavelengths with lower wavenumbers are found in FIR, whereas the shortest wavelengths with higher wavenumbers are found in NIR.[13]

The constituent atoms of chemical compounds are constantly in motion, vibrating in different modes. Figure 2.11 illustrates the six types of vibrational modes, even in a very simple molecule like water (H_2O). These modes include symmetric stretch,..., and twisting. Chemical compounds can absorb infrared (IR) light by matching these molecular vibration frequencies with IR light, which excites the vibrational modes within the molecules.

In water, for example, the symmetric and antisymmetric stretches happen between 2700 and 3700 cm^{-1}, whereas the deformation vibration happens at about 1650 cm^{-1}.

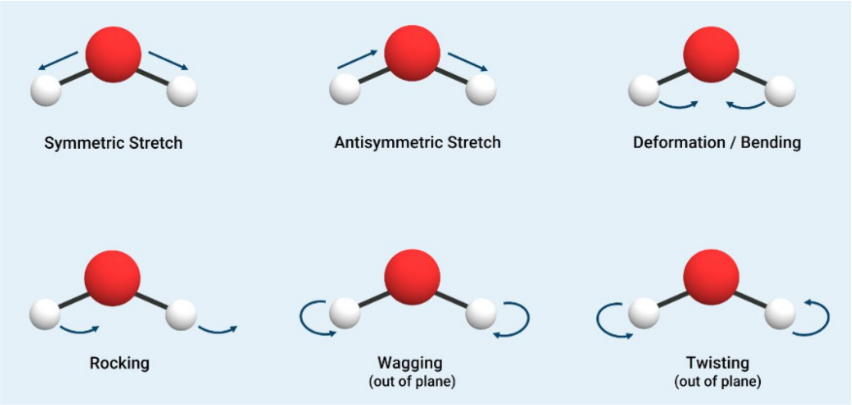

Figure 2.11 Six distinct types of vibrational modes of H_2O molecule.[14]

2.8 Nano-FTIR Absorption Spectroscopy

Fourier Transform Infrared (FTIR) spectroscopy is widely used for chemical identification. It provides absorption spectra in the mid-infrared frequency range, typically between 400 and 4000 cm^{-1}, equal to wavelengths between 2.5 and 25 μm. These spectra can be compared with databases to recognise various materials rapidly. Because of its effectiveness, FTIR spectroscopy is commonly used in analytical chemistry, biology, and medicine. However, the spatial resolution of FTIR microscopy is limited by diffraction to around one wavelength, which restricts its ability to discern features smaller than a few micrometres.[15]

Recently, scattering-type scanning near-field optical microscopy (s-SNOM) has opened the door to ultra-resolving infrared microscopy. s-SNOM can be seen as an extension of atomic force microscopy (AFM) and can provide both infrared images and topographical data, making it a valuable tool for achieving nanoscale spatial resolution in the infrared domain.[16]

With this technique, a metallic tip is chosen to serve as an antenna, precisely focusing the incident light at the tip's apex. The near-field interaction between the tip and the sample determines how light is scattered from it. By scanning the surface of the sample and catching the dispersed light, a near-field image is produced. Interestingly, the resolution of this method depends only on the size of the tip's apex, typically about 20 nanometers (nm), and not on the illumination's wavelength.[17]

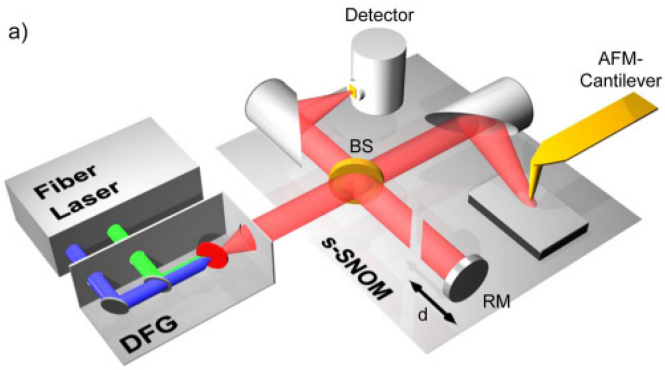

Figure 2.12 Experimental setup of Nano-FTIR.

2.9 Solar Cell Characterization

It is recommended to analyze the current-voltage (I-V) curves in bright and dim light conditions to determine how well a solar cell performs. This technique allows one to directly evaluate the solar cell's Power Conversion Efficiency (PCE), which serves as a reliable gauge of its quality.

Standard conditions are employed when conducting I-V measurements under illumination. These conditions involve using a standard air mass 1.5 global (AM1.5G) spectrum with an incident power of 100 milliwatts per square centimetre (mW/cm²), also referred to as the intensity of one sun. This standardised illumination enables consistent and comparable evaluations of solar cell performance.

This procedure involves gradually adjusting the bias voltage. Simultaneously measured is the corresponding photocurrent (Figure 2.13), which yields essential parameters such as the power conversion efficiency (η), fill factor (FF), open-circuit voltage (Voc), short-circuit current (Isc) or current density (Jsc), and so on that reflect the performance of the solar cell. The formula that follows relates these parameters:

$$\eta = \frac{Pm}{Pin} = \frac{Isc\ Voc\ FF}{Pin\ Aaperture} = \frac{Jsc\ Voc\ FF}{Pin} \tag{2.7}$$

Where P is the power output, I is the current, V is the voltage, J is the current density, A is the cell's aperture area, and η is the power conversion efficiency.[18]

External factors such as the light source and temperature can affect the results of this process. A solar cell's performance is temperature-sensitive, and its power conversion efficiency generally changes linearly around room temperature. The temperature coefficient for power conversion efficiency is approximately -0.045% per degree Celsius (°C) for silicon solar cells.[19]

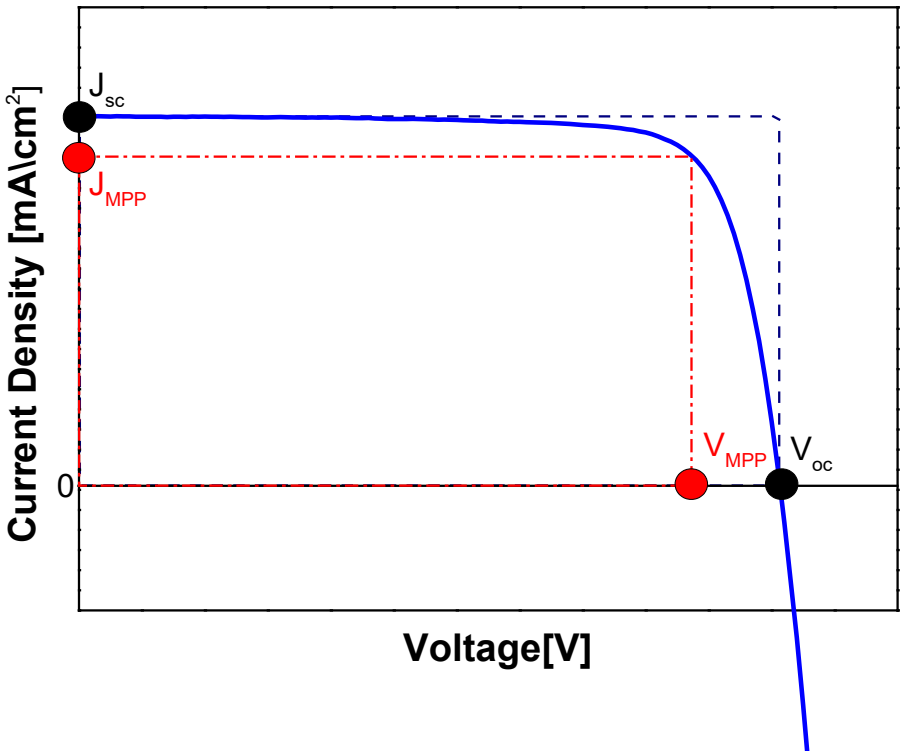

Figure 2.13 A typical *J-V* curve obtained from a solar cell under illumination.

Standardized measurement settings are necessary for comparing samples, architectures, and lab results. One of the most critical parameters is the light intensity, standardized to 1000 W/m2, or one sun, the total light intensity. The air mass 1.5 global (AM1.5G) standard sunshine spectrum is produced from a realistic atmospheric transmittance model with the sun at approximately 41 degrees above the horizon. Figure 2.13 shows a typical J-V curve derived from a solar cell under light.

2.10 References

1. Bunaciu, A. A.; Udriştioiu, E. g.; Aboul-Enein, H. Y., *Critical Reviews in Analytical Chemistry* **2015,** 45, 289-299.
2. *Britannica.com/science/X-ray-diffraction*
3. Pazoki, M., Hagfeldt, A., & Edvinsson, T. (Eds.). (**2019**). *Characterisation Techniques for Perovskite Solar Cell Materials*. Elsevier.
4. Kirchartz, T., Márquez, J. A., Stolterfoht, M., & Unold, T. (**2020**). Photoluminescence-based characterisation of halide perovskites for photovoltaics. *Advanced energy materials*, *10*(26), 1904134.
5. Herz, L. M. **(2016**). Charge-carrier dynamics in organic-inorganic metal halide perovskites. *Annual review of physical chemistry*, *67*, 65-89.
6. Wahl, M. Technical Note on Time-Correlated Single Photon Counting *PicoQuant GmbH* [Online], 2014.
7. Abou-Ras, D., Nichterwitz, M., Romero, M. J., & Schmidt, S. S. (**2016**). Electron microscopy on thin films for solar cells. *Advanced characterization techniques for thin film solar cells*, *1*, 371-420.
8. Anapath.ch/electron-microscopy-2/
9. Reimer, L., & Microscopy, S. E. (**1985**). Physics of image formation and microanalysis. *Springer*, *45*, 135.
10. Schwartz, A. J., Kumar, M., Adams, B. L., & Field, D. P. (Eds.). (**2009**). *Electron backscatter diffraction in materials science* (Vol. 2, pp. 35-52). New York: Springer.
11. Graves, P. R. G. D. J., & Gardiner, D. (**1989**). Practical raman spectroscopy. *Springer*, *10*.
12. *Edinst.com/blog/what-is-raman-spectroscopy/*
13. Stuart, B. H. (**2004**). *Infrared spectroscopy: fundamentals and applications*. John Wiley & Sons.
14. Bruker.com/en/products-and-solutions/infrared-and-raman/ft-ir-routine-spectrometer/what-is-ft-ir-spectroscopy.html
15. Shao, L., Pollard, M. J., Griffiths, P. R., Westermann, D. T., & Bjorneberg, D. L. (**2007**). Rejection criteria for open-path Fourier transform infrared spectrometry during continuous atmospheric monitoring. *Vibrational spectroscopy*, *43*(1), 78-85.
16. Huth, F., Govyadinov, A., Amarie, S., Nuansing, W., Keilmann, F., & Hillenbrand, R. (**2012**). Nano-FTIR absorption spectroscopy of molecular fingerprints at 20 nm spatial resolution. *Nano letters*, *12*(8), 3973-3978.
17. Keilmann, F.; Hillenbrand, R. Nano-Optics and Near-Field Optical Microscopy; Artech House: Boston/London, **2008**
18. Wang, Y., Liu, X., Zhou, Z., Ru, P., Chen, H., Yang, X., & Han, L. (**2019**). Reliable measurement of perovskite solar cells. *Advanced Materials*, *31*(47), 1803231.
19. Ahmed, A., Elsakka, M., Elminshawy, N., Mohamed, A., & Sundaram, S. (**2023**). Recent Advances in Floating Photovoltaic Systems. *The Chemical Record*, e202300229

3 1,10-Phenanthroline as an efficient bifunctional passivating agent for $MAPbI_3$ perovskite solar cells

This chapter is based on the following publication:

Buyruk, A., Blätte, D., Günther, M., Scheel, M. A., Hartmann, N. F., Döblinger, M., ... & Ameri, T. (2021). 1, 10-Phenanthroline as an efficient bifunctional passivating agent for MAPbI3 perovskite solar cells. *ACS Applied Materials & Interfaces*, *13*(28), 32894-32905.

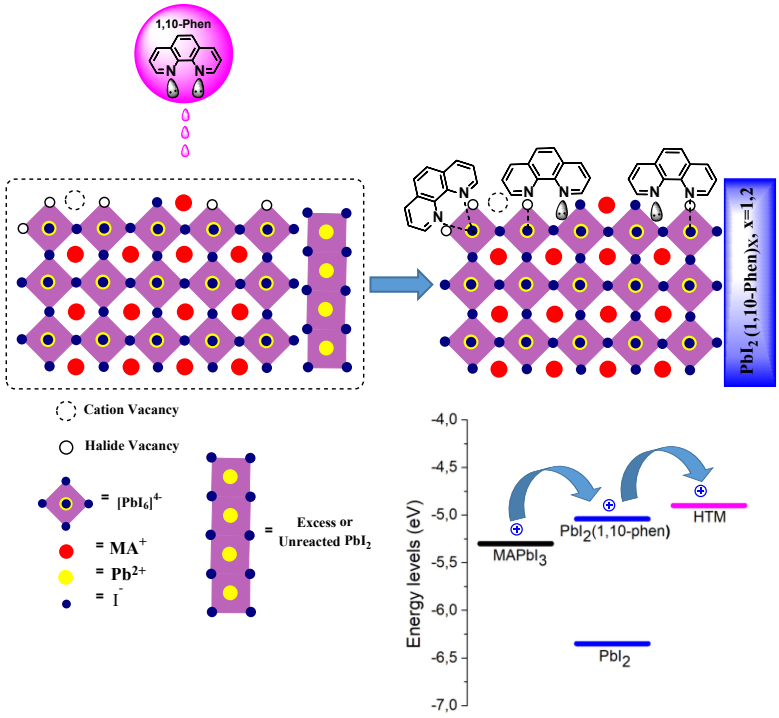

Keywords

defects passivation, multiple ligand, 1,10-phenanthroline, lead iodide, perovskite solar cel

3.1 Introduction

The perovskite solar cell (PSC) technology is one of the most promising candidates to compete with the commercially available photovoltaic technologies such as crystalline silicon and copper indium gallium selenide, the dominant PV technologies on the market[1] over the last 2 decades, due to its remarkable properties such as high device efficiency[2], easy solution and low-temperature processability[3-5], chemical composition tunability, and low-cost production.[6-8] However, the chemical and structural properties of this material and its low-temperature processing inevitably create detrimental defects at the surface and the grain boundaries (GBs) of the *perovskite polycrystalline structure*[9-11], which can significantly deteriorate the photovoltaic performance and stability.[12-14] For instance, the methylammonium ion (MA^+) in $MAPbI_3$, which can form volatile salts, can be easily released from the 3D lattice at elevated temperature, the typical working condition of solar cells, and/or with moisture.[15-17] The release of MA^+ causes also the generation of further types of defects, such as under-coordinated Pb and Pb-I antisite defects.[18-19] Trap states resulted from the MA^+ loss are expected to form significant potential wells at the surface and grain boundaries (GBs) for charge carriers and thus lead to serious charge carrier trapping, charge accumulation, and recombination losses.[20] Meanwhile, the presence of these defects facilitates the permeation of moisture along GBs, which again accelerates trap state formation and raises instability issues.[21] Passivation of the defects has been developed as one of the most promising strategies to obtain an improved stability-performance balance.[22-23] In this regard, different types of materials, such as Lewis bases, Lewis acids, metal cations, metal anions, alkyl ammonium halogenides, aromatic ammonium halogenides, wide bandgap materials, hydrophobic materials, and metal salts, depending on the properties and functions, have been used at the interfaces of the perovskite and in the bulk structure of the perovskite to heal the defects.[22] To date, pyridine and thiophene are the only two archetype Lewis bases to passivate the perovskite surface defects.[24] Based on the intensive study of Lewis bases, considerable progress in understanding the basics and developing novel concepts has been made, one of which is multiple ligand passivation. Unlike the archetype mono-ligand passivators, this new class of Lewis-base passivators contains more heteroatoms and consequently more than one electron lone pair to create coordination bonds, thus passivating the double and triple halide vacancies at the surface of the perovskite.[25-26] Following this approach, multiple coordination bonds with the under-coordinated lead (Pb^{2+}) ions have recently been shown to significantly enhance the stability of the metal-ligand complex.[27]

Importantly, the excess used PbI_2 in the perovskite precursor solutions aiming at better crystallization[28] and passivation[29] effects poses also some problems by changing the surface electronic states and inducing traps in some cases[30] as well as by causing long-term stability issues.[31]

To address the points stressed above, 1,10-phenanthroline (1,10-phen) is implemented as a bidentate

chelating ligand between the photoactive layer ($MAPbI_3$) and the hole transport layer (Spiro-OMeTAD). The 1,10-phen solution with the optimized concentration of 2.5 $mg.mL^{-1}$ is prepared from chlorobenzene (CB) and is spin-coated on the freshly prepared neat $MAPbI_3$ perovskite film at room temperature without further annealing. The multiple bonding ability is expected to allow 1,10-phen not only to passivate mono and double halide vacancies on the perovskite surface but also to convert the interface buried PbI_2 into beneficial complex species, resulting in a more stable metal-ligand complex and a remarkable improvement in the performance and stability of the device.

To investigate the effects of the 1,10-phen surface treatment, a complementary set of advanced optoelectric and structural characterization methods is employed from which a detailed description of the passivation mechanism is derived.

3.2 Results and Discussion

After the surface treatment of the reference perovskite-based solar cell with the 1,10-phen small molecules, optical absorption characteristics in the range of 400 – 800 nm are mostly unaffected (**Figure 1b**), as would be expected for surface functionalization by 1,10-phen, which absorbs only in the UV range below 300 nm.[32] The slight enhancement of UV-Vis absorption in the treated film might arise from the small variation in thickness and area of measurement position or scattering from the top surface after treatment. To evaluate the charge carrier recombination dynamics of the perovskite film after treatment, steady-state photoluminescence (PL) and time-resolved PL (TRPL) measurements were performed.

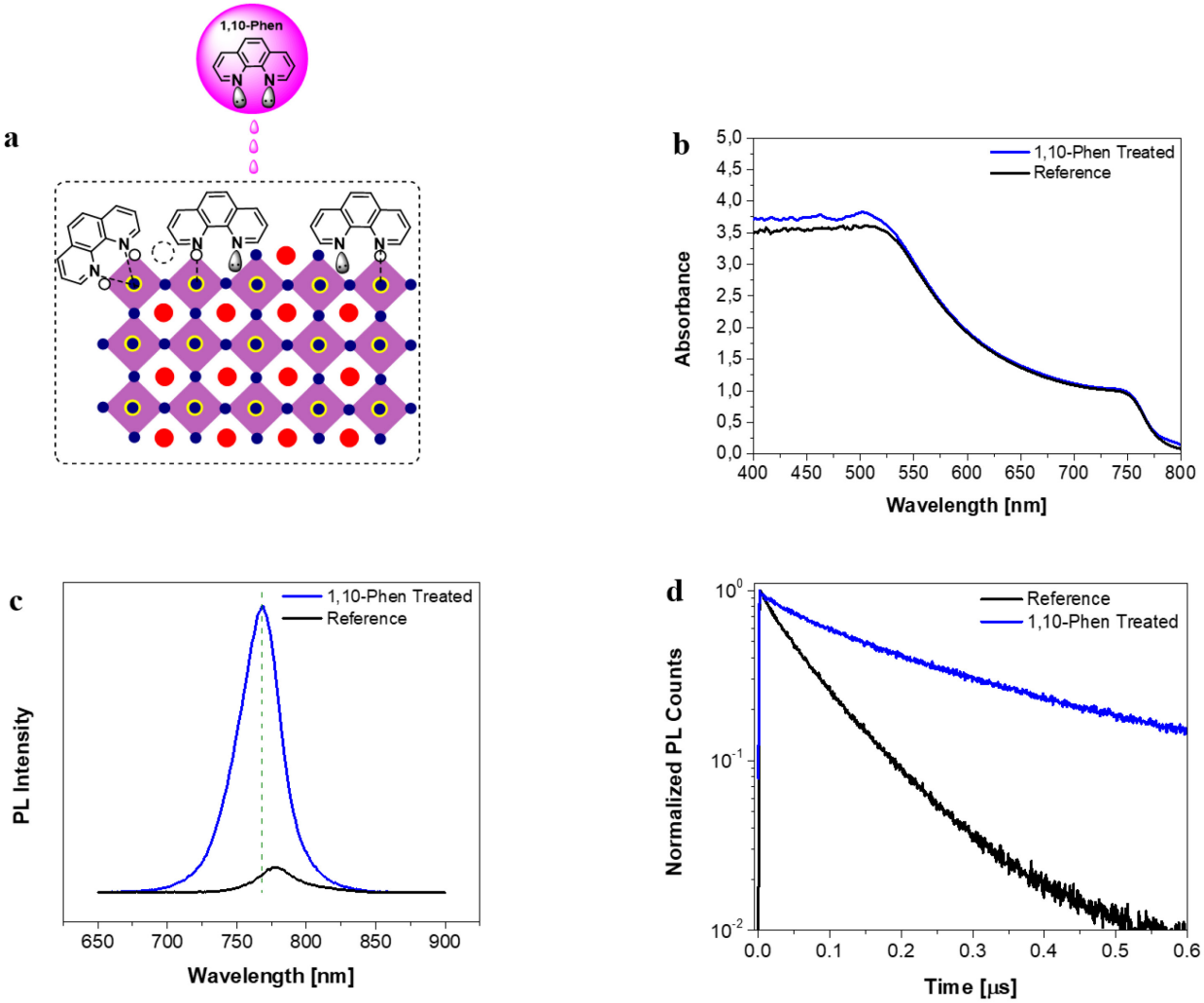

Figure 1. a) Schematic illustration of the perovskite crystal with representative defects and possible passivation mechanisms after the 1,10-phen surface treatment. b) UV-Vis absorption spectrum; c) steady-state PL spectra (excitation wavelength of 375 nm); and d) time-resolved PL decay curves of the reference $MAPbI_3$ and 1,10-phen treated $MAPbI_3$ films.

The steady-state PL spectrum of the 1,10-phen treated perovskite film shows an over tenfold enhanced and blue-shifted PL compared to the $MAPbI_3$ reference (**Figure 1c**), which is a good indicator of the passivated defects and reduced non-radiative recombination at the perovskite surface. Based on the TRPL results, presented in **Figure 1d** and **Table S1**, the surface passivation with 1,10-phen extends the lifetime of the perovskite photoluminescence, on average from 77 ns to 225 ns, which establishes a strong indication of suppressed trap-assisted recombination at the surface.[33] We propose that, after passivation treatment, the under-coordinated lead (Pb^{2+}) ions can be ligand-saturated through lone pair electrons of 1,10-phen (**Figure 1a**). In fact, in addition to the lead-based surface defects, excess/unreacted lead iodide (PbI_2), which are problematic for the long-term stability, can be effectively converted into ′neutralized′ and beneficial species by strong bidentate anchoring. In order to prove our hypothesis and obtain more information on the complexation tendency of lead atoms, we first mimicked the chemical bonding of the 1,10-phen with the under-coordinated surface lead ions and excess/unreacted lead iodide (PbI_2) by preparing model PbI_2(1,10-phen) and PbI_2(1,10-phen)$_2$ complexes[34] (**Figure S1**) at room temperature (more details are presented in the experimental section). 1,10-phen and its PbI_2 complex were studied with Raman spectroscopy. After complexation of PbI_2 with 1,10-phen, the typical Raman bands of PbI_2 (71, 95, and 111 cm^{-1})[35], shown in **Figure 2a**, and the Raman signals of the 1,10-phen powder (for example the peaks at 411, 711, 1035, 1295, and 1404 cm^{-1}), shown in **Figure 2b**, are retained with a uniform upshift. Furthermore, new Raman bands are observed for the complex at 249 and 265 cm^{-1} wavenumbers, shown in **Figure 2a** with an asterisk, which is attributed to the Pb-N(1,10-phen) stretching vibrations.[36-38] Indeed, these up-shifted and observed new signals in Raman spectrum for the complex powder are both good indicators of chemical interactions between the small molecule ligand and Pb atoms and support the anchoring ability of the 1,10-phen on the unreacted PbI_2 and under-coordinated lead ions of the perovskite surface.

X-ray diffraction (XRD), grazing-incidence wide-angle X-ray scattering (GIWAXS), and scanning electron microscopy (SEM) measurements were used to investigate the crystallinity and morphological properties of the reference $MAPbI_3$ and the 1,10-phen-treated films. In the XRD patterns of the reference film, the peak relating to the intentionally used excess PbI_2 (+5%) is prominently observed at 12.63°. In contrast, this PbI_2 peak almost vanishes in the XRD pattern of the 1,10-phen treated film, which we attribute to the surface treatment (**Figure 2c**). This is consistent with the Raman spectroscopic results (**Figure 2a-b**) relating to the complexation ability of 1,10-phen with lead ions and excess PbI_2. Furthermore, a new peak is observed at around 9.56° in the 1,10-phen treated film, which can be attributed to a newly formed phase. Indeed, the corresponding SEM images reveal the formation of additional platelets on the surface of the perovskite film (**Figure 4b**) after 1,10-phen treatment. In order to examine the new phase formed after the surface treatment, X-ray diffraction patterns of 1,10-phen and its model coordination compounds with PbI_2 (PbI_2(1,10-phen) and PbI_2(1,10-phen)$_2$)[34] in powder

forms were evaluated (**Figure 2d**). The new peak observed in the 1,10-phen treated film does not overlap with the pure 1,10-phen XRD patterns. However, this peak is very close to that of the PbI_2(1,10-phen) and PbI_2(1,10-phen)$_2$ peaks at 9.60° and 9.46°, respectively. We attribute this feature to the presence of a combination of *the two* coordination compounds. Besides that, a weak peak relating to PbI_2(1,10-phen)$_2$ complex at around 12.53° is observed. It suggests the formation of mixed-complex forms (PbI_2(1,10-phen)$_x$, X=1,2) after surface treatment, during which a large portion of the excess used PbI_2 (+5%) is reacted with 1,10-phen to form the predicted model coordination compounds.

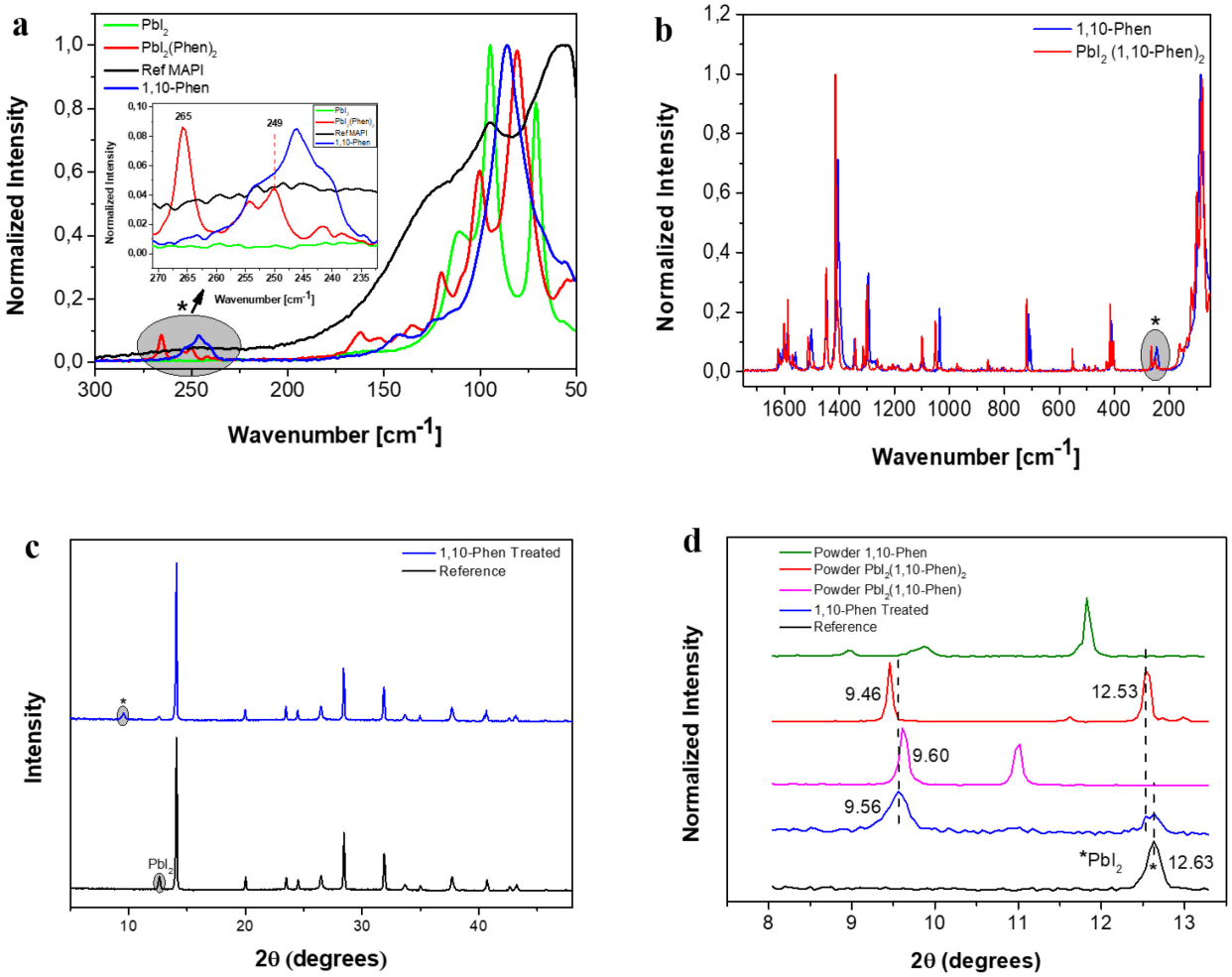

Figure 2. a) Raman spectra of the $MAPbI_3$ reference, and powder forms of PbI_2, 1,10-phen, and PbI_2(1,10-phen)$_2$. b) Raman spectra of powder forms of 1,10-phen and PbI_2 (1,10-phen)$_2$ complex. c) XRD patterns of $MAPbI_3$ reference and 1,10-phen treated films d) XRD pattern between 8° and 13° *2 theta* of $MAPbI_3$ reference, 1,10-phen treated films, and powder forms of 1,10-phen, PbI_2(1,10-phen) and PbI_2(1,10-phen)$_2$.

To confirm the formation of new species on the surface of the $MAPbI_3$ film, 2D GIWAXS-images were taken at various grazing-incidence angles of the pristine $MAPbI_3$ thin film and the 1,10-phen treated

film (**Figure 3** (a, b) and (c, d), respectively). The grazing-incidence geometry allows for highly surface-sensitive measurements with an X-ray scattering depth of a few nm at incidence angles below the critical angle (**Figure S3**).[39-41] Thus, it is possible to confirm the formation of new species that are predominantly present at the surface of the perovskite layer. Indexing pseudo-XRD patterns obtained by radial cuts of the 2D GIWAXS-data is found in the supporting information (**Figure S2**). Two new Bragg rings appear at 0.65 $Å^{-1}$ and 0.76 $Å^{-1}$ for the 1,10-phen treated sample, which correspond to a d-spacing of 9.67 and 8.27 Å, respectively. This agrees well with the newly observed Bragg peak in the XRD measurement at 9.56°, which is attributed to the $PbI_2(1,10\text{-phen})_x$. The highest intensity is seen at an incidence angle of around (0.15 ± 0.05) ° which puts the critical angle of the new species in that regime. This is well below the critical angle of the perovskite material of around 0.17 ° at an X-ray energy of 12.4 keV. The density of the new species can thus be estimated to be well below the density of the perovskite material. The new species is partially oriented, which is evident from the radial intensity distribution of both Bragg rings, showing a maximum around χ = 0° and 45 ° for the rings at 0.65 $Å^{-1}$ and 0.76 $Å^{-1}$, respectively (indicated by white arrows in **Figure 3c**). The high degree of orientation agrees well with the surface morphology seen in the SEM images (**Figure 4b**) and can be attributed to oriented growth induced by the $MAPbI_3$ perovskite surface.

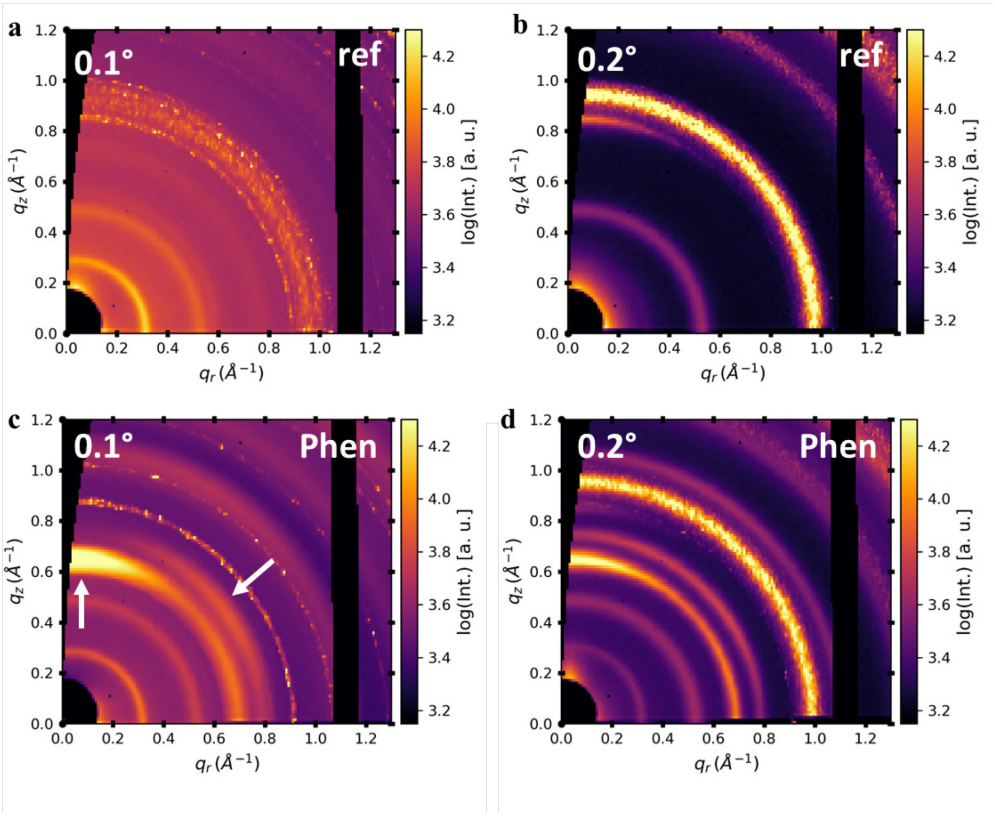

Figure 3) 2D GIWAXS data of the (a, b) $MAPbI_3$ reference sample and (c, d) the 1,10-phen treated sample at an incidence angle of (a, c) 0.1 and (b, d) 0.2°, respectively. The surface treatment leads to two new Bragg rings at around 0.65 $Å^{-1}$ and 0.76 $Å^{-1}$ (as indicated with white arrows).

Based on the SEM images analysis, the $MAPbI_3$ grain size and distribution in the reference and surface-treated films are similar to each other (**Figure 4a-b**). In addition, the surface of the treated sample reveals the presence of new platelets with a height in the 300-350 nm range (Figure S11), whose edges are predominantly tilted towards the perovskite surface. Atomic number sensitive backscatter electron images indicate the lower overall atomic weight of the surface phase. EDX analysis by SEM reveals a strongly increased carbon content of the plates (**Figure 5c**), while X-rays typical for Pb, I, and N signals were also observed (**Figure S6)**. However, this top-view measurement geometry does not exclude signals from the subjacent perovskite, also containing Pb, I, and N. For further analysis of the surface phase, a cross-section (prepared by Focussed Ion Beam (FIB) machining, see Supplementary Information) of the 1,10-phen treated film was studied by atomic number sensitive HAADF-STEM (**Figure S4**). The dark contrast of the additional phase as compared to the $MAPbI_3$ perovskite film illustrates an overall lower atomic number. In **Figure 6** the platelet surface phase can be observed not only as rod-like features but also as thin-film (around 10 nm) coverage on the perovskite, hinting to wetting of the perovskite by the surface phase. EDX maps of the STEM cross-section image, shown in **Figure 7,** reveal the presence of C, N, Pb, and I in the rod-like features, the latter two at lower relative amounts compared to the perovskite. (**Figure S6**).

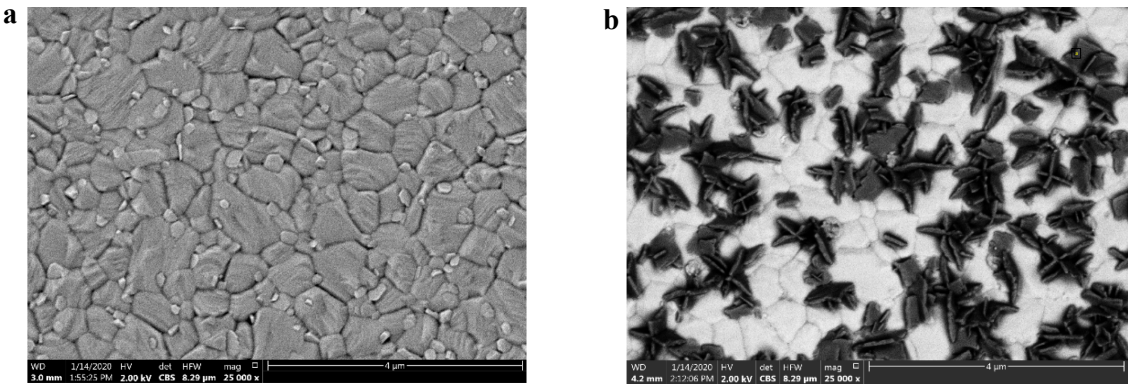

Figure 4. SEM top-view images of untreated (**a**) and surface treated (**b**) $MAPbI_3$ perovskite film, recorded at 2kV with a backscatter electron detector. The darker contrast of the platelets on top of the $MAPbI_3$ film in the right image illustrates the lower overall atomic weight of the surface phase.

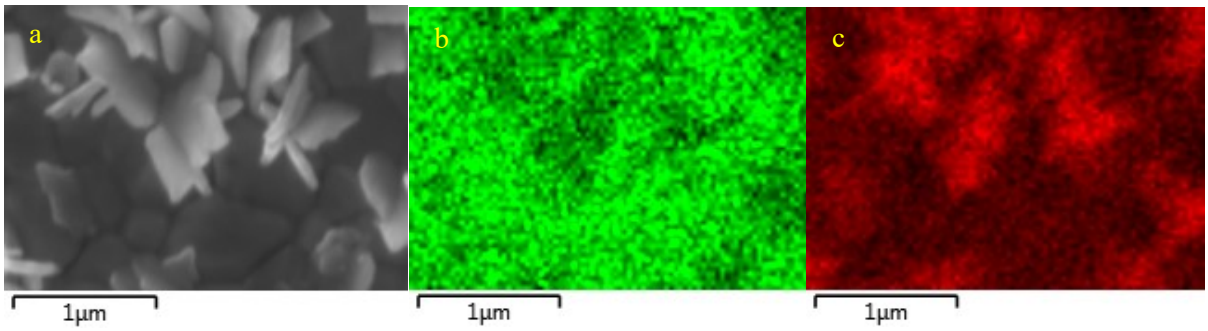

Figure 5. a) Top-view SEM image of 1,10-phen treated $MAPbI_3$ perovskite recorded with secondary electrons showing the additional platelets after treatment with bright contrast. b) Pb–distribution map using Pb-M series X-rays (~ 2.35 keV). The darker shade of green illustrates a lower Pb content in the platelets than in $MAPbI_3$. c) C–distribution map using C-K X-rays (~ 0.28 keV). The relative amount of carbon in the platelets is higher than in $MAPbI_3$.

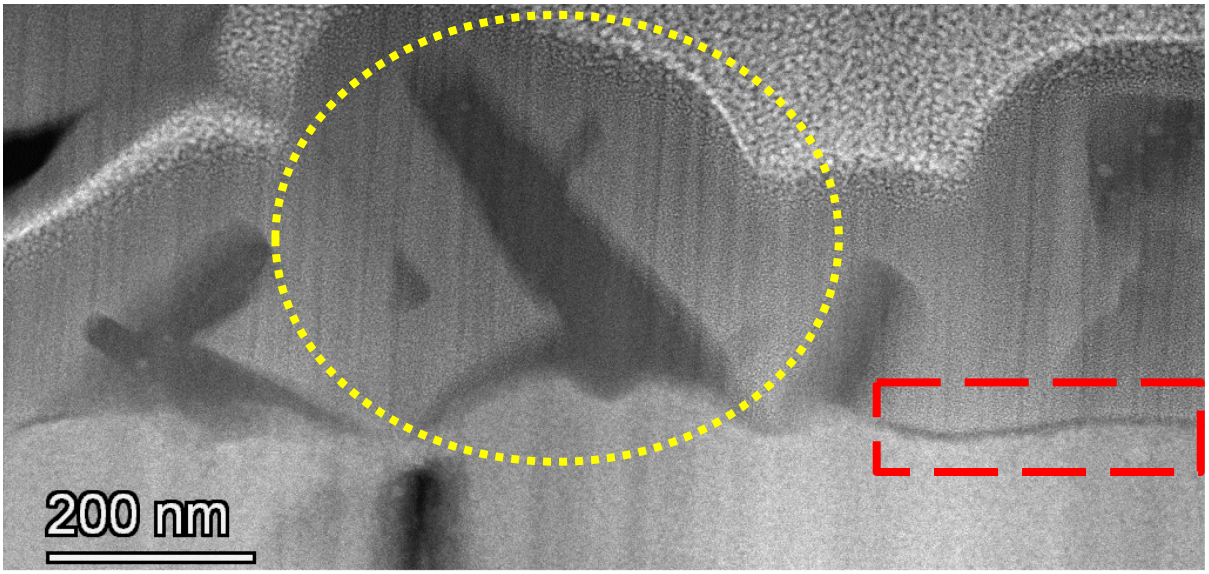

Figure 6. Cross-sectional STEM-HAADF image of 1,10-phen treated $MAPbI_3$ (obtained with FIB). A rod-like dark surface phase (yellow circle) is standing on the perovskite film. A thin layer of dark material (red rectangle) on the perovskite hints at the wetting of the perovskite by the surface phase. The dark surface phase is surrounded by layers of a protective platinum film, successively grown by electron beam induced (dark grey) and ion beam induced (coarse light grey) deposition. An EDX map of this area is shown in **Figure S4**.

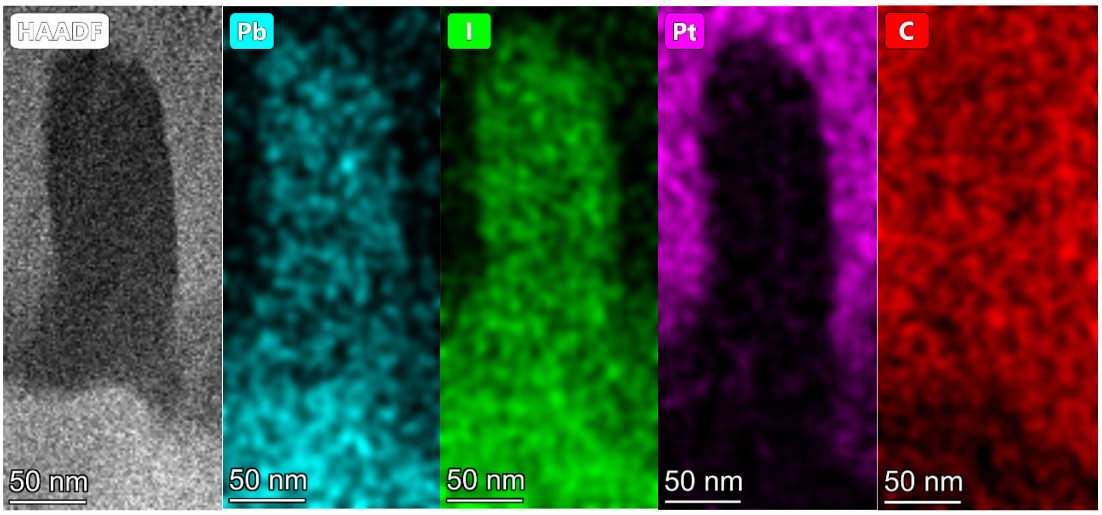

Figure 7. HAADF-STEM image of perovskite film, rod-like surface-grown feature, and surrounding Pt layer and corresponding EDX maps of Pb, I, Pt, and C. Brighter colors indicate a higher relative elemental amount. In the surface phase, the Pb- and I- content is lower than in the perovskite while the C-content is higher. The energy of carbon K-alpha is close to the energy of platinum N-Lines, therefore the surrounding Pt also appears as if it would contain carbon. The nitrogen count rate is too low for a meaningful elemental map.

To complement the information obtained with the above electron microscopic analyses, the recently developed nano-FTIR technique was used to elucidate the chemical structure of the treated sample with 10-20 nm spatial resolution.[42-43] 1,10-phen (powder), PbI_2 (1,10-phen)$_2$ (powder), the reference film ($MAPbI_3$ neat), and the 1,10-phen treated film were studied separately with nano-FTIR to visualize the chemical composition of the sample surface (**Figure 8a-b**). First, the 1,10-phen treated film was studied in comparison with the powder forms of 1,10-phen and PbI_2(1,10-phen)$_2$ (**Figure 8a**). The two most prominent absorption bands at 725, and 861 cm^{-1} (**Table S2**; C–H bending vibrations of the N-containing rings and the central aromatic ring, respectively) in the 1,10-phen treated film demonstrate the presence of the 1,10-phen molecule with mono- and bis-complex forms on top of the $MAPbI_3$. Further, the above TEM analysis (**Figure 6**) gives evidence for different morphologies of 1,10-phen present depending on the sample position. In order to gain more insight into the local structure of the treated surface, neat perovskite (reference) and treated films were studied with the sample positions for nano-FTIR spectra recording marked in the topography image (**Figure 8b inset**). For the neat perovskite (reference) and treated films, the 1280-1800 cm^{-1} range was selected and studied to understand the formation of the different morphologies upon 1,10-phen treatment. The band at 1470 cm^{-1} observed in the nano-FTIR spectra of both reference and 1,10-phen treated films on silicon wafers (**Figure 8b**) is a well-known vibrational mode of $MAPbI_3$ (symmetric NH_3^+ bend).[44] The 1,10-phen treated films show additional peaks at 1493 cm^{-1} and 1515 cm^{-1} (**Figure 8b**, spectra A and B) which are due to vibrational

IR-active modes of PbI_2 $(1,10\text{-phen})_x$ (x=1,2) [45] although with different relative contributions (**Table S2**). At position B, located on top of one of the plate-shaped formations observed in SEM and TEM measurements (**Figure 4b; Figure 6**, yellow circle), the PbI_2 $(1,10\text{-phen})_x$ signatures are most prominent. At position A, which is a location directly over the smooth surface formed by the thinner capping layer observed in the TEM measurement (**Figure 6**, red rectangle) the contributions are substantially reduced. These observations in the nano-FTIR of treated film originating from different spots verify the formation of two different morphologies with the same chemical composition for 1,10-phen passivated film. Together, these observations support the notion of the formation of two distinct morphologies of $PbI_2(1,10\text{-phen})_x$ on the surface of $MAPbI_3$ film with the same chemical compositions, namely as a thinner film and as relatively big plate-shaped formations.

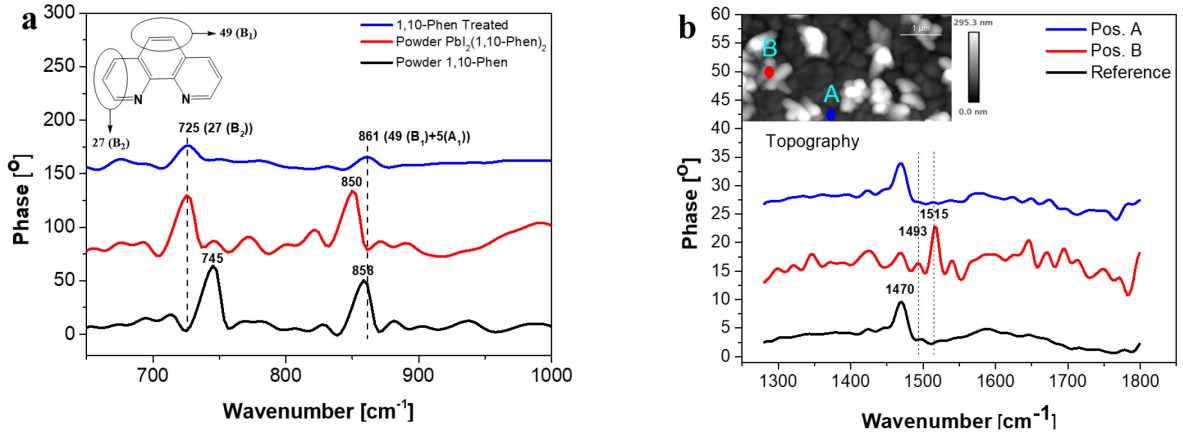

Figure 8. a) nano-FTIR spectra of 1,10-phen treated $MAPbI_3$ film on a silicon wafer, powder forms of 1,10-phen and $PbI_2(1,10\text{-phen})_2$. The inset shows 27($B_2$) and 49($B_1$) modes of 1,10-phen, arising from C–H bending vibrations of the N-containing rings and the central aromatic ring, respectively. b) nano-FTIR spectra of reference (untreated $MAPbI_3$) and 1,10-phen treated films on silicon wafers as a function of nano-scale sample position. The inset shows a 2 µm x 5 µm topography-scan of the treated film with the positions marked where spectra have been recorded.

To evaluate the surface passivating performance of 1,10-phen for $MAPbI_3$ under optimized conditions, an n–i–p planar heterojunction perovskite solar cell was fabricated with the following structure: Glass/FTO/ SnO_2/$MAPbI_3$/ w/- or w/o 1,10-phen /spiro-OMeTAD/ Au. The current density-voltage (*J-V*) curves of the best performance devices are presented in **Figure 9a** and their corresponding performance parameters are listed in **Table 1**. Comparing with the reference cell made with $MAPbI_3$, the 1,10-phen surface-treated device shows higher PCE performance, mainly due to the improved V_{oc} and fill factor (*FF*) (**Figure 9d**, **Figure S7b**). The best reference device gives a PCE of 18.03%, with a V_{oc} of 1.09 V, J_{sc} of 22.35 $mAcm^{-2}$, and fill factor (*FF*) of 74%. In comparison with the best

reference device, the 1,10-phen surface-treated device shows a striking enhancement, a PCE of 20.16%, with a V_{oc} of 1.13 V, J_{sc} of 22.58 $mAcm^{-2}$, and fill factor (*FF*) of 79%. The reference device suffers from a severe hysteresis index (HI) of 0.28, while the 1,10-phen treated device shows a decreased HI of 0.15 under the same scanning conditions. The enhanced V_{oc} of the treated device indicates the effective passivation of surface defects and reduced trap-assisted recombination. The higher *FF* value for the treated device (**Figure S7b**) can be also related to a more efficient hole-extraction at the modified interface of the highly polarized perovskite layer and the nonpolarized HTL, as will be discussed later on. The integrated photocurrent densities, calculated based on external quantum efficiency (EQE) (**Table 1.**), 21.31 $mAcm^{-2}$ for the reference, and 21.75 $mAcm^{-2}$ for the 1,10-phen-treated device are in line with the J_{sc} values from the solar simulator. The slightly higher photocurrent densities in the treated device can be attributed to a more efficient hole-extraction at the modified interface after defect passivation. Significantly, the average performance values of over 50 samples, fabricated at different experimental runs, show a similar trend of improvement as the champion devices (**Figures 9c**, **9d**, **S7a**, and **S7b**).

Table 1. Photovoltaic parameters for the champion devices. The reverse scan values are reported in parentheses.

Sample	J_{sc} **[mA/cm²]**	J_{sc} [a] **[mA/cm²]**	V_{oc} **[V]**	***FF*** **[%]**	**PCE [%]**
Reference (RS*)	22.35 (22.26)	21.31	1.09 (1.03)	74 (57)	18.03 (13.07)
1,10-phen treated (RS)	22.58 (22.60)	21.75	1.13 (1.11)	79 (66)	20.16 (16.56)

a) The integrated photocurrent density calculated from the EQE spectrum.

* RS: Reverse Scans

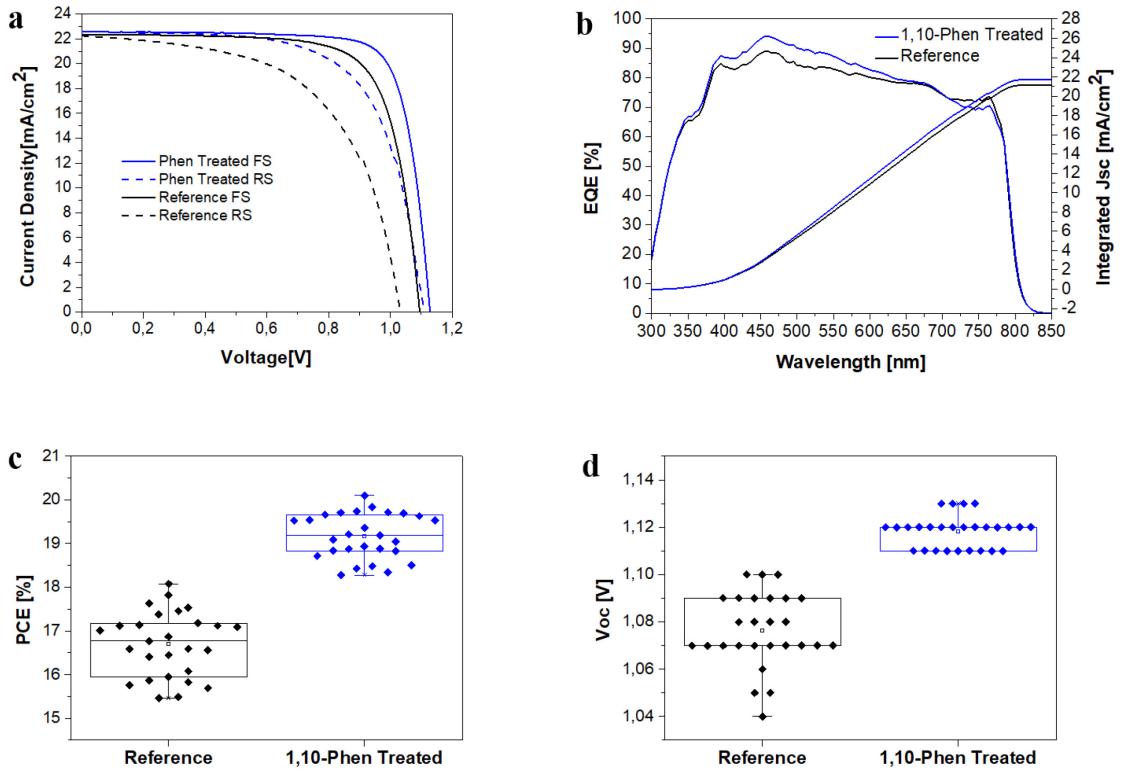

Figure 9. a) *J–V* characteristics and b) EQE spectra and integrated photocurrents of the best reference and 1,10-phen treated PSC devices; c) chart-box presentation of PCE and d) V_{oc} of over 50 (totally) reference and 1,10-phen treated PSC devices, conducted in 5 different experimental runs.

To evaluate the surface passivation effects on trap-density via the space-charge limited current (SCLC) method, electron-only devices were prepared with the device configuration of ITO/SnO_2/$MAPbI_3$ / **w/- or w/o 1,10-phen** /PCBM/Au.[46] The dark *J-V* characteristics of both electron-only devices, reference (w/o phen) and the 1,10-phen treated one (w/ phen), are shown in **Figure 10a**. The trap-density can be calculated according to the following equation[47]

$n_t = 2\,\varepsilon\varepsilon_0 V_{TFL} / eL^2$

where ε and ε_0 are the dielectric constants of perovskite and vacuum permittivity, respectively, L is the thickness of the perovskite films, e is the elementary charge, and V_{TFL} is the trap-filled limit voltage. The observed linear region at low bias corresponds to the ohmic response. Above the low bias voltage, after the kink points which show filled trap states marked with black and blue circles for reference and 1,10-phen treated electron only devices, respectively, both devices show a sudden nonlinear increase in current response corresponding to the SCLC region. The calculated trap-densities (n_t) of reference and 1,10-phen treated films are 8.98×10^{15} and 5.00×10^{15} cm^{-3}, respectively, confirming that surface passivation can lower the trap-density.

To enhance the understanding of the recombination behavior in the reference cell and in the passivated one, light intensity-dependent *JV*-measurements were performed.[48] The dependence of the V_{OC} on light intensity for the reference and the treated sample is shown in **Figure 10b**. According to $V_{OC} \sim n \cdot \frac{kT}{e} \cdot \ln(I)$ with the Boltzmann constant k, the temperature *T*, and the elementary charge *e*, the ideality factor *n* can be calculated from the slope of V_{OC} versus the natural logarithm of the light intensity *I*. From the linear fits, an ideality factor of 1.54 and 1.04 is obtained for the reference cell and the treated cell, respectively. The considerably reduced ideality factor indicates that trap-assisted recombination is suppressed to a great extent by the treatment with 1,10-phen.

To gain additional insight into the effect of the passivation on defect states, the photocurrent contributed by sub-bandgap states was further analyzed. As shown by Yavari et al, these sub-bandgap states in perovskite solar cells directly relate to the defect state density.[49] The results are shown in **Figure S8**, where the photocurrent signal of the 1,10-phen treated cell is below that of the untreated cell in the sub-bandgap region above 820 nm. At wavelengths below 820 nm, the respective photocurrent is higher due to the EQE increase discussed above. Above 820 nm, only sub-bandgap states can contribute to the photocurrent. Thus, the EQE measurements imply that the 1,10-phen treatment greatly reduced the formation of defect states, thereby reducing non-radiative loss pathways and increasing the V_{OC} and the overall device performance.

Additionally, Fourier-transform photocurrent spectroscopy (FTPS) was applied, which is very well suited to study photocurrent contributions from sub-bandgap states. The results are shown in **Figure 10c**. In the region from 805 nm to 825 nm, before the noise masks the signal, 1,10-phen treated films showed a significantly lower photocurrent from sub-bandgap states, which agrees with the less pronounced trend observed in the EQE.

Finally, we investigated the trap-assisted non-radiative V_{OC} losses after defect passivation. The losses can be calculated from the difference of the radiative limit of the V_{OC} - including only radiative losses - and the measured V_{OC}.

$$\Delta V_{OC} = V_{OC,rad} - V_{OC} \quad (1)$$

The relationship of $V_{OC,rad}$ with the currents of the solar cell, namely the photogenerated current J_{ph} and the dark saturation current density $J_{o,rad}$, is shown as:[50-51]

$$V_{OC,rad} = \frac{kT}{q} \ln\left(\frac{J_{ph}}{J_{o,rad}} + 1\right) \quad (2)$$

As established by U. Rau, J_o can be calculated from the EQE_{PV} spectra and the black body spectrum Φ_{BB}.[52]

$$J_0 = \frac{q}{EQE_{EL}} \int EQE_{PV}(E) \Phi_{BB}^{T}(E) dE \quad (3)$$

Hereby EQE_{EL} is the electroluminescence EQE, which in the case of the radiative limit is considered to be unity and thus $J_{o,rad}$ can be deducted from the EQE_{PV} measurement.[53-54] Lastly, since EQE_{PV} is evaluated at short circuit, J_{ph} in the following equation becomes J_{sc}, which can be calculated as the integrated current of the EQE_{PV} spectrum.[55]

$$J_{sc} = q \int EQE_{PV}(E)\Phi_{AM1.5g}(E)dE \quad (4)$$

The results are shown in **Table 2**. Due to the exponential increase of the blackbody radiation towards longer wavelengths, the higher EQE values of the treated cell at lower wavelengths and the higher EQE values of the untreated cell in the sub-bandgap region both result in fairly similar $J_{o,rad}$ values. Hence, J_{sc} and $J_{o,rad}$ were only marginally increased in the treated cells, which did not alter $V_{OC,rad}$. However, due to the distinct increase of the measured V_{OC}, non-radiative losses must have been substantially decreased by 50 mV due to a reduction of defect state density.

Table 2. Photovoltaic parameters of reference and treated cells for non-radiative loss calculations.

Sample	J_{sc} **[mA/cm²]**	$J_{0,rad}$ **[mA/cm²]**	$V_{oc,\ rad}$	$V_{oc,\ measured}$	ΔV_{oc}
Reference	21.30	1.48×10^{-21}	1.29	1.09	0.20
1,10-phen treated	21.70	1.55×10^{-21}	1.29	1.14	0.15

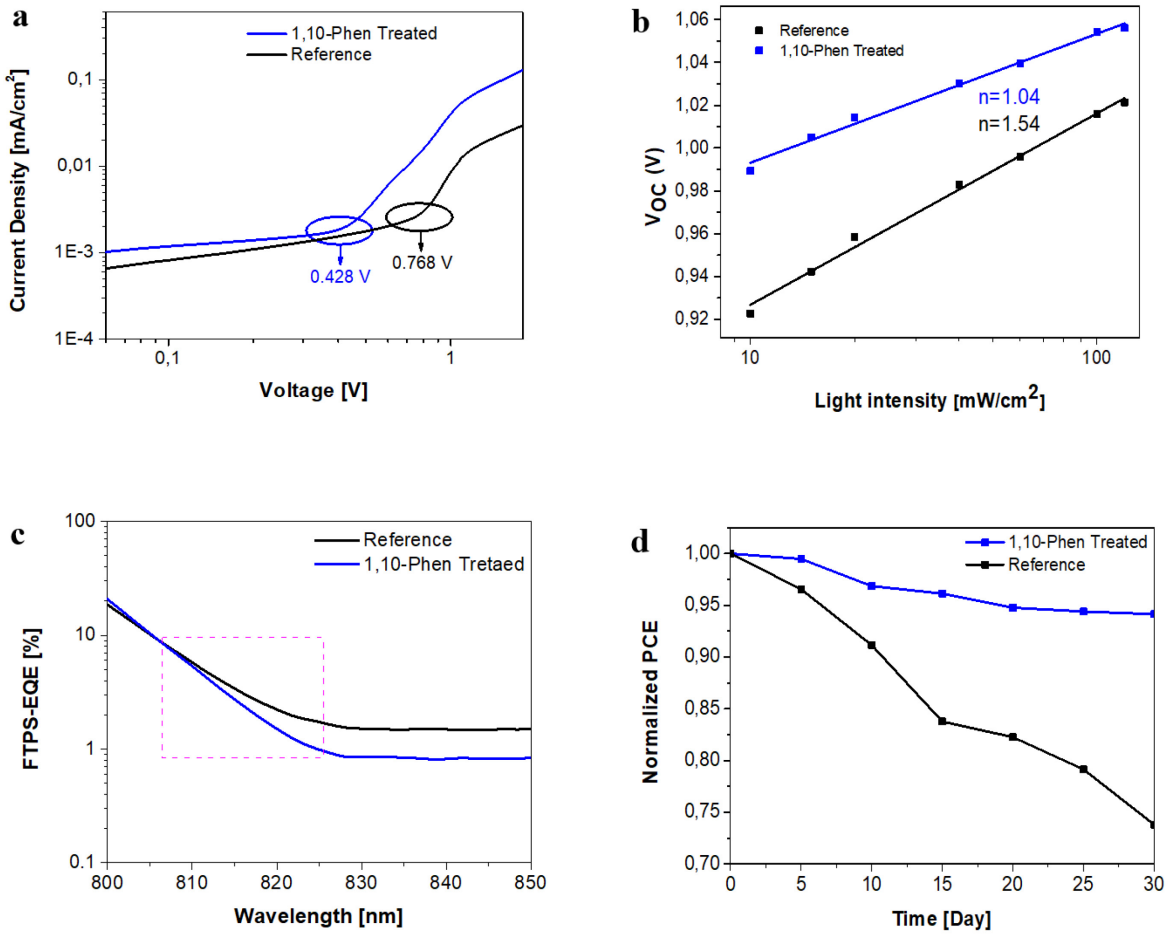

Figure 10. a) Dark *J-V* characteristics of electron-only devices, b) light intensity-dependent V_{oc} data, c) Fourier-transform photocurrent spectroscopy results, and d) stability test of reference and 1,10-phen treated devices without encapsulation.

To understand the impact of the newly formed (PbI_2 (1,10-phen)$_x$ (x=1,2)) on the perovskite surface on charge extraction at the HTL interface and device performance, various $MAPbI_3$ films (Glass/FTO/SnO_2/$MAPbI_3$/ with or without 1,10-phen) and n–i–p planar heterojunction perovskite solar cells (Glass/FTO/SnO_2/$MAPbI_3$/ with or without 1,10-phen /spiro-OMeTAD/Au) were prepared in the same batch with stoichiometric (no excess PbI_2) and excess PbI_2 (+5%) contents for XRD measurements and solar cells studies, respectively. Importantly, the XRD results for the surface-treated perovskite films with increasing concentration of 1,10-phen solution prepared from two different solvents (chlorobenzene and toluene), shown in **Figure S9**, reveal that treated samples with a higher concentration of 1,10-phen in chlorobenzene solution show stronger peaks of newly formed (PbI_2 (1,10-phen)$_x$ (x=1,2)) accompanied by partially and completely vanished PbI_2 peaks for excess PbI_2- and stoichiometric films, respectively. The SEM top and cross-section view images of untreated (reference) and surface treated $MAPbI_3$ perovskite films (with excess PbI_2 (+5%)) with different concentrations of 1,10-phen were also recorded to observe the surface morphological changes of the films (**Figure S10**

and **Figure S11**). With increasing concentration of 1,10-phen solution, the surface of treated samples shows more platelet formation, which is in good agreement with the XRD results. Obviously, the excess (+5%) or unreacted PbI_2 gets more and more consumed with increased concentrations of 1,10-phen. This trend confirms that PbI_2 is converted into $PbI_2(1,10\text{-phen})_x$ (x=1,2) with the coordination of 1,10-phen. Unlike the samples treated with chlorobenzene solution of 1,10-phen, the samples treated with a toluene solution (**Figure S9**), show no new reflections due to (PbI_2 (1,10-phen)$_x$ (x=1,2)) in the XRD patterns of both stoichiometric and excess PbI_2 films. These different results can be attributed to the solubility of 1,10-phen (monohydrate and anhydrate forms) in chlorobenzene and toluene.[56] Perovskite solar cell devices prepared under the same conditions as the XRD samples were analyzed to understand the effects of the additional new lead complexes on the device performance, as a result of the reaction of excess/unreacted lead iodide (PbI_2) with 1,10-phen (**Figure S12**). On the one hand, solar cell devices treated in the toluene solution in which new complex species are not observed, show enhancements that result from higher V_{oc} and fill factor (*FF*), which can be attributed to 1,10-phen-saturated under-coordinated lead (Pb^{2+}) ions on the surface. On the other hand, in the case of the treatment of the PbI_2 excess $MAPbI_3$ devices with a chlorobenzene solution of the passivation agent, the devices not only show doubled enhancement in V_{oc} and fill factor (*FF*) but also higher J_{sc}, which shows the beneficial effects of the defect passivation and complex formation on the perovskite surface on charge extraction and device performance.

To further solidify this hypothesis, samples were fabricated with the following structure: glass/$MAPbI_3$/ with or without 1,10-phen /spiro-OMeTAD to evaluate the impact of the new surface species (**Figure 4b**) at the interface of $MAPbI_3$/spiro-OMeTAD on the interfacial charge transfer dynamics, and studied with steady-state photoluminescence (PL)(**Figure S13**) and time-resolved PL (TRPL)(**Figure S14**) measurements. The treated (with 1,10-phen) sample showed notable quenching of the steady-state photoluminescence, indicating accelerated carrier extraction at the modified $MAPbI_3$/spiro-OMeTAD interface and contributing to the enhanced fill factor (*FF*) and J_{sc} in device performance (**Figure S7b, Figure S7a**).[57] Regarding the time-resolved PL (TRPL) measurements, the decrease (from 11 ns to 8 ns) in the fast component ($\boldsymbol{\tau_1}$) of the decay lifetime of the treated sample with higher fractional amplitude supports the observed notable quenching of the treated sample in the steady-state photoluminescence measurements.[58] All these quenching experiments show that the treated interface transfers the photogenerated holes from perovskite to spiro-OMeTAD faster than the neat perovskite (without 1,10-phen). And finally, regarding the DFT calculated HOMO (highest occupied molecular orbital) energy levels (**Figure S15**) of model $PbI_2(1,10\text{-phen})$ (-5.04 eV) and $PbI_2(1,10\text{-phen})_2$ (-4.69 eV) complexes, which are consistent with the energy level calculations of $PbI_2(dmp)$[59] (a complex very similar to $PbI_2(1,10\text{-phen})$), one of them perfectly matches the related energy levels of spiro-OMeTAD (HOMO, -4.90 eV) and $MAPbI_3$(valence band edge, -5.30 eV)[60], leading a favorable cascade band

alignment (**Figure S16**) for more efficient hole transfer at the modified interface.

In order to assess the stability of the devices, the performance of the unencapsulated passivated and reference devices were tracked under the conditions of a relative humidity of 40–45% at room temperature. As shown in **Figure 10d**, 1,10-phen treated and the reference devices retain 94% and 74% of starting PCE after 30 days (720 hours), respectively. To understand the impact of the 1,10-phen treatment on the surface hydrophobicity, the water-contact angles of bare perovskite (reference) and 1,10-phen treated films were measured. As shown in **Figure S17**, the bare perovskite and the treated film exhibit a water-contact angle of around 61 and 73°, respectively. The greater water contact angle of the treated film compared to the reference shows the enhanced hydrophobicity of the treated surface. In addition to the shelf-stability test, explained above, the performance of the unencapsulated passivated and reference devices was tracked under continuous 1-sun illumination with a fixed temperature of 60 °C for 12 hours in the glove-box to evaluate light-thermal stability (**Figure S18**). Under these conditions, the treated and reference devices retain 75% and 52% of their starting PCE, respectively. These results establish that the defect passivation upon 1,10-phen surface treatment and converting excess/unreacted lead iodide (PbI_2) into ′neutralized′ and beneficial species (PbI_2(1,10-phen)$_{x,}$ x=1,2) impact not just the device performance, but also device stability, which will be of particular importance towards the application of perovskite solar cells.

3.3 Conclusion

In summary, we have successfully implemented 1,10-phenanthroline, known as a bidentate chelating ligand, firstly to heal detrimental defects on $MAPbI_3$ surfaces, which adversely affect the photovoltaic performance and stability of corresponding devices, and secondly to convert excess or unreacted PbI_2, which is also detrimental for the long-term stability of solar cell devices, into beneficial species (PbI_2(1,10-phen)$_{x,}$ x=1,2) for efficient hole transfer at the modified interface. Combining the nano-Fourier transform infrared (nano-FTIR) spectroscopy and high-angle annular dark-field scanning *transmission electron microscopy* (HAADF-STEM) techniques, we confirmed surface coverage of the treated films with PbI_2(1,10-phen)$_x$, which is found to form two different morphologies either as platelet-shape formation or a very thin capping layer with the same chemical composition. As a result, 1,10-phen surface-treated devices show over 10% performance improvements demonstrated by the champion PCE of 20.16 %, with a V_{oc} of 1.13 V, J_{sc} of 22.58 $mAcm^{-2}$, and fill factor (*FF*) of 79%. We attribute these substantial improvements to passivation of the mono and double halide vacancy defects (under-coordinated lead ions) at the surface of the perovskite, which cause non-radiative recombination and voltage losses, and of excess/unreacted lead iodide (PbI_2), which are problematic for the long-term stability of the PSCs. Moreover, under the conditions of a relative humidity of 40–45% at room temperature, the unencapsulated passivated device showed significantly higher stability compared to

the untreated reference device.

3.4 References

(1) Torabi, N.; Behjat, A.; Zhou, Y.; Docampo, P.; Stoddard, R. J.; Hillhouse, H. W.; Ameri, T. Progress and Challenges in Perovskite Photovoltaics from Single- to Multi-Junction Cells. *Materials Today Energy* **2019,** *12*, 70-94, DOI: 10.1016/j.mtener.2018.12.009.

(2) https://www.nrel.gov/pv/assets/pdfs/best-research-cell-efficiencies.20200406.pdf.

(3) Abdi-Jalebi, M.; Dar, M. I.; Senanayak, S. P.; Sadhanala, A.; Andaji-Garmaroudi, Z.; Pazos-Outón, L. M.; Richter, J. M.; Pearson, A. J.; Sirringhaus, H.; Grätzel, M. Charge Extraction Via Graded Doping of Hole Transport Layers Gives Highly Luminescent and Stable Metal Halide Perovskite Devices. *Science advances* **2019,** *5* (2), eaav2012.

(4) Jung, E. H.; Jeon, N. J.; Park, E. Y.; Moon, C. S.; Shin, T. J.; Yang, T.-Y.; Noh, J. H.; Seo, J. Efficient, Stable and Scalable Perovskite Solar Cells Using Poly (3-Hexylthiophene). *Nature* **2019,** *567* (7749), 511-515.

(5) Liu, Y.; Akin, S.; Pan, L.; Uchida, R.; Arora, N.; Milić, J. V.; Hinderhofer, A.; Schreiber, F.; Uhl, A. R.; Zakeeruddin, S. M. Ultrahydrophobic 3d/2d Fluoroarene Bilayer-Based Water-Resistant Perovskite Solar Cells with Efficiencies Exceeding 22%. *Science advances* **2019,** *5* (6), 2543.

(6) Xing, G.; Mathews, N.; Sun, S.; Lim, S. S.; Lam, Y. M.; Grätzel, M.; Mhaisalkar, S.; Sum, T. C. Long-Range Balanced Electron-and Hole-Transport Lengths in Organic-Inorganic Ch3nh3pbi3. *Science* **2013,** *342* (6156), 344-347.

(7) Lee, M. M.; Teuscher, J.; Miyasaka, T.; Murakami, T. N.; Snaith, H. J. Efficient Hybrid Solar Cells Based on Meso-Superstructured Organometal Halide Perovskites. *Science* **2012,** *338* (6107), 643-647.

(8) De Wolf, S.; Holovsky, J.; Moon, S.-J.; Löper, P.; Niesen, B.; Ledinsky, M.; Haug, F.-J.; Yum, J.-H.; Ballif, C. Organometallic Halide Perovskites: Sharp Optical Absorption Edge and Its Relation to Photovoltaic Performance. *The journal of physical chemistry letters* **2014,** *5* (6), 1035-1039.

(9) Guo, Y.; Sato, W.; Shoyama, K.; Halim, H.; Itabashi, Y.; Shang, R.; Nakamura, E. Citric Acid Modulated Growth of Oriented Lead Perovskite Crystals for Efficient Solar Cells. *Journal of the American Chemical Society* **2017,** *139* (28), 9598-9604.

(10) Yi, C.; Luo, J.; Meloni, S.; Boziki, A.; Ashari-Astani, N.; Grätzel, C.; Zakeeruddin, S. M.; Röthlisberger, U.; Grätzel, M. Entropic Stabilization of Mixed a-Cation Abx 3 Metal Halide Perovskites for High Performance Perovskite Solar Cells. *Energy & Environmental Science* **2016,** *9* (2), 656-662.

(11) Liu, L.; Mei, A.; Liu, T.; Jiang, P.; Sheng, Y.; Zhang, L.; Han, H. Fully Printable Mesoscopic Perovskite Solar Cells with Organic Silane Self-Assembled Monolayer. *Journal of the American Chemical Society* **2015,** *137* (5), 1790-1793.

(12) Cao, J.; Lv, X.; Zhang, P.; Chuong, T. T.; Wu, B.; Feng, X.; Shan, C.; Liu, J.; Tang, Y. Plant Sunscreen and Co (Ii)/(Iii) Porphyrins for Uv-Resistant and Thermally Stable Perovskite Solar Cells: From Natural to Artificial. *Advanced Materials* **2018,** *30* (27), 1800568.

(13) Zheng, X.; Chen, B.; Dai, J.; Fang, Y.; Bai, Y.; Lin, Y.; Wei, H.; Zeng, X. C.; Huang, J. Defect Passivation in Hybrid Perovskite Solar Cells Using Quaternary Ammonium Halide Anions and Cations. *Nature Energy* **2017,** *2* (7), 1-9.

(14) Zhao, T.; Chueh, C.-C.; Chen, Q.; Rajagopal, A.; Jen, A. K.-Y. Defect Passivation of Organic–Inorganic Hybrid Perovskites by Diammonium Iodide toward High-Performance Photovoltaic Devices. *ACS Energy Letters* **2016,** *1* (4), 757-763.

(15) Wang, Z.; Lin, Q.; Chmiel, F. P.; Sakai, N.; Herz, L. M.; Snaith, H. J. Efficient Ambient-Air-Stable Solar Cells with 2d–3d Heterostructured Butylammonium-Caesium-Formamidinium Lead Halide Perovskites. *Nature Energy* **2017,** *2* (9), 17135.

(16) Bai, Y.; Xiao, S.; Hu, C.; Zhang, T.; Meng, X.; Lin, H.; Yang, Y.; Yang, S. Dimensional Engineering of a Graded 3d–2d Halide Perovskite Interface Enables Ultrahigh Voc Enhanced Stability in the P-I-N Photovoltaics. *Advanced Energy Materials* **2017,** *7* (20), 1701038.

(17) Leijtens, T.; Eperon, G. E.; Noel, N. K.; Habisreutinger, S. N.; Petrozza, A.; Snaith, H. J. Stability of Metal Halide Perovskite Solar Cells. *Advanced Energy Materials* **2015,** *5* (20), 1500963.

(18) Xu, J.; Buin, A.; Ip, A. H.; Li, W.; Voznyy, O.; Comin, R.; Yuan, M.; Jeon, S.; Ning, Z.; McDowell, J. J. Perovskite–Fullerene Hybrid Materials Suppress Hysteresis in Planar Diodes. *Nature communications* **2015,** *6* (1), 1-8.

(19) Deschler, F.; Price, M.; Pathak, S.; Klintberg, L. E.; Jarausch, D.-D.; Higler, R.; Hüttner, S.; Leijtens, T.; Stranks, S. D.; Snaith, H. J. High Photoluminescence Efficiency and Optically Pumped Lasing in Solution-Processed Mixed Halide Perovskite Semiconductors. *The journal of physical chemistry letters* **2014,** *5* (8), 1421-1426.

(20) Ye, S.; Rao, H.; Zhao, Z.; Zhang, L.; Bao, H.; Sun, W.; Li, Y.; Gu, F.; Wang, J.; Liu, Z. A Breakthrough Efficiency of 19.9% Obtained in Inverted Perovskite Solar Cells by Using an Efficient Trap State Passivator Cu (Thiourea) I. *Journal of the American Chemical Society* **2017,** *139* (22), 7504-7512.

(21) Wang, Q.; Chen, B.; Liu, Y.; Deng, Y.; Bai, Y.; Dong, Q.; Huang, J. Scaling Behavior of Moisture-Induced Grain Degradation in Polycrystalline Hybrid Perovskite Thin Films. *Energy & Environmental Science* **2017,** *10* (2), 516-522.

(22) Gao, F.; Zhao, Y.; Zhang, X.; You, J. Recent Progresses on Defect Passivation toward Efficient Perovskite Solar Cells. *Advanced Energy Materials* **2019**, DOI: 10.1002/aenm.201902650.

(23) Akin, S.; Arora, N.; Zakeeruddin, S. M.; Grätzel, M.; Friend, R. H.; Dar, M. I. New Strategies for Defect Passivation in High-Efficiency Perovskite Solar Cells. *Advanced Energy Materials* **2019**, DOI: 10.1002/aenm.201903090.

(24) Noel, N. K.; Abate, A.; Stranks, S. D.; Parrott, E. S.; Burlakov, V. M.; Goriely, A.; Snaith, H. J. Enhanced Photoluminescence and Solar Cell Performance Via Lewis Base Passivation of Organic–Inorganic Lead Halide Perovskites. *ACS nano* **2014,** *8* (10), 9815-9821.

(25) Zhang, H.; Wu, Y.; Shen, C.; Li, E.; Yan, C.; Zhang, W.; Tian, H.; Han, L.; Zhu, W. H. Efficient and Stable Chemical Passivation on Perovskite Surface Via Bidentate Anchoring. *Advanced Energy Materials* **2019,** *9* (13), DOI: 10.1002/aenm.201803573.

(26) Fu, S.; Li, X.; Wan, L.; Wu, Y.; Zhang, W.; Wang, Y.; Bao, Q.; Fang, J. Efficient Passivation with Lead Pyridine-2-Carboxylic for High-Performance and Stable Perovskite Solar Cells. *Advanced Energy Materials* **2019,** *9* (35), DOI: 10.1002/aenm.201901852.

(27) Wu, Z.; Jiang, M.; Liu, Z.; Jamshaid, A.; Ono, L. K.; Qi, Y. Highly Efficient Perovskite Solar Cells Enabled by Multiple Ligand Passivation. *Advanced Energy Materials* **2020,** *10* (10), DOI: 10.1002/aenm.201903696.

(28) Kim, Y. C.; Jeon, N. J.; Noh, J. H.; Yang, W. S.; Seo, J.; Yun, J. S.; Ho-Baillie, A.; Huang, S.; Green, M. A.; Seidel, J. Beneficial Effects of Pbi2 Incorporated in Organo-Lead Halide Perovskite Solar Cells. *Advanced Energy Materials* **2016,** *6* (4), 1502104.

(29) Jacobsson, T. J.; Correa-Baena, J.-P.; Halvani Anaraki, E.; Philippe, B.; Stranks, S. D.; Bouduban, M. E.; Tress, W.; Schenk, K.; Teuscher, J. l.; Moser, J.-E. Unreacted Pbi2 as a Double-Edged Sword for Enhancing the Performance of Perovskite Solar Cells. *Journal of the American Chemical Society* **2016,** *138* (32), 10331-10343.

(30) Yang, X.; Luo, D.; Xiang, Y.; Zhao, L.; Anaya, M.; Shen, Y.; Wu, J.; Yang, W.; Chiang, Y. H.; Tu, Y. Buried Interfaces in Halide Perovskite Photovoltaics. *Advanced Materials*, 2006435.

(31) Tumen-Ulzii, G.; Qin, C.; Klotz, D.; Leyden, M. R.; Wang, P.; Auffray, M.; Fujihara, T.; Matsushima, T.; Lee, J. W.; Lee, S. J. Detrimental Effect of Unreacted Pbi2 on the Long-Term Stability of Perovskite Solar Cells. *Advanced Materials* **2020,** *32* (16), 1905035.

(32) Cola, L. Absorption and Luminescence Properties of 1, 10-Phenanthroline, 2, 9-Diphenyl-1, 10-Phenanthroline, 2, 9-Dianisyl-1, 10-Phenanthroline and Their Protonated Forms in Dichloromethane Solution. *Journal of the Chemical Society, Faraday Transactions* **1992,** *88* (4), 553-556.

(33) Li, W.; Zhang, C.; Ma, Y.; Liu, C.; Fan, J.; Mai, Y.; Schropp, R. E. In Situ Induced Core/Shell Stabilized Hybrid Perovskites Via Gallium (Iii) Acetylacetonate Intermediate Towards Highly Efficient and Stable Solar Cells. *Energy & Environmental Science* **2018,** *11* (2), 286-293.

(34) Glatfelter, A.; Dybowski, C.; Bai, S.; Perry, D. L. Syntheses of Photo-Active Lead (Ii)-1, 10-Phenanthroline Materials. *Materials Letters* **2007,** *61* (2), 437-439.

(35) Preda, N.; Mihut, L.; Baibarac, M.; Baltog, I.; Lefrant, S. A Distinctive Signature in the Raman and Photoluminescence Spectra of Intercalated Pbi2. *Journal of Physics: Condensed Matter* **2006,** *18* (39), 8899.

(36) Baran, E. J.; Wagner, C. C.; Rossi, M.; Caruso, F. Crystal Structure and Ir Spectrum of Diaqua (O-Phenanthroline) Bis (Saccharinato) Lead (Ii). *Zeitschrift für anorganische und allgemeine Chemie* **2000,** *626* (3), 701-705.

(37) Bowmaker, G. A.; Harrowfield, J. M.; Miyamae, H.; Shand, T. M.; Skelton, B. W.; Soudi, A. A.; White, A. H. Lewis-Base Adducts of Lead (Ii) Compounds. Xii. Synthetic, Spectroscopic and Structural Studies of Some 1: 1 Adducts of Lead (Ii)(Pseudo-) Halides with Aromatic Bidentate Ligands. *Australian journal of chemistry* **1996,** *49* (10), 1089-1097.

(38) Andrade, G. F.; Temperini, M. L. 1, 10-Phenanthroline Adsorption on Iron Electrode Monitored by Surface-Enhanced Raman Scattering (Sers). Comparison to Sers of Phen and Its Transition Metal Complex on Silver Electrode. *The Journal of Physical Chemistry C* **2007,** *111* (37), 13821-13830.

(39) Müller-Buschbaum, P. Grazing Incidence Small-Angle Neutron Scattering: Challenges and Possibilities. *Polym. J.* **2012,** *45* (1), 34-42, DOI: 10.1038/pj.2012.190.

(40) Dosch, H.; Batterman, B. W.; Wack, D. C. Depth-Controlled Grazing-Incidence Diffraction of Synchrotron X Radiation. *Phys. Rev. Lett.* **1986,** *56* (11), 1144-1147, DOI: 10.1103/PhysRevLett.56.1144.

(41) Als-Nielsen, J.; McMorrow, D. Elements of Modern X-Ray Physics. *Wiley* **2011**.

(42) Szostak, R.; Silva, J.; Turren-Cruz, S.-H.; Soares, M.; Freitas, R.; Hagfeldt, A.; Tolentino, H.; Nogueira, A. Nanoscale Mapping of Chemical Composition in Organic-Inorganic Hybrid Perovskite Films. *Science advances* **2019,** *5* (10), eaaw6619.

(43) Huth, F.; Govyadinov, A.; Amarie, S.; Nuansing, W.; Keilmann, F.; Hillenbrand, R. Nano-Ftir Absorption Spectroscopy of Molecular Fingerprints at 20 Nm Spatial Resolution. *Nano letters* **2012,** *12* (8), 3973-3978.

(44) Pérez-Osorio, M. A.; Milot, R. L.; Filip, M. R.; Patel, J. B.; Herz, L. M.; Johnston, M. B.; Giustino, F. Vibrational Properties of the Organic–Inorganic Halide Perovskite Ch3nh3pbi3 from Theory and Experiment: Factor Group Analysis, First-Principles Calculations, and Low-Temperature Infrared Spectra. *The Journal of Physical Chemistry C* **2015,** *119* (46), 25703-25718.

(45) Glatfelter, A.; Dybowski, C.; Bai, S.; Kragten, D.; Blake, M. J.; Segarra, S.; Perry, D. L. Infrared Studies of Lead (Ii) Halide-1, 10-Phenanthroline Photosensitive Materials. *Spectrochimica Acta Part A: Molecular and Biomolecular Spectroscopy* **2009,** *71* (5), 1922-1926.

(46) Tan, H.; Jain, A.; Voznyy, O.; Lan, X.; De Arquer, F. P. G.; Fan, J. Z.; Quintero-Bermudez, R.; Yuan, M.; Zhang, B.; Zhao, Y. Efficient and Stable Solution-Processed Planar Perovskite Solar Cells Via Contact Passivation. *Science* **2017,** *355* (6326), 722-726.

(47) Dong, Q.; Fang, Y.; Shao, Y.; Mulligan, P.; Qiu, J.; Cao, L.; Huang, J. Electron-Hole Diffusion Lengths> 175 Mm in Solution-Grown Ch3nh3pbi3 Single Crystals. *Science* **2015,** *347* (6225), 967-970.

(48) Tress, W.; Yavari, M.; Domanski, K.; Yadav, P.; Niesen, B.; Baena, J. P. C.; Hagfeldt, A.; Graetzel, M. Interpretation and Evolution of Open-Circuit Voltage, Recombination, Ideality Factor and Subgap

Defect States During Reversible Light-Soaking and Irreversible Degradation of Perovskite Solar Cells. *Energy & Environmental Science* **2018,** *11* (1), 151-165.

(49) Yavari, M.; Ebadi, F.; Meloni, S.; Wang, Z. S.; Yang, T. C.-J.; Sun, S.; Schwartz, H.; Wang, Z.; Niesen, B.; Durantini, J. How Far Does the Defect Tolerance of Lead-Halide Perovskites Range? The Example of Bi Impurities Introducing Efficient Recombination Centers. *Journal of Materials Chemistry A* **2019,** *7* (41), 23838-23853.

(50) Vandewal, K.; Tvingstedt, K.; Gadisa, A.; Inganäs, O.; Manca, J. V. On the Origin of the Open-Circuit Voltage of Polymer–Fullerene Solar Cells. *Nature materials* **2009,** *8* (11), 904-909.

(51) Yao, J.; Kirchartz, T.; Vezie, M. S.; Faist, M. A.; Gong, W.; He, Z.; Wu, H.; Troughton, J.; Watson, T.; Bryant, D. Quantifying Losses in Open-Circuit Voltage in Solution-Processable Solar Cells. *Physical review applied* **2015,** *4* (1), 014020.

(52) Rau, U. Reciprocity Relation between Photovoltaic Quantum Efficiency and Electroluminescent Emission of Solar Cells. *Physical Review B* **2007,** *76* (8), 085303.

(53) Galli, D.; Gasparini, N.; Forster, M.; Eckert, A.; Widling, C.; Killian, M. S.; Avgeropoulos, A.; Gregoriou, V. G.; Scherf, U.; Chochos, C. L. Suppressing the Surface Recombination and Tuning the Open-Circuit Voltage of Polymer/Fullerene Solar Cells by Implementing an Aggregative Ternary Compound. *ACS applied materials & interfaces* **2018,** *10* (34), 28803-28811.

(54) Tvingstedt, K.; Malinkiewicz, O.; Baumann, A.; Deibel, C.; Snaith, H. J.; Dyakonov, V.; Bolink, H. J. Radiative Efficiency of Lead Iodide Based Perovskite Solar Cells. *Scientific reports* **2014,** *4*, 6071.

(55) Vandewal, K.; Tvingstedt, K.; Gadisa, A.; Inganäs, O.; Manca, J. V. Relating the Open-Circuit Voltage to Interface Molecular Properties of Donor: Acceptor Bulk Heterojunction Solar Cells. *Physical Review B* **2010,** *81* (12), 125204.

(56) Braun, D. E.; Schneeberger, A.; Griesser, U. J. Understanding the Role of Water in 1, 10-Phenanthroline Monohydrate. *CrystEngComm* **2017,** *19* (41), 6133-6145.

(57) Cho, K. T.; Paek, S.; Grancini, G.; Roldán-Carmona, C.; Gao, P.; Lee, Y.; Nazeeruddin, M. K. Highly Efficient Perovskite Solar Cells with a Compositionally Engineered Perovskite/Hole Transporting Material Interface. *Energy & Environmental Science* **2017,** *10* (2), 621-627.

(58) Akman, E.; Akin, S. Poly (N, N′-Bis-4-Butylphenyl-N, N′-Bisphenyl) Benzidine-Based Interfacial Passivation Strategy Promoting Efficiency and Operational Stability of Perovskite Solar Cells in Regular Architecture. *Advanced Materials* **2021,** *33* (2), 2006087.

(59) Shaabani, B.; Mirtamizdoust, B.; Viterbo, D.; Croce, G.; Hammud, H., A Novel Metal–Ligand Iodo-Bridged Lead (Ii) Compound: Synthesis, Crystal Structure, Thermal Properties, and Dft Calculations of [Pb (Dmp) I2] N. Wiley Online Library: **2010**, 636, 1596-1600.

(60) Harwell, J. R.; Baikie, T.; Baikie, I.; Payne, J. L.; Ni, C.; Irvine, J. T. S.; Turnbull, G. A.; Samuel, I. D. W. Probing the Energy Levels of Perovskite Solar Cells Via Kelvin Probe and Uv Ambient

Pressure Photoemission Spectroscopy. *Physical Chemistry Chemical Physics* **2016,** *18* (29), 19738-19745.

3.5 Experimental Section

1. Materials and reagents

The SnO_2 colloid precursor was purchased from Alfa Aesar (tin(IV) oxide, 15% in H_2O colloidal dispersion); before spin-coating as an ETL, the nanoparticles were diluted with DI water to 2.67%. The passivating material – 1,10-phenanthroline – was purchased from Sigma-Aldrich. The $MAPbI_3$ precursors – PbI_2 and MAI – were purchased from TCI. The Spiro-OMeTAD as an HTL material was purchased from Borun Chem. Solvents used for perovskite film fabrication were purchased from Sigma-Aldrich.

2. Solar cell fabrication

The Zn powder and 3M HCl assisted, patterned FTO (3cm x 3cm) substrates were rinsed with deionized water. The rinsed substrates were sonicated in 2% *detergent* solution, DI water, ethanol, and isopropanol for 15 min, respectively. Subsequently, the dried substrates were further cleaned with ultraviolet ozone treatment for 25 min before SnO_2 nanoparticle coating. The diluted SnO_2 nanoparticle solution (2.67 wt%) was spin-coated onto the FTO substrate in ambient air at 4000 r.p.m. for 35 s, and then annealed at 150 ^oC for 30 min. Before perovskite coating, SnO_2 coated substrates were cleaned once again with ultraviolet ozone treatment for 10 min. Using the one-step "anti-solvent" method, the precursors of the perovskite – PbI_2 (1.68 M, 5% excess), MAI (1.60 M), and DMSO (1.60 M) in 1 mL DMF – were deposited on top of the SnO_2 layer at 1000 rpm for 10 s, followed by 3500 rpm for 20 s. Ethyl acetate as an anti-solvent was dropped onto the perovskite film at the last 10th second during the spin coating. The sample was then annealed at 130 ^oC for 10 min. For the surface treatment, the 1,10-phenanthroline (2.5 $mg.mL^{-1}$) in chlorobenzene solution as a passivator was spin-coated onto the perovskite films at 1000 r.p.m for 30 s followed by 5000 r.p.m for 5 s. The HTM was deposited by spin-coating (3000 rpm for 30 s) a solution of spiro-OMeTAD, which consisted of 72.3 mg spiro-OMeTAD, 35 µl bis(trifluoromethane) sulfonimide lithium salt (LiTFSI) stock solution (270 mg LiTFSI in 1 ml acetonitrile), 30 µl 4-*tert*-butylpyridine and 1 ml chlorobenzene. Finally, a 70 nm thin film of Au was thermally evaporated under high vacuum on top of the hole transport layer.

3. General Characterization Techniques:

UV–vis spectra were recorded using a Perkin Elmer Lambda 1050 spectrometer with an integrating sphere. Time-resolved photoluminescence (TRPL) spectroscopy was performed with a Picoquant Fluotime 300 spectrofluorometer, using an excitation wavelength of 375 nm. Current-Voltage (*J-V*) curves were measured under ambient conditions using a Newport OrielSol 2A solar simulator with a Keithley 2400 source meter under simulated AM 1.5G sunlight, with an incident power of 100 $mW\ cm^{-2}$, calibrated with a Fraunhofer ISE certified silicon cell (KG5-filtered). The active area of the solar cells

was defined by a square metal aperture mask of 0.0831 cm^2. *J-V* curves were recorded by scanning the input bias from 0 V to 1.5 V (forward scan) at a scan rate of 0.1 V/s after the devices had been at 1.5 V for 5 s under illumination. For the light intensity-dependent *J-V*-measurements, a white light LED was used as illumination. The LED intensity was adjusted with a Keithley 2200-20-5 Power Supply. A highly linear photodiode was used to control the light intensity over a range of 0.1 – 1.2 suns. *J-V*-curves were measured with a Keithley 2401 Sourcemeter.

External Quantum Efficiency (EQE)

To obtain the EQE spectra, the respective solar cell was illuminated with the chopped light of a tungsten lamp, split into its wavelength components with the help of a monochromator. The light beam was further split to illuminate the sample as well as a reference silicon photodetector (Hamamatsu S2281-01) at the same time. The resulting wavelength-dependent current response of both devices was recorded simultaneously by two lock-in amplifiers (Signal Recovery 7265, Stanford Research Systems 830) at a chopping frequency of 14 Hz. The incident illumination power, determined via the reference photodetector, was used to calculate the EQE response of the perovskite solar cell.

FTPS

FTPS measurements were conducted using a Bruker Vertex 70 FTIR instrument focusing light from a Tungsten halogen lamp through a CaF_2 beamsplitter with integrated gold mirrors onto the solar devices. The current collected from the solar cell at short-circuit conditions was fed through a FEMTO DHPCA-100 current amplifier adjusted to an amplification of $x10^3$ and an analog-digital converter back into the FTIR instrument for Fourier transformation. To further reduce noise, 10000 measurement scans were conducted and averaged for each measured pixel. The signals were then scaled to the respective EQE signals obtained separately.

XRD

X-Ray Diffraction (XRD) measurements were performed with a Bruker D8 Discover X-ray diffractometer operating at 40 kV and 30 mA, employing Ni-filtered Cu Kα1 radiation (λ = 1.5406 Å) and a position-sensitive LynxEye detector.

GIWAXS

Grazing-incidence wide-angle X-ray scattering (GIWAXS) data was taken with a Pilatus 300k detector (Dectris) at an energy of 12.4 keV (X-ray wavelength 1.0 Å) at the P03 beamline at DESY, Germany.[1] Data were collected at an incidence angle between 0.1 and 0.8 ° with a sample-detector distance (SDD) of 186 mm. 2D-GIWAXS data was corrected for path attenuation, detector absorption, photon polarization, solid angle, and flat field using the software GIXSGUI.[2]

To index the Bragg rings, pseudo-XRD patterns were created by radial integration of the available q-range of the 2D GIWAXS-images. X-ray powder diffraction patterns for analyzing pseudo-XRD data were simulated using the software VESTA.[3]

SEM

For SEM as well as for the preparation of SEM cross-sections and STEM samples, a FEI Helios Nanolab G3 UC DualBeam equipped with an Oxford Aztec Advanced X-Max 80 EDX detector was used. SEM images were recorded at an acceleration voltage of 2 kV. Cross-sectional images were recorded with a backscatter electron detector, top view images were recorded with both a backscatter electron detector and secondary electron through-the-lens detector. For surface protection of SEM cross-sections, a ~ 2 nm thick carbon layer, followed by electron– and ion-induced platinum layers were deposited. The cross-sections were prepared using Ga^+-ions cutting not at a right angle but at 52° degrees. EDX maps were recorded at 5 keV electron energies, thereby achieving a relatively good spatial compositional resolution. A drawback of this setting is the low sensitivity for Iodine L-series X-rays (at around 3.9 keV).

STEM-HAADF

Lamellae for STEM-HAADF in cross-section geometry were prepared by using the 1,10-phenanthroline treated $MAPbI_3$ perovskite on a SnO_2 substrate, which was subsequently covered by a protective Pt-film by electron- and ion-beam induced deposition, as shown in the STEM-EDX map of **Figure S4** (STEM-HAADF 1633 Color Mix). STEM was performed in annular dark field mode on a probe-corrected FEI Titan Themis at 300 kV.

nano-FTIR

For nano-FTIR measurements, a commercially available near-field microscope (neaSNOM, attocube systems AG) was used. For this technique, based on scattering-type scanning optical near-field microscopy (s-SNOM), a sharp, metal-coated AFM tip was illuminated by a broadband IR source. The light backscattered from the oscillating metallic tip was analyzed with an asymmetric Fourier transform spectrometer, which was based on a Michelson interferometer.[4] This allowed for the simultaneous recording of optical amplitude and phase of the backscattered light. To suppress the background light the tip was oscillated harmonically with a small tapping amplitude A and frequency Ω (here A = 65 nm, Ω = 247 kHz) and the detector signal was demodulated at higher harmonics $n\Omega$ of this frequency. For $n \geq 2$ the background is completely suppressed, delivering local near-field amplitude and phase spectra. To eliminate the microscope response function, the spectra were normalized to the spectra obtained from a spectrally flat reference (Si substrate). This resulted in local reflectivity and absorption spectra of the investigated materials. The latter was used for chemical identification according to

standard FTIR databases.[5]

For nano-FTIR samples (silicon wafer/$MAPbI_3$/ w/-, w/o 1,10-phen), silicon wafer (2,5cm X 2,5cm) substrates were used. The substrates were sonicated in 2% *detergent* solution, DI water, ethanol, and isopropanol for 15 min, respectively. Subsequently, dried substrates were further cleaned via ultraviolet ozone treatment for 15 min before perovskite coating. Neat perovskite and 1,10-phen treated perovskite films were fabricated using the same method employed for solar cell fabrication.

Pseudo-XRD

Pseudo-XRD patterns were generated by radial cuts of the complete 2D GIWAXS-data. Patterns were indexed following a procedure similar to XRD and compared to simulated XRD data generated by the software VESTA.[63] All reflexes were successfully indexed to $MAPbI_3$, FTO, Kapton-foil and the new surface species (black dashed rectangle in **Figure S2**). Depending on the incidence angle, the surface sensitivity changed. With increasing incidence angle the X-ray scattering depth increases (**Figure S3**). Below the critical angle of a given material, the scattering signal is very weak due to external total reflection.[39] Thus, first, the new species appeared starting at 0.1 °, then $MAPbI_3$ (starting at 0.15 °), and at incidence angles around 0.35 ° the FTO signal became visible.

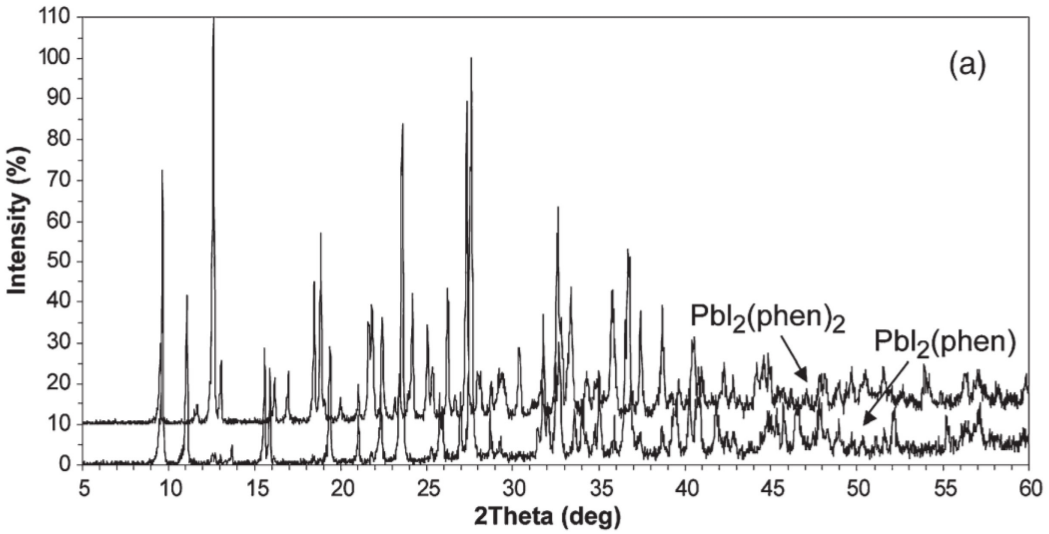

Figure S1. X-ray diffractograms of PbI_2(1,10-phen) and Pb_2(1,10-phen)$_2$, reprinted with permission. [34]

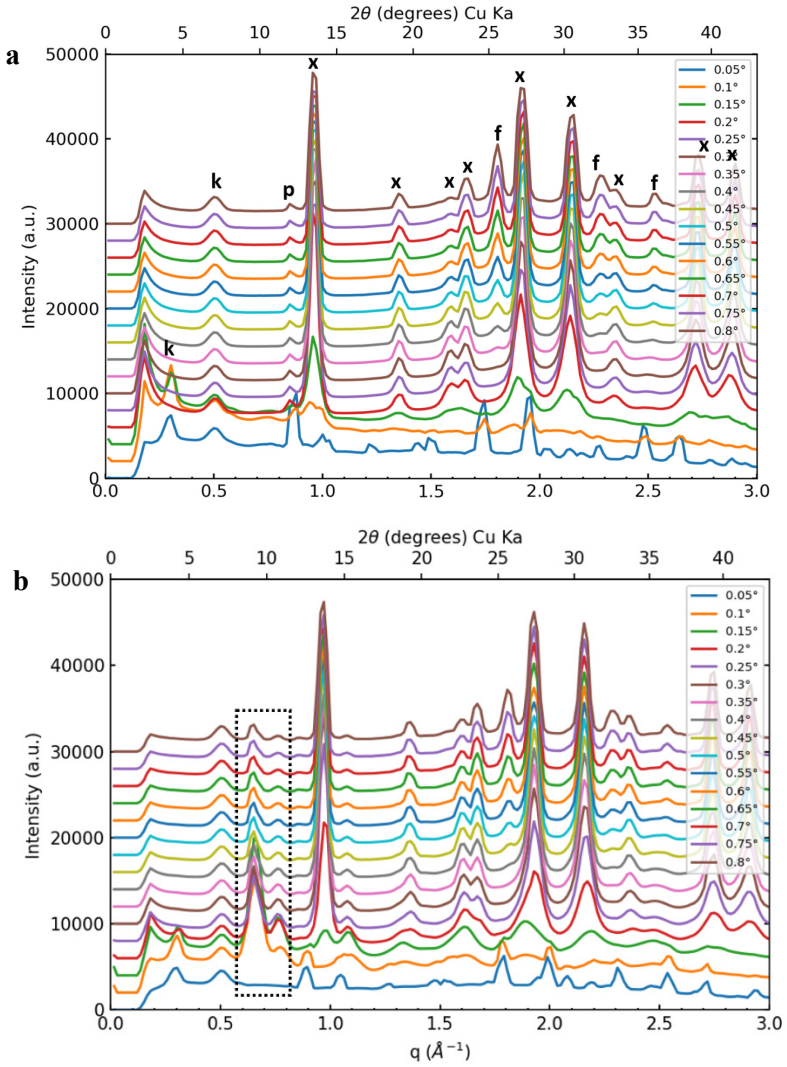

Figure S2. Pseudo-XRD data from radial cuts of 2D GIWAXS images, taken at different incidence angles of $MAPbI_3$. (**x**: $MAPbI_3$; **k**: Kapton; **p**: PbI_2; **f**: FTO) (a), and 1,10-phenanthroline treated sample (b).

X-Ray Scattering Depth

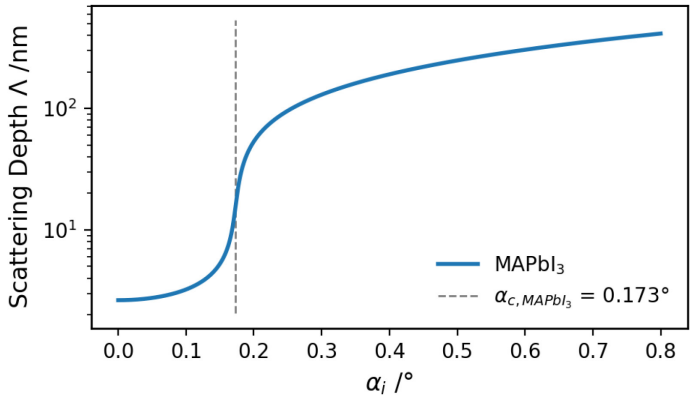

Figure S3. Calculated X-ray scattering depth (scattered intensity decreases by 1/e) depending on the incidence angle α_i into a $MAPbI_3$ thin-film for an X-ray wavelength of 1.0 Å.[40] A $MAPbI_3$ density of 4.159 g/cm^3 and $\alpha_i = \alpha_f$ was assumed in the calculation. The position of the critical angle of $MAPbI_3$ is indicated by the dashed line.

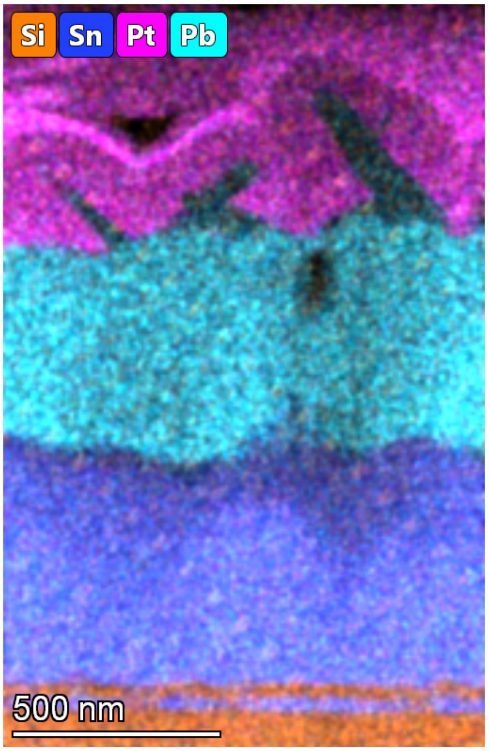

Figure S4. STEM-HAADF image of a cross-sectional sample of the 1,10-phenanthroline treated $MAPbI_3$ perovskite overlaid with an EDX compositional map of Si, Sn, Pt, and Pb. The layer sequence from bottom to top: Si-wafer (orange), SnO_2 (purple), $MAPbI_3$ perovskite (turquoise), surface phase (dark turquoise), platinum (pink).

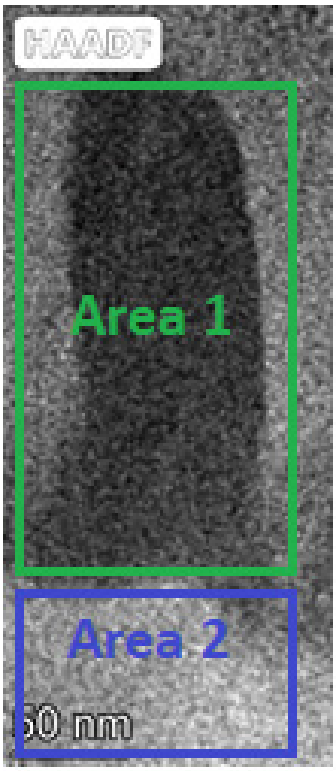

Figure S5. Areas of perovskite film and rod-like feature whose integrated EDX spectra are presented in **Figure S6**.

The integrated EDX spectra of a rod-like feature (Area 1 in **Fig. S5, green**) and perovskite film (Area 2 in **Fig. S5, blue**) are shown in **Figure S6**. They reveal the presence of carbon, iodine, lead, and to a lesser extent, nitrogen. Quantifications of the surface phase show consistently a higher relative amount of carbon and a lower amount of lead and iodine as compared to the perovskite.

Because of the sample geometry and the rather large thickness, we assume that absorption plays an important role. This is consistent with different measured Pb/I elemental ratios in the perovskite, depending on whether the Pb-L series or Pb-M was used for quantification. For example, the evaluation of the spectra using Pb-M results in compositions of C_{35} N_2 I_{51} Pb_{13} and C_{80} N_5 I_{13} Pb_2 for perovskite and surface phase, respectively. In contrast, the evaluation of the spectra using Pb-L results in compositions of C_{32} N_3 I_{43} Pb_{23} and C_{78} N_5 I_{12} Pb_5 for perovskite and surface phase.

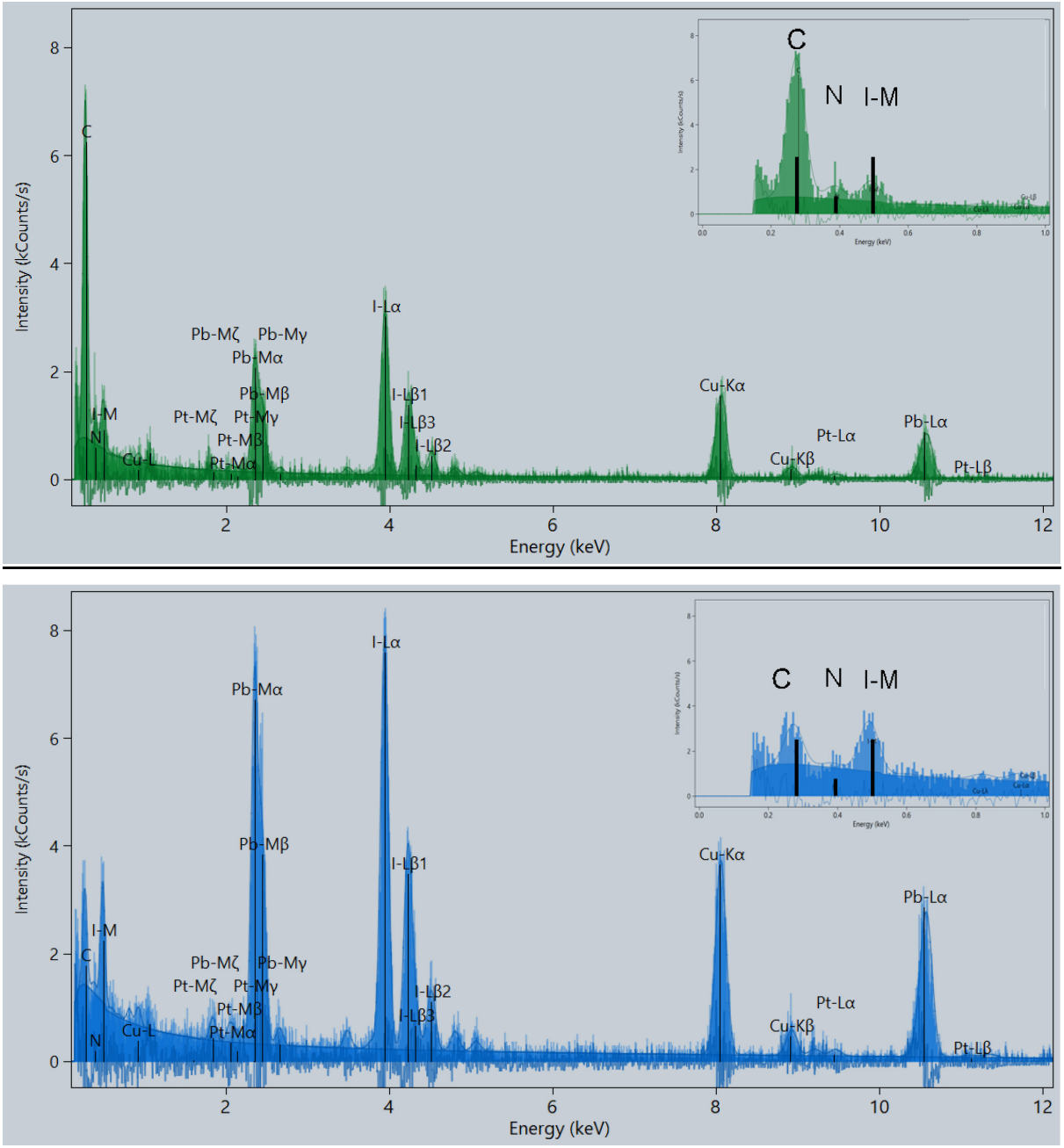

Figure S6. Integrated EDX spectra of surface phase (green) and perovskite (blue) regions are shown. The respective upper right corners show a magnified detail of the low energy region up to 1 keV X-ray energy. Both spectra include a spectrum fit, a background fit, and the residual

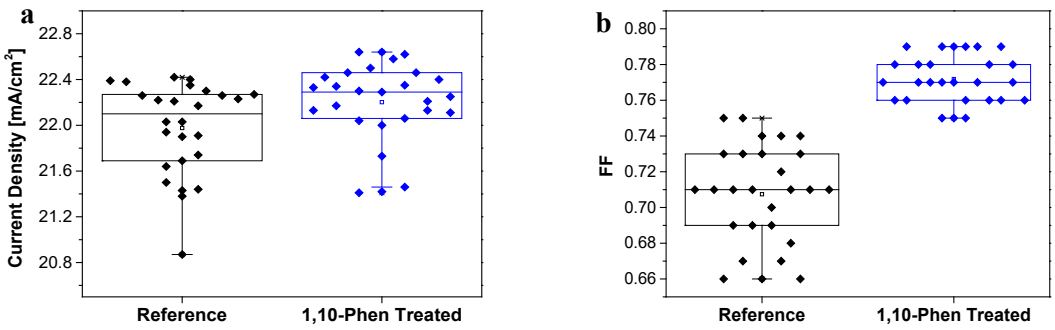

Figure S7. Chart-box presentation of the current densities (a) and fill factors of (b) the reference and 1,10-phen treated PSC devices.

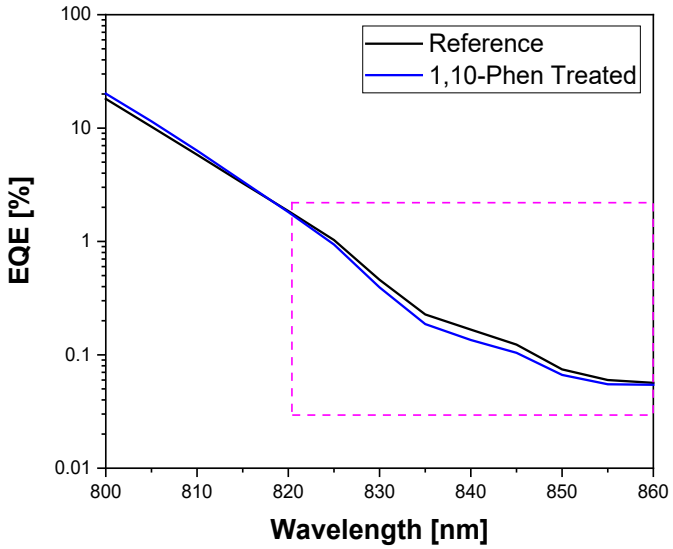

Figure S8. EQE spectra of the $MAPbI_3$ reference and the 1,10-phen treated devices.

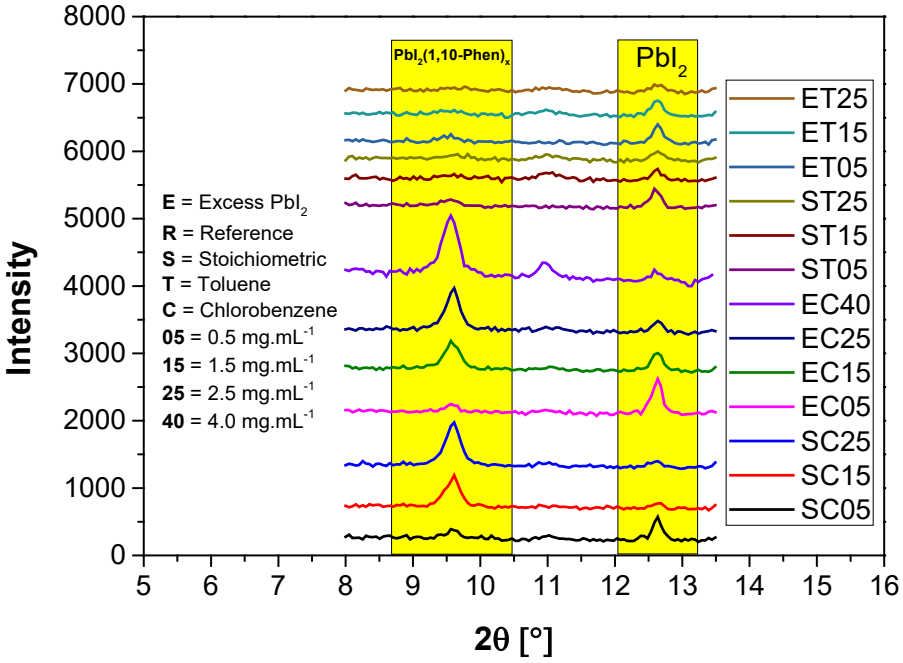

Figure S9. XRD pattern between 8° and 13° 2 theta of treated films with increasing concentration of 1,10-phen in chlorobenzene and toluene for treatment optimization.

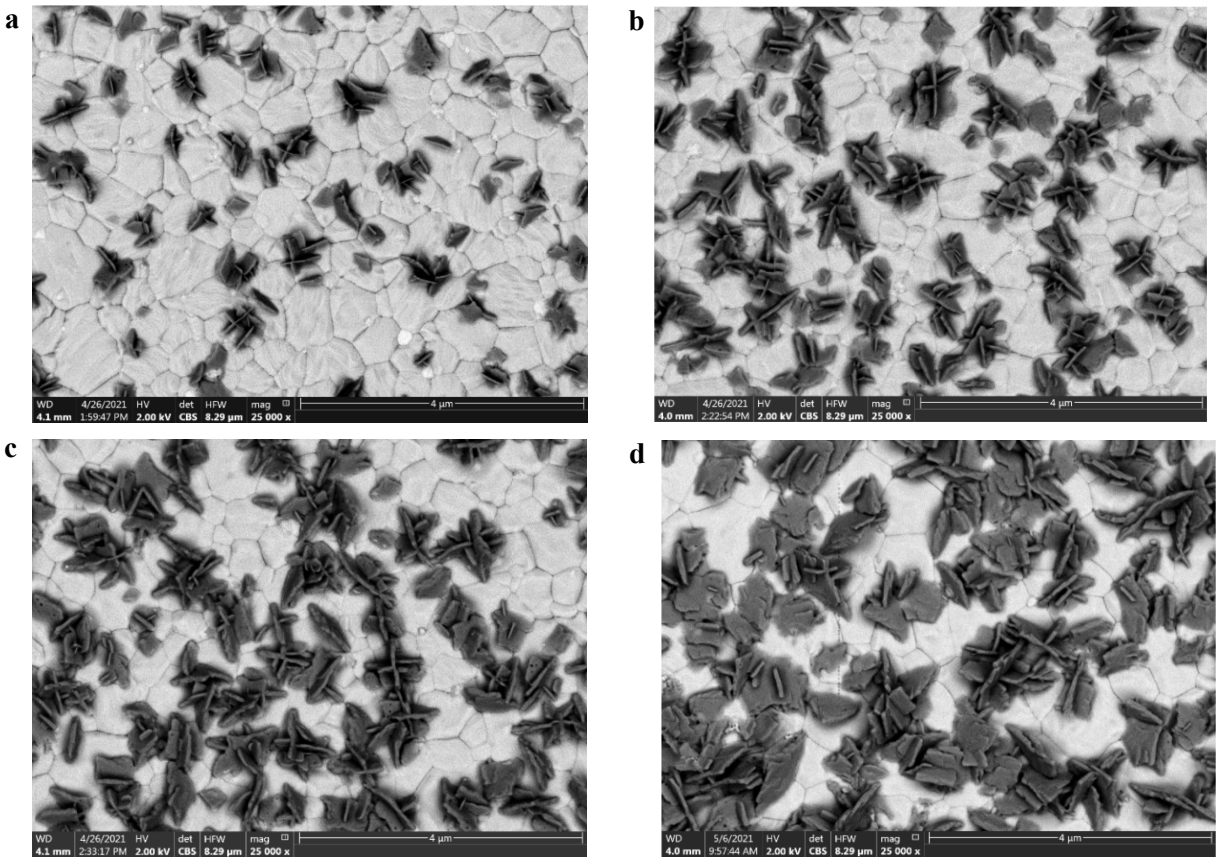

Figure S10. SEM top-view images of surface-treated $MAPbI_3$ perovskite (*5* mol % *excess* PbI_2) film with increasing concentration of 1,10-phen solution; **(a)** 0.5, **(b)** 1.5, **(c)** 2.5 (optimum concentration for device performance), **(d)** 4.0 $mg.mL^{-1}$ in chlorobenzene.

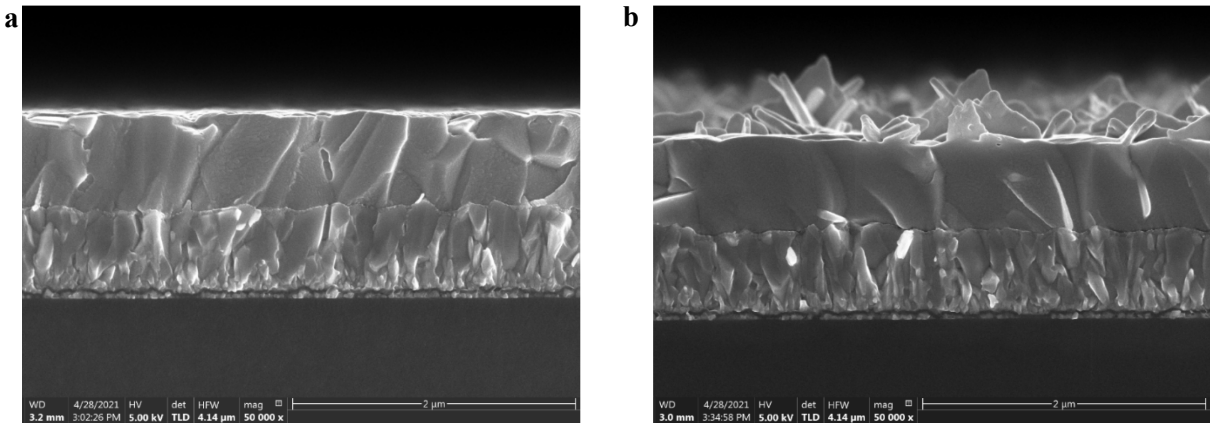

Figure S11. SEM cross-section images of (**a**) untreated and (**b**) surface-treated $MAPbI_3$ perovskite film (2.5 $mg.mL^{-1}$ in chlorobenzene).

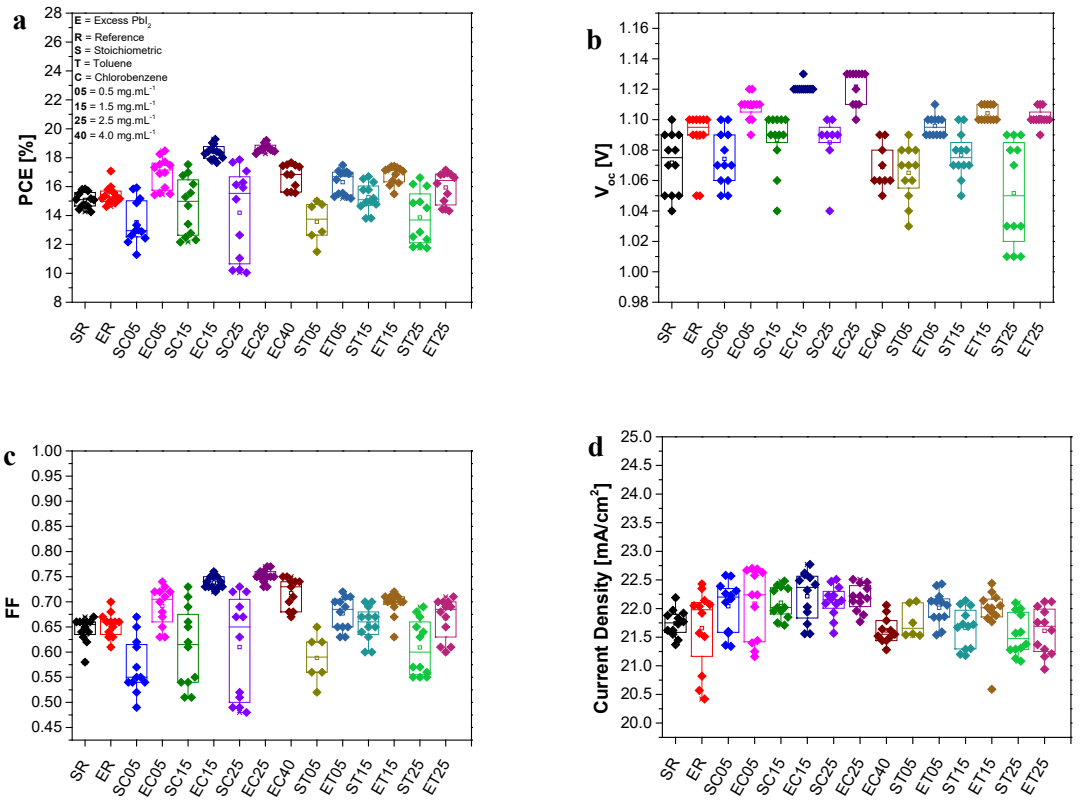

Figure S12. Chart-box presentation of the power conversion efficiencies (PCE) (a), open-circuit voltages (V_{oc}) (b), fill factors (FF) (c), and the current densities (J_{sc}) (d) of 1,10-phen treated PSC devices for treatment optimization.

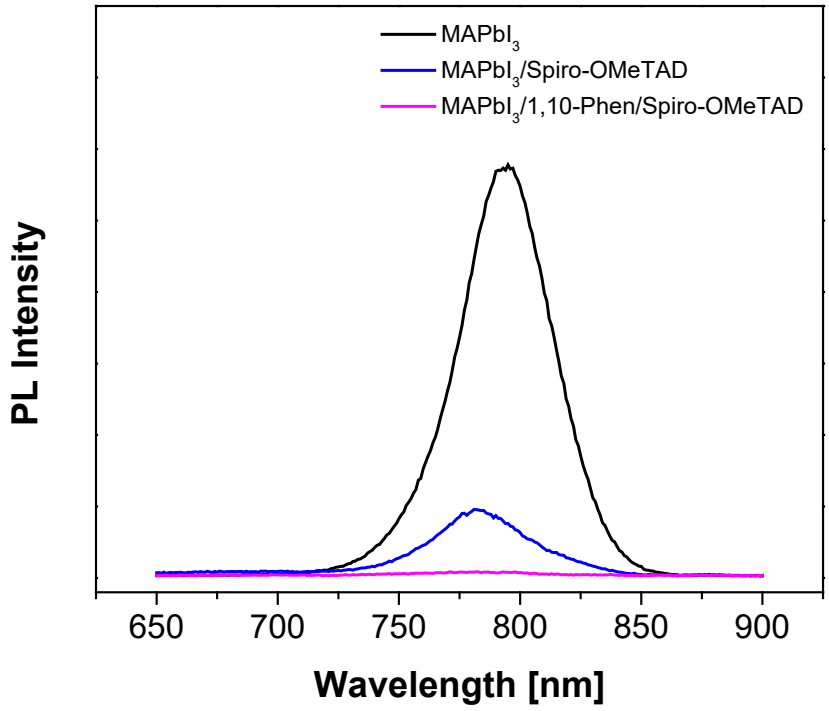

Figure S13. Steady-state PL spectra of the $MAPbI_3$, $MAPbI_3$/Spiro-OMeTAD, and 1,10-phen treated $MAPbI_3$/ Spiro-OMeTAD films (1,10-phen 2.5 $mg.mL^{-1}$ in chlorobenzene).

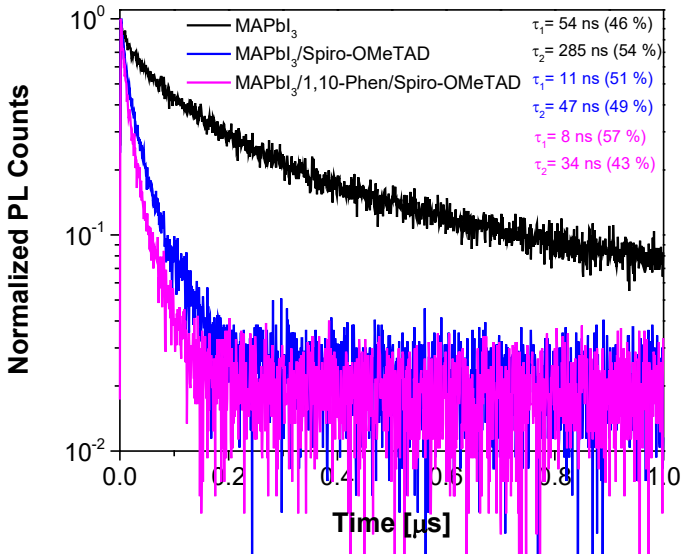

Figure S14. Time-resolved PL spectra of the $MAPbI_3$, $MAPbI_3$/Spiro-OMeTAD, and 1,10-phen treated $MAPbI_3$/Spiro-OMeTAD films (1,10-phen 2.5 $mg.mL^{-1}$ in chlorobenzene).

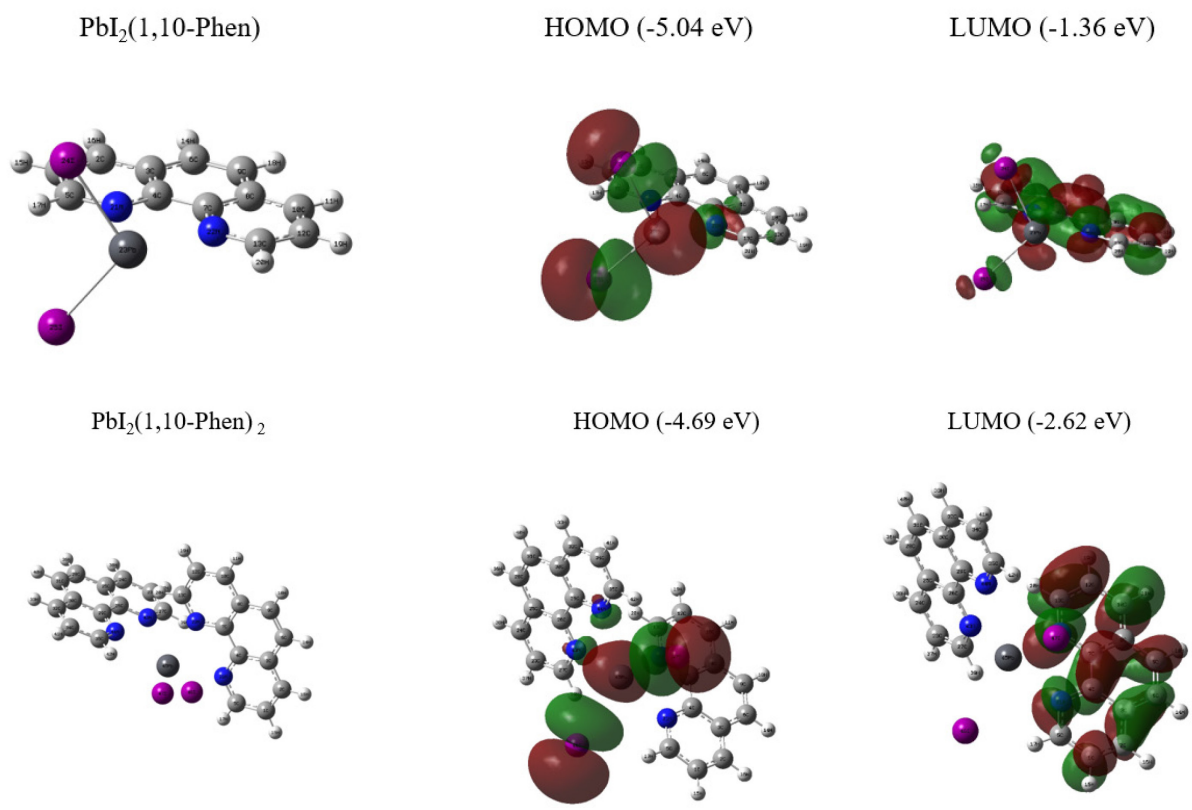

Figure S15. HOMO and LUMO energy levels of model coordination compounds based on DFT calculations**.** (Complexes were optimized and calculated with B3LYP density functional and LanL2DZ basis set with **Gaussian 09 Revision A0.2 suite.)**

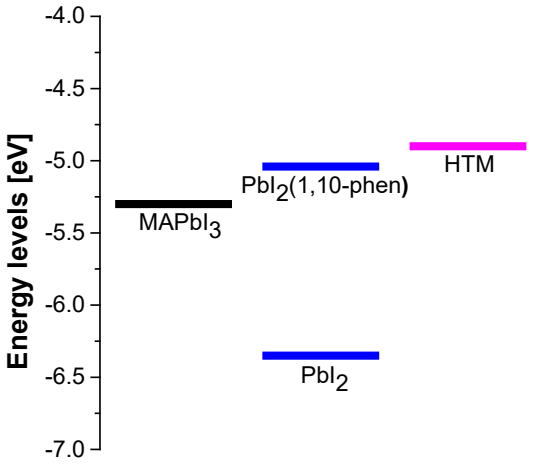

Figure S16. VB/HOMO energy levels of the corresponding layers.

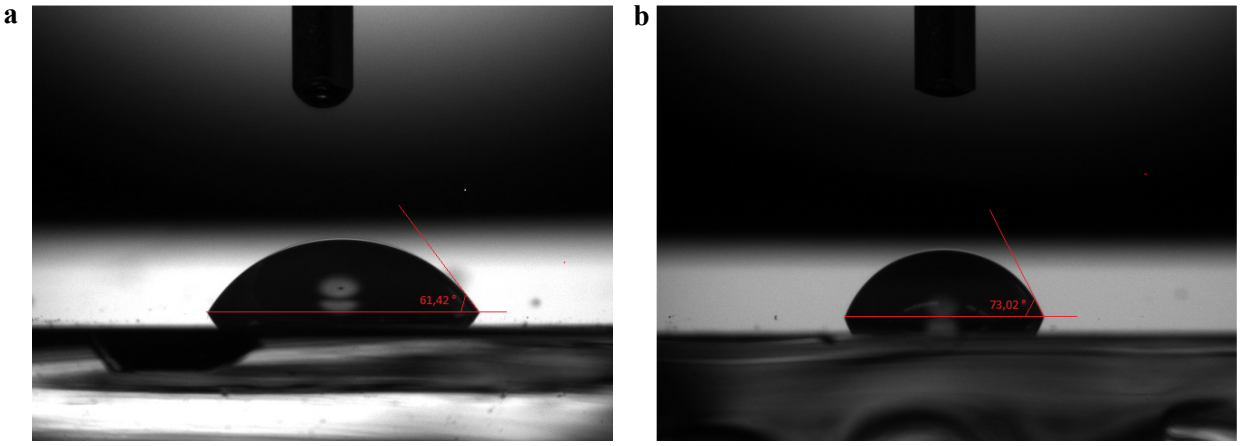

Figure S17. Contact angle measurements of untreated (a) and surface treated (b) $MAPbI_3$ perovskite film.

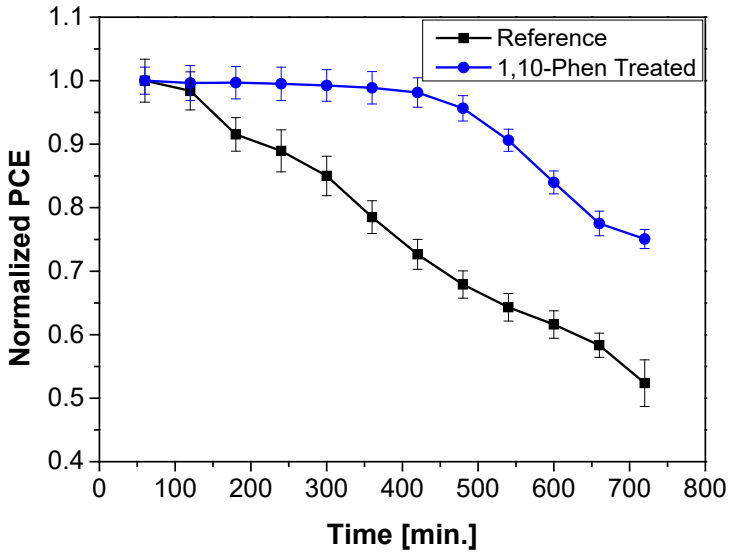

Figure S18. Photo and thermal stabilities of reference and 1,10-phen treated perovskite solar cells under continuous 1-sun illumination at a temperature of 60 °C for 12 hours.

Table S1. Time-resolved photoluminescence decay components of $MAPbI_3$ reference and 1,10-phen treated $MAPbI_3$ films.

Sample	A_1(%)	τ_1 (µs)	A_2 (%)	τ_2 (µs)	$\tau_{ave.}$ (µs)
Reference	58.18	0.049	41.82	0.114	0.077
1,10-phen treated	29.92	0.078	70.08	0.320	0.225

Table S2. IR-active vibrational bands (in cm^{-1}) of 1,10-phenanthroline (phen), PbX_2(phen)(mono), and $PbX_2(phen)_2$(bis), where X = I, in KBr, reprinted with permission. [45]

1,10-Phenanthroline			$PbI_2(phen)_x$	
			1:1	1:2
Mode	Literature [1]	This work	This work	This work
26 (B_2)	624 (m)	623 (m)	637 (m)	634 (m)
4 (A_1)	708 (wm)	706 (w)		
27 (B_2)	724 (m)	724 (w)	722 (s)	719 (m) + 725 (s)
51 (B_1)	738 (vs)	739 (s)		
50 (B_1)	779 (m)	778 (w)	781 (m)	771 (m)
60 (A_2)	810 (w)	814 (w)	806 (w)	
49 (B_1)	840 (s)	840 (ssh)	828 (wsh) + 853 (m)	846 (s)
5 (A_1)	853 (vs)	855 (s)	860 (m)	859 (m)
28 (B_2)	896 (vvw)	882 (w)	894 (w)	892 (w)
57 (A_2)	956 (w)	956 (w)	958 (vw)	957 (w)
46 (B_1)	969 (w)	969 (w)		968 (w)
29 (B_2)	988 (m)	987 (m)	982 (vw)	989 (wsh)
Comb. band	997 (w)	995 (w)	994 (vw)	994 (w)
6 (A_1)	1037 (m)	1036 (w)	1031 (vw)	1037 (vw)
30 (B_2)	1079 (m)	1079 (w)	1086 (w)	1087 (wsh)
7 (A_1)	1092 (s)	1091 (m)	1098 (s)	1096 (m)
31 (B_2)	1137 (m)	1138 (m)	1143 (s)	1141 (w)
9 (A_1)	1186 (vw)	1185 (w)		1188 (vw)
33 (B_2)	1207 (wsh)	1207 (wsh)	1205 (w)	1205 (w)
10 (A_1)	1212 (wm)	1216 (m)	1221 (w)	1221 (m)
12 (A_1)	1295 (w)	1295 (w)	1299 (w)	1300 (w)
35 (B_2)	1312 (vw)	1312 (w)	1313 (w)	1313 (w)
13 (A_1)	1345 (ms)	1345 (m)	1344 (m)	1340 (m)
36 (B_2)	1405 (m)	1406 (w)	1412 (m)	1415 (m)
37 (B_2)	1422 (s)	1422 (s)	1425 (s)	1423 (s)
15 (A_1)	1446 (s)	1447 (w)	1449 (vw)	1445 (w)
38 (B_2)	1492 (m)	1492 (w)	1494 (m)	1492 (m)
16 (A_1)	1502 (s)	1503 (m)	1514 (s)	1512 (s)
39 (B_2)	1561 (m)	1562 (m)	1571 (m)	1569 (m)
40 (B_2)	1585 (ms)	1586 (m)	1586 (m)	1586 (m)
17 (A_1)	1597 (vw)	1598 (vw)	1600 (w)	1601 (vw)
18 (A1)	1615 (m)	1616 (w)	1619 (m)	1621 (m)

s = strong; m = medium; w = weak; v = very; sh = shoulder; br = broad.

4. Synthesis of PbI_2(1,10-phen)$_2$:

PbI_2 (0.5 M) and excess 1,10-phenanthroline (1.5 M) DMF solutions were mixed and stirred at room temperature for 3 hours. After mixing for a few minutes, precipitates appeared. At the end of the reaction, enough amount of toluene was added to the reaction mixture to adequately precipitate the complex. Then, the precipitate was filtered and subsequently washed several times with diethyl ether. Finally, it was dried at 60 ^{O}C in air for 24 h, producing a yellow powder of solid PbI_2(1,10-phen)$_2$.

Synthesis of PbI_2(1,10-phen):

PbI_2 (0.5 M) and 1,10-phenanthroline (0.5 M) DMF solutions were mixed and stirred at room temperature for 3 hours. After mixing for a few minutes, precipitates appeared. At the end of the reaction, enough amount of toluene was added to the reaction mixture to adequately precipitate the complex. Then, the precipitate was filtered and subsequently washed several times with diethyl ether. Finally, it was dried at 60 ^{O}C in air for 24 h, producing a yellow powder of solid PbI_2(1,10-phen).

References

(1) Buffet, A.; Rothkirch, A.; Döhrmann, R.; Körstgens, V.; Abul Kashem, M. M.; Perlich, J.; Herzog, G.; Schwartzkopf, M.; Gehrke, R.; Müller-Buschbaum, P. P03, the Microfocus and Nanofocus X-Ray Scattering (Minaxs) Beamline of the Petra Iii Storage Ring: The Microfocus Endstation. *Journal of Synchrotron Radiation* **2012,** *19* (4), 647-653.

(2) Jiang, Z. Gixsgui: A Matlab Toolbox for Grazing-Incidence X-Ray Scattering Data Visualization and Reduction, and Indexing of Buried Three-Dimensional Periodic Nanostructured Films. *Journal of Applied Crystallography* **2015,** *48* (3), 917-926.

(3) Momma, K.; Izumi, F. Vesta 3for Three-Dimensional Visualization of Crystal, Volumetric and Morphology Data. *J. Appl. Crystallogr.* **2011,** *44* (6), 1272-1276, DOI: 10.1107/s0021889811038970.

(4) Huth, F.; Schnell, M.; Wittborn, J.; Ocelic, N.; Hillenbrand, R. Infrared-Spectroscopic Nanoimaging with a Thermal Source. *Nature materials* **2011,** *10* (5), 352-356.

(5) Meyns, M.; Primpke, S.; Gerdts, G. Library Based Identification and Characterisation of Polymers with Nano-Ftir and Ir-Ssnom Imaging. *Analytical Methods* **2019,** *11* (40), 5195-5202.

4 A Novel Multi-Functional Thiophene-Based Organic Cation as Passivation, Crystalline Orientation, and Organic Spacer Agent for Low-Dimensional 3D/1D Perovskite Solar Cells

This chapter is based on the following publication:

Buyruk, A†., Semerci, A†., Emin, S., Hooijer, R., Kovacheva, D., Mayer, P., ... & Ameri, T. (2023). A Novel Multi-Functional Thiophene-Based Organic Cation as Passivation, Crystalline Orientation, and Organic Spacer Agent for Low-Dimensional 3D/1D Perovskite Solar Cells. *Advanced Optical Materials*, 2300267.

† Equal first-author contribution

†† Surface treatment in this study is performed by Ali Buyruk and the bulk treatment by Ali Semerci.

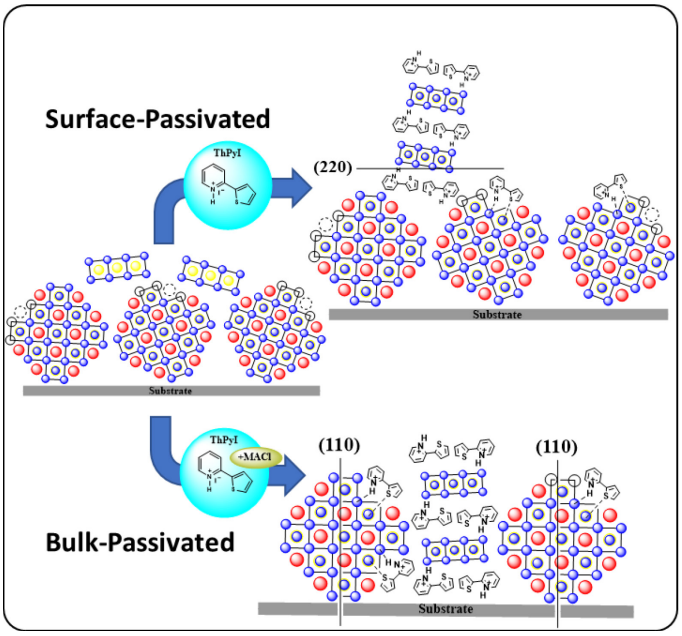

Keywords

1D perovskite, 3D/1D perovskite, solar cell, passivation, bulk-passivated 3D perovskite, crystalline orientation promote

4.1 Introduction

Over the past decade, three-dimensional (3D) organic-inorganic halide perovskites (OIHPs) have emerged as promising absorber materials for photovoltaic applications. These materials possess superior properties, including a high absorption coefficient, a long diffusion length of charge carriers, fast charge transport, and a tunable bandgap. The power conversion efficiency (PCE) of 3D OIHPs has witnessed a rapid increase from 3.8% to an impressive 25.2%.[1-9]

Despite these achievements, the moderate intrinsic stability of 3D methylammonium lead iodide perovskite (MAPI) against moisture and heat has raised concerns for potential commercialization. [10-14] The instability of 3D MAPI is attributed to its crystalline structure, and ionic migration has been identified as a significant factor affecting the photovoltaic properties of perovskite solar cells. Ionic migration leads to the generation and displacement of vacancies in perovskite materials. While OIHPs function as mixed ionic–electronic conductors with iodide ions as the majority ionic carriers, the diffusion coefficient for I^- ions is several orders of magnitude higher than that for organic cations like $CH_3NH_3^+$ or $NH_2CH=NH^{2+}$. The limited degrees of freedom for ion migration in organic cations contribute to the poor stability of 3D perovskite structures. [15-17]

The vulnerability of 3D halide perovskites to water and oxygen molecules, particularly at vacancy sites, accelerates degradation through a vacancy-assisted mechanism. When methylammonium lead iodide (MAPI) is exposed to water, it degrades into lead iodide (PbI_2), iodide anions, and methylammonium cations. [16-17] Additionally, surface and bulk defects in 3D polycrystalline perovskites play a significant role in influencing carrier recombination, impacting the overall performance of solar cells. Effectively addressing these challenges is crucial for advancing the stability and reliability of three-dimensional organic-inorganic halide perovskites (3D OIHPs) in practical photovoltaic applications.

Simultaneously, there is a growing interest in the lower-dimensional counterparts of 3D halide perovskites. These materials feature layers of larger organic cations that separate slabs of octahedral perovskite-like inorganic layers. This structural arrangement has profound effects on band structure, charge carrier transport, and often results in much-improved stability. [14] However, the insulating nature of organic spacers in low-dimensional perovskites can limit conductivity, potentially contributing to lower photovoltaic performance despite their enhanced environmental stability. [18] Balancing these factors becomes essential in harnessing the potential of lower-dimensional perovskites for efficient and stable photovoltaic applications.

To address the above-mentioned challenges, a strong research focus has been put on developing new strategies and approaches to suppress recombination processes and to overcome the stability issues of 3D halide perovskite structures.[19-20] Among the various passivating additives, it has been reported that

ammonium salts can effectively diminish the impact of defects caused by dangling bonds or vacancies.[21-22] Another strategy for passivation is the introduction of low-dimensional perovskites in the 3D perovskite system.[23] Following this approach, the passivation of defects can be achieved, and the intrinsic stability issues of the 3D MAPI structure can be addressed. Therefore, passivated and mixed-dimensional perovskite solar cells (PSCs) have been fabricated using small organic molecular spacers.[24] The low-dimensional (1D or 2D) perovskite structures found in the resulting mixed-dimensional perovskites serve both as passivating agents to reduce the impact of defects and as heterojunctions that enhance the fluorescence lifetimes in the perovskite structure.[21] Hence, mixed-dimensional perovskites recently evolved as suitable photovoltaic (PV) candidates due to their encouraging environmental stability and wide tunability of optical properties.[25-30] Here, the higher perovskite stability could be attributed to the hydrophobic nature of the organic spacers used. [31-32] For example, 1D perovskitoids can be used both on top of 3D perovskite films or in the bulk perovskite by adding the desired organic cations to the precursor solution to improve efficiency and stability of perovskite PV devices.[33-35]

It has been demonstrated that the metal halide bonds can break upon illumination, followed by rearrangement of the perovskite crystal structure.[30] The individual metal halide octahedra formed during this reorganization are more stable than the regularly bonded ones.[36] In 1D perovskitoid structures, the $[PbI_6]^{4-}$ octahedral framework structure based on edge, face, or corner-sharing connect to the organic spacers. In this case, the metal halide octahedra are surrounded by organic spacer molecules.[37] Among the reasons for the instability of tin and lead based perovskites are the high-energy orbitals ($5s^2$ (Sn^{2+}) /$6s^2$ (Pb^{2+})) near the top of the valance band, which are more reactive.[38] The edge or face-sharing binding motif of 1D structures stabilizes these high-energy orbitals, which leads to better environmental stability. [39] For example, Liu et.al employed 1D PbI_2-bipyridine (BPy) to incorporate into the 3D MAPI perovskite structure. Thereby, the obtained 1D perovskite layers reduced the ion migration by improving the stability of the 3D/1D perovskite structure.[40] Gao et al. used thiazole ammonium iodide (TAI) to form a 1D $TAPbI_3$ capping layer on 3D MAPI, improving the stability and performance of corresponding PSCs compared to the 3D MAPI control device.[39] Yang et al. used polymerizable propargylammonium to fabricate 1D structures at the surface and grain boundaries in a mixed-dimensional 3D/1D perovskite. By this means, they enhanced the charge transport and decreased the tensile strain of perovskite layers.[34]

Solar cells featuring grain boundary passivation have been documented to exhibit enhanced performance in contrast to those lacking passivation, owing to the role of grain boundaries as potential recombination centers. In the realm of methylammonium lead iodide (MAPI) perovskites, point defects emerge as the most extensively investigated imperfections. The spectrum of observed defects in MAPI encompasses vacancies, interstitials, and anti-site occupations, totaling twelve distinct types. [41] The

presence of defects at grain boundaries within polycrystalline perovskites represents a prominent catalyst for the recombination of photo-generated carriers. Varied passivation strategies targeting defects include the application of polymers, quaternary ammonium salts, and other organic compounds. Noteworthy examples of tailored passivation techniques involve the utilization of polymers, quaternary ammonium salts, and other organic compounds.[42-50] In the quest to mitigate non-radiative recombination both within the bulk and at grain boundaries, diverse additives, such as inorganic species (e.g., Cl^-, SCN^-) or organic molecules, have been incorporated into perovskite materials. [51]

In this study, an innovative organic spacer, namely 2-(thiophene-2yl-) pyridine-1-ium iodide (ThPyI), was synthesized for the purpose of constructing perovskite solar cells with mixed-dimensional bulk passivation in 3D and surface passivation in 3D/1D configurations. The ThPyI organic spacer is designed to induce the formation of 1D structures at the grain boundaries of surface-passivated 3D perovskite films. Additionally, the ThPyI organic spacer is envisioned as a promising passivating agent capable of mitigating various defects within the 3D methylammonium lead iodide (MAPI) perovskite, while also serving as a suitable material for the creation of 3D/1D heterostructure perovskites to facilitate efficient charge separation.

By employing two distinct passivation approaches, bulk and surface treatment, the influence of the ThPyI organic spacer on the photovoltaic performance, stability, structural, and optoelectronic properties of the corresponding perovskite solar cells was systematically investigated. The optimized power conversion efficiency (PCE) of the bulk-passivated 3D and surface-passivated 3D/1D mixed-dimensional perovskite solar cells reached 14.10% and 19.60%, respectively. Notably, these values represent a significant enhancement in stability compared to the reference 3D perovskite solar cells.

4.2 Results and Discussion

The molecular structure of the ThPyI organic spacer used in this work is illustrated in **Figure 1a**. The characterization of ThPyI was performed with nuclear magnetic resonance (^{1}H-,^{13}C-NMR) and mass spectroscopy (**Figure S1a-d**, Supporting Information). The so-called surface-passivated 3D/1D device was prepared by spin-coating of ThPyI on top of MAPI films.

As for the bulk-passivated 3D perovskite, the fabrication process is similar to the case of MAPI, with the addition of ThPyI into the precursor solution. The latter sample comprising both ThPyI and methylammonium chloride (MACl) agents is called "bulk-passivated 3D" from here on. For the purpose of comparison with the bulk-passivated 3D perovskite, MAPI-based control devices were fabricated with and without MACl additive. It is worthwhile mentioning that based on a known effect, MACl is added to the bulk-passivated 3D MAPI to achieve preferential orientation of the crystal grains.[34] However, in the surface-passivated samples the use of MACl was avoided due to the use of excess PbI_2 (5% mol) in the precursor solution. Further processing details are provided in the experimental section. Interestingly, both methods of ThPyI-based surface and bulk passivation result in the formation of a new perovskite-related phase, which is identified as the 1D perovskitoid structure ($C_{18}H_{16}I_8N_2Pb_3S_2$), as explained in the following.

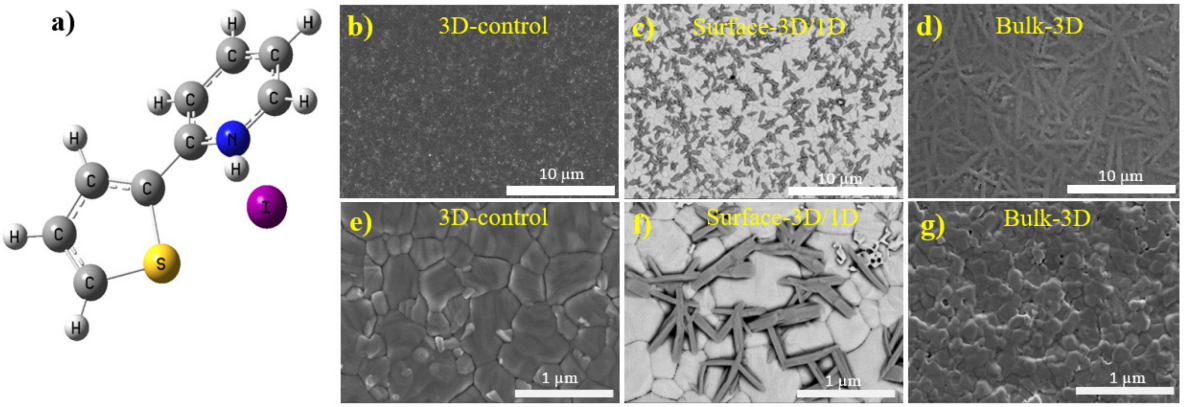

Figure 1. a) Molecular structure of ThPyI spacer. SEM images of b, e) 3D MAPI control film, c, f) surface-passivated 3D/1D, and d, g) bulk-passivated 3D MAPI perovskite film.

To evaluate the morphology of 3D control, bulk-passivated 3D, and surface-passivated 3D/1D MAPI perovskite films, scanning electron microscopy (SEM) measurements were performed. As shown in the top-view SEM images of the corresponding films in **Figure 1b-g,** the active MAPI layers completely cover the substrate surface. The grain-based morphology in the 3D control and the surface-passivated 3D/1D films looks very similar. However, on the surface-passivated 3D/1D perovskite film, needle-like

new features form preferentially at the 3D perovskite grain boundaries as shown in **Figure 1c**. These needles assemble into an interconnected network which may affect the charge transport across the grains. In comparison to the 3D MAPI control, bulk-passivated 3D MAPI perovskite film shows a different surface morphology. In the 3D control with MACl, the interconnected needles were no longer observable (**Figure S2**, Supporting Information).

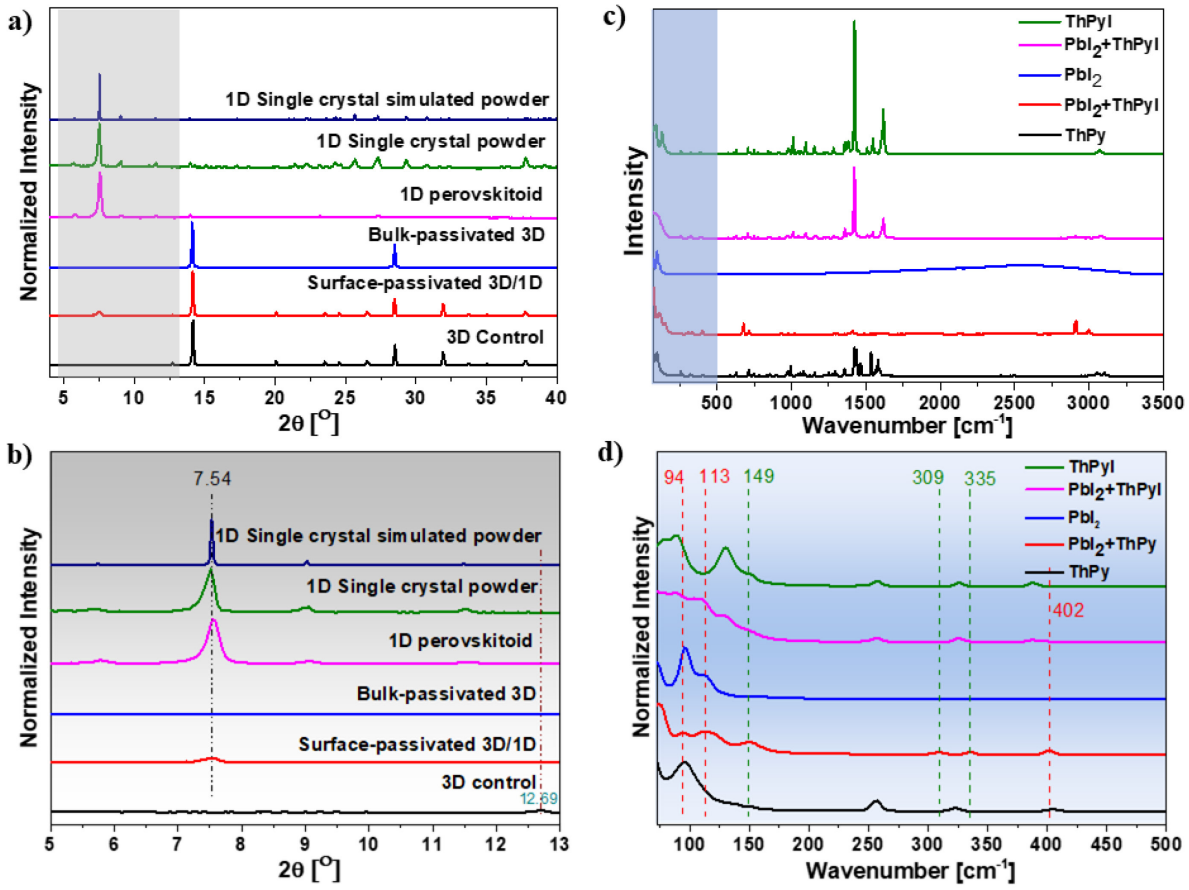

Figure 2. XRD patterns of pure 1D perovskitoid film and 1D single crystal powder, simulated 1D, 3D control, bulk-passivated 3D, and surface-passivated 3D/1D perovskite thin films showing a) wide scan and b) enlarged XRD pattern from 5 and 13 $^{\circ}$ *2θ*. C) Raman spectra of powder forms taken of the ThPy ligand, ThPyI, PbI_2, the mixture of PbI_2 + ThPy, and the mixture of PbI_2 + ThPyI. D) Narrow range Raman spectra taken from c).

The grains of bulk-passivated 3D perovskite seem to be more closely connected (or fused) which appears to obscure their grain boundaries. At lower magnification (× 2000) the bulk-passivated 3D perovskite shows interconnected needle-shape formations as shown in **Figure 1d**. It is well-known that needle-like morphology can offer enhanced charge collection compared to pure planar films.[52-54] Here, the bulk-passivated 3D film shows homogenous composition without any formations assigned to an

additional phase.

X-ray diffraction (XRD) measurements were employed to investigate the crystallinity of a 1D single crystal, 3D control, surface-passivated 3D/1D, and bulk-passivated 3D perovskite films as shown in **Figure 2a**. The main XRD peaks of the 3D control appear at 14.19º and 28.50º *2θ*, which correspond to (110) and (220) planes, respectively. As illustrated in the XRD data, the bulk-passivated 3D perovskite film (3D Bulk with MACl) fabricated using MACl also exhibits these two dominant diffraction peaks. The lack of additional reflections or any peak shift indicates that the addition of the ThPyI organic spacer into the 3D perovskite film does not change the MAPI lattice. The absence of other diffraction peaks from MAPI or a possible second phase (including below <12º *2θ*) confirms both the phase purity and the preferential orientation of the MAPI grains. Here, the preferential orientation is achieved by the addition of MACl, which is widely used in the literature as an additive to boost the PCE.[55]

As observed in the XRD pattern of the surface-passivated perovskite, a new peak appears at low *2θ* values (7.54º). This additional peak can be related to the needle-like formations at the 3D perovskite grain boundaries shown in **Figure 2c, f**. Moreover, this new phase did not result from PbI_2 or from the pure ThPyI organic spacer according to the XRD patterns. To elucidate the structure of the needle-like formations on the surface-passivated perovskite film, single crystals were grown by reacting stoichiometric ratios of PbI_2 and ThPyI (**Figure S3**, Supporting Information). The structural analysis of the needle-shaped single crystals was performed using both powder XRD data shown in **Figure 2** and single crystal diffraction (**Figure S4**, Supporting Information).

To further confirm the presence of both the 3D control MAPI and the 1D perovskitoid, powder XRD measurements and Rietveld refinements were carried out. The results of the Rietveld refinement of the structure and the Rietveld plot of the fit are presented in **Figures S5-6 and Table S2** in the Supporting Information. The whole powder pattern fitting procedure of the 1D-film (**Figure S6**) revealed a single phase 1D perovskitoid with unit cell parameters a = 25.494(4) Å, b = 61.82(1) Å and c = 4.5968(8) Å, which are close to those observed for the single crystal phase (**Table S1,** Supporting Information).
According to the single crystal diffraction results and the calculated powder diffraction pattern, the single crystal data perfectly matches the XRD pattern of the 1D perovskitoid structure {with reflections at 5.7º (040), 7.5º (220), 9.0º (240), 11.0º (260), and 11.4º (080)} The crystal structure of the 1D perovskitoid corresponds to the unit cell formula $C_{18}H_{16}I_8N_2Pb_3S_2$ given in **Figure 3**. In the crystal structure, three edge-shared octahedra are accompanied by two edge-to-edge aligned organic spacer (ThPyI) molecules, which engage in strong N^+-H···I-Pb hydrogen-bonding interactions (**Figure S4**, Supporting Information). According to the obtained crystallographic data, the 1D perovskitoid features an orthorhombic crystal system (*Fdd*2 space group) (**Table S1,** Supporting Information). In good

agreement with the single crystal XRD data of the 1D perovskitoid, the new peak emerging at 7.54º for the surface-passivated sample can be assigned to the 1D perovskitoid phase as shown in **Figure 2b**. We note that under these conditions, reflections corresponding to the 1D phase are missing in the diffractogram of bulk-passivated 3D MAPI. However, when the passivation is done without (wo) added MACl, the dominant peak at 7.54° is clearly seen, which indicates the formation of the 1D perovskitoid phase (**Figure S7**, Supporting Information).

To gain additional insight about the needles formed on the surface of the 3D/1D perovskite film, Raman spectroscopy was employed as shown in **Figure 2c, d**.

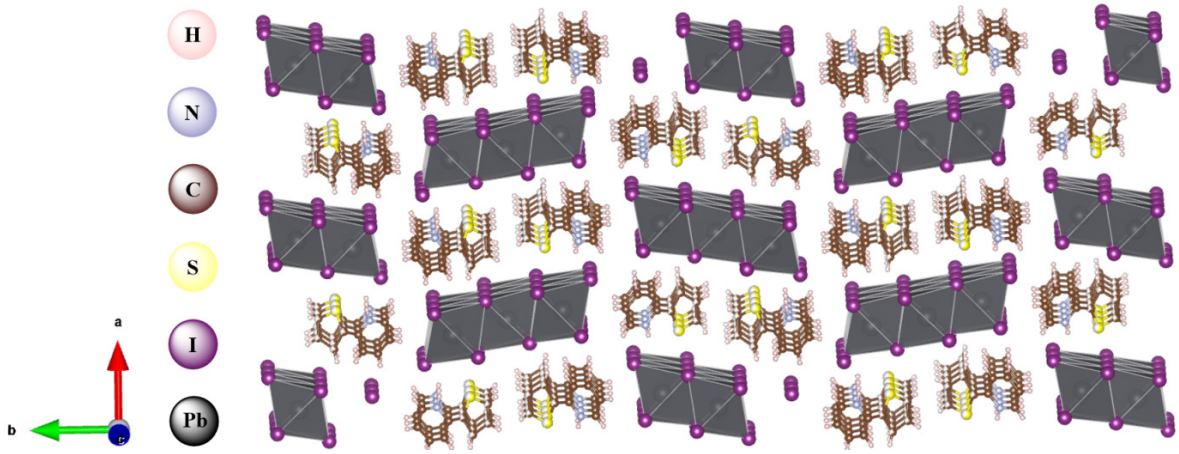

Figure 3. Schematic representation of the crystal structure of the 1D perovskitoid unit cell. The free iodine atoms which appear in the schematic are part of the octahedra of the adjacent unit cell which is not involved here.

The Raman spectra of the ThPyI organic spacer, its neutral form (ThPy, unprotonated), PbI_2, and mixtures of PbI_2 + ThPy, and PbI_2 + ThPyI were compared to eliminate the possibility that the needles derive from a basic complex form of PbI_2 with the organic spacer (**Figure S8,** Supporting Information).[56] The Raman vibrational frequencies of the mixture of PbI_2 + ThPy appear at 74, 94, 112, 149, 309, 335, and 402 cm^{-1} (red and green dashed lines in **Figure 2d**). Some of these signals (red dashed lines) are shifted compared to those of PbI_2 and ThPy. Moreover, two Raman vibrational frequencies of free ThPy at 258 and 323 cm^{-1} disappear, while two new vibrational frequencies appear at 309 and 335 cm^{-1} (green dashed lines). These new signals are in the region of the metal-nitrogen stretching vibrations (200-600 cm^{-1}). In sum, these observations suggest that a new phase has formed via a chemical reaction between PbI_2 and ThPy.[57]

Unlike the mixture of PbI_2 + ThPy, the Raman spectrum of the mixture of PbI_2 + ThPyI shows no shifts and/or new signals. This indicates that here the Raman signals are due to the unreacted mixture of PbI_2 and ThPyI since these overlap with the signals of pure PbI_2 and ThPyI. To support the Raman results

for the unreacted PbI_2 + ThPyI mixture, its solution-state ^{1}H-NMR was evaluated (**Figure S1d-e,** Supporting Information). In the PbI_2–ThPyI solution, no new ^{1}H-NMR signal associated with a chemical reaction was recorded. Interestingly, the signal of the proton (N^+-H) of the pyridine group shows an up-field shift (shielding effect), which is a specific hint as to the strong N^+-H···I-Pb-I hydrogen-bonding interactions. In addition to the up-field shifted proton (N^+-H), obvious up-field shifts for the neighboring protons of both rings (ThPy) are also observed. Together, these results confirm that complexation between ThPyI and PbI_2 is not the cause of the needle-like formations after surface treatment.

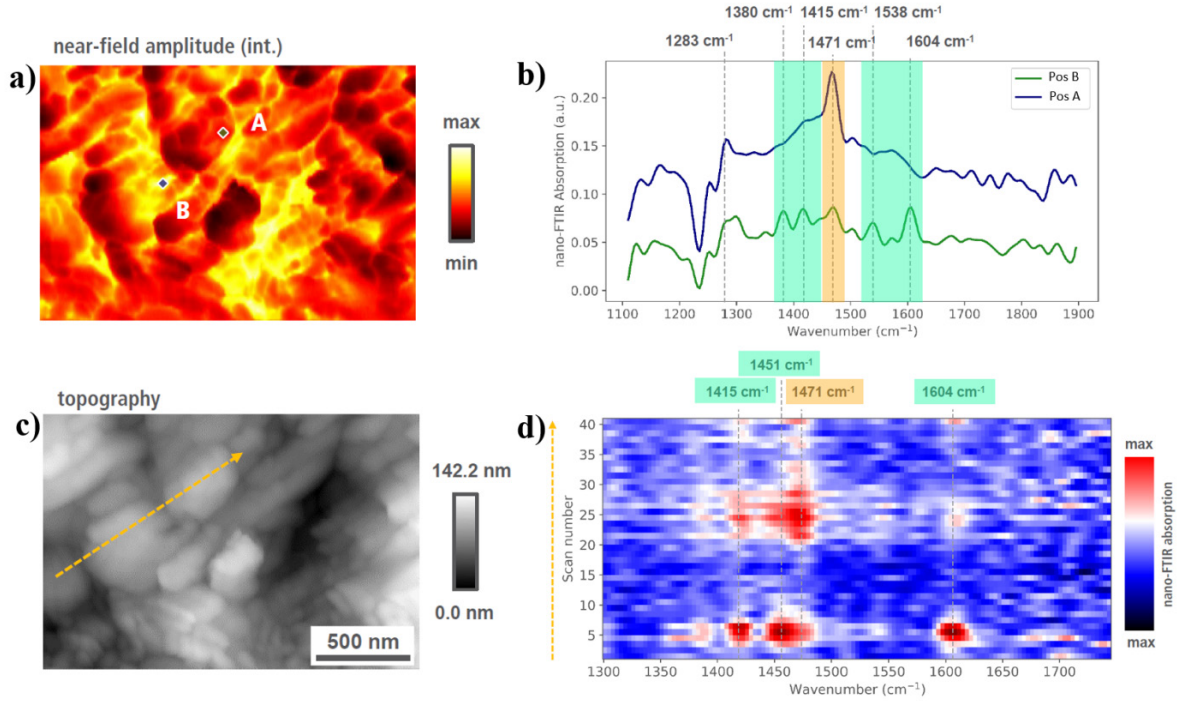

Figure 4. Nano-FTIR analysis of surface-passivated 3D/1D perovskite film. a) broadband, integrated near-field amplitude image, b) spectra recorded from the positions in A and B shown in a), c) topography of the surface, and d) spectral image recorded from the line scan in c).

To study the needle-like formations on the surface-passivated 3D/1D perovskite sample at the nanoscale (10-20 nm spatial resolution), nano-FTIR spectroscopy was used.[58]

Two locations were identified from the broadband near-field amplitude image taken on the surface-passivated 3D/1D sample, presented in **Figure 4a**. While spot (A) was taken on the top of a 3D perovskite grain, spot (B) was recorded from the needle-like formations (1D phase) which is observed in SEM images (**Figure 1c-f**). The selected broadband infrared range for these two spots varied from 1100 to 1900 cm^{-1} as given in **Figure 4b**. In spot B the intense vibration at 1471 cm^{-1} (orange highlight) was assigned to the well-known symmetric NH_3^+ bending of methylammonium in MAPI. [59]

Additionally, four new signals (highlighted in green) were observed for position B corresponding to the needle-like formation, which are not seen in the MAPI grain (position A).[60] Furthermore, these new signals are similar but slightly shifted to lower wavenumbers compared to those seen in the ThPyI organic spacer (**Figure S9,** Supporting Information). The new vibrations can be assigned to the 1D perovskitoid phase. The observed shift to lower wavenumbers in the 1D perovskitoid is attributed to the local environment in the 1D perovskitoid crystal structure. To probe the distribution of the 1D formations in detail, position-dependent measurements (one spectrum at every 30 nm) along a 1.2 µm sample distance were carried out as indicated by the orange dashed arrow in **Figure 4c**. We note that the signals from the 1D phase formations are predominantly observed at the 3D perovskite grain boundaries as shown in **Figure 4c-d**.

Grazing incidence wide-angle X-ray scattering (GIWAXS) was conducted to evaluate the orientation of perovskite crystallites in the 3D control, bulk-passivated 3D MAPI and surface-passivated 3D/1D perovskite films with and without MACl respectively. The 3D reference crystallizes with random orientation, observable through the diffraction rings as shown in **Figure 5a**. This result is in accordance with previous studies.[61] The reflection along the azimuthal angle around 0°, below the first diffraction ring corresponding to MAPI, corresponds to the (001) plane of PbI_2. Excess PbI_2 is common for untreated 3D MAPI thin films and is caused by surface degradation of the perovskite film, as well as by the excess use of PbI_2 in the precursor solution. [62]

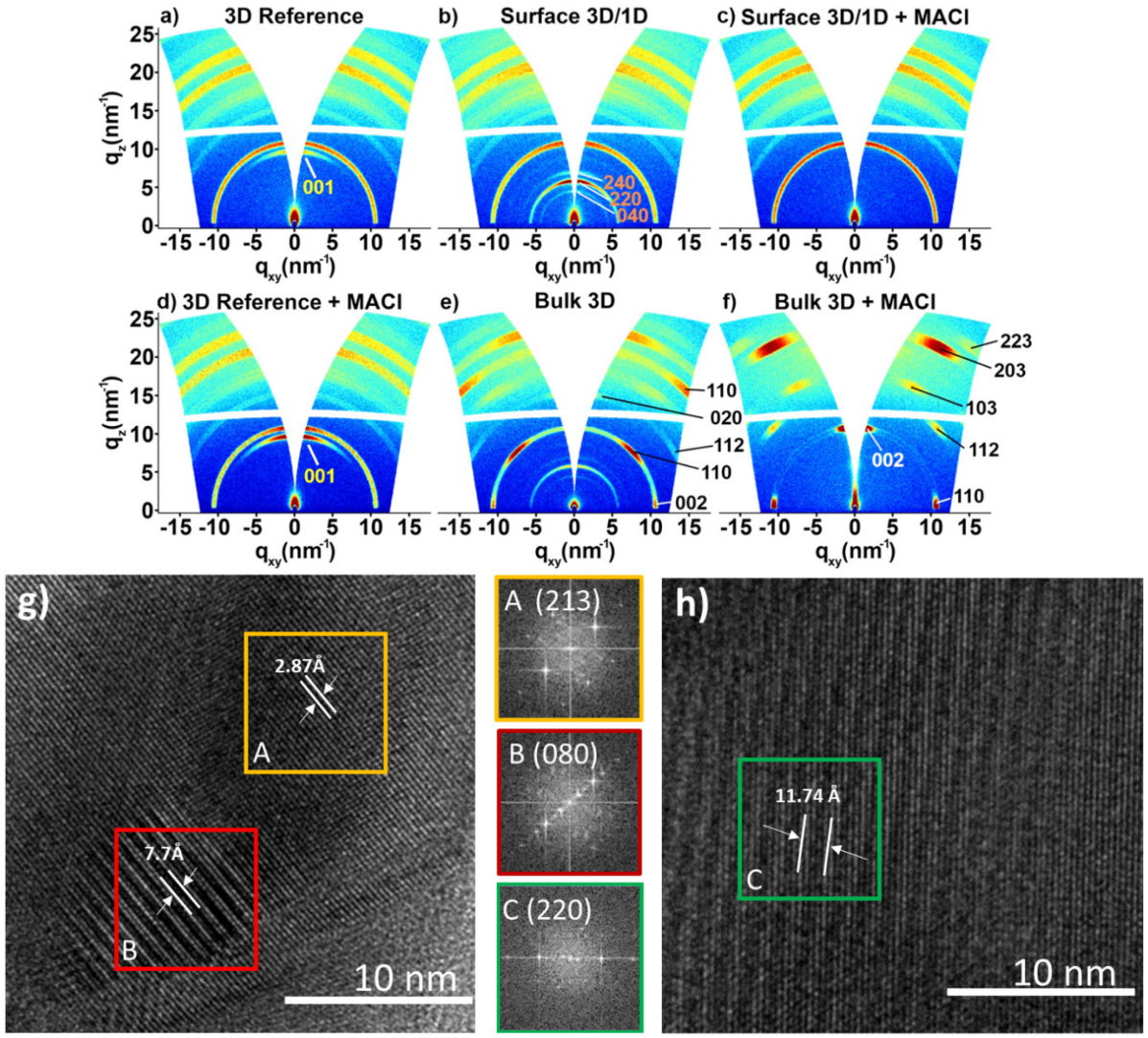

Figure 5. GIWAXS data of a) 3D control MAPI (with +5% excess PbI_2), b) surface-passivated 3D/1D without MACl, c) surface-passivated 3D/1D with MACl, d) 3D control MAPI of the bulk-passivated sample with MACl, e) bulk-passivated 3D MAPI without MACl, and f) bulk-passivated 3D MAPI with MACl. g,h) TEM images of bulk-passivated 3D MAPI (without MACl) perovskite film and corresponding fast Fourier transforms (FFT) taken from the marked areas in A, B and C.

The 3D reference with MACl displays the same features, although the intensity of the PbI_2 reflection is increased and the MAPI diffraction rings show a slight (110) horizontal orientation (orientation always with regard to the substrate plane), as shown in **Figure 5d**. The surface-passivated 3D/1D samples display a new set of reflections in the lower *q* region, shown in **Figure 5b**. These reflections appear with a horizontal orientation and can be assigned to the (040), (220) and (240) reflections of the 1D perovskitoid phase. The surface-passivated 3D/1D samples with MACl do not show any preferential orientation, or any diffraction corresponding to the 1D perovskitoid phase, see **Figure 5e**. The bulk-passivated 3D MAPI without MACl samples display oriented reflections for the 3D MAPI phase,

indexed and shown in **Figure 5c**, as well as the reflections of the 1D perovskitoid phase with a horizontal orientation.

These GIWAXS result are consistent with the XRD results where the 1D perovskitoid phase can be clearly seen in the bulk-passivated 3D film MAPI without MACl (**Figure S7a**, Supporting information). Lastly, the bulk passivated 3D MAPI with MACl displays a different orientation for the MAPI reflections and only a very weak reflection of the (220) plane corresponding to the 1D perovskitoid phase. For both bulk-passivated 3D MAPI samples, the ThPyI spacer has a strong influence on the orientation of the MAPI film, while the (110) planes reorient from horizontal to vertical orientation with respect to the substrate if MACl is additionally employed to control the crystallization. The absence of any strong diffraction, corresponding to the 1D phase in the bulk-passivated 3D MAPI with MACl sample (**Figure 5f** and **Figure S7a**, Supporting information), points towards an interaction between MACl and ThPyI in the crystallization process. The additional MA^+ in the crystallization competes with the amount of Pb^{2+} ions, which is the same for both thin films, i.e., the same amount of PbI_2 in the precursor solution. This is also evident in the surface passivated 3D/1D samples, where if MACl is used in combination with the ThPyI spacer no 1D phase is observed, but rather a complete consumption of the excessive PbI_2 into MAPI (Fig. 5e).

In conclusion for the surface-passivated 3D/1D samples, the combination of the data from the SEM, Nano FTIR and GIWAXS confirm the formation of the 1D phase at the surface and grain boundaries of the perovskite thin film. The ThPyI bulk passivated sample shows evidence of the 1D phase formation in addition to a pronounced horizonal orientation of (110) planes of the 3D MAPI perovskite phase. However, when MACI is used as a co-additive in the bulk-passivated sample, the 3D MAPI perovskite orientation is changed toward vertical (110) orientation and the diffraction peaks of the 1D phase are missing or have a noticeable intensity attenuation. At this stage it is not clear if the ThPyI spacer in the presence of MACl forms an amorphous 1D phase or if it prefers to stay in amorphous molecular (pure ThPyI) form. The impact of the ThPyI and MACl agents on the morphology of surface-passivated and bulk-passivated perovskite films is schematically illustrated in **Figure 6a-f**.To further elucidate the structural properties of the bulk passivated 3D MAPI samples (without MACl), high-resolution transmission electron microscopy (HR-TEM) studies were carried out as shown in **Figure 5g, h**. The HR-TEM images from selected locations confirm the existence of different lattice spacings. The calculated *d*-spacings corresponding to these planes are summarized (**Table S3,** Supporting Information). The narrow interplanar lattice spacing of 2.87 Å corresponds to the (231) diffraction peak of the 3D MAPI phase in **Figure 5g**.

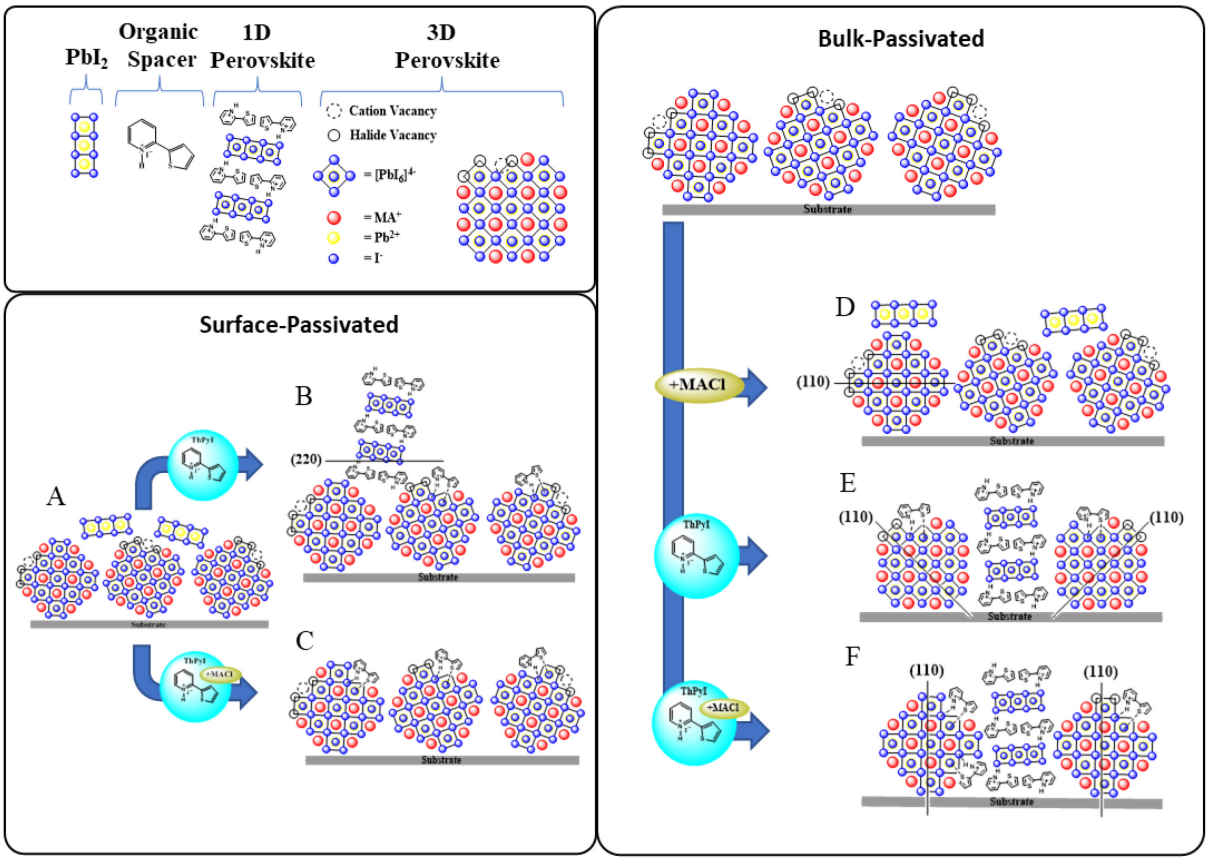

Figure 6. Schematic representation of crystal domain orientation in a) 3D MAPI control (with +5% excess PbI_2), b) ThPyI-surface-passivated 3D/1D c) ThPyI-surface-passivated 3D/1D with MACl d) 3D MAPI control with MACl e) ThPyI-bulk-passivated 3D without MACl, and f) ThPyI-bulk-passivated 3D with MACl.

On the other hand, the lattice spacings of 7.7 and 11.74 Å match the (080) and (220) planes of the 1D perovskitoid, respectively, as shown in **Figure 5g, h.** Overall, the interplanar lattice distances agree with the corresponding XRD data (**Table S4,** Supporting Information). The HR-TEM results demonstrate that the 1D perovskitoid phase distributes in the 3D perovskite phase. TEM images were also recorded from bulk-passivated 3D MAPI prepared using MACl. In this case we observed nanoscopic objects like nanorods which after recrystallization under the intensive electron beam yielded crystallites (of unknown structure) with lattice spacing equal to 7.7 Å (**Figure S10**, Supporting Information).

UV-vis absorption spectroscopy was employed to investigate the optoelectronic characteristics of the perovskite films (**Figure S11a,** Supporting Information). In comparison with the 3D MAPI control film, surface-passivated 3D/1D films (thickness of about 600 nm) show no significant changes, implying that the 1D perovskitoid on top of the 3D structure does not significantly change the absorption features of the photoactive film. However, the bulk-passivated 3D film exhibits a weaker absorption while retaining

the spectral features of MAPI. This is attributed to the different thickness of the bulk-passivated 3D film (400 nm).

In line with the similar optical absorption spectrum, the surface-passivated 3D/1D hybrid device shows an EQE response similar to the 3D MAPI control (**Figure S12a,** Supporting Information). In the case of the bulk-passivated 3D MAPI sample, the EQE is higher than that of the corresponding 3D MAPI reference with MACl (**Figure S12b,** Supporting Information). To determine the energy levels of the bulk-passivated 3D MAPI phase, ultraviolet photoelectron spectroscopy (UPS) was employed (**Figure S11b,** Supporting Information). The valence band maximum (VB) and conduction band minimum (CB) of the bulk-passivated 3D perovskite are estimated at –5.81 and –4.21 eV, respectively, which are very close to the values of 3D MAPI. These energy levels are also compatible with the hole transport layer comprising poly(3,4-ethylenedioxythiophene) poly(styrenesulfonate) (PEDOT:PSS), (–5.1 eV; VB) and the electron transport layer comprising phenyl-C_{61}-butyric acid methyl ester, $PC_{61}BM$, (–3.8 eV; VB).

Steady-state photoluminescence (SSPL) and time-resolved photoluminescence decay (TRPL) measurements were carried out to unravel the charge recombination processes in the 3D MAPI control, bulk-passivated 3D, and surface-passivated 3D/1D films as shown in **Figure 7a–d.** In the case of the bulk-passivated 3D sample, a perovskite film with MACl is considered as the control sample to specify the influence of the ThPyI passivator additive. Notably, more intense PL emission peaks are observed in the surface-passivated 3D/1D and bulk-passivated 3D perovskite films compared to the 3D control, shown in **Figure 7a, b.**

The high PL intensity is an indicator for the elimination of sub-bandgap states in perovskite films that are linked to defect states.[64] The emission peak of the surface-passivated 3D/1D perovskite is slightly blue shifted compared with the 3D control film in **Figure 7a**, which can be attributed to the 1D phase formed on top (**Figure S13**, Supporting Information). The emission peak of the bulk-passivated 3D perovskite appears at similar wavelength comparable with the 3D control with MACl as shown in **Figure 7b**. [65]

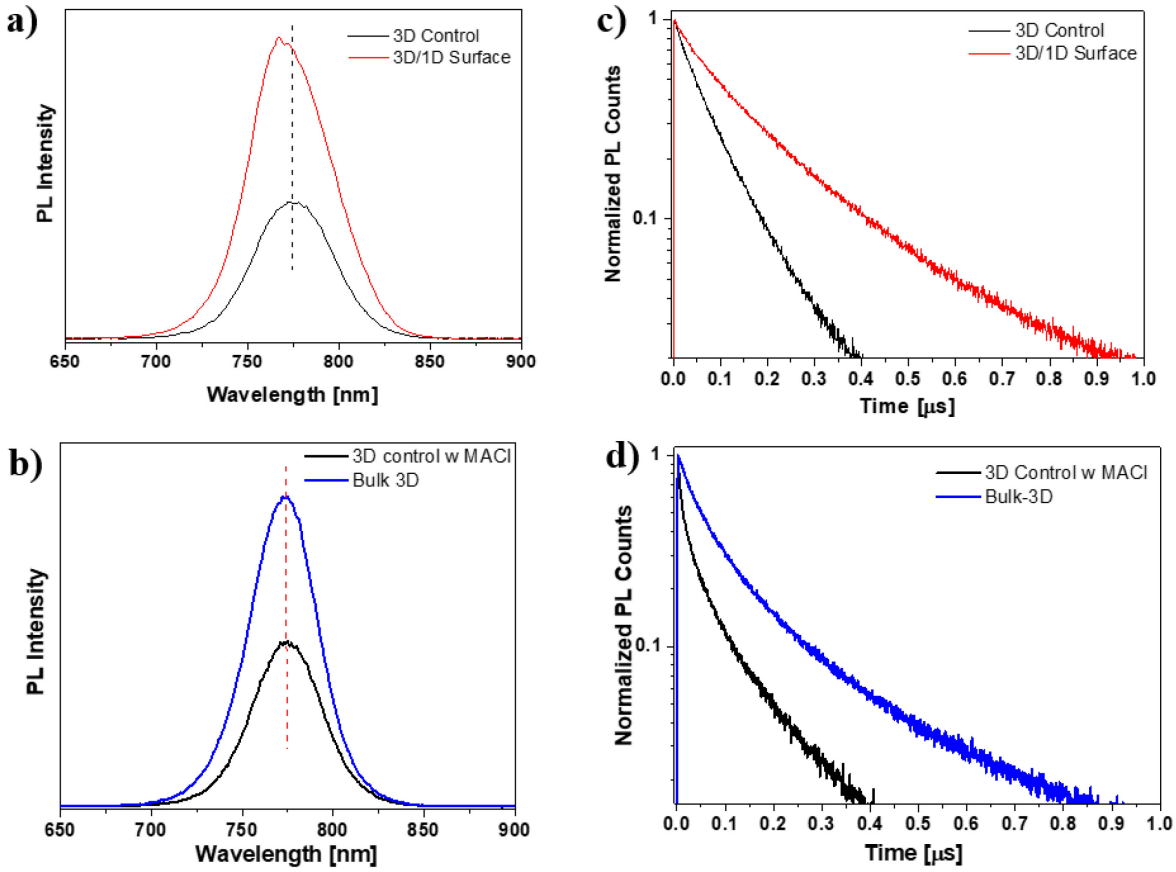

Figure 7. a, b) SSPL and TRPL spectra of 3D MAPI control and surface-passivated 3D/1D film, c, d) SSPL and TRPL spectra of 3D control with MACl and bulk-passivated 3D film.

The TRPL decay spectra of the corresponding films prepared on glass substrates are shown in **Figure 7c, d.** The TRPL curve was fitted using the following biexponential equation (1):

$$y = A_1 exp(\frac{-t}{\tau_1}) + A_2\, exp(\frac{-t}{\tau_2}) + y_0 \qquad (1)$$

where A_1 and A_2 are the amplitudes. The symbols τ_1 and τ_2 express short and long charge carrier recombination times, respectively.[66] Here, we propose that τ_1 is related to the trap-assisted nonradiative recombination arising at the grain boundaries. On the other hand, τ_2 is associated with bulk carrier recombination.[67] The resulting charge carrier lifetimes of the perovskite films are listed (**Table S5**, Supporting Information).

In the 3D control film, the τ_1 and τ_2 values are equal to 50 and 114 ns, respectively. The values τ_1 and τ_2 of both bulk-passivated 3D and surface-passivated 3D/1D films are significantly extended compared to the control sample. The low τ_1 value indicates that the trap-assisted nonradiative recombination is reduced and radiative recombination of carriers dominates the PL decay in the bulk-passivated 3D and 3D/1D phases.[68]

The trap-state density of the corresponding films was quantified by the space-charge-limited current (SCLC) method for electron/hole-only devices, using the following equation (2):

$$N_t = 2\varepsilon\varepsilon_0 V_{TFL}/qL^2 \quad (2)$$

where N_t is the trap-state density of electron or hole, ε is the relative dielectric constant of MAPI perovskite ($\varepsilon = 25$), ε_0 is vacuum permittivity (8.85×10^{-12} F m^{-1}), V_{TFL} is the trap-filled limit voltage, q is elementary charge (1.602×10^{-19} C) and L is the thickness of the perovskite film.[69] Electron-only devices were fabricated for this measurement and dark *J-V* curves were recorded (**Figure S14,** Supporting Information).

The linear region seen in the dark *J-V* curve at low bias voltage is the ohmic region. The intermediate bias region where the traps are filled with the charge carriers is known as the trap-filled region. The trap-free region is defined at the high-bias voltage. The V_{TLF} is determined as the bias voltage at the inflection point between the ohmic region and the trap-filled region. The calculated trap state density of the 3D MAPI control device is 7.58×10^{15} cm^{-3}. For the surface-passivated 3D/1D device, the trap-state density is calculated to be 6.18×10^{15} cm^{-3}. The lower trap-state density in the surface-passivated 3D/1D perovskite device confirms that the low-dimensional 1D phase has a passivation effect and reduces the traps in the corresponding devices. In the case of bulk-passivated 3D perovskite the trap-state density was found to be 1.20×10^{16} cm^{-3}, and for the 3D MAPI control with the same device architecture it was found to be equal to 1.31×10^{16} cm^{-3}. These results suggest that in the bulk-passivated 3D film the ThPyI also acts as a passivator for the trap states, albeit with more moderate effect.

To evaluate further the effect of the 1D phase on the photovoltaic performance, the normal (*n-i-p*) planar perovskite solar cells for the 3D MAPI control and the surface-passivated 3D/1D phases were fabricated as shown in **Figure 8a**. The device architecture of bulk-passivated 3D MAPI was kept inverted (*p-i-n*) because of the need for better energy alignment between the different layers given in **Figure 8b.**

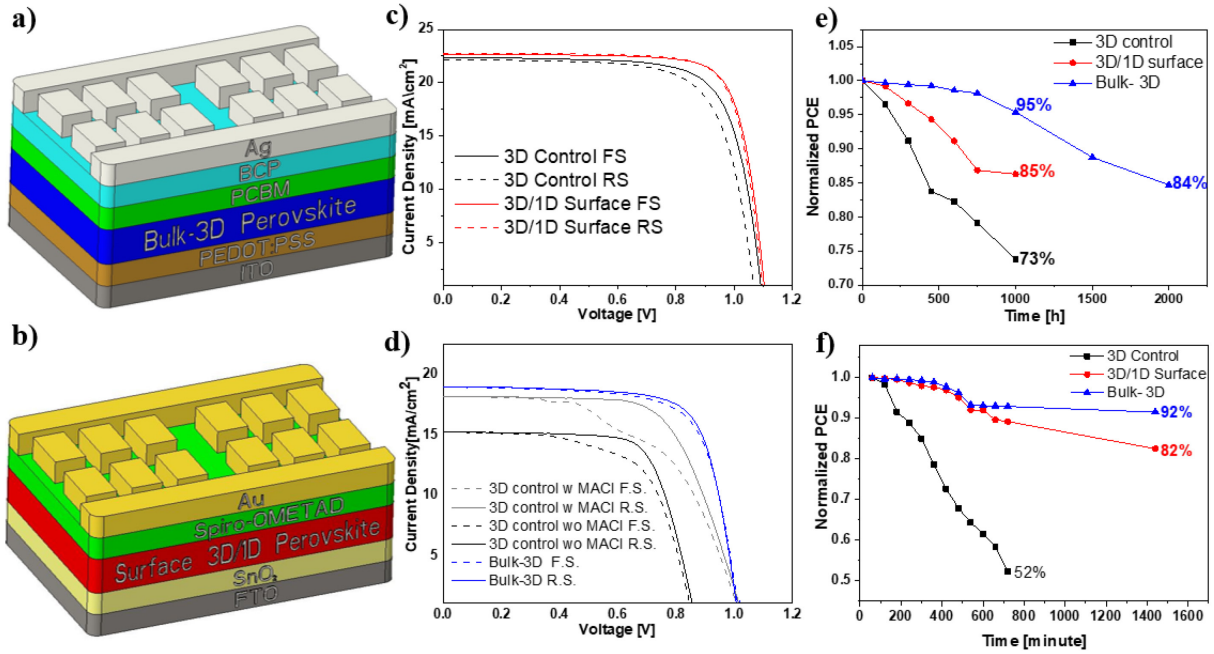

Figure 8. Device structure of a) bulk-passivated 3D and b) surface-passivated 3D/1D perovskite devices. c, d) *J-V* curves of surface-passivated 3D/1D and bulk-passivated 3D perovskite devices e) long-term stability, and f) light-thermal stability of 3D control, surface-passivated 3D/1D, and bulk-passivated 3D devices.

As noted above, to increase the preferential orientation of perovskite slabs, MACl was used as an additive which plays an important role in improving the PCE of bulk-passivated 3D MAPI. Bulk-passivated 3D devices with and without MACl were fabricated for the purpose of comparison. Devices with the MACl/MAI 0.5 weight ratio show the highest performance (**Figure S15,** Supporting Information**)**. The results of photovoltaic *J-V* characterization of the optimized devices, performed under AM 1.5G (1000 W/m^2), are presented in **Figure 8c, d** and **Table S6 (**Supporting Information). Moreover, statistical distributions of the photovoltaic parameters are given (**Figure S16,** Supporting Information). The 3D MAPI control perovskite film yielded a short-circuit current density (J_{sc}) of 22.35 mA/cm^2, an open-circuit voltage (V_{oc}) of 1.09 V, and a fill factor (*FF*) of 74%, which gives an overall PCE equal to 18.08% (for the best performing device). As seen in the forward and backward scans, the 3D control device suffers from hysteresis. On the other hand, the surface-passivated

3D/1D device exhibits a higher PCE (19.60%) with improved V_{oc} of 1.11 V, J_{sc} of 22.69 mA/cm^2, and a FF of 78%. The improved V_{oc} suggests that the low-dimensional 1D phase grown at the grain boundaries of the 3D perovskite suppresses the trap-assisted recombination that is associated with

surface defects. As for the optimized bulk-passivated 3D MAPI perovskite, the overall PCE was 14.10% with a J_{sc} of 18.98 mA/cm^2, V_{oc} of 1.02, and FF of 74% (For the best performing device). Hence, the efficiency of bulk-passivated 3D MAPI devices is lower than that of the surface-passivated 3D/1D perovskite device, presumably since it contains a high fraction of organic passivation agent (ThPyI: PbI_2; 2:3 mole ratio). We note that this is one of the first studies where 3D MAPI perovskite is prepared with a high volume fraction of organic agents in bulk-passivated perovskite solar cells.

The stability of the unencapsulated devices was studied under ambient conditions in air (room temperature, relative humidity 40-45%) as shown in **Figure 8c.** The surface-passivated 3D/1D perovskite device retained 86% of its PCE after a 1000 h stability test (under dark) whereas the PCE of the 3D control device dropped to 74% of its original PCE. On the other hand, the bulk-passivated 3D perovskite device showed the best environmental stability among these devices, keeping 95.3% of its initial PCE after 1000 h, and 84% after 2000 h under N_2 atmosphere (dark). Furthermore, a combined light-thermal stability test of the corresponding devices was conducted under one sun at 60 °C for 24 h under N_2 atmosphere. The bulk-passivated 3D device also showed the highest light-thermal stability by retaining 92% of its initial efficiency under continuous light soaking after 24 h as shown in **Figure 8d**. In comparison, the initial PCE of surface-passivated 3D/1D and 3D MAPI control devices decreased to 82% and 52%, respectively. The improved stability of the surface-passivated 3D/1D device is attributed to the presence of the low-dimensional 1D phase, which is proposed to inhibit ion migration, moisture penetration, to improve film quality, and to reduce defects in the perovskite film. On the other hand, the high-volume fraction of hydrophobic ThPyI spacer used in the bulk-passivated 3D MAPI film should efficiently prevent moisture penetration, which apparently explains the higher stability. Remarkably, and in line with this assessment, the bulk-passivated 3D MAPI film retained its structure in air for four months after which time only a very weak diffraction peak of PbI_2 emerged (**Figure S17,** Supporting Information).

To find out the impact of the ThPyI-based low-dimensional new phase treatment on the hydrophobicity, the water contact angles of 3D $MAPbI_3$ control, 1D perovskitoid, surface-passivated 3D/1D, and bulk-passivated 3D perovskite films were measured. (**Figure S18,** Supporting Information). The pure 1D perovskitoid shows the highest water contact angle of around 73° compared to the others. As compared to the 3D $MAPbI_3$ control with an angle of 60°, the surface- and bulk-treated forms of the 3D perovskite films exhibit increased water contact angles of around 67° and 69°, respectively. The greater water contact angles of the 1D and treated 3D perovskite films compared to the 3D $MAPbI_3$ control reveal the enhanced hydrophobicity of the treated forms of the 3D perovskite.

The same films that were evaluated in the water contact angle measurements were immersed in water to further solidify their behavior in water. As expected, 3D control $MAPbI_3$ and its surface- and bulk-

treated 3D films were decomposed into PbI_2 in a few seconds, which shows it with the characteristic yellow color of PbI_2. Interestingly, in the 1D film, no changes related to the color was observed. After removing the samples from the water and drying the corresponding films, XRD measurements were carried out to understand their behavior in water (**Figure S19,** Supporting Information). In comparison with the 3D control film and its treated forms, which show complete decomposition into PbI_2, the ThPyI-based low-dimensional pure new phase shows no decomposition. These water contact angle measurements and XRD diffractions of the water-immersed films show the water stability of the 1D phase compared with its 3D counterparts.

4.3 Conclusions

In summary, a novel thiophene based ThPyI organic spacer with heterocyclic structure was developed and used both as a defect passivator and as an organic spacer in surface- and bulk-passivated 3D MAPI-based perovskite devices. Our results demonstrate that the ThPyI organic spacer is a suitable candidate for creating 1D perovskitoids in perovskite-based photovoltaic devices. TRPL results showed that the fluorescence lifetimes in both passivated devices become longer and contribute to the better performance. Moreover, the ThPyI based perovskite devices offered high efficiency and environmental stability compared to their 3D counterparts. The bulk-passivated 3D PV devices showed significantly higher environmental as well as light-thermal stability even compared to the surface-passivated devices. Importantly, this novel organic agent promoted the preferential orientation of the 3D perovskite slabs crystalline orientation (vertical orientation of the (110) planes with respect to the substrate) in the films much more efficiently than the MACl additive. This study enriches the literature on thiophane-based organic spacers and presents a different perspective on organic spacer design. We envision that the above results can help to bring on a rational strategy for the design of organic agents that play a multiple role as defect passivator, crystalline orientation promoter and organic spacer for various perovskite-based solar cells.

4.4 References

[1] Q. Jiang, Y. Zhao, X. Zhang, X. Yang, Y. Chen, Z. Chu, Q. Ye, X. Li, Z. Yin, J. You, *Nat. Photonics* **2019**, *13*, 460.

[2] N. Torabi, A. Behjat, Y. Zhou, P. Docampo, R. J. Stoddard, H. Hillhouse, **T. Ameri**, *Mater. Today Energy*, **2019**, *12*, 70

[3] W. Zhang, G. E. Eperon, H. J. Snaith, *Nat. Energy* **2016**, *1*, 1.

[4] G. Xing, N. Mathews, S. Sun, S. S. Lim, Y. M. Lam, M. Graẗzel, S. Mhaisalkar, T. C. Sum, *Science* **2013**, *342*, 344.

[5] H. S. Kim, C. R. Lee, J. H. Im, K. B. Lee, T. Moehl, A. Marchioro, S. J. Moon, R. Humphry-Baker, J. H. Yum, J. E. Moser, M. Grätzel, N. G. Park, *Sci. Rep.* **2012**, *2*, 1.

[6] N. G. Park, M. Grätzel, T. Miyasaka, K. Zhu, K. Emery, *Nat. Energy* **2016**, *1*, 1.

[7] X. Li, D. Bi, C. Yi, J. D. Décoppet, J. Luo, S. M. Zakeeruddin, A. Hagfeldt, M. Grätzel, *Science* **2016**, *353*, 58.

[8] S. de Wolf, J. Holovsky, S. J. Moon, P. Löper, B. Niesen, M. Ledinsky, F. J. Haug, J. H. Yum, C. Ballif, *J.Phys. Chem. Lett.* **2014**, *5*, 1035.

[9] C. C. Stoumpos, C.D. Malliakas, M.G. Kanatzidis, *Inorg. Chem*. **2013**,*52*, 9019.

[10] X. Li, M.I. Dar, C. Yi, J. Luo, M. Tschumi, S. M. Zakeeruddin, M. K. Nazeeruddin, H. Han, M. Grätzel, *Nat. Chem.* **2015**, *7*, 703.

[11] E. Khorshidi, B. Rezaei, D. Blätte, A. Buyruk, M. A. Reus, J. Hanisch, B. Böller, P. Müller-Buschbaum, **T. Ameri**, *Sol. RRL*, **2022**, *6*, 2200023

[12] E. Khorshidi, B. Rezaei, J. Hanisch, B. Böller, M. A. Reus, P. Müller-Buschbaumde, **T. Ameri,** *ACS Appl. Mater. Interfaces,* **2022,** *14*, 54623

[13] L. Wang, H. Zhou, J. Hu, B. Huang, M. Sun, B. Dong, G. Zheng, Y. Huang, Y. Chen, L. Li, Z. Xu, N. Li, Z. Liu, Q. Chen, L. D. Sun, C. H. Yan, *Science* **2019**, *363*, 265.

[14] C. Ortiz-Cervantes, P. Carmona-Monroy, D. Solis-Ibarra, *ChemSusChem*, **2019**,*12*, 1560.

[15] C. Li, S. Tscheuschner, F. Paulus, P. E. Hopkinson, J. Kießling, A. Köhler, Y. Vaynzof, S. Huettner, *Adv. Mater*. **2016**, *28*, 2446.

[16] C. Eames, J. M. Frost, P. R. F. Barnes, B. C. O'regan, A. Walsch, M. F. Islam, *Nat. Commun.*, **2015**, *6*, 7497

[17] M. I. Saidaminov, J. Kim, A. Jain, R. Quintero-Bermudez, H. Tan, G. Long, F. Tan, A. Johnston, Y. Zhao, O. Voznyy, E. H. Sargent, *Nat. Energy,* **2018***, 3,* 648

[18] A. S. R. Bati, M. Batmunkh, J. G. Shapter, *Adv. Energy Mater.* **2020**, *10*, 1902253.

[19] H. Zhang, Y. Wu, C. Shen, Er. Li, C. Y, W. Zhang, H. Tian, L. Han, W. Zhu, *Adv. Energy Mater.* **2019**, *9,* 1803573.

[20] E. H. Jung, N. J. Jeon, E. Y. Park, C. S. Moon, T. J. Shin, T. Y. Yang, J.H. Noh, J. Seo, *Nature* **2019**, *567*, 511.

[21] E. Aydin, M. de Bastiani, S. de Wolf, *Adv. Mater.* **2019**, *31*, 1900428.

[22] F. Gao, Y. Zhao, X. Zhang, J. You, *Adv.Energy Mater.* **2020**, *10*, 1902650.

[23] Y. Huang, H. Luo, B. Zhang, K. Su, W. Chen, G. Sui, L. Liang, B. Zhang, J. Song, P. Gao, *Appl. Mater.Today*. **2022**,*28*, 101550.

[24] A. Krishna, S. Gottis, M. K. Nazeeruddin, F. Sauvage, *Adv. Funct. Mater.* **2019**, *29*, 1806482.

[25] L. Mao, C. C. Stoumpos, M. G. Kanatzidis, *J. Am. Chem. Soc.* **2018**, *141*, 1171.

[26] H. Tsai, W. Nie, J. C. Blancon, C. C. Stoumpos, R. Asadpour, B. Harutyunyan, A. J. Neukirch, R. Verduzco, J. J. Crochet, S. Tretiak, L. Pedesseau, J. Even, M. A. Alam, G. Gupta, J. Lou, P. M. Ajayan, M. J. Bedzyk, M. G. Kanatzidis, A. D. Mohite, *Nature* **2016**, *536*, 312.

[27] J. Qian, Q. Guo, L. Liu, B. Xu, W. Tian, *J. Mater. Chem. A* **2017**, *5*, 16786.

[28] W. Fu, J. Wang, L. Zuo, K. Gao, F. Liu, D. S. Ginger, A. K. Y. Jen, *ACS Energy Lett.* **2018**, *3*, 2086.

[29] Y. Chen, Y. Sun, J. Peng, J. Tang, K. Zheng, Z. Liang, *Adv. Mater.* **2018**, *30*, 170348.

[30] J. Fan, Y. Ma, C. Zhang, C. Liu, W. Li, R. E. Schropp, Y. Mai, *Adv. Energy Mater.* **2018,** *8*, 1703421.

[31] P. Chen, Y. Bai, S. Wang, M. Lyu, J. Yun, L. Wang, *Adv. Funct. Mater.* **2018**, *28*, 1706923.

[32] C. C. Stoumpos, L. Mao, C. D. Malliakas, M. G. Kanatzidis, *Inorg. Chem.* **2017**, *56*, 56.

[33] D. Bi, P. Gao, R. Scopelliti, E. Oveisi, J. Luo, M. Grätzel, A. Hagfeldt, M. K. Nazeeruddin, *Adv. Mater.* **2016**, *28*, 2910.

[34] N. Yang, C. Zhu, Y. Chen, H. Zai, C. Wang, X. Wang, H. Wang, S. Ma, Z. Gao, X. Wang, J. Hong, Y. Bai, H. Zhou, B.B. Cui, Q. Chen, *Energy Environ. Sci.* **2020**, *13*, 4344.

[35] H. Lin, C. Zhou, Y. Tian, T. Siegrist, B. Ma, *ACS Energy Lett.* **2018**, *3*, 54.

[36] C. Zhou, Y. Tian, M.Wang, A. Rose, T.Besara, N. K. Doyle, Z. Yuan, J. C. Wang, R. Clark, Y. Hu, T. Siegrist, S. Lin, B. Ma, *Angew. Chem., Int. Ed.* **2017**, *56*, 9018.

[37] T. Kong, H. Xie, Y. Zhang, J. Song , Y. Li, L. Lim, A. Hagfeld, D. Bi, *Adv.Energy Mater.* **2021**, *11*, 2101018.

[38] J. Im, C. C. Stoumpos, H. Jin, A. J. Freeman, M. G. Kanatzidis, *J. Phys. Chem. Lett.* **2015**, *6*, 3503.

[39] L. Gao, I. Spanopoulos, W. Ke, S. Huang, I. Hadar, L. Chen, X. Li, G. Yang, M.G. Kanatzidis, *ACS Energy Lett.* **2019,** *4*, 1763.

[40] P. Liu, Y. Xian, W. Yuan, Y. Long, K. Liu, N. U. Rahman, W. Li, J. Fan, *Adv. Energy Mater.* **2020**, *10*, 1903654.

[41] M. Pratheek, T. Abhinav, S. Bhattacharya, G. K. Chandra, P. Predeep, *Mater Sci.Technol.* **2021**, *4*, 282.

[42] S. Gharibzadeh, P. Fassl, I. M. Hossain, P. Rohrbeck, M. Frericks, M. Schmidt, T. Duong, M. R. Khan, T. Abzieher, B. A .Nejand, F. Schackmar, O. Almora, T. Feeney, R. Singh, D. Fuchs, U. Lemmer, J. P. Hofmann, S. A. L. Weber, U. W. Paetzold, *Energy Environ.Sci*. **2021**, *14*, 5875.

[43] G. Kim, H. Min, K. S. Lee, D. Y. Lee, S. M. Yoon, S.I. Seok, *Science* **2020**, *370*, 108.

[44] M. Jeong, I. W. Choi, E. M. Go, Y. Cho, M. Kim, B. Lee, S. Jeong, Y. Jo, H. W. Choi, J. Lee, J. H. Bae, S. K. Kwak, D. S. Kim, C. Yang, *Science* **2020**, *369*, 1615.

[45] C. Zhang, S. Wu, L. Tao, G. M. Arumugam, C. Liu, Z. Wang, S. Zhu, Y. Yang, J. Lin, X. Liu, R. E. I. Schropp, Y. Mai, *Adv. Energy Mater.* **2020**, *10*, 2002004.

[46] Z. Liu, F. Cao, M. Wang, M. Wang, L. Li, *Angew. Chem., Int. Ed.* **2020**, *59*, 4161.

[47] C. Ma, N. G. Park, *ACS Energy Lett.* **2020**, *5*, 3268.

[48] F. Li, X. Deng, F. Qi, Z. Li, D. Liu, D. Shen, M. Qin, S. Wu, F. Lin, S. H. Jang, J. Zhang, X. Lu, D. Lei, C. S. Lee, Z. Zhu, A. K. Y. Jen, *J. Am. Chem. Soc.* **2020**, *142*, 20134.

[49] L. Liu, S. Huang, Y. Lu, P. Liu, Y. Zhao, C. Shi, S. Zhang, J. Wu, H. Zhong, M. Sui, H. Zhou, H. Jin, Y. Li, Q. Chen, *Adv. Mater.* **2018**, *30*, 1800544.

[50] J. Peng, D. Walter, Y. Ren, M. Tebyetekerwa, Y. Wu, T. Duong, Q. Lin, J. Li, T. Lu, M. A. Mahmud, O. L. C. Lem, S. Zhao, W. Liu, Y. Liu, H. Shen, L. Li, F. Kremer, H. T. Nguyen, D. Y. Choi, K. J. Weber, K. R. Catchpole, T. P. White, *Science* **2021**, *371*, 390.

[51] X. Lin, D. Cui, X. Luo, C. Zhang, Q. Han, Y. Wang, L. Han, *Energy Environ. Sci.* **2020**, *13*, 3823.

[52] Y. Kuang, K. H. M. van der Werf, Z. S. Houweling, R. E. I. Schropp, *Appl. Phys. Lett.* **2011**, *98*, 113111.

[53] B. M. Kayes, H. A. Atwater, N. S. Lewis, *J. Appl. Phys.* **2005**, *97*, 114302.

[54] T. M. Koh, V. Shanmugam, J. Schlipf, L. Oesinghaus, P. Müller-Buschbaum, N. Ramakrishnan, V. Swamy, N. Mathews, P. P. Boix, S. G. Mhaisalkar, *Adv. Mater.* **2016**, *28*, 3653.

[55] C. Fei, L. Guo, B. Li, R. Zhang, H. Fu, J. Tian, G. Cao, *Nano Energy*. **2016** *27*, 17.

[56] A. Buyruk, D. Blätte, M. Günther, M. A. Scheel, N. F. Hartmann, M. Döblinger, A. Weis, A. Hartschuh, P. Müller-Buschbaum, T. Bein, T. Ameri, *ACS Appl. Mater. Interfaces* **2021**, *13*, 32894.

[57] H. Gökce, S. Bahceli , *Spectrochim. Acta A Mol. Biomol. Spectrosc.* **2012,** *96*, 139.

[58] R. Szostak, J. C. Silva, S. H. Turren-Cruz, M. M. Soares, R. O. Freitas, A. Hagfeldt, H. C. N. Tolentino, A. F. Nogueira, *Sci. Adv.* **2019**, *5*, eaaw6619.

[59] M. A. Pérez-Osorio, Q. Lin, R. T. Phillips, R. L. Milot, L. M. Herz, M. B. Johnston, F. Giustino, *J. Phys. Chem. C* **2018** *122*, 21703.

[60] H. Gökce, S. Bahceli, *J. Mol. Struct.* **2011**, *1005*, 100.

[61] W. S. Yang, B. W. Park, E. H. Jung, N. J. Jeon, Y. C. Kim, D. U. Lee, S. S. Shin, J. Seo, E. K. Kim, J. H. Noh, S. il Seok, *Science* **2017**, *356*, 1376.

[62] M. H. Li, H. H. Yeh, Y. H. Chiang, U. S. Jeng, C. J. Su, H. W. Shiu, Y. J. Hsu, N. Kosugi, T. Ohigashi, Y. A. Chen, P. S. Shen, P. Chen, T. F. Guo, *Adv- Mater.* **2018**, *30*, 1801401.

[63] D. H. Cao, C. C. Stoumpos, O. K. Farha, J. T. Hupp, M. G. Kanatzidis, *J. Am. Chem. Soc.* **2015**, *137*, 7843.

[64] M. Yavari, F. Ebadi,S. Meloni , Z. S. Wang , T. C. J. Yang, S. Sun, H. Schwartz, Z. Wang, B. Niesen , J. Durantini, P. Rieder, K. Tvingstedt, T. Buonassisi, W. C. H. Choy, A. Filippetti, T. Dittrich, S. Olthof, J. P.

[65] W. Wang, M. Cai, Y. Wu, K. Ji, B. Cheng, X. Liu, H. Lv, S. Dai, *Symmetry* **2022**, *14*, 1099.

[66] T. J. Jacobsson, J. P. Correa-Baena, E. Halvani Anaraki, B. Philippe, S. D. Stranks, M. E. F. Bouduban, W. Tress, K. Schenk, J. Teuscher, J. E. Moser, H. Rensmo, A. Hagfeldt, *J. Am. Chem. Soc.* **2016**, *138*, 10331.

[67] B. Wu, H. T. Nguyen, Z. Ku, G. Han, D. Giovanni, N. Mathews, H. J. Fan, T. C. Sum, *Adv. Energy Mater.* **2016**, *6*, 1600551.

[68] P. Chen, Y. Bai, S. Wang, M. Lyu, J. H. Yun, L. Wang, *Adv. Funct. Mater*. **2018**, *28*, 1706923.

[69] R. H. Bube, *J.Appl. Phys.* **2004**, *33*, 173.

4.5 Experimental Section

1. Materials and reagents

The SnO_2 colloid precursor was purchased from Alfa Aesar (tin (IV) oxide, 15% in H_2O colloidal dispersion). Before spin-coating as an ETL, the SnO_2 nanoparticles were diluted with DI water to 2.67 wt.%. The organic spacer precursor 2-(2-thienyl) pyridine (unprotonated form), as well as PbI_2 and MAI were purchased from TCI. MACl, BCP, solvents (DMSO, DMF, etc.) and freshly delivered hydroiodic acid (HI ~57 wt.%) were purchased from Sigma-Aldrich. The Spiro-OMeTAD used as an HTL material was purchased from Borun Chem. The PEDOT:PSS aqueous solution and $PC_{61}BM$ were purchased from Ossila.

2. Solar cell fabrication:

2a. Fabrication of bulk-passivated 3D MAPI solar cell

ITO substrates (3 cm x 3 cm) were first etched using 3 M HCl and Zn powder and later rinsed with deionized water. This was followed by sonication of the substrates in 2% *detergent (*Hellmanex™ III) aqueous *solution*, DI water, ethanol, and isopropanol for 15 min each, respectively. Afterwards the substrates were dried in nitrogen flow and treated with nitrogen plasma for 15 min. PEDOT: PSS was spin-coated onto pre-cleaned ITO substrates at 2500 rpm for 40 s and annealed at 140 ℃ for 20 min in air. After this process, the substrates were transferred into a glovebox for device fabrication.

Bulk-passivated 3D perovskite precursor solution was prepared from the stoichiometric ratio of PbI_2, MAI and ThPyI at molar ratio 3:2:2, respectively, in a 1 ml DMF: DMSO (8:1 volume ratio) mixture. For the devices where MACl was used as an additive for preferential crystal orientation, the amount of MACl was adjusted to MACl/MAI 0.5 wt.%. The prepared solution was stirred for 12 h at 70 ℃ . The prepared bulk-passivated 3D perovskite solution was spin coated onto ITO/PEDOT:PSS substrate at 6000 rpm for 40 s. Toluene (350 µl) was dropped onto the perovskite film during the last 15 s of the spin-coating process, followed by heat treatment at 100 ℃ for 15 min. $PC_{61}BM$ (20 mg/mL in CB) and BCP (0.6 mg/mL in IPA) were spin-coated subsequently onto the perovskite active layer at 1000 rpm for 30 s, respectively. In the last step, a 100 nm thick silver electrode was thermally evaporated under vacuum ($1x10^{-6}$ Pa). The active area was fixed to 0.0831 cm^2 using a metal mask. 3D MAPI control devices with and without MACl were fabricated using similar steps as given above but without using ThPyI in the precursor solutions.

2b. Solar cell fabrication with surface-passivated 3D/1D perovskite

FTO substrates (3 cm x 3 cm) were first etched using 3 M HCl and Zn powder and later rinsed with deionized water. This was followed by sonication of the substrates in 2% *detergent (*Hellmanex™ III) solution, DI water, ethanol, and isopropanol for 15 min each, respectively. Afterwards the substrates were dried in nitrogen flow and treated with nitrogen plasma for 15 min. A diluted SnO_2 nanoparticle solution (2.67 wt% in water) was spin-coated onto the FTO substrate in air at 4000 r.p.m. for 35 s, and then annealed in air at 150 ºC for 30 min. Before the perovskite coating, the SnO_2 coated substrates were cleaned once again using the UV-O_3 environment for 10 min. Using the one-step "anti-solvent" method, the precursors of the perovskite – PbI_2 (1.68 M, 5% excess), MAI (1.60 M), and DMSO (1.60 M) in 1 mL DMF were deposited on top of the SnO_2 layer at 1000 rpm for 10 s, followed by fast spinning at 3500 rpm for 20 s. Ethyl acetate as an anti-solvent was dropped onto the perovskite film during the last 10 s while spinning. The sample was then annealed at 130 ºC for 10 min. For the surface treatment, the 2-(thiophen-2-yl) pyridin-1-ium iodide salt in isopropanol solution (3.9 mg/ml) was spin-coated onto the perovskite films at 1000 r.p.m for 30 s followed by 5000 r.p.m for 5 s. This was followed by heat treatment of the latter substrate at 100 ºC for 10 min. The hole transport material (HTM) was deposited by spin-coating (3000 rpm for 30 s) a solution containing 72.3 mg spiro-OMeTAD, 35 µl bis(trifluoromethane) sulfonimide lithium salt (LiTFSI) stock solution (270 mg LiTFSI in 1 ml acetonitrile), 30 µl 4-*tert*-butylpyridine and 1 ml chlorobenzene. Finally, a 70 nm thin film of Au was thermally evaporated under high vacuum on top of the HTM layer.

3. General characterization techniques:

UV–vis absorption (UV-vis)*:* were recorded using a Perkin Elmer Lambda 1050 spectrometer with an integrating sphere. Time-resolved photoluminescence

Photoluminescence (PL): spectroscopy was performed with a Picoquant Fluotime 300 spectrofluorometer using an excitation wavelength of 375 nm. Current-voltage (*J-V*) characteristics were measured under ambient conditions using a Newport OrielSol 2A solar simulator (AM 1.5G - 100 mW cm^{-2}) and a Keithley 2400 source meter.

The solar simulator: was calibrated with a Fraunhofer ISE certified silicon cell (KG5-filtered). The active area of the solar cells was defined by a square metal aperture mask with an area equal to 0.0831 cm^2. *J-V* curves were recorded by scanning the input bias from -0.1 V to 1.2 V (forward scan) at a scan rate of 0.1 V/s after the devices had been at 1.2 V for 5 s under illumination. For the light intensity-dependent *J-V*-measurements, a white light LED was used as a light source. The LED intensity was adjusted with a Keithley 2200-20-5 Power Supply. A highly linear photodiode was used to control the

light intensity over a range of 0.1 – 1.2 suns. *J-V*-curves were measured with a Keithley 2401 source meter.

External Quantum Efficiency (EQE): To obtain the EQE spectra, the PV cells were illuminated with a chopped light (tungsten lamp) and the beam was passed through a monochromator. Further, the light beam was split to illuminate the sample as well as a reference silicon photodetector (Hamamatsu S2281-01) at the same time. The resulting wavelength-dependent current response of both devices was recorded simultaneously by two lock-in amplifiers (Signal Recovery 7265, Stanford Research Systems 830) at a chopping frequency of 14 Hz. The incident illumination power, determined via the reference photodetector, was used to calculate the EQE response of the perovskite solar cell.

X-Ray Diffraction (XRD): (XRD) measurements were performed with a Bruker D8 Discover X-ray diffractometer operating at 40 kV and 30 mA. The diffracted X-ray beam was passed through a Ni filter. The Cu Kα1 radiation (λ = 1.5406 Å) and a position-sensitive LynxEye detector were used.

Powder X-Ray Diffraction (P-XRD): P-XRD measurements were carried out on a STOE STADI P diffractometer in Debye–Scherrer geometry, operating at 40 kV and 40 mA, using monochromated (Ge(111) single crystal monochromator) Cu-$K_{\alpha 1}$ radiation (λ = 1.5406 Å) and a DECTRIS MYTHEN 1K detector.

Grazing-incidence wide-angle X-ray scattering (GIWAXS): GIWAXS data measurements were performed on an Anton-Paar Saxspoint 2.0 with a Primux 100 microfocus source with Cu-$K_{\alpha 1}$ radiation (λ = 1.5406 Å) and a Dectris Eiger R 1M 2D Detector.

Scanning Electron Microscopy (SEM): For SEM, an FEI Helios Nanolab G3 UC DualBeam scanning electron microscope (SEM) equipped with an Oxford Aztec Advanced X-Max 80 EDX detector was used. SEM images were recorded at an acceleration voltage of 2 kV. Top view images were recorded using both a backscattered electron detector and a secondary electron through-the-lens detector.

***HR-TEM studies*:** Transmission electron microscopy (TEM) studies were carried out with a JEOL 2100F instrument operating at 200 kV. MAPI perovskite thin films (without MACI) were used as source material. Sample preparations were achieved by removing perovskite from the substrate and transferring it on the surface of a lacey coated copper TEM grid.

***Single-Crystal X-Ray Diffraction (SC-XRD)*:** The frames were integrated with the Bruker SAINT software package.[1] Data were corrected for absorption effects using the Multi-Scan method (SADABS).[2]. The structure was solved and refined using the Bruker SHELXTL Software Package.[3]

All hydrogen atoms have been calculated in ideal geometry riding on their parent atoms. The structure has been refined as a 2-component inversion twin. The domain volume ratio refined to 0.87/0.13. The disorder of the organic cation has been described by a split model. The ratio of site occupation factors of the two disordered parts refined to 0.58/0.42. All atoms of the organic cation have been refined isotropically. Atoms of the main part have been used as geometrical model for the minor part (SAME instruction in SHELX). The SIMU restraint has been applied for disordered atoms with a distance of 0.8 A or closer. The figures have been drawn at the 25% ellipsoid probability level.[4] In the case of disorder the less-occupied parts have been neglected for the figures.

Crystallographic data have been deposited with the Cambridge Crystallographic Data Centre, CCDC, 12 Union Road, Cambridge CB21EZ, UK. Copies of the data can be obtained free of charge on quoting the depository numbers CCDC-2237540 (https://www.ccdc.cam.ac.uk/structures/).

Nano-FTIR: For nano-FTIR measurements, a commercially available near-field microscope (neaSNOM, Neaspec) was used. For this technique, based on scattering-type scanning optical near-field microscopy (s-SNOM), a sharp, metal-coated AFM tip was illuminated by a broadband IR source. The light backscattered from the oscillating metallic tip was analyzed with an asymmetric Fourier transform spectrometer, which was based on a Michelson interferometer.[4] This allowed for the simultaneous recording of optical amplitude and phase of the backscattered light. To suppress the background light the tip was oscillated harmonically with a small tapping amplitude A and frequency Ω (here A = 65 nm, Ω = 247 kHz) and the detector signal was demodulated at higher harmonics $n\Omega$ of this frequency. For $n \geq 2$ the background is completely suppressed, delivering local near-field amplitude and phase spectra. To eliminate the microscope response function, the spectra were normalized to the spectra obtained from a spectrally flat reference (Si substrate). This resulted in local reflectivity and absorption spectra of the investigated materials. The latter was used for chemical identification according to standard FTIR databases.[5]

To record the nano-FTIR data, silicon wafer (2.5 cm X 2.5 cm) substrates were used. The substrates were sonicated in 2% *detergent* solution, DI water, ethanol, and isopropanol for 15 min each, respectively. Subsequently, dried substrates were further cleaned via ultraviolet ozone treatment for 15 min before the perovskite coating. The architecture of the thin film follows the order: silicon wafer/$MAPbI_3$/ w/-, w/o the 2-(thiophen-2-yl)pyridin-1-ium iodide salt. Neat perovskite and surface treated perovskite films were fabricated using the same method employed for solar cell fabrication.

Space-Charge Limited Current (SCLC): To evaluate the surface passivation effects on trap-density via the space-charge limited current (SCLC) method, electron-only devices were prepared with the device configuration of ITO/SnO_2/$MAPbI_3$ w or wo ThPyI /PCBM/Au. For bulk-passivated 3D MAPI, the electron-only device configuration is ITO/SnO_2/ Perovskite with MACl w or wo ThPyI /PCBM/BCP/Ag.

Ultraviolet Photoelectron Spectroscopy (UPS). Photoelectron spectroscopy was performed with a PHI 5000 VersaProbe at the Clustertool at InnovationLab GmbH in Heidelberg. The samples were introduced from the glovebox with exposures to air <1 min. UPS was carried out with a He-discharge lamp using the He-I emission with an energy of 21.22 eV. Pass energies of 2.95, and 0.59 eV were used for UPS valence band and UPS secondary electron cut-offs, respectively. For the measurements of the secondary electron cut-off, a bias of −5 V was applied. The take-off angle for all measurements was 90°. The Fermi level of clean silver (Ar sputtered) was used to calibrate the UPS data.

4. Syntheses:

4a. Synthesis of 2-(thiophen-2-yl)pyridin-1-ium iodide salt

The organic spacer precursor (2g, 12.16 mmol) – 2-(2-thienyl)pyridine (unprotonated form) – was dissolved in 20 ml IPA. After cooling down to 0 °C in an ice bath, subsequently hydriodic acid ~57 wt.% (1.93 ml, 14.59 mmol) was dropped into the solution. After stirring at 0 °C for 2 h, a yellowish precipitate was observed and then collected by filtration. Collected solids were washed with diethyl ether for three times, dried under vacuum at 50 °C for 24 h to afford the yellowish solid product (3.24 g 92 % yield). ^{1}H NMR (400 MHz, DMSO-d_6) δ 8.62 (ddd, J = 5.3, 1.7, 1.0 Hz, 1H), 8.14 – 8.03 (m, 2H), 7.92 (dd, J = 3.7, 1.2 Hz, 1H), 7.80 (dd, J = 5.0, 1.2 Hz, 1H), 7.50 (ddd, J = 6.9, 5.2, 1.7 Hz, 1H), 7.24 (dd, J = 5.0, 3.7 Hz, 1H), 7.13 (s, 1H). ^{13}C NMR (101 MHz, DMSO) δ 149.47, 146.65, 140.68, 140.29, 130.38, 128.85, 127.59, 123.21, 120.79. HRMS (ESI, m/z): calculated for $C_9H_8NS^+$ 162.04; found 162.03733 $[M+H]^+$.

4b. Synthesis of single crystals

PbI_2 (0.3 M) and 2-(2-thienyl)pyridine, unprotonated form) (0.3 M) were mixed in a round bottom flask in fresh hydriodic acid ~57 wt.% (20 mL) and stirred at room temperature for 10 minutes. Subsequently, the resulting mixture was heated up to 140 °C and stirred at this temperature for 1 h. After stirring for 1 h, the transparent yellow solution was slowly cooled down to room temperature. During the cooling, at about 110 °C, yellow needle-shape crystals were observed in the solution. The needle-shaped crystals were collected by filtration to remove unreacted PbI_2, which is soluble in the reaction mixture, and subsequently washed several times with diethyl ether. Finally, they were dried at 60 °C in air for 24 h.

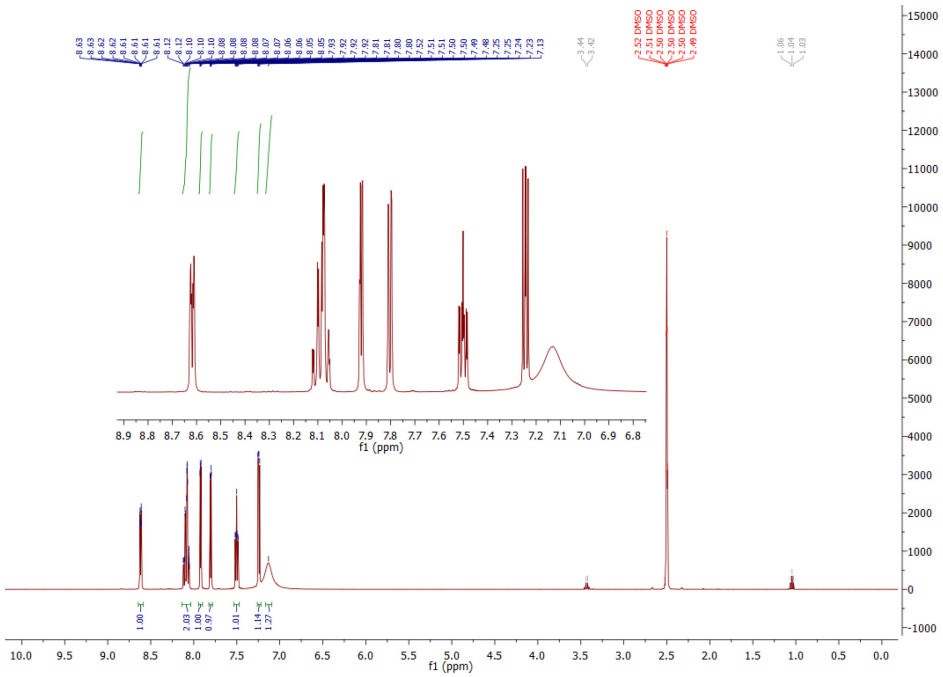

Figure S1a. ^{1}H-NMR spectra of ThPyI organic spacer

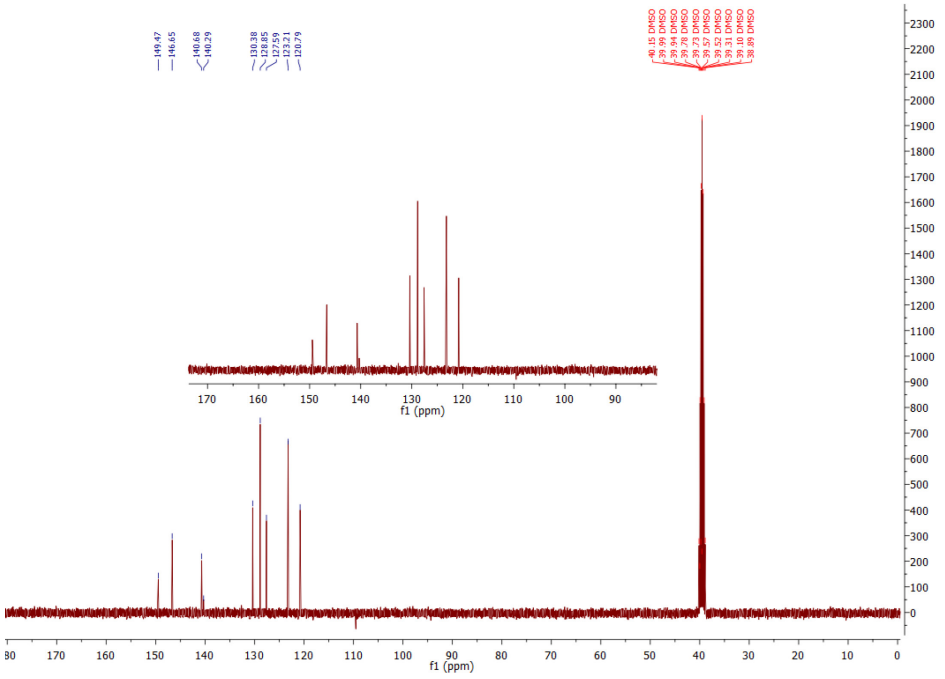

Figure S1b. ^{13}C-NMR spectra of ThPyI organic spacer

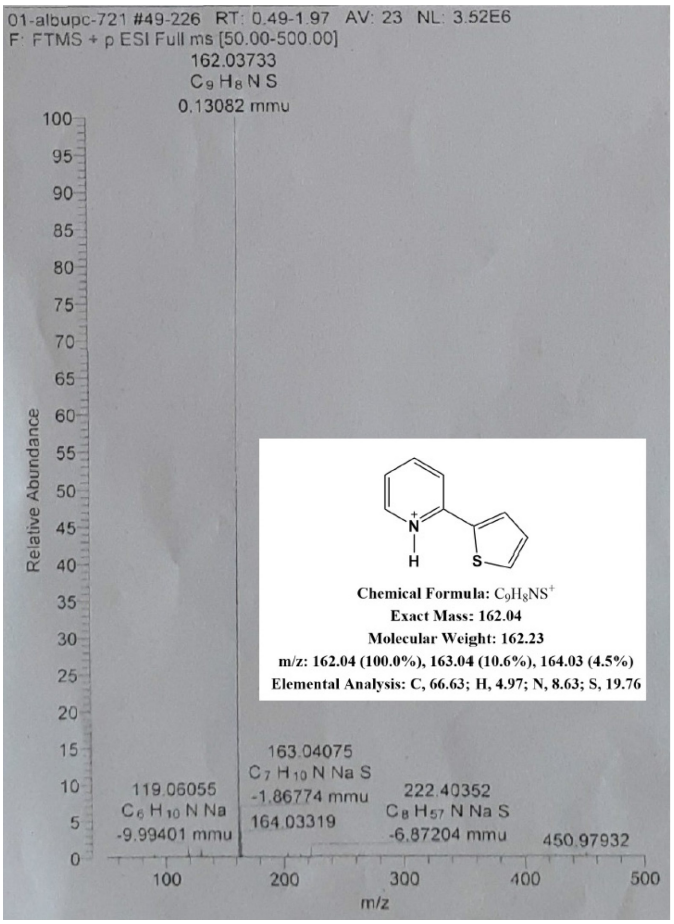

Figure S1c. Mass spectrum of ThPyI organic spacer with a distinctive *m/z* peak at 162.037.

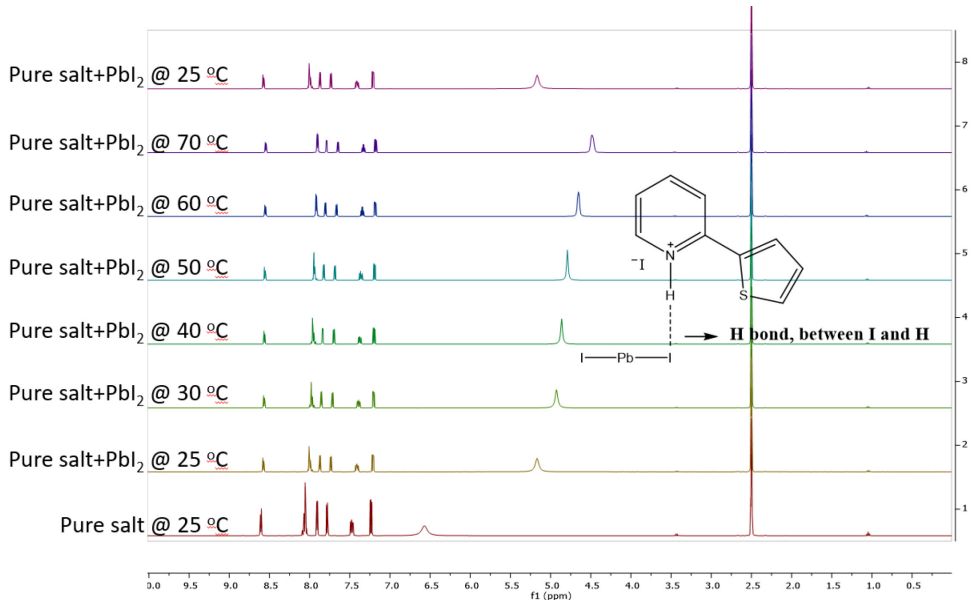

Figure S1d. ^{1}H-NMR spectra of PbI_2 + ThPyI mixture at different temperatures

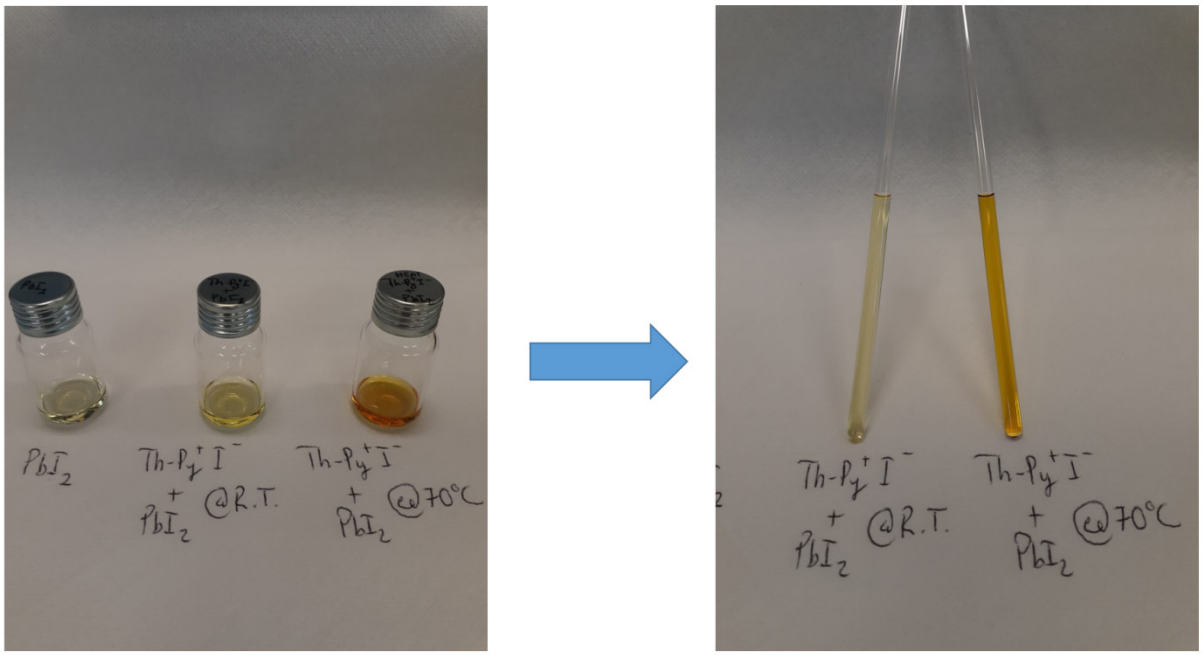

Figure S1e. Photos of the PbI_2 + ThPyI mixture after heating at different temperatures.

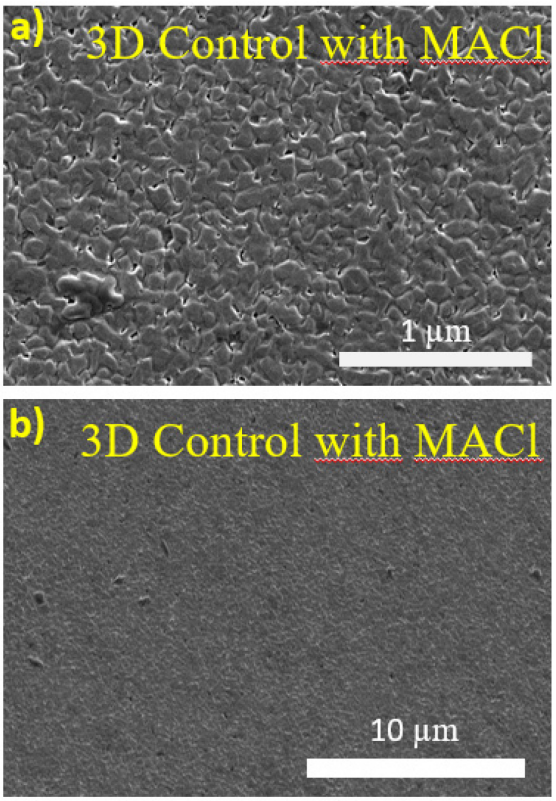

Figure S2. SEM images of a, b) 3D control with MACl.

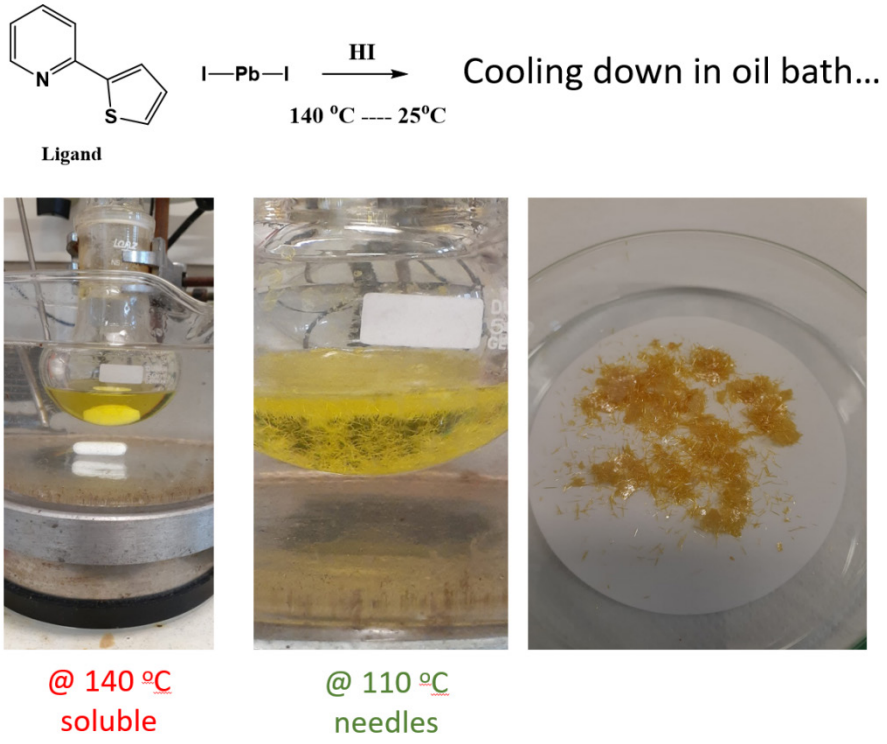

Figure S3. Photos of the 1D single crystals forming during the synthesis.

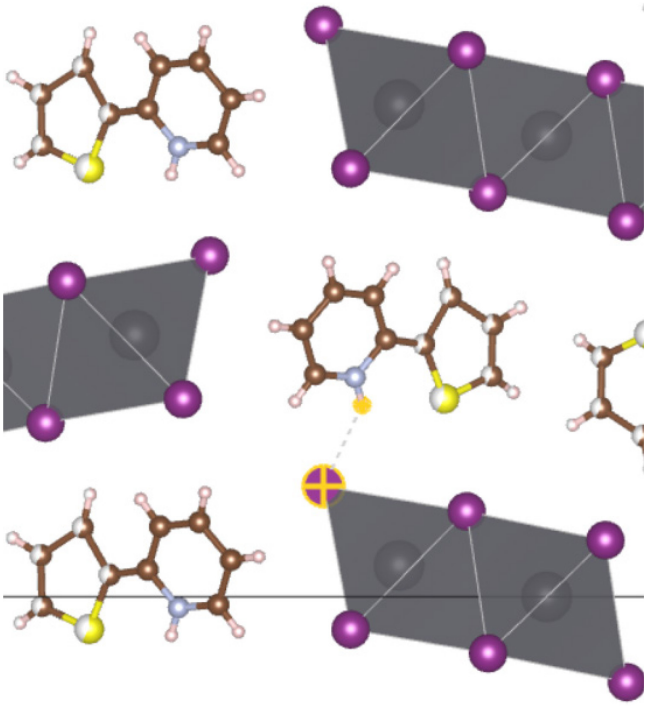

Figure S4. N^{+}-H···I-PbI_5 hydrogen-bonding interaction (l(H1-I4) = **2.8118(2) Å.**

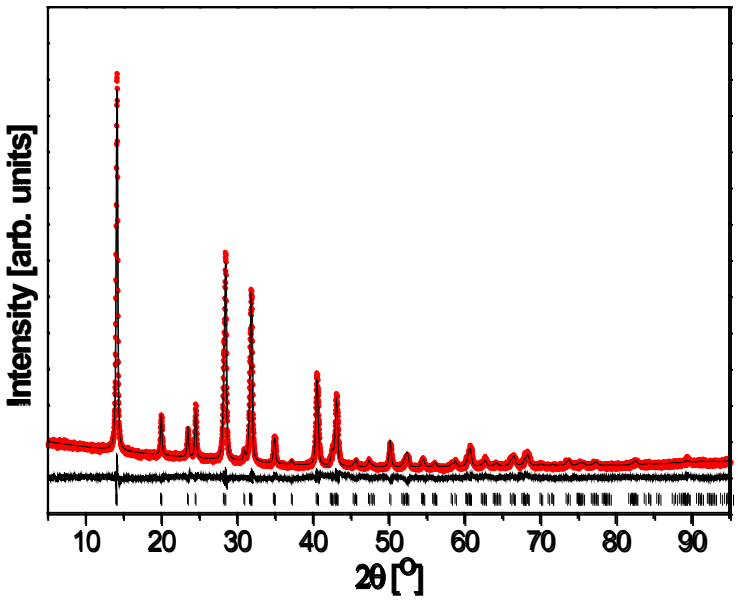

Figure S5. Rietveld plot for the 3D-control sample. Red dots – Y_{obs}, black line – Y_{calc}, line below – Difference, Vertical bars – Bragg positions.

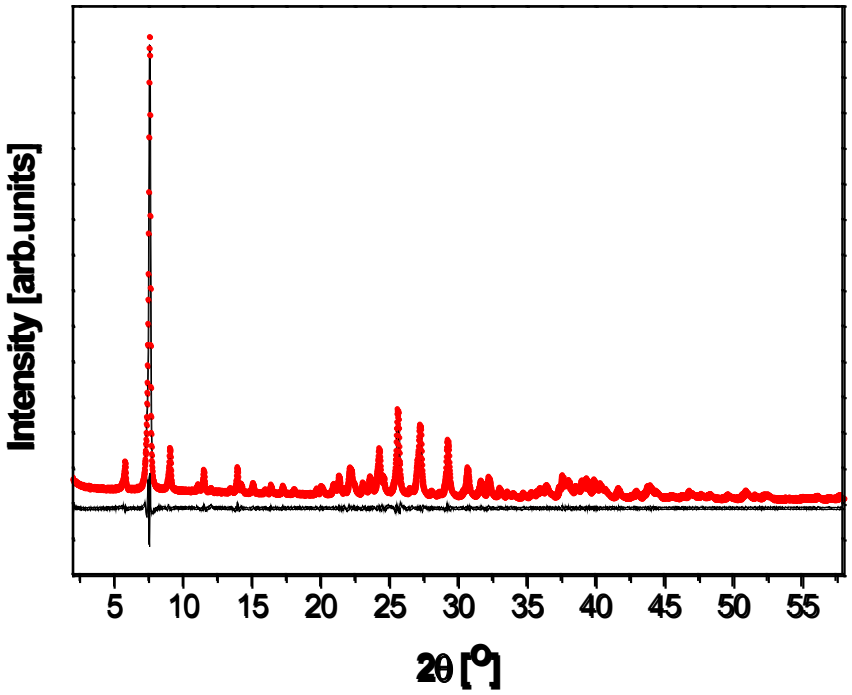

Figure S6. Le Bail Profile fitting of powder diffraction pattern of the1D film.

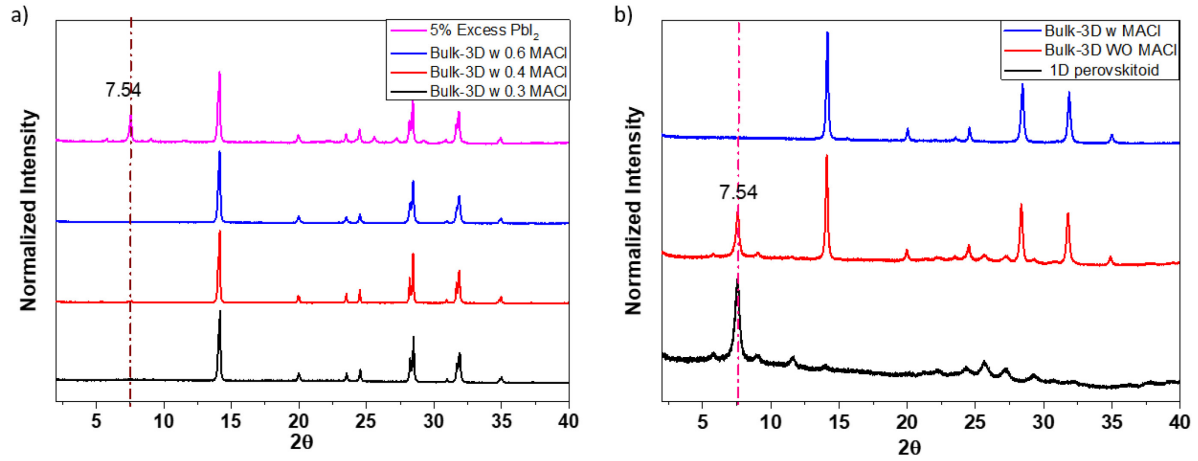

Figure S7. a) Powder XRD patterns of bulk-passivated 3D MAPI with different amount of MACl added (MACl/MAI wt. ratio) b) XRD patterns of 1D and bulk-passivated 3D perovskite with MACI (MACl/MAI (0.5 wt. ratio) and without MACI.

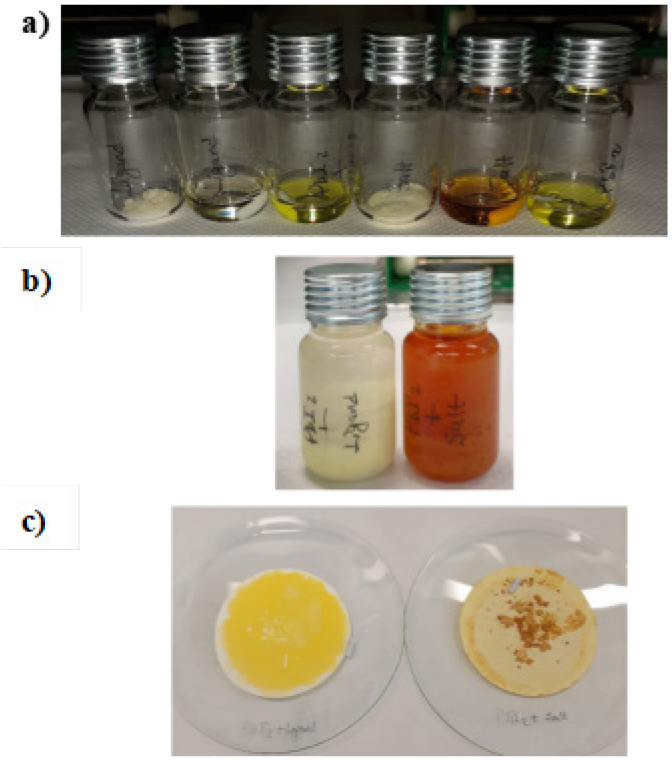

Figure S8. Left to right: a) Photos of the ThPy ligand (unprotonated form of the organic salt) in its pure (solid) form, its solution form in DMF, and its mixture with PbI_2 in DMF; photos of the ThPyI (organic salt) in its pure (solid) form, its solution form in DMF, and its mixture with PbI_2 in DMF. b) Photos of the mixtures of PbI_2 + ThPy, and PbI_2 + ThPyI in DMF with a large amount of toluene, which was stirred at room temperature for 1 hour. c) Photos of the PbI_2 + ThPy, and PbI_2 + ThPyI precipitates in powder forms which were many times washed with toluene and isopropanol to remove unreacted ligand and its salt form, respectively, dried under vacuum at room temperature for 24 hours.

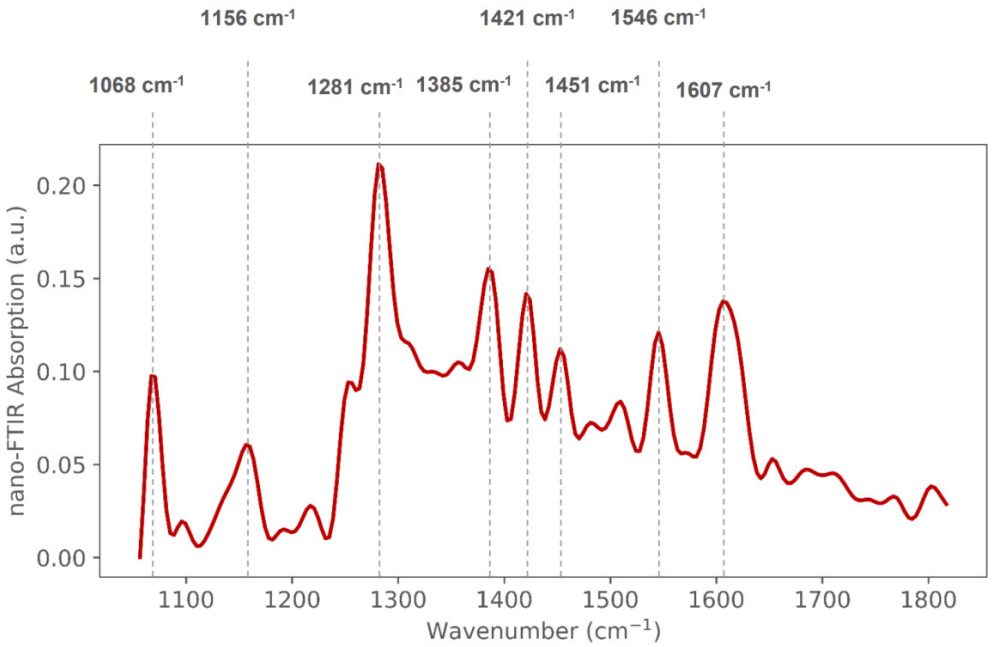

Figure S9. Nano-FTIR Spectra of pure ThPyI.

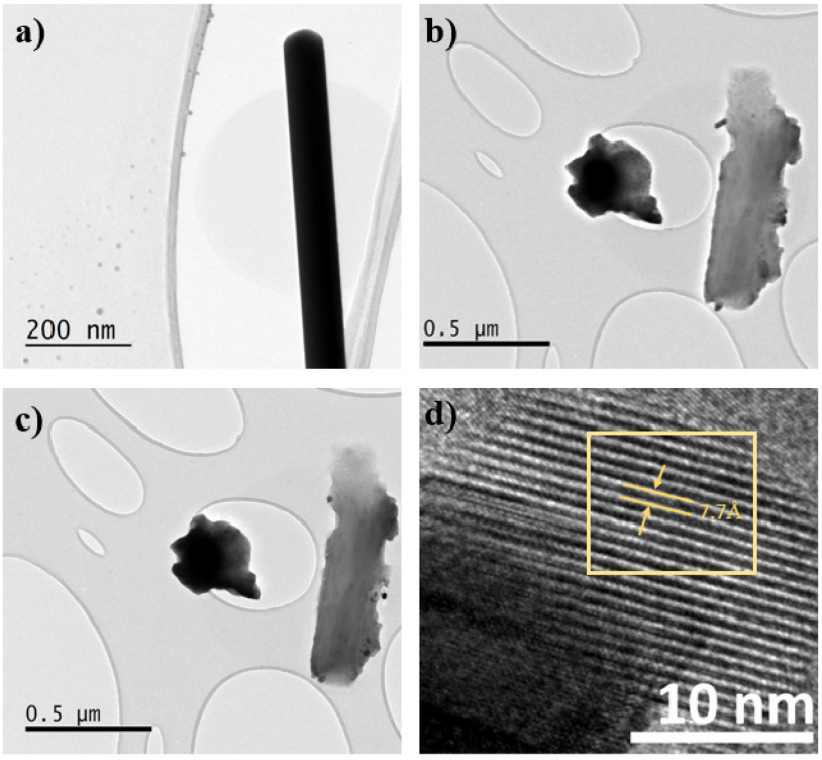

Figure S10. TEM images of bulk-passivated 3D (with MACI) perovskite film.

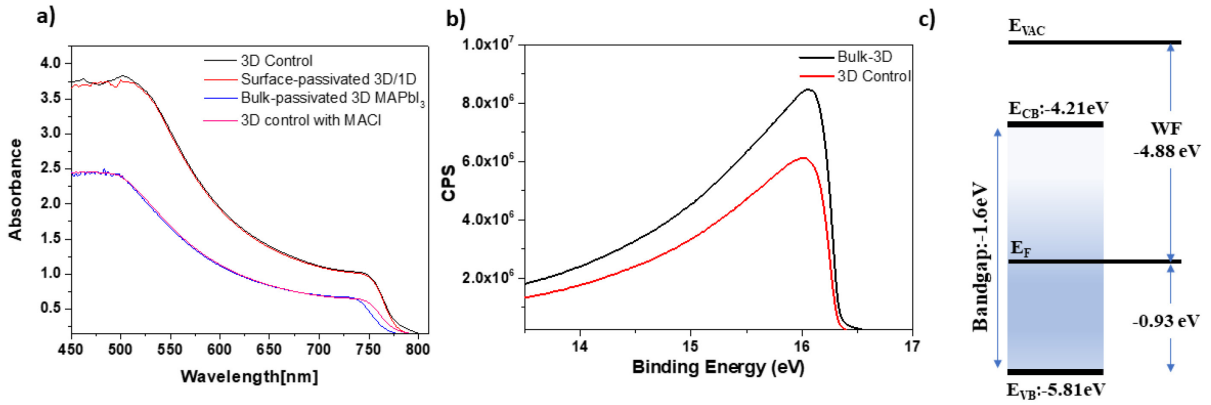

Figure S11. Absorption spectra of 3D MAPI control, surface-passivated 3D/1D and bulk-passivated 3D MAPI. b) Helium Iα ($h\nu$ = 21.22 eV) spectra of SE (secondary electron) cutoff of bulk-passivated 3D perovskite films. c) Schematic energy level diagrams of bulk-passivated 3D perovskite film.

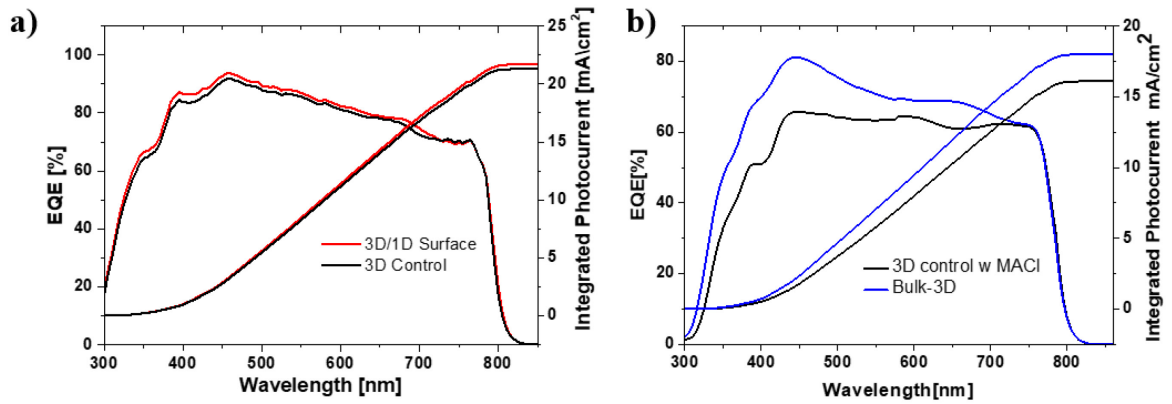

Figure S12. a) EQE of 3D MAPI Control and 3D/1D surface passivated device, b) EQE of 3D MAPI control with MACl and bulk-passivated 3D perovskite.

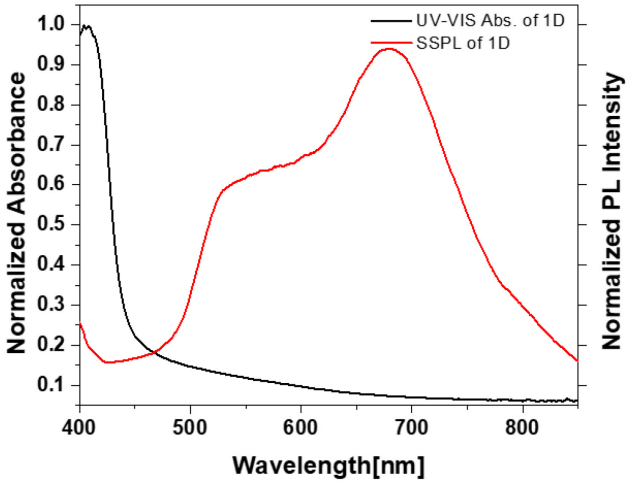

Figure S13. Absorption spectra and SSPL spectra of the1D perovskitoid.

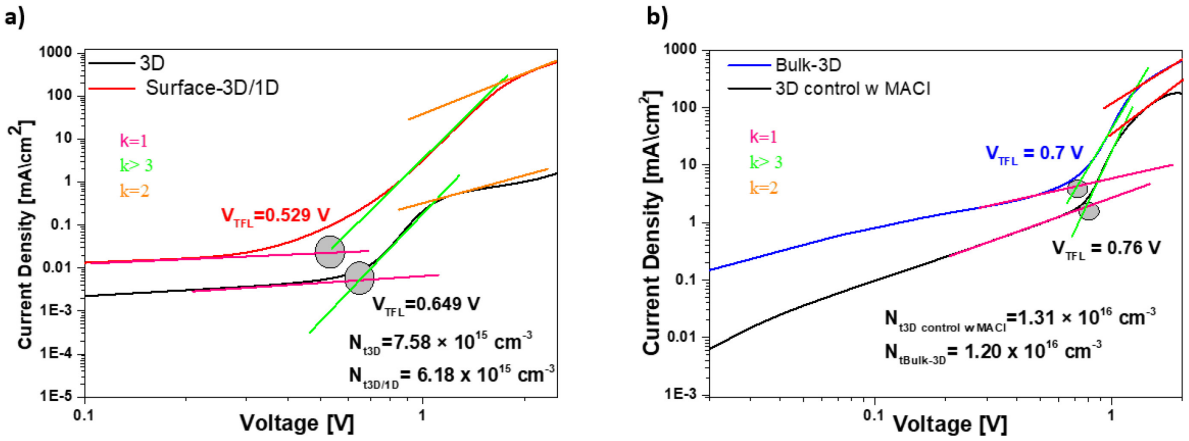

Figure S14. a-b) Electron only devices of the 3D MAPI control, surface-passivated 3D/1D, 3D MAPI control with MACl, and bulk-passivated 3D.

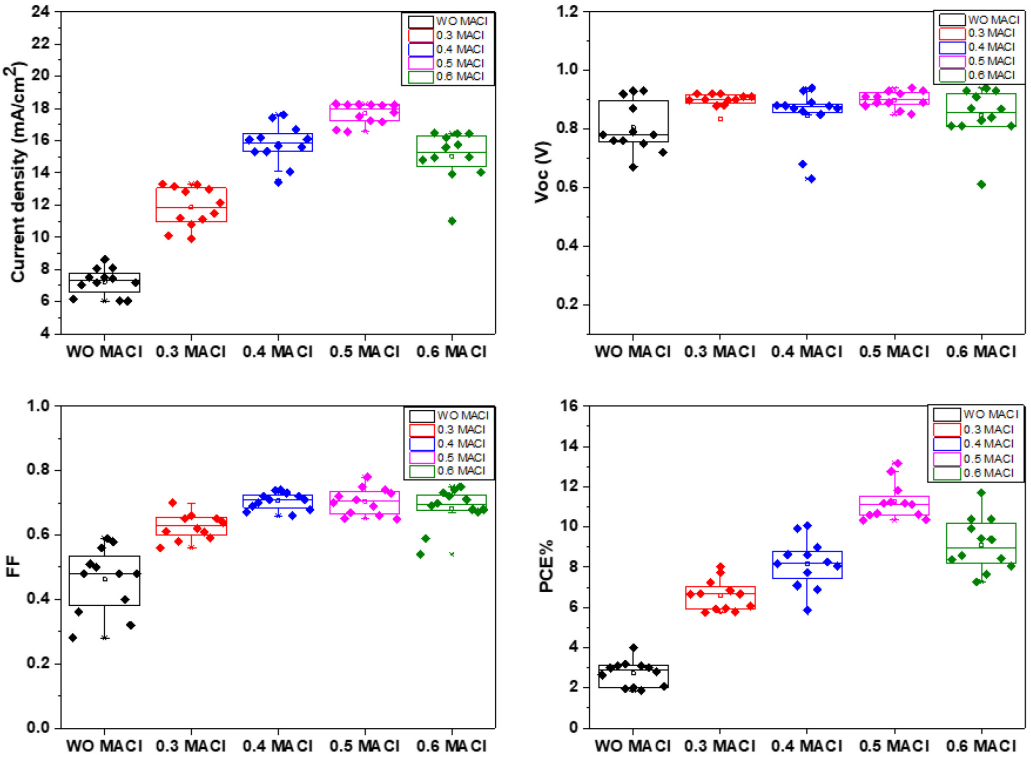

Figure S15. The statistical distribution of photovoltaic parameters of the bulk-3D MAPI with different ratios of MACl in the presence of ThPyI (for example 0.3 MACl means MACl/MAI: 0.3 wt. ratio).

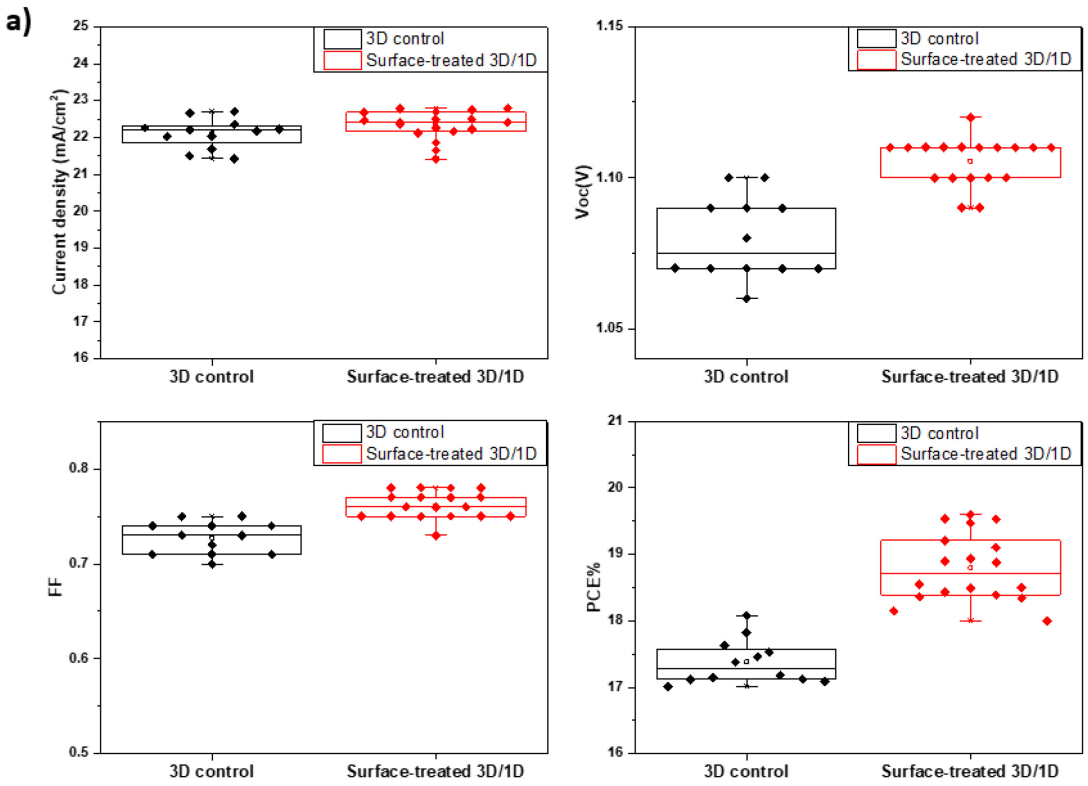

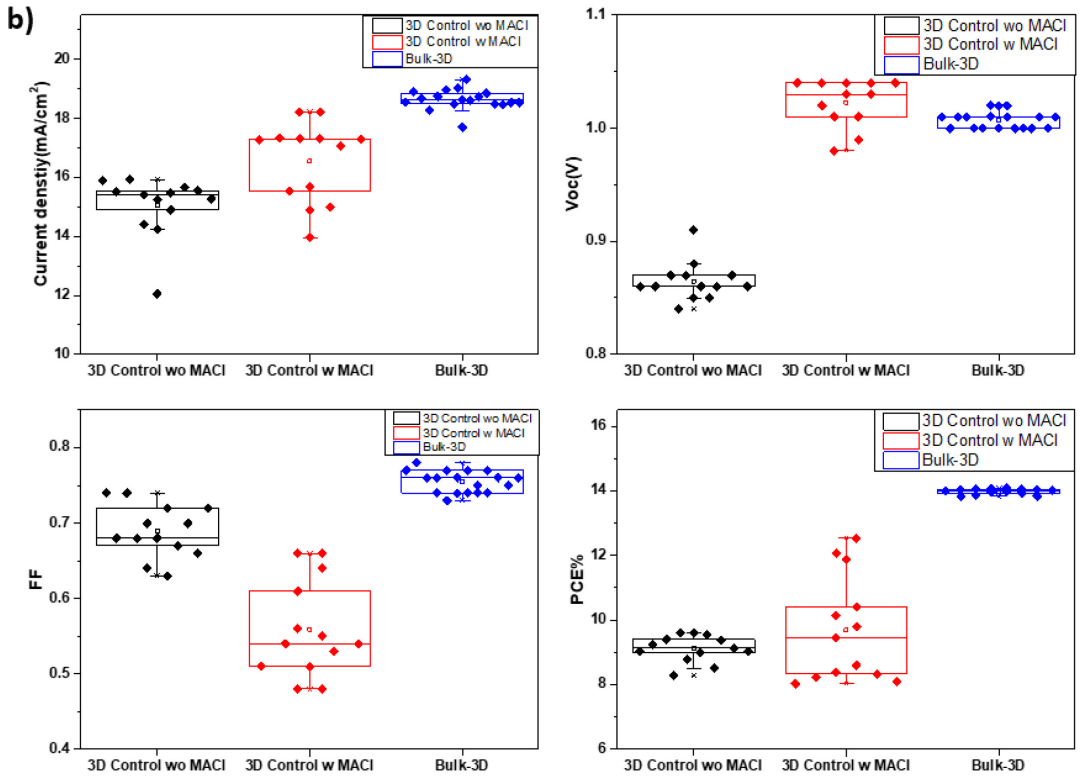

Figure S16. The statistical distribution of photovoltaic parameters of a) Surface-passivated and b) Bulk passivated devices.

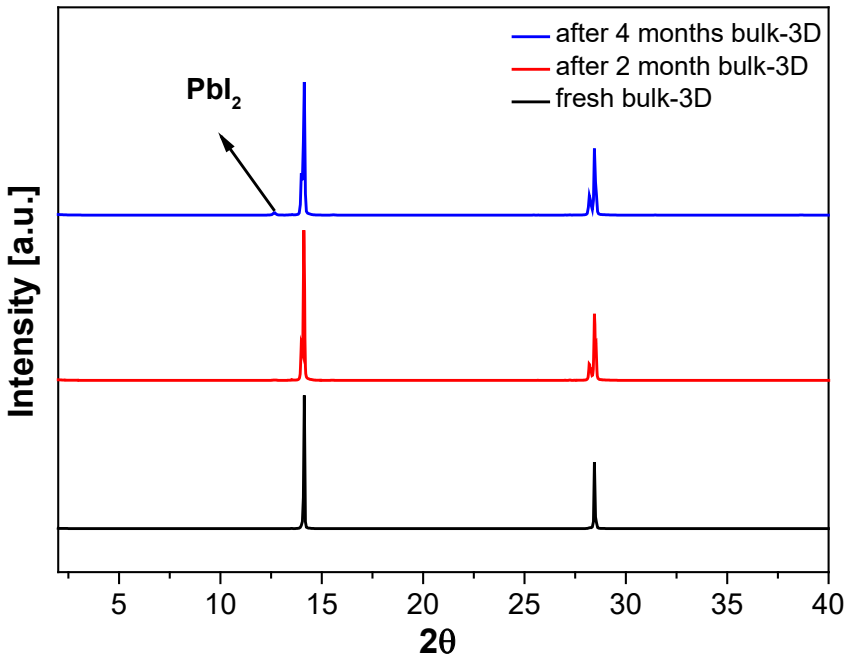

Figure S17. XRD patterns of bulk-passivated 3D perovskite thin films in air after 2 and 4 months.

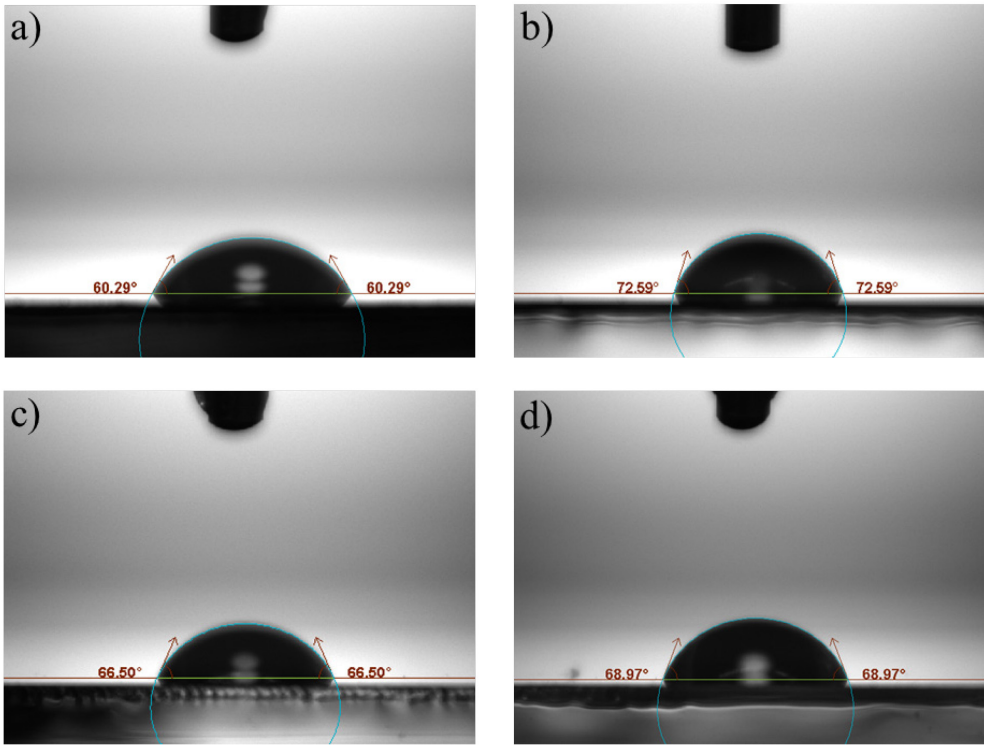

Figure S18. Contact angle measurements of a) 3D $MAPbI_3$ control, b) 1D perovskitoid, c) surface-passivated 3D/1D, and d) bulk-passivated 3D perovskite film.

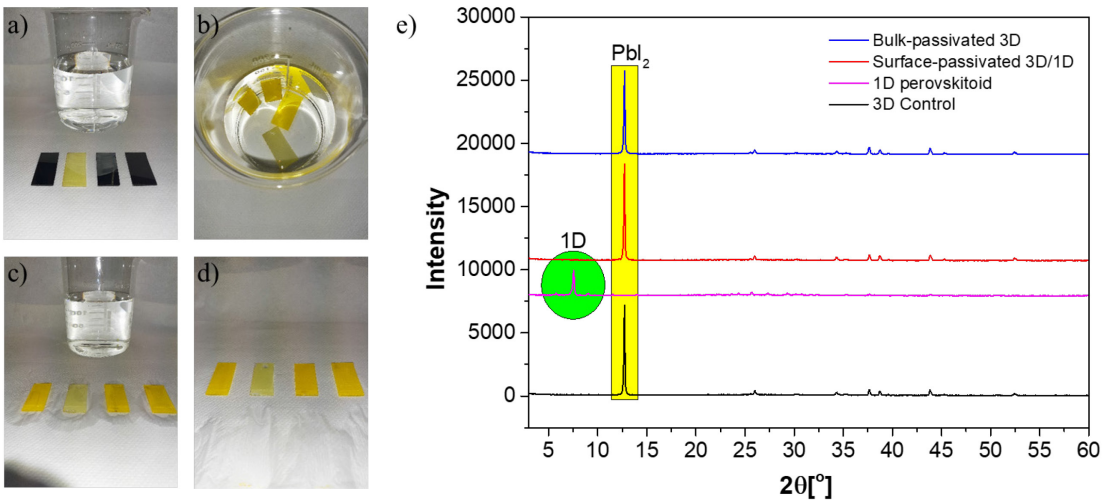

Figure S19. Photos of films, from left to right: a) 3D control, 1D, surface-passivated 3D/1D and bulk-passivated 3D, before water immersion, b) in water, c) after immersion (c), d) after drying, and e) XRD measurements.

Table S1. Crystallographic data of the 1D single crystal.

net formula	$C_{18}H_{16}I_8N_2Pb_3S_2$
*M*r/g mol-1	1961.22
crystal size/mm	0.140 × 0.020 × 0.020
T/K	297.(2)
radiation	MoKα
diffractometer	'Bruker D8 Venture TXS'
crystal system	orthorhombic
space group	'F d d 2'
a/Å	25.389(3)
b/Å	61.606(6)
c/Å	4.5767(5)
α/°	90
β/°	90
γ/°	90
V/Å3	7158.5(13)
Z	8
calc. density/g cm-3	3.639
μ/mm-1	21.106
absorption correction	Multi-Scan
transmission factor range	0.33–0.68
refls. measured	24469
*R*int	0.0577
mean σ(*I*)/*I*	0.0488
θ range	3.094–28.281
observed refls.	3993
x, y (weighting scheme)	0.0099, 1443.4072
hydrogen refinement	constr
Flack parameter	0.126(18)
refls in refinement	4361
parameters	117
restraints	16
R(*F*obs)	0.0620
*R*w(*F*2)	0.1383
S	1.144

shift/errormax	0.001
max electron density/e Å-3	2.351
min electron density/e Å-3	-3.356

Table S2. Refined structural parameters of the 3D-Control sample.

Refinement was performed using Topas V4.2 SG- I4cm.[5]

Unit cell parameters

a (Å) 8.8706(15)

c (Å) 12.6404(23)

Site	Np	x	y	z	Atom	Occ	Beq
C1	4	0.50000	0.00000	0.61000	C	1	9.475
H1c1	16	0.41950	0.06230	0.58460	H	0.25	11.08
H1n1	16	0.46420	0.91500	0.75200	H	0.25	11.08
H2c1	16	0.59420	0.03860	0.58460	H	0.25	11.08
H2n1	16	0.59150	0.01150	0.75200	H	0.25	11.08
H3c1	16	0.48630	0.89910	0.58460	H	0.25	11.08
H3n1	16	0.44420	0.07350	0.75200	H	0.25	11.08
I1	4	0.00000	0.00000	0.1214(58)	I	1	9.8(3)
I2	8	0.72360(27)	0.22360(27)	0.3590(53)	I	1	6.57(1)
N1	4	0.50000	0.00000	0.72900	N	1	9.475
Pb1	4	0.00000	0.00000	0.3727(51)	Pb	1	3.41(8)

Table S3. a) Part of the Calculated Powder Diffraction Pattern for CuKa1 radiation of the ThPyI based 1D crystal structure data obtained from single crystal.

h	k	l	d (Å)	F(real)	F(imag)	|F|	2θ	I	M	ID(λ)	Phase
0	4	0	15.4015	331.564	59.7401	336.903	5.73363	2.23302	2	1	1
2	2	0	11.737	2072.66	303.527	2094.77	7.52601	100	4	1	1
2	4	0	9.79595	-751.68	-114.89	760.41	9.02013	9.15337	4	1	1
2	6	0	7.98325	-251.85	-77.194	263.416	11.0741	0.72611	4	1	1
0	8	0	7.70074	-767.67	-66.537	770.553	11.4817	2.88768	2	1	1
2	8	0	6.58405	209.808	42.3422	214.038	13.4373	0.32396	4	1	1
4	0	0	6.34735	954.273	47.4506	955.452	13.9409	2.99516	2	1	1
4	2	0	6.21674	-399.51	-9.8048	399.634	14.2353	1.00437	4	1	1
4	4	0	5.86851	478.925	61.4956	482.857	15.0847	1.30293	4	1	1
2	10	0	5.54243	242.154	47.2985	246.73	15.9779	0.3025	4	1	1

Table S4. The interplanar lattice distances of some planes.

h	k	l	d (Å)
2	2	0	11.74
0	8	0	7.7
2	3	1	2.87

Table S5. Time-resolved photoluminescence decay components of MAPI reference, surface, and bulk-treated MAPI films.

Sample	A_1(%)	τ_1 (μs)	A_2 (%)	τ_2 (μs)	$\tau_{ave.}$ (μs)
3D MAPI Control	58.19	0.050	41.81	0.114	0.076
Surface passivated 3D/1D	38.14	0.068	61.86	0.214	0.158
Bulk-passivated 3D	36.06	0.055	63.94	0.154	0.118
3D control with MACl	50.12	0.049	49.88	0.087	0.068

Table S6. Photovoltaic Parameters for the champion devices (reverse scan values are reported in parentheses).

Device	Jsc (mA\cm^2)	PCE %	Voc (V)	FF	Integrated Photocurrent (mA\cm^2)	Hysteresis Index %
3D Control	22.35 (22.17)	18.08 (17.01)	1.09 (1.07)	0.74 (0.72)	21.305 (Jsc -4,7%)	5.92
3D/1D Surface	22.69 (22.79)	19.60 (19.53)	1.11 (1.10)	0.78 (0.78)	21.692 (Jsc -4,4%)	0.35
3D control with MACl	17.81 (16.54)	12.53 (9.68)	1.03 (1.02)	0.66 (0.55)	16.09 (Jsc-9.6%)	16.9
Bulk- 3D MAPI	18.98 (18.94)	13.00 (14.10)	1.02 (1.01)	0.72 (0.74)	18.00 (Jsc-5.11 %)	2.55

REFERENCES

[1] APEX, Bruker, and Bruker AXS SAINT. Inc.: Madison, Wisconsin, USA, **2012**

[2] G. M. Sheldrick, *SADABS, Empirical Absorption Correction Program*, University of Göttingen, Germany,**1997**.

[3] Sheldrick, G. M. *Acta Cryst.,* **2015**. *A71*, 3.

[4] Farrugia, L. J. J. *Appl. Cryst*., **2012**. *45*, 849.

[5] TOPAS V4.2, General Profile and Structure Analysis Software for Powder Diffraction Data. In Tutorial; Bruker AXS: Karlsruhe, Germany, 2009.

5 In-situ Polymerized 2,5-dimercapto-1,3,4-thiadiazole as a Bulk Defect Passivation Agent for Enhanced Longevity and Performance of Ag_3BiI_6 Photovoltaics

This chapter is based on the following manuscript in preparation:

Ali Buyruk., ... , Achim Hartschuh,Thomas Bein, and Tayebeh Ameri.

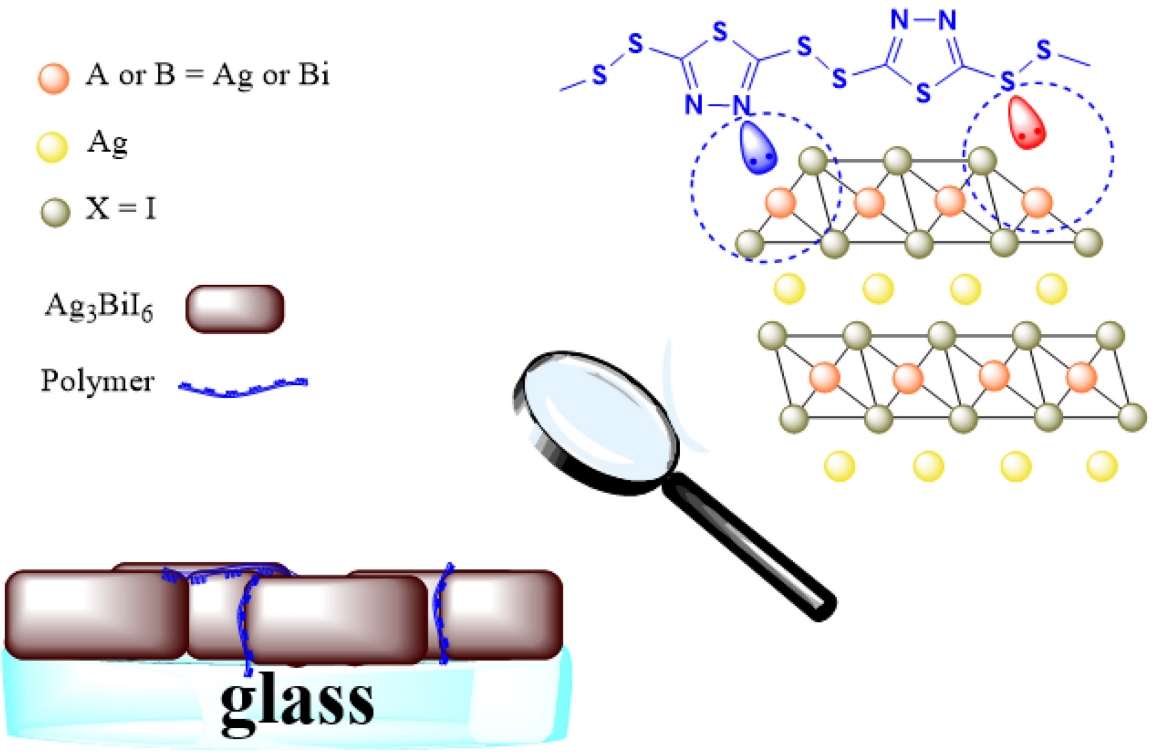

Keywords

Silver-Bismuth Halides, in-situ polymerization, solar cell, polymer, bulk-passivation.

5.1 Introduction

Lead halide perovskites (OIHPs) have made remarkable strides in enhancing power conversion efficiency (PCE) for photovoltaic applications, reaching levels as high as 26.0%, putting them on par with silicon-based solar cells.[1-2] Nevertheless, the environmental concerns associated with lead (Pb)[3] have prompted the exploration of Pb-free alternatives, including the use of divalent metals like tin (Sn^{2+}) or germanium (Ge^{2+}) though these alternatives encounter stability issues.[4-6]An alternative strategy involves heterovalent substitution, where a trivalent cation such as Bi^{3+} is combined with a monovalent cation like Ag^{+} to create double perovskites resulting in $A_2M'M''X_6$ ($Cs_2AgBiBr_6$, $Cs_2AgInCl_6$, $Cs_2AgSbCl_6$, etc.).[7-10]

In contrast to traditional perovskite materials, perovskite-inspired substances like silver-bismuth halides, characterized by their chemical formula $Ag_aBi_bX_{a+3b}$ and rudorffite structures, are emerging as a promising option for serving as light absorbers in solar cells. Their appeal is underpinned by several key attributes, including their appropriate band gap energy (Eg) and their exceptional light-absorbing properties.[11]

When compared to double perovskites and A_3BiX_9 compounds (where A can be Cs^{+}, Rb^{+}, or $CH_3NH_3^{+}$ and X^{-} can be I^{-}, Br^{-}, or Cl^{-}), which typically possess wide indirect band gaps (Eg > 2.0 eV), silver-bismuth halides stand out due to their significantly smaller Eg falling within the range of 1.6 to 1.93 eV, characterized as direct band gaps. This specific feature renders them highly suitable for utilization in photovoltaic (PV) applications.[12-13]

Additionally, silver-bismuth halides, known as ABI compounds (e.g., Ag_3BiI_6, Ag_2BiI_5), have attracted attention due to their narrower band gaps, making them well-suited for thin-film photovoltaics. Despite a theoretical PCE estimate exceeding 25%, most ABI solar cells have struggled to achieve more than 2% PCE. Various techniques, such as antisolvent dripping, hot-dynamic spin coating, and doping, have been explored to boost PCE, yet challenges related to carrier loss due to recombination persist.[14]

Furthermore, previous research has indicated that ABI compounds, such as Ag_3BiI_6, Ag_2BiI_5, with ratios of ($AgI:BiI_3$) 3:1 and 2:1 contain contributions from AgI phases, and recent findings have demonstrated rapid nonradiative relaxation of these AgI domains within less than 10 picoseconds after being photoexcited. This property is unfavorable for photovoltaic applications, as it results in unwanted light absorption below 430 nm and may lead to the gradual formation of metallic silver over time.[15] In light of these considerations, it is advisable to prefer "AgI-poor" compounds (with at least a 1:1 ratio) for improved device stability. Overall, a recent study suggests that Ag_3BiI_6, Ag_2BiI_5 in their pure forms may not be ideal absorbers for photovoltaic cells.[16] However, consequently, researchers are exploring

elemental modifications for this class of compounds rather than their pure forms. These modifications include the partial substitution of Ag(I) and Bi(III) with equivalent amounts of Cu(I) or the exchange of Bi(III) with stoichiometric amounts of Sb(III) with the aim of achieving higher power conversion efficiancy, and stability.[17-20] In this study, as an alternative to elemental modifications of photo-active layer, a widely recognized material, poly(2,5-dimercapto-1,3,4-thiadiazole),[21] has been employed with in-situ polymerization during the film formation of the photo-active layer to enhance the efficiency and stability of solar cells based on Ag_3BiI_6 through a bulk polymer treatment approach to alleviates harmful defects within the inner structure of Ag_3BiI_6, which have a negative impact on the performance and stability of photovoltaic devices.

5.2 Results and Discussion

In the initial phase of this study, the polymerization of 2,5-dimercapto-1,3,4-thiadiazole (in the following contents called a polymer) was confirmed through the use of Raman and IR spectroscopy. Polymerization was conducted in the preparation condition of reference Ag_3BiI_6 precursor solution, which is A solvent mixture of DMF and DMSO (DMF:DMSO = 1:3), in the oxidation system of iodine (I_2). Briefly, the I_2 solution of the solvent mixture was added dropwise to the monomer-containing same solvent mixture, mixed at room temperature, and then the resulting polymers were obtained by filtration and washing. (for the synthesis details are presented in Supporting Information). [21]

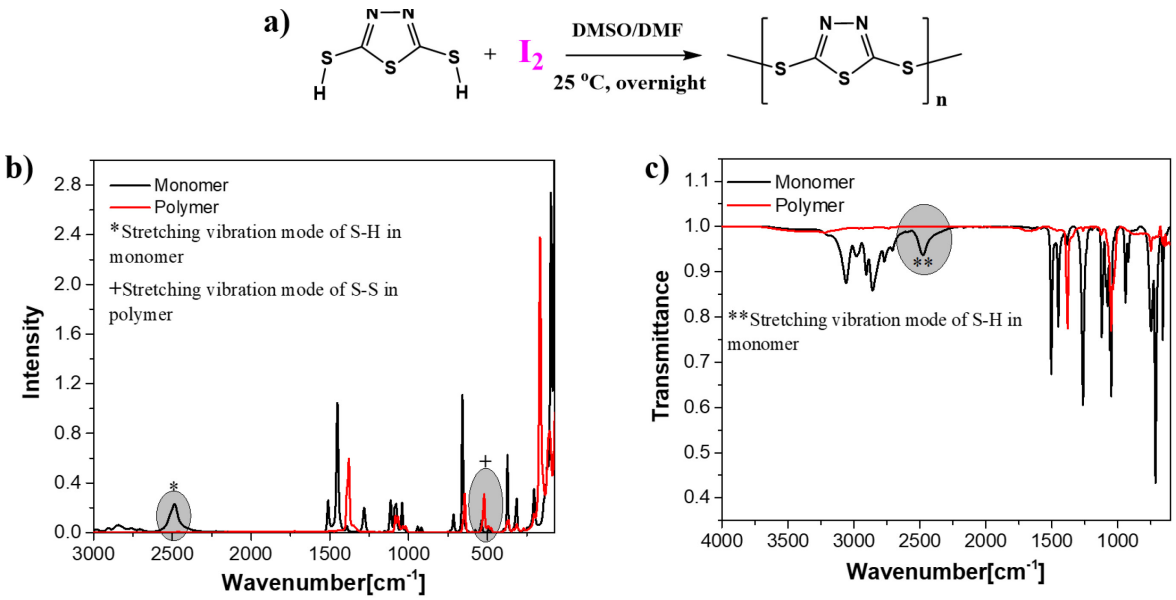

Figure 5.1 Polymerization of 2,5-dimercapto-1,3,4-thiadiazole (a), its Raman(b) and, FT-IR(c) spectras.

Following the polymerisation of 2,5-dimercapto-1,3,4-thiadiazole under the condition of the synthetic route described in Figure 5.1a, the powder form of the polymer was analysed with the help of Raman and IR spectroscopy (Figure 5.2b,c). Upon comparing the monomer with the polymer, it is evident that the –S–H stretching bands at 2485 cm^{-1}(*) and 2476 cm^{-1}(**) in Raman(*) and FT-IR(**) spectra, respectively, disappear in the polymer spectra, and a new band at 520 cm^{-1}(+), associated with S–S stretching in Raman spectra, emerges. This indicates that the polymerisation of the monomer involves the formation of –S–S– bonds.[22-23]

The crystalline and morphological properties of both the reference Ag_3BiI_6 (without polymer treatment) and the poly(2,5-dimercapto-1,3,4-thiadiazole) bulk-treated Ag_3BiI_6 films with varying treatment amounts of polymer (from 0% to 10% of the total wt of Ag_3BiI_6 precursors) were assessed using various techniques, including X-ray diffraction (XRD), and scanning electron microscopy (SEM).

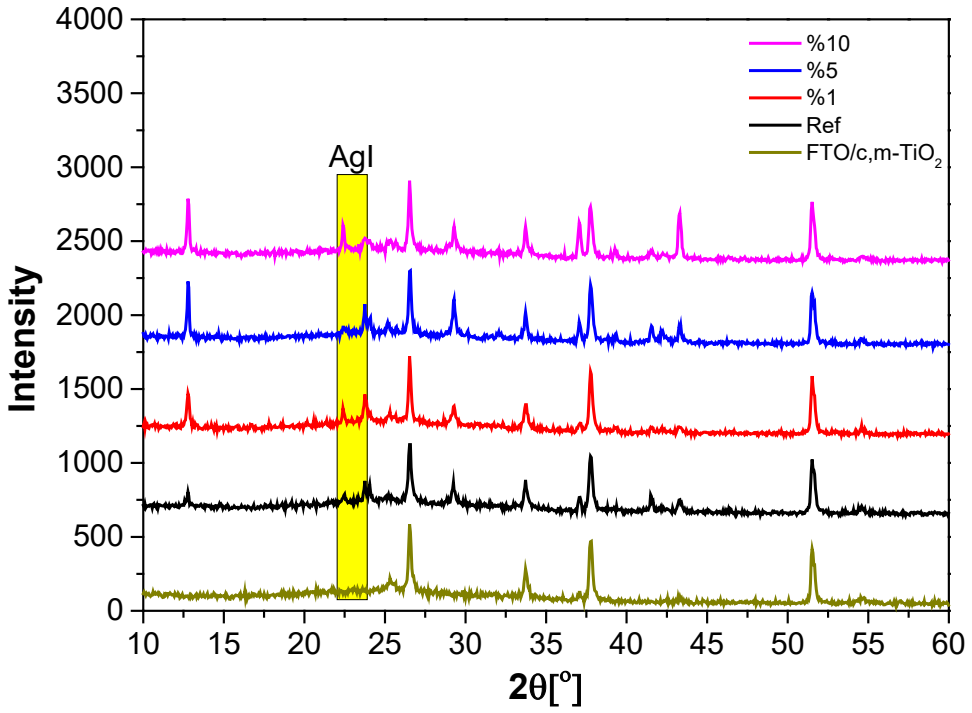

Figure 5.2 XRD patterns of reference Ag_3BiI_6 and the poly(2,5-dimercapto-1,3,4-thiadiazole) bulk-treated films with varying treatment amounts of polymer (from 0% to 10% of the total wt of Ag_3BiI_6 precursors).

In the XRD patterns of the reference film, the presence of Ag_3BiI_6 was observed, along with a minor amount of unreacted hexagonal AgI as an impurity at 2θ =22.4° and 23.7°. The detection of a small quantity of the AgI phase in the silver-rich Ag_3BiI_6 films, highlighted by the yellow column in Figure 5.2, is a characteristic feature of this crystalline phase. This observation aligns with previous research on rudorffites conducted by Turkevych et al.[11] The introduction of minor quantities of polymer into Ag_3BiI_6 did not produce significant alterations in the XRD patterns of the resulting films. Remarkably, the treatment with this polymer did not lead to the formation of distinct crystalline phases composed of separated polymer. Instead of inducing a change in the crystal phase of Ag_3BiI_6, it resulted in higher XRD reflections for the treated samples compared to the reference. This finding is supported by SEM images (Figure 5.3) that demonstrate improved crystal quality with larger grains and reduced grain boundaries.

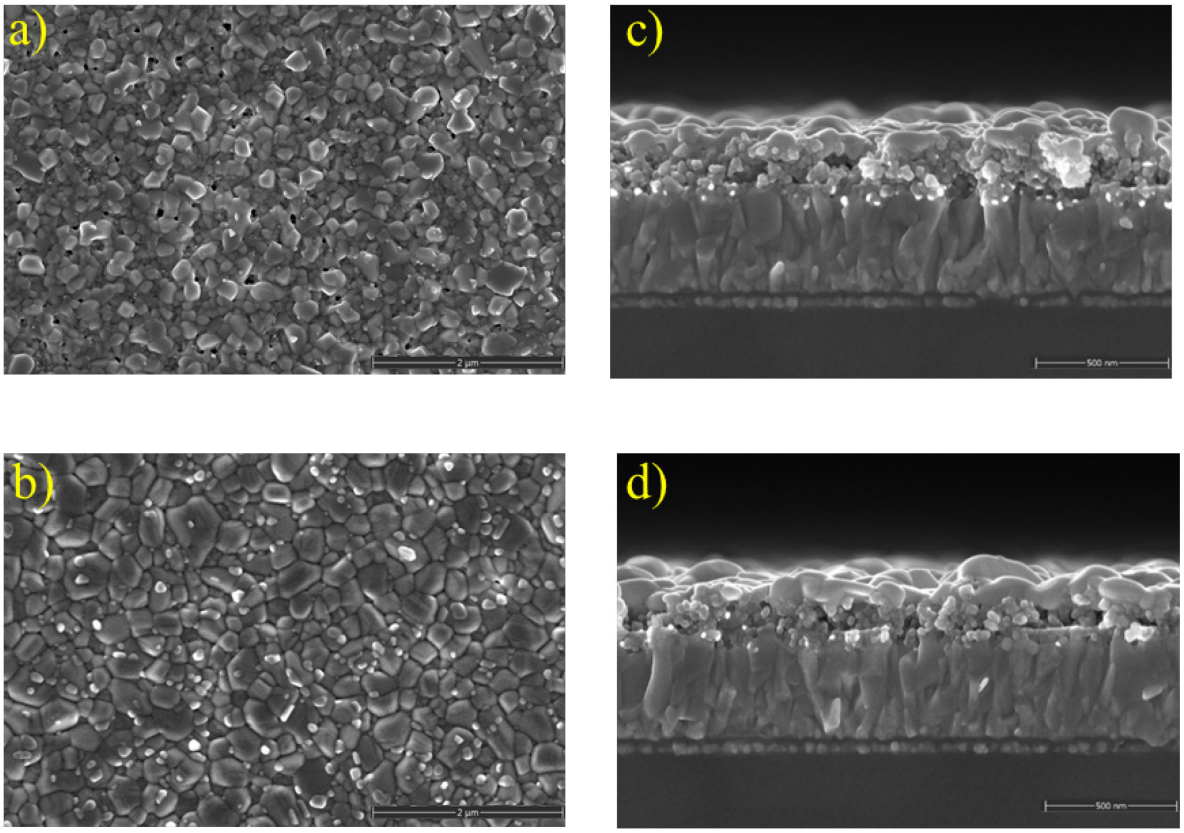

Figure 5.3 SEM top-view images of untreated (a) and polymer bulk-treated (5% wt) (b) Ag_3BiI_6 films; cross-section images of untreated (c), and polymer bulk-treated (5% wt) (d) Ag_3BiI_6 films.

After conducting crystalline and morphological analyses on both the reference Ag_3BiI_6 and the polymer bulk-treated films with varying treatment amounts of polymer, their optical properties were investigated

using UV-Vis and photoluminescence (PL) spectroscopy in their film forms. Reference Ag_3BiI_6 and their bulk-treated film forms with the increasing content of polymer (directly prepared on glass) show the optical absorption characteristics within the 400–800 nm range remain largely unchanged (Figure 5.4a).[24] Any minor enhancement observed in UV-Vis absorption in the treated film may be attributed to slight variations in film thickness and the area of the measurement position. The spectra of all reference Ag_3BiI_6, and their bulk-treated films exhibited a faint and consistent peak in the 420–425 nm range.[24] This peak could be attributed to a minor presence of unreacted AgI within these films, which aligns with the X-ray diffraction (XRD) data, shown in Figure 5.2.[11]

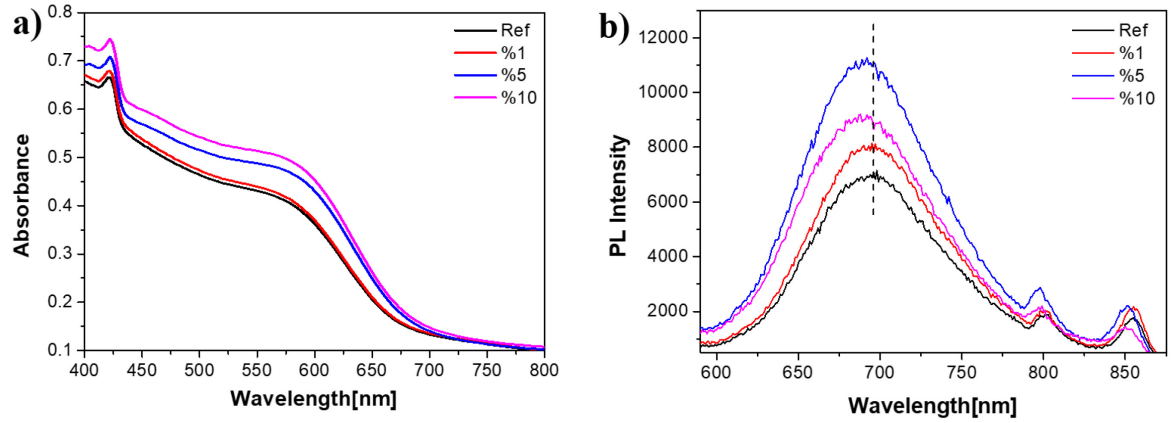

Figure 5.4 UV-Vis absorption spectrum (a) and, steady-state PL spectra (excitation wavelength of 375 nm)(b), of reference Ag_3BiI_6, and their bulk-treated film forms on glass with the increasing content of polymer.

To assess the charge carrier recombination dynamics in the reference, and bulk-tretaed films, steady-state photoluminescence (PL) measurements were conducted. The PL spectra of both the reference and its treated ones show the typical characteristics of Ag_3Bi_6.[11] The steady-state photoluminescence (PL) spectrum of the polymer bulk-tretaed films exhibits a remarkable enhancement in PL intensity and a blue-shifted emission compared to the reference film (Figure 5.4b), which shows its highest PL in the 5%wt tretaed form. This pronounced enhancement and blue-shift in PL are strong indicators of defect passivation (suppressing the trap-assisted recombination channel) and reduced non-radiative recombination in the bulk structure. We propose that the polymer formed in the bulk structure of the Ag_3BiI_6 passivate the under-coordinated Bi\Ag center atoms in the corner-sharing octahedra, which is one of the point defetcs of Ag_3BiI_6, through the lone pair electrons of lewis base sites on the polymer chain, such as dimercapto bridge (-S-S-), 1,3,4-thiadiazole ring (-N-N-), as illustrated in Figure 5.5.

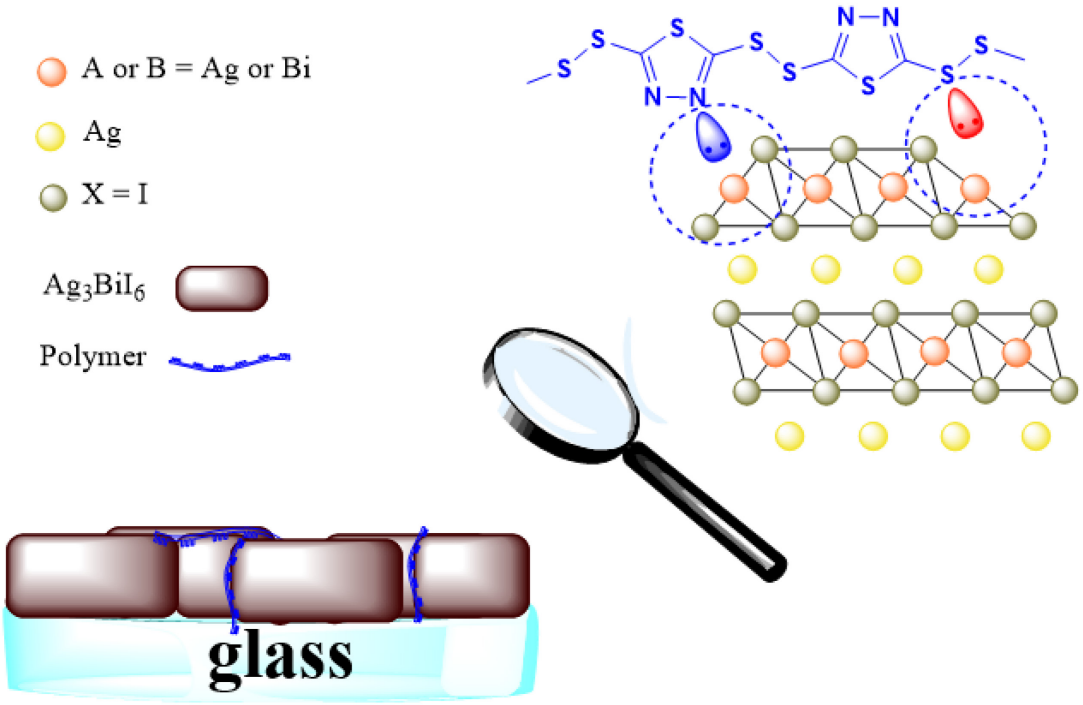

Figure 5.5 Proposed defect mechanism of Ag_3BiI_6, through the lone pair electrons of Lewis base sites on the polymer chain, such as dimercapto bridge (-S-S-, red color lone pair electrons), 1,3,4-thiadiazole ring (-N-N-, blue color lone pair electrons).

To assess the treatment effect in the bulk structure of Ag_3BiI_6 with the increasing amount of polymer (from 0% to 10% wt of Ag_3BiI_6 precursor), we fabricated a planar heterojunction perovskite solar cell with an n-i-p structure: Glass/FTO/c,m-TiO_2/ Ag_3BiI_6 with or without polymer/P3HT/Au. Precursor solutions were prepared by mixing silver(I) and bismuth(III) iodides in a mixture of dimethylsulfoxide (DMSO) and dimethylformamide (DMF) at a 3:1 volume ratio, followed by stirring at room temperature overnight. To treat the solution with the increasing amount of polymer, monomer and its excess I_2 as an oxidant was added to the reference precursor solution with different amounts (1,3,5 and 10% of wt of Ag_3BiI_6 precursor), and all solutions were further 30 minutes stirred at room temperature to convert to monomer into the polymer before spin-coating. A red solution, comprising AgI, BiI_3, and a polymer in a mixed solvent of DMSO and DMF, was applied to a glass/FTO/c,m-TiO_2 substrate using a spin-coating method with the assistance of nitrogen gas (N_2). The film was then subjected to two annealing steps: first at 60 °C for 1 minute and then at 140 °C for 15 minutes, as illustrated in Figure 5.6. This process resulted in the formation of a visually uniform film with enhanced homogeneity and a reduced presence of pinholes, as shown in Figure 5.3. Further details on the fabrication and characterization procedures are provided in the Experimental Section.

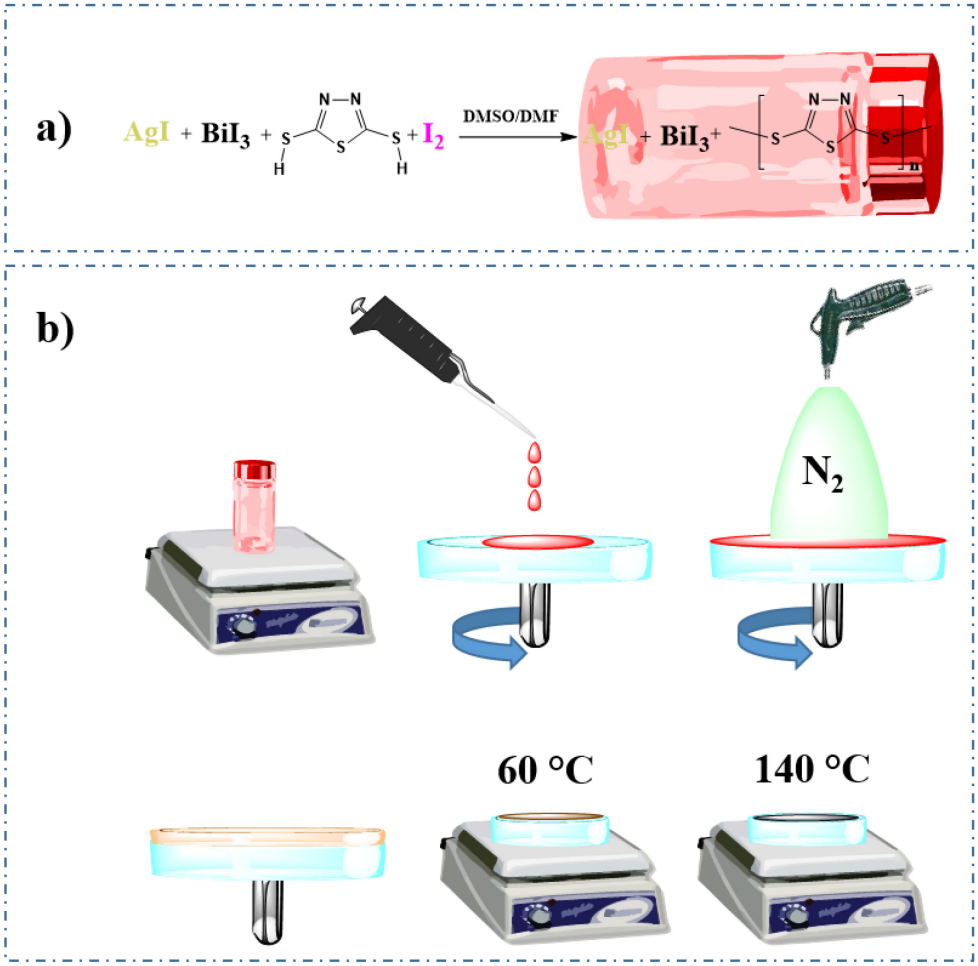

Figure 5.6 A concise overview of the process: a) preparation of precursor solutions, and b) depositing of Ag_3BiI_6 films with and without polymer.

The current density-voltage (J-V) characteristics of the highest-performing devices are depicted in Figure 5.8a, and their corresponding performance parameters are detailed in Table 1.

In comparison to the reference cell using Ag_3BiI_6 alone, all polymer-treated devices exhibited superior power conversion efficiency (PCE), attributable to improvements in open-circuit voltage (Voc), current density(mA\cm$_2$), and fill factor (FF) (Figure 5.8). The top-performing reference device achieved a PCE of 0.76%, featuring a Voc of 0.53 V, Jsc of 2.93 mAcm^{-2}, and a FF of 49%. In contrast, the 5% per cent polymer-treated device showed a remarkable enhancement, which is approximately double that of the reference, achieving a PCE of 1.37%, with a Voc of 0.75 V, Jsc of 3.44 mAcm^{-2}, and FF of 53%. The reference device exhibited significant hysteresis (HI) of 41%, while the polymer treated device showed reduced HI of 7% under identical scanning conditions. The improved Voc of the treated device indicates effective bulk defect passivation and reduced trap-assisted recombination, which shows a strong correlation in photoluminescence (PL) measurements, as shown in Figure 5.4b. The higher FF value for

the treated device can be attributed to more efficient charge extraction at the polymer-modified Ag_3BiI_6 interfaces between hole- and electron-transporting layers. The slightly higher photocurrent densities in the treated device can be also attributed to more efficient charge extraction at the modified polymer-treated interfaces after bulk passivation. Importantly, the average performance values from over 70 solar cells, fabricated in different experimental runs, exhibited a consistent trend of improvement, similar to the champion devices, shown in Figure 5.7.

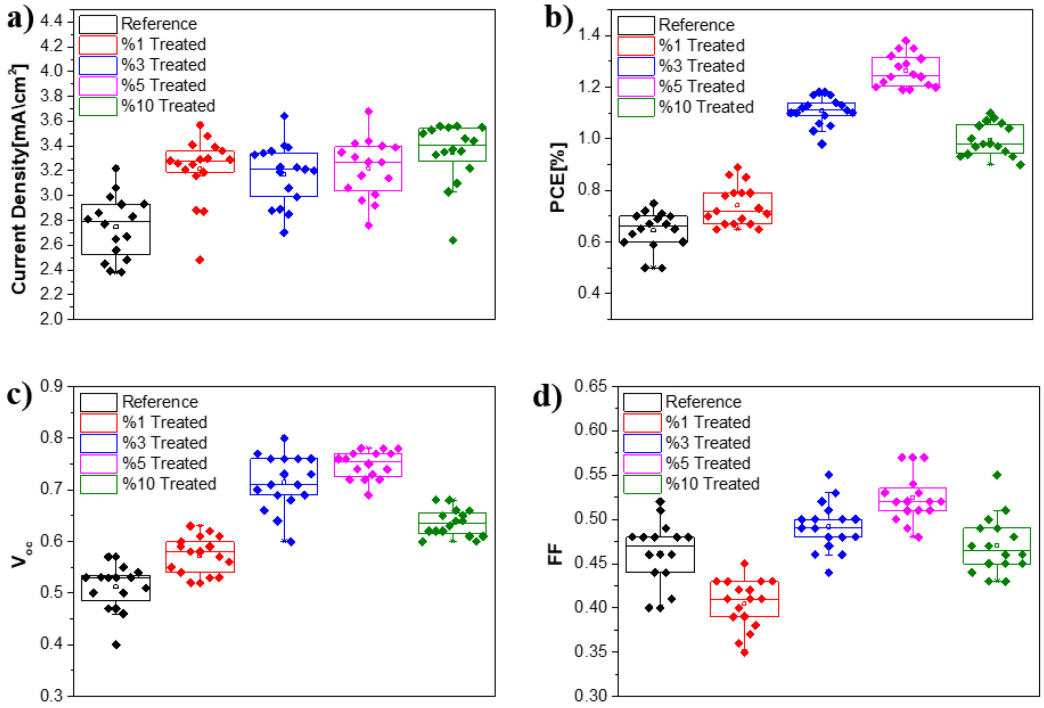

Figure 5.7 Chart-box presentation of current density a), PCE (b), V_{oc}(c), and fill factor (d), of 70 (reference and treated ones, totally) reference (without polymer treatment) and bulk-treated (from %1 to %10 Tretaed) with the increasing amount of polymer solar cell devices, conducted in 5 different experimental runs, each experiments with same number of solar cell devices.

To assess the impact of bulk passivation on trap-density using the space-charge limited current (SCLC) method, electron-only devices were fabricated with the device structure of glass/FTO/c,m-TiO_2/ Ag_3BiI_6 with or without polymer/PCBM/Au. The dark current-voltage (J-V) characteristics of both electron-only devices, the reference (without polymer) and the polymer-treated one (with %5 wt polymer treated), are presented in Figure 5.8b.

Table 1. Photovoltaic parameters for the champion devices. The reverse scan values are reported in parentheses.

Sample	J_{sc} [mA/cm^2]	V_{oc} [V]	*FF* [%]	PCE [%]	Hysteresis %
Reference (RS*)	2.93 (2.85)	0.53 (0.42)	49 (38)	0.76 (0.45)	41 %
Polymer treated %5 (RS*)	3.44 (3.42)	0.75 (0.73)	53 (51)	1.37 (1.27)	7%

* RS: Reverse Scans

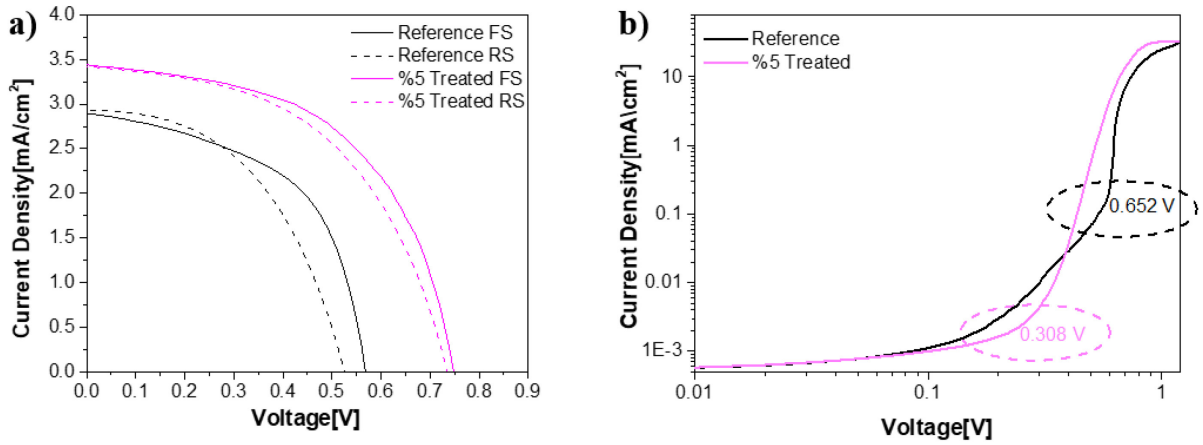

Figure 5.8 a) *J–V* characteristics of the best reference, and polymer treated (5%) PSC devices b) dark *J-V* characteristics of electron-only devices of the reference, and polymer treated (5%).

Trap-density can be determined using the following equation:

$$n_t = 2\varepsilon\varepsilon_0 V_{TFL}/eL^2$$

Where ε and ε_0 represent the dielectric constants of the Ag_3BiI_6 and vacuum, respectively. L is the thickness of the Ag_3BiI_6 films, e is the elementary charge, and V_{TFL} is the trap-filled limit voltage. The linear region at low bias corresponds to the ohmic response. Beyond the low bias voltage, after the kink points denoting filled trap states (marked with black and magenta dashed circles for reference and polymer-treated electron-only devices, respectively), both devices exhibit a sudden nonlinear increase in current response, signifying the onset of the SCLC region. The calculated trap-densities (n_t) for the reference and polymer-treated films are XX × 10^{15} and XX × 10^{15} cm^{-3}, respectively, indicating that bulk passivation reduces the trap-density.

To evaluate the stability of the devices, both the unencapsulated polymer-treated one (with 5%) and the reference devices were subjected to a relative humidity of 40–45% at room temperature. As shown in Figure 5.9a, the polymer-treated device retained 78% of its initial PCE after 30 days (720 hours), while the reference device retained 27%.

Our investigation further delved into the performance of the unencapsulated polymer treated and reference devices under continuous 1-sun illumination at a fixed temperature of 60 °C for 24 hours to evaluate light-thermal stability (Figure 5.9b). The results were even more compelling. Under these rigorous conditions, the treated device retained a staggering 93.3% of its initial PCE, while the reference device struggled at 12.5%. These findings underscore the pivotal role of defect passivation through the polymer bulk treatment in not just impacting device performance, but also in significantly enhancing device stability, a crucial factor for the application of the Ag_3BiI_6-based solar cells.

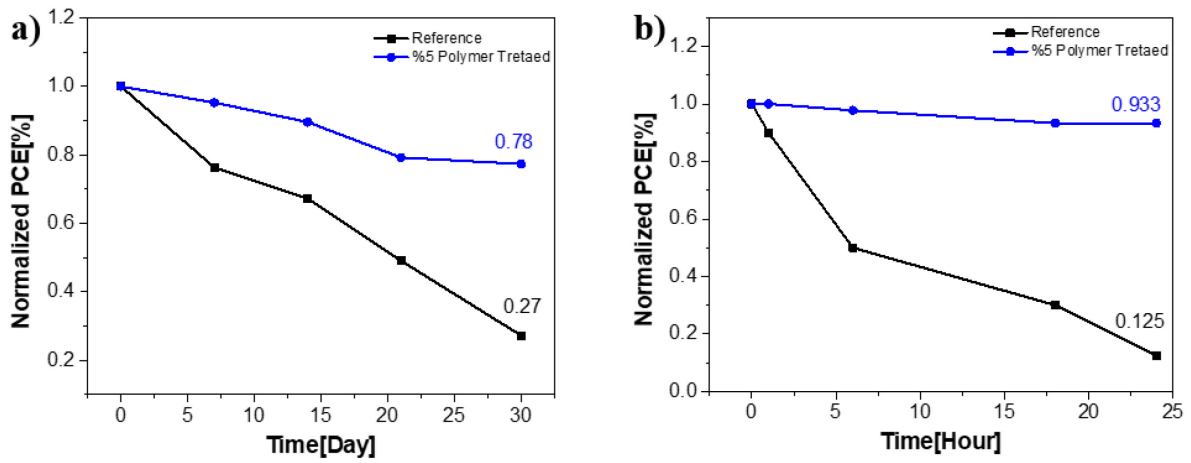

Figure 5.9 a) Long-term stability, and b) light-thermal stability of reference, polymer tretaed (5% wt) devices.

5.3 Conclusions

In summary, we have successfully applied a bulk polymer treatment approach to enhance the efficiency and stability of Ag_3BiI_6-based solar cells. This treatment serves a dual purpose. Firstly, it effectively mitigates detrimental defects within the bulk structure of Ag_3BiI_6, which negatively impact the photovoltaic performance and stability of the devices. Secondly, it improves uniformity while minimizing the presence of pinholes in the films.

As a result, the polymer-treated devices have demonstrated a remarkable performance improvement, with the top-tier power conversion efficiency (PCE) reaching 1.38%. This improvement is attributed to

the effective passivation of mono and double halide vacancy defects (under-coordinated silver/bismuth ions) within the bulk structure of Ag_3BiI_6, which are responsible for non-radiative recombination and voltage losses.

Furthermore, under conditions of 40-45% relative humidity at room temperature, the unencapsulated bulk-passivated devices have exhibited significantly enhanced stability compared to untreated reference devices. Additionally, the bulk polymer treated Ag_3BiI_6 device exhibited the highest light-thermal stability, retaining 93.3% of its initial efficiency after continuous light exposure for 24 hours compared with its reference form, with retained 12.5% of its initial performance. Polymer treatment concepts not only enhance their efficiency but also, in addition to shelf stability, make the treated device under harsh conditions. This work represents a substantial step towards enhancing the performance and stability of Silver-Bismuth Halides, particularly Ag_3BiI_6-based solar cells.

5.4 References

1. NREL. Chart of Best Research-Cell Efficiencies Provided by NREL, https://www.nrel.gov/pv/cell-efficiency.html.
2. Torabi, N., Behjat, A., Zhou, Y., Docampo, P., Stoddard, R. J., Hillhouse, H. W., & Ameri, T. (**2019**). Progress and challenges in perovskite photovoltaics from single-to multi-junction cells. *Materials Today Energy*, *12*, 70-94.
3. Ding, G., Zheng, Y., Xiao, X., Cheng, H., Zhang, G., Shi, Y., & Shao, Y. (**2022**). Sustainable development of perovskite solar cells: Keeping a balance between toxicity and efficiency. *Journal of Materials Chemistry A*, *10*(15), 8159-8171.
4. Krishnamoorthy, T., Ding, H., Yan, C., Leong, W. L., Baikie, T., Zhang, Z., ... & Mhaisalkar, S. G. (**2015**). Lead-free germanium iodide perovskite materials for photovoltaic applications. *Journal of Materials Chemistry A*, *3*(47), 23829-23832.
5. Zhu, Z., Jiang, X., Yu, D., Yu, N., Ning, Z., & Mi, Q. (**2022**). Smooth and compact $FASnI_3$ films for lead-free perovskite solar cells with over 14% efficiency. *ACS Energy Letters*, *7*(6), 2079-2083.
6. De Angelis, F. (**2021**). The prospect of lead-free perovskite photovoltaics. *ACS Energy Letters*, *6*(4), 1586-1587.
7. Tress, W., & Sirtl, M. T. (**2022**). $Cs_2AgBiBr_6$ Double Perovskites as Lead-Free Alternatives for Perovskite Solar Cells?. *Solar RRL*, *6*(2), 2100770.

8. Lei, H., Hardy, D., & Gao, F. (**2021**). Lead-free double perovskite $Cs_2AgBiBr_6$: fundamentals, applications, and perspectives. *Advanced Functional Materials*, *31*(49), 2105898.
9. Liu, Y., Nag, A., Manna, L., & Xia, Z. (2021). Lead-free double perovskite $Cs_2AgInCl_6$. *Angewandte Chemie*, *133*(21), 11696-11707.
10. Wei, F., Deng, Z., Sun, S., Hartono, N. T. P., Seng, H. L., Buonassisi, T., ... & Cheetham, A. K. (**2019**). Enhanced visible light absorption for lead-free double perovskite Cs 2 AgSbBr 6. *Chemical Communications*, *55*(26), 3721-3724.
11. Turkevych, I.; Kazaoui, S.; Ito, E.; Urano, T.; Yamada, K.; Tomiyasu, H.; Yamagishi, H.; Kondo, M.; Aramaki, S. Photovoltaic Rudorffites: Lead-Free Silver Bismuth Halides Alternative to Hybrid Lead Halide Perovskites. ChemSusChem **2017**, 10 (19), 3754−3759.
12. Mei, J.; Liu, M.; Vivo, P.; Pecunia, V. Two-Dimensional Antimony-Based Perovskite-Inspired Materials for High-Performance Self-Powered Photodetectors. Adv. Funct Mater. **2021**, 31 (50), 2106295.
13. Pecunia, V.; Occhipinti, L. G.; Chakraborty, A.; Pan, Y.; Peng, Y. Lead-Free Halide Perovskite Photovoltaics: Challenges, Open Questions, and Opportunities. APL Materials **2020**, 8, 100901.
14. Chakraborty, A., Pai, N., Zhao, J., Tuttle, B. R., Simonov, A. N., & Pecunia, V. (**2022**). Rudorffites and Beyond: Perovskite-Inspired Silver/Copper Pnictohalides for Next-Generation Environmentally Friendly Photovoltaics and Optoelectronics. *Advanced Functional Materials*, *32*(36), 2203300.
15. Micic, O. I., Meglic, M., Lawless, D., Sharma, D. K., & Serpone, N. (**1990**). Semiconductor photophysics. 5. Charge carrier trapping in ultrasmall silver iodide particles and kinetics of formation of silver atom clusters. *Langmuir*, *6*(2), 487-492.
16. Merker, A., Morgenroth, M., Scholz, M., Lenzer, T., & Oum, K. (**2023**). Critical Evaluation of the Photovoltaic Performance of (AgI) x (BiI3) y Thin Films from the Viewpoint of Ultrafast Spectroscopy and Photocurrent Experiments. *The Journal of Physical Chemistry C*, *127*(3), 1487-1498.
17. Buizza, L. R. V.; Sansom, H. C.; Wright, A. D.; Ulatowski, A. M.; Johnston, M. B.; Snaith, H. J.; Herz, L. M. Interplay of Structure, Charge-Carrier Localization and Dynamics in Copper-Silver-BismuthHalide Semiconductors. Adv. Funct. Mater. **2022**, 32, 2108392.
18. Iyoda, F.; Nishikubo, R.; Wakamiya, A.; Saeki, A. Ag-(Bi, Sb, In, Ga)-I Solar Cells: Impacts of Elemental Composition and Additives on the Charge Carrier Dynamics and Crystal Structures. ACS Appl. Energy Mater. **2020**, 3, 8224−8232

19. Bablich, A.; Schneider, D. S.; Kienitz, P.; Kataria, S.; Wagner, S.; Yim, C.; McEvoy, N.; Engstrom, O.; Müller, J.; Sakalli, Y.; et al. Few-Layer MoS2/a-Si:H Heterojunction Pin-Photodiodes for Extended Infrared Detection. ACS Photonics **2019**, 6, 1372−1378.

20. Park, J. W.; Lim, Y.; Doh, K.-Y.; Jung, M. T.; Jeon, Y. I.; Yang, I. S.; Choi, H.-s.; Kim, J.; Lee, D.; Lee, W. I. Enhancement of the Photovoltaic Properties of Ag2BiI5 by Cu Doping. Sustainable Energy Fuels **2021**, 5, 1439−1447.

21. Li, C., Huang, S., Min, C., Du, P., Xia, Y., Yang, C., & Huang, Q. (**2017**). Highly productive synthesis, characterization, and fluorescence and heavy metal ion adsorption properties of poly (2, 5-dimercapto-1, 3, 4-thiadiazole) nanosheets. *Polymers*, *10*(1), 24.

22. AYDOĞDU, Gözde, et al. A novel electrochemical DNA biosensor based on poly-(5-amino-2-mercapto-1, 3, 4-thiadiazole) modified glassy carbon electrode for the determination of nitrofurantoin. *Sensors and Actuators B: Chemical*, **2014**, 197: 211-219.

23. Revin, S.B.; John, S.A. Electropolymerization of 3-amino-5-mercapto-1,2,4-triazole on glassy carbon electrode and its electrocatalytic activity towards uric acid. *Electrochim. Acta* **2011**, *56*, 8934–8940.

24. Pai, Narendra, et al. Silver bismuth sulfoiodide solar cells: tuning optoelectronic properties by sulfide modification for enhanced photovoltaic performance. *Advanced Energy Materials*, **2019**, 9.

5.5 Experimental Section

1. Materials and reagents

The c, and m-TiO_2 (Titanium(IV) isopropoxid, and Titania paste-transparent) precursors were purchased from Sigma-Aldrich. The passivating polymer precursors – 2,5-dimercapto-1,3,4-thiadiazole, and its oxidant (I_2) – were purchased from Sigma-Aldrich. The Ag_3BiI_6 precursors – AgI and BiI_3 – were purchased from Sigma-Aldrich and TCI, respectively. The Poly(3-hexylthiophene-2,5-diyl) (P3HT) as an HTL material was purchased from Sigma-Aldrich. Solvents used for perovskite film fabrication were purchased from Sigma-Aldrich.

2. Solar cell fabrication

The Zn powder and 4M HCl assisted, patterned FTO (15 ohm, 3cm x 3cm) substrates were rinsed with deionized water. The rinsed substrates were sonicated in 2% *detergent* solution, DI water, acetone, and isopropanol for 15 min, respectively. Subsequently, the dried substrates were further cleaned with ultraviolet ozone treatment for 15 min before A compact TiO_2 coating. A compact TiO_2 layer was produced using a sol-gel precursor solution. To prepare the sol-gel solution, 35 µL of 2 M HCl was added dropwise to a solution containing 370 µL of titanium-isopropoxide in 2.53 mL of dry 2-propanol, all while vigorously stirring. The process involved applying 100 µL of the solution onto 3 cm × 3 cm substrates through spin-coating for 45 seconds at 2000 rpm. Subsequently, the coated substrates were calcinated at 500 °C for 30 minutes in an air environment, resulting in the formation of a 30-40 nm thick compact TiO_2 layer. Following the deposition of the compact TiO_2 layer, the next step involved applying 100 µL of a dispersion containing mp-TiO_2 nanoparticles (a mixture of 6 parts ethanol to 1 part TiO_2 paste) through spin-coating for 30 seconds at 5000 rpm. The coated substrates were then calcined at 500 °C for 30 minutes in an air environment, leading to the formation of a 150-200 nm thick mp-TiO_2 layer. After cooling, the photo-active layer (with and, without polymer) was applied on top of the TiO_2 layer in an N_2-filled glove box.

Using the gas "gas-assisted(N_2)" method, the precursors of the Silver-Bismuth Halides (with, without polymer precursors) – AgI (0.9M, 211.3 mg), BiI_3 (0.3 M, 176.9 mg), with the increasing content (for monomer, from 1% (3.88 mg) to 10% (38.8 mg) weight ratio of total amount of the Ag_3BiI_6 precursors) of monomer (x mol) with its oxidant (I_2, 1.5x mol) in 1 of mL DMSO:DMF mixture (3:1) – were deposited on top of the c,m-TiO_2 layer at 6000 rpm for 40 s. Nitrogen (N_2) was flown over the spinning substrate between 10 and 40 s of coating process. The resultant films were annealed in an N_2-filled glove box at 60 °C for 1, and 140 °C 15 min. on hotplate, and then allowed to cool to ambient temperature naturally. The HTM was deposited by spin-coating (5000 rpm for 30 s) a solution of P3HT, which is 15 mg in 1 ml chlorobenzene. Subsequently, after the hole transport material (HTM) coating, the samples underwent an additional annealing step at 120 °C for 10 minutes. Finally, a 60 nm thin

layer of gold (Au) was thermally evaporated onto the top of the hole transport layer under high vacuum conditions.

3. General Characterization Techniques:

UV–vis spectra were recorded using a Perkin Elmer Lambda 1050 spectrometer with an integrating sphere. Time-resolved photoluminescence (TRPL) spectroscopy was performed with a Picoquant Fluotime 300 spectrofluorometer, using an excitation wavelength of 375 nm. Current-Voltage (*J-V*) curves were measured under ambient conditions using a Newport OrielSol 2A solar simulator with a Keithley 2400 source meter under simulated AM 1.5G sunlight, with an incident power of 100 mW cm^{-2}, calibrated with a Fraunhofer ISE certified silicon cell (KG5-filtered). The active area of the solar cells was defined by a square metal aperture mask of 0.0831 cm^2. *J-V* curves were recorded by scanning the input bias from -0.1 V to 0.85 V (forward scan) at a scan rate of 0.1 V/s after the devices had been at 0.85 V for 5 s under illumination. For the light intensity-dependent *J-V*-measurements, a white light LED was used as illumination. The LED intensity was adjusted with a Keithley 2200-20-5 Power Supply.

XRD

X-Ray Diffraction (XRD) measurements were performed with a Bruker D8 Discover X-ray diffractometer operating at 40 kV and 30 mA, employing Ni-filtered Cu Kα1 radiation (λ = 1.5406 Å) and a position-sensitive LynxEye detector.

SEM

For SEM as well as for the preparation of SEM cross-sections and STEM samples, a FEI Helios Nanolab G3 UC DualBeam equipped with an Oxford Aztec Advanced X-Max 80 EDX detector was used. SEM images were recorded at an acceleration voltage of 2 kV. Cross-sectional images were recorded with a backscatter electron detector, top view images were recorded with both a backscatter electron detector and secondary electron through-the-lens detector. For surface protection of SEM cross-sections, a ~ 2 nm thick carbon layer, followed by electron– and ion-induced platinum layers were deposited. The cross-sections were prepared using Ga^+-ions cutting not at a right angle but at 52° degrees. EDX maps were recorded at 5 keV electron energies, thereby achieving a relatively good spatial compositional resolution. A drawback of this setting is the low sensitivity for Iodine L-series X-rays (at around 3.9 keV).

4. Polymerization of 2,5-dimercapto-1,3,4-thiadiazole

The following is the usual synthesis of PBT (polybenzothiadiazole): With constant stirring, 30 mg (0.2 mol) of BT monomer was dissolved in 1 millilitre of absolute ethanol. After that, the mixture was moved

to a 10-millilitre conical flask with a glass stopper and agitated at 25 °C. The flask was then filled dropwise with 3 millilitres of an ethanol solution containing 76.4 mg (0.3 mmol) of I2. After adding the oxidant solution, the solution's colour changed from pale yellow to brown-black, and polymer precipitation was evident within two to three minutes. To ensure that all monomers had polymerized, the reaction was allowed to run for a full day. Twenty millilitres of deionized water were added to the reaction mixture to aid in the precipitation of the polymer once the reaction was finished. Centrifugation was used to separate the polymer precipitates, and after that, ethanol and deionized water were completely diluted until the washing solution had a light or colourless consistency. PBT nanosheet powders were then produced by drying the polymer precipitates for an entire night at 60 °C at room temperature.

6 Conclusion

In this thesis, our central emphasis was on conducting exhaustive research on the defects manifesting at the surfaces and grain boundaries of polycrystalline lead-based perovskite materials and lead-free silver-bismuth halides. These defects substantially adversely influence the performance and durability of photovoltaic devices utilizing these materials. To counteract these inevitably occurring defects, which are the products of the low-temperature solution-based processing methods, we investigated various materials and concepts to devise potential solutions for these challenges.

In the surface passivation of the lead-based perovskite films, 1,10-phenanthroline, a bidentate chelating ligand, was successfully implemented to address two critical issues. Firstly, it was used to remediate detrimental defects on the surfaces of $MAPbI_3$ that negatively impact the photovoltaic performance and stability of corresponding devices. Secondly, 1,10-phenanthroline was employed to convert excess or unreacted PbI_2, which is also detrimental to the long-term stability of solar cell devices, into beneficial species (PbI_2(1,10-phen)$_x$, where x can be 1 or 2) for efficient hole transfer at the modified interface.

Our study utilized advanced techniques such as nano-Fourier transform infrared (nano-FTIR) spectroscopy and high-angle annular dark-field scanning transmission electron microscopy (HAADF-STEM) to confirm the surface coverage of the treated films with PbI_2(1,10-phen)$_x$ complexes. This coverage was observed to form two different morphologies: platelet-shaped formations and very thin capping layers with the same chemical composition.

As a result, the 1,10-phenanthroline-treated devices exhibited remarkable improvements, with a champion power conversion efficiency (PCE) of 20.16%, a Voc of 1.13 V, Jsc of 22.58 $mAcm^{-2}$, and a fill factor (FF) of 79%. These substantial enhancements were attributed to the passivation of both mono and double halide vacancy defects (under-coordinated lead ions) at the perovskite surface, as well as the converting of excess/unreacted lead iodide (PbI_2) into beneficial complexes.

Moreover, under the conditions of a relative humidity of 40–45% at room temperature, the unencapsulated passivated device demonstrated significantly higher stability compared to the untreated reference device. This demonstrates how our method may be used to improve perovskite solar cells' stability, which is essential for their widespread use.

Then, our research focused on the development and application of a novel thiophene-based organic spacer, ThPyI, with a heterocyclic structure in perovskite solar cells. This organic spacer served a dual role as a defect passivator and an organic spacer in both surface- and bulk-passivated 3D methylammonium lead iodide (MAPI)-based perovskite devices.

Our findings indicated that the ThPyI organic spacer is a promising candidate for the creation of a new 1D perovskitoid phase, which is really stable even in water, on the surface, as well as in the bulk of the 3D perovskite films. Time-resolved photoluminescence (TRPL) results showed that the fluorescence lifetimes in both passivated devices increased, contributing to improved device performance. Additionally, the ThPyI-treated perovskite devices exhibited high efficiency and environmental stability when compared to their 3D counterparts. Notably, the bulk-passivated 3D photovoltaic devices demonstrated superior environmental and light-thermal stability, even when compared to the surface-passivated devices.

Crucially, our novel organic spacer played a crucial role in promoting the preferred orientation of the 3D perovskite slabs, with a vertical orientation of the (110) planes relative to the substrate. This orientation enhancement was achieved more efficiently with ThPyI than with the commonly used MACl additive. Our study contributes to the knowledge of thiophene-based organic spacers and offers a fresh perspective on organic spacer design.

Our findings open the door for a rational strategy in the design of organic agents that can serve multiple functions, acting as defect passivators, crystalline orientation promoters, and organic spacers in various perovskite-based solar cells.

In the passivation of the alternative lead-free solar cell concept, a bulk polymer treatment approach was successfully employed to enhance the efficiency and stability of Ag_3BiI_6-based solar cells. In this bulk-treatment concept, increasing amounts of monomer and its oxidant (I_2) were added to the Ag_3BiI_6 precursor solution to form in-situ polymerization. This approach served a multifunctional purpose. Firstly, it effectively mitigated detrimental defects, which had a negative impact on the photovoltaic performance and stability of the devices within the bulk structure of Ag_3BiI_6. Secondly, it improved the uniformity of the films while minimizing the presence of pinholes.

As a result, the polymer-treated devices exhibited a remarkable improvement in performance, with the highest power conversion efficiency (PCE) reaching 1.38%, causing a 79 % improvement compared to the reference. This improvement was attributed to the effective passivation of mono and double halide vacancy defects (under-coordinated silver/bismuth ions) within the bulk structure of Ag_3BiI_6, which were responsible for non-radiative recombination and voltage losses.

Furthermore, under conditions of 40-45% relative humidity at room temperature, the unencapsulated bulk-passivated devices demonstrated significantly enhanced stability when compared to untreated reference devices. Notably, the bulk-polymer-treated Ag_3BiI_6 device exhibited the highest light-thermal stability, retaining 93.3% of its initial efficiency after continuous light exposure for 24 hours, in contrast to its reference counterpart, which retained only 12.5% of its initial efficiency. This polymer treatment not only enhanced the efficiency of the devices but also significantly improved their shelf stability and resilience under harsh conditions.

Overall, our works presented in this thesis represents a substantial advancement in enhancing the performance and stability of lead-based perovskite, and Silver-Bismuth Halides based solar cells, making them more viable for practical photovoltaic applications.

7 Publications

In-situ Polymerized 2,5-dimercapto-1,3,4-thiadiazole as a Bulk Defect Passivation Agent for Enhanced Longevity and Performance of Ag_3BiI_6 Photovoltaics

Ali Buyruk,…, Achim Hartschuh,Thomas Bein, and, Tayebeh Ameri, *Manuscript in preparation*

A Novel Multi-Functional Thiophene-Based Organic Cation as Passivation, Crystalline Orientation, and Organic Spacer Agent for Low-Dimensional 3D/1D Perovskite Solar Cells.

Ali Buyruk, Ali Semerci, Saim Emin, Rik Hooijer, Daniela Kovacheva, Peter Mayer, Manuel A Reus, Dominic Blätte, Marcella Günther, Nicolai F Hartmann, Soroush Lotfi, Jan P Hofmann, Peter Müller-Buschbaum, Thomas Bein, Tayebeh Ameri, *Advanced Optical Materials*, **2023**, 2300267.

Hydrophobic graphene quantum dots for defect passivation and enhanced moisture stability of $CH_3NH_3PbI_3$ perovskite solar cells.

Elahe Khorshidi, Behzad Rezaei, Dominic Blätte, Ali Buyruk, Manuel A Reus, Jonas Hanisch, Bernhard Böller, Peter Müller-Buschbaum, Tayebeh Ameri, *Solar RRL*, **2022**, 6.7: 2200023.

The Influence of CsBr on Crystal Orientation and Optoelectronic Properties of $MAPbI_3$-Based Solar Cells

Yuqin Zou, Shuai Yuan, Ali Buyruk, Johanna Eichhorn, Shanshan Yin, Manuel A Reus, Tianxiao Xiao, Shambhavi Pratap, Suzhe Liang, Christian L Weindl, Wei Chen, Cheng Mu, Ian D Sharp, Tayebeh Ameri, Matthias Schwartzkopf, Stephan V Roth, Peter Müller-Buschbaum, *ACS Applied Materials & Interfaces*, **2022**, 14.2: 2958-2967.

Tailoring ordered mesoporous titania films via introducing germanium nanocrystals for enhanced electron transfer photoanodes for photovoltaic applications

Nian Li, Renjun Guo, Wei Chen, Volker Körstgens, Julian E Heger, Suzhe Liang, Calvin J Brett, Md Asjad Hossain, Jianshu Zheng, Peter S Deimel, Ali Buyruk, Francesco Allegretti, Matthias Schwartzkopf, Jonathan GC Veinot, Guido Schmitz, Johannes V Barth, Tayebeh Ameri, Stephan V Roth, Peter Müller-Buschbaum, *Advanced functional materials*, **2021**, 31.34: 2102105.

1,10-Phenanthroline as an Efficient Bifunctional Passivaing Agent for $MAPbI_3$ Perovskite Solar Cells

Ali Buyruk, Dominic Blätte, Marcella Günther, Manuel A Scheel, Nicolai F Hartmann, Markus Döblinger, Andreas Weis, Achim Hartschuh, Peter Müller-Buschbaum, Thomas Bein, Tayebeh Ameri, *ACS Applied Materials & Interfaces*, **2021**, 13.28: 32894-32905.

Sodium dodecylbenzene sulfonate interface modification of methylammonium lead iodide for surface passivation of perovskite solar cells

Yuqin Zou, Renjun Guo, Ali Buyruk, Wei Chen, Tianxiao Xiao, Shanshan Yin, Xinyu Jiang, Lucas P Kreuzer, Cheng Mu, Tayebeh Ameri, Matthias Schwartzkopf, Stephan V Roth, Peter Müller-Buschbaum, *ACS applied materials & interfaces*, **2020**, 12.47: 52643-52651.

Tailoring the orientation of perovskite crystals via adding two-dimensional polymorphs for perovskite solar cells

Renjun Guo, Ali Buyruk, Xinyu Jiang, Wei Chen, Lennart K Reb, Manuel A Scheel, Tayebeh Ameri, Peter Müller-Buschbaum, *Journal of Physics: Energy*, **2020**, 2.3: 034005.

Advanced Printed Semiconductors for Energy and Electronic Applications

Tayebeh Ameri, Lili Ke, Nicola Gasparini, Rezvan Soltani, Marcella Günther, Ali Buyruk, Amir A Amin, Vid. Proc. Adv. Mater., Volume 2, Article ID 2105171 (**2021**)

8 Poster Presentation

Passivation of Defects with Organic Ammonium Salts for Efficient and Stable $MAPbI_3$ Perovskite Solar Cells

Ali Buyruk, Thomas Bein, and Tayebeh Ameri

e-conversion Conference Venice 2019

Passivation of Defects with Organic Ammonium Salts for Efficient and Stable $MAPbI_3$ Perovskite Solar Cells

Ali Buyruk, Thomas Bein, and Tayebeh Ameri

Soltech Conference Nurnberg 2019